Gas Explosion Characterization, Wave Propagation

Small-Scale Experiments

Larsen, Gunner Chr.

Publication date:
1985

Document Version
Publisher's PDF, also known as Version of record

Risø-R-525

Risø-R-525

RISØ

Gas Explosion Characterization, Wave Propagation
(Small-Scale Experiments)

G. C. Larsen

Risø National Laboratory, DK-4000 Roskilde, Denmark
August 1985

RISØ-R-525

GAS EXPLOSION CHARACTERIZATION, WAVE PROPAGATION
(Small-Scale Experiments)

G.C. Larsen

Abstract. A number of experiments have been performed with blast waves arising from the ignition of homogeneous and well defined mixtures of methane, oxygen and nitrogen, contained within spherical balloons with controlled initial dimensions.

The pressure characteristics has been studied for blast waves with and without influence from reflected waves.

The influence of obstacles in the flow field has also been treated. Both configurations with one box and two closely spaced boxes have been considered, and a wave-wave interaction

(continued on next page)

August 1985
Risø National Laboratory, DK-4000 Roskilde, Denmark

phenomenon was observed in the case of closely spaced obstacles. Moreover reflection coefficients have been established and some pressure variations over the surfaces have been observed.

An acoustic approximation has been used to model the blast wave originating from an expanding sphere. It has been demonstated, that the generated pressure pulse is very sensitive to the expansion rate. Calculated and measured data have been compared, and a reasonable agreement has been found.

INIS Descriptors: BALLOONS; CONFIGURATION INTERACTION; EXPERIMENTAL DATA; EXPLOSIONS; HOMOGENEOUS MIXTURES; METHANE; NITROGEN; OXYGEN; PRESSURE MEASUREMENT; REFLECTION; SIMULATION; WAVE PROGAGATION

ISBN 87-550-1122-5
ISSN 0106-2840

Grafisk Service Center, Risø 1985

CONTENTS PAGE

1. PREFACE

The interest in hazards originating from the explosion of large quantities of volatile solvents and combustible gases has increased considerably during the past few decades. The reasons for this is that larger and larger quantities of dangerous materials are produced, transported and consumed in the industrial part of the world, giving rise to an increased risk of a large fuel-release and subsequent ignition. This development has made it still more urgent to consider explosion loads in the design phase of nuclear power plants. However, an evident lack of knowledge in the field had demanded for a detailed analysis of the mechanisms involved.

Several research programmes have been promoted by the EEC in the last few years. These contain theoretical as well as experimental research on the subjects

- diffusion and spreading of gas clouds
- burning mechanisms and burning models
- blast wave propagation.

The present report is devoted to the last category of projects.

Several persons have supported the work. I especially wish to thank professor L. Bjørnø, Technical University of Denmark, Dr. H. Schmidt and Dr. S. Krenk, Risø National Laboratory, for their kind advices. Section 4 in this report is based on the work by Dr. Schmidt and Dr. Krenk (11).

Moreover, I want to thank Ms. Rose-Marie Poulsen and Ms. Inge Ilsøe who typed the manuscript, and Ms. Anna Taboryska and Ms. Agnete Michelsen who prepared the drawings.

Risø, May 1984

2. INTRODUCTION

This report describes a series of small-scale experiments carried out with simulated unconfined gas cloud explosions. The first part of the experiments, further described in section 3.4, concerns the pressure characteristics of an undisturbed blast wave. These results can be used as input parameters to fluid dynamic computercodes or compared with the results of computer simulations of the combustion process.

The second part of the experiments, further described in section 3.5, is devoted to the blast-wave/boundary interaction influenced by the boundary geometry. Special emphasis is put on the study of the end-effects at geometric obstacles of finite length. These results will be useful in evaluating under conditions in which a 3-dimensional calculation model reasonably can be approximated with a 2-dimensional one.

In some experiments, high-speed photography is performed, and attempts have also been made to measure particle velocities by hot wire anemometry. However, the velocities proved to be low, less than 1 $^{m}/s$, and as it was not possible to calibrate the hot wire at the test location, and no reliable formulas for transforming calibration under different temperature and pressure conditions exist for that low velocities, the measured results were discarded.

3. EXPERIMENTS

In this section the experimental programme for the small-scale experiments is outlined together with an evaluation of the results obtained.

3.1. Description of the general experimental setup

The physical surroundings for the experimental work is a tent with a ground area of 6 x 8.7 m^2 and a maximum height of 3.95 m. This tent is supplemented by a caravan for the recording instrumentation. These are illustrated in Fig. 1 below.

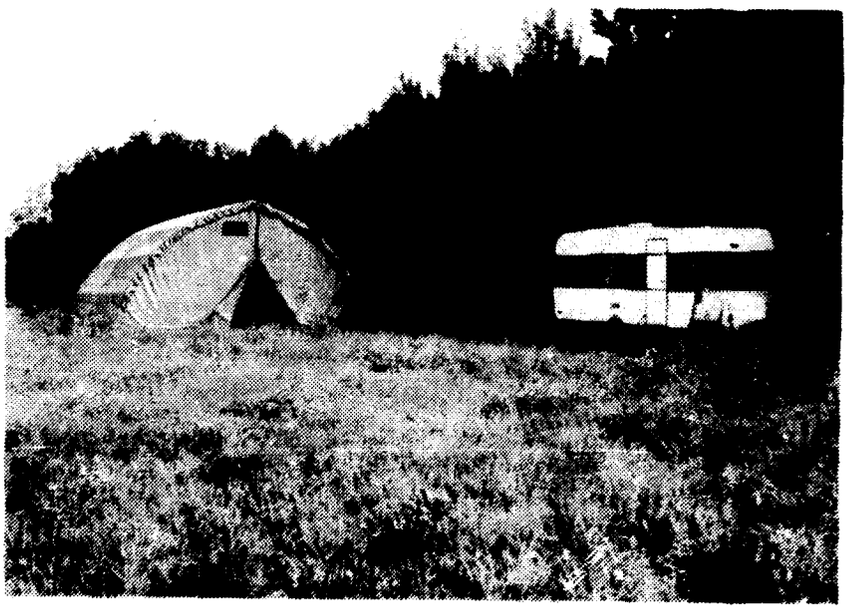

Fig. 1. The tent and caravan.

Basically, the explosions arise from the ignition of homogeneous and well-defined mixtures of methane, oxygen and nitrogen, contained within spherical balloons of controlled initial dimensions.

The gas mixture is produced in the apparatus schematically shown in Fig. 2.

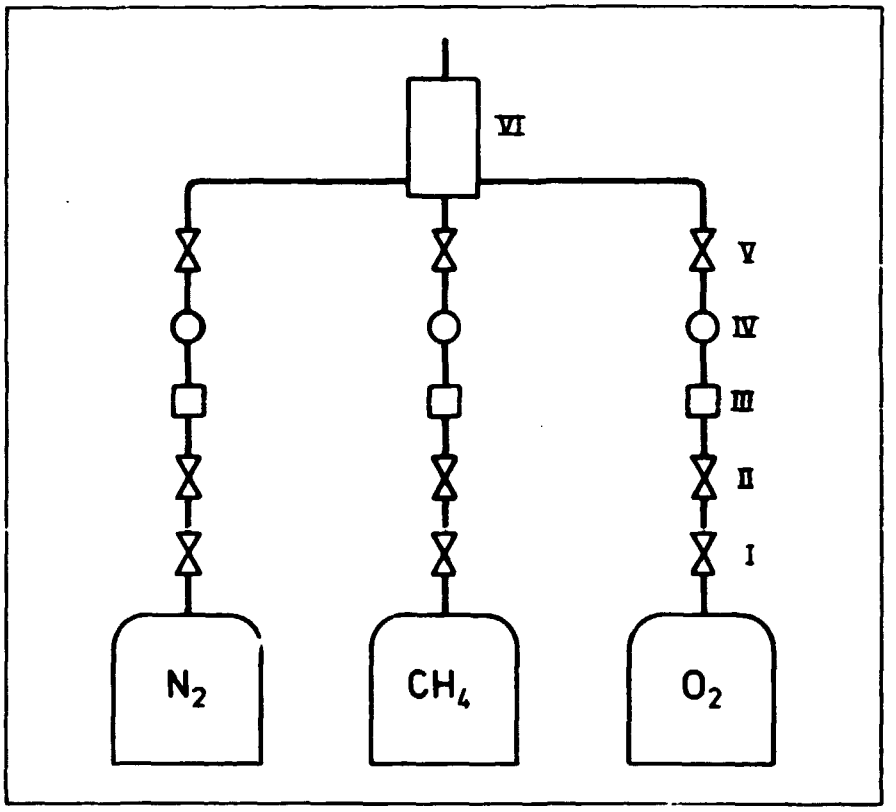

Fig. 2. The gas mixture generator.

Methane, oxygen and nitrogen are let through needle valves (I), pressure reducing valves (II), flowmeters (III), manometers (IV), and check valves (V) into a mixing chamber (VI). The mixing chamber consists of the steel tube (L = 400 mm, ø = 25 mm) filled up with a wire mesh. The resulting mixture composition is let out at the top of the tube.

The balloons are mounted on the holder schematically shown in Fig. 3.

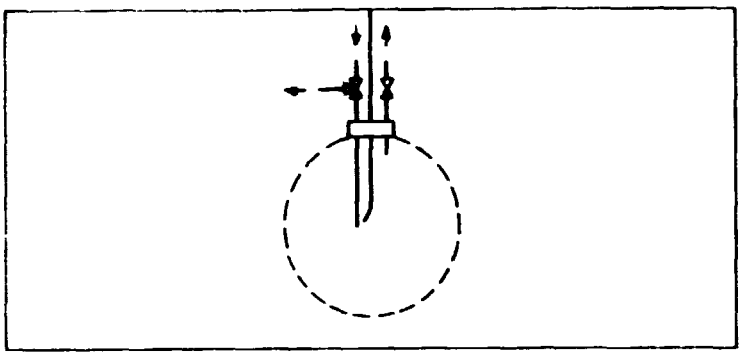

Fig. 3. The balloon holder.

A gap for producing a high voltage, low-energy ignition spark is mounted on this holder together with a fuel inlet and a fuel outlet. Valves are mounted on both the inlet and the outlet in order to get rid of the atmospheric air present in the system.

The pressure field generated by the explosion is recorded by means of pressure transducers. Three different types of pressure transducers have been used in the these experiments. Types and general data are found in Table 1 below.

TYPE	AVERAGE SENSITIVITY (mv/Pa)	FREQUENCY RANGE ± 2 DB	DIAMETER (mm)
B&K 4147	3.7	0.01 Hz - 18 kHz	12.7
B&K 4136	1.6	3.9 Hz - 70 kHz	6.4
RISØ* MADE	1.13/20	43 Hz - 1.5 kHz	16.0

TYPE	PREAMPLIFIER	AMPLIFICATION FACTOR	NUMBER OF UNITS
B&K 4147	B&K 2631	1	2
B&K 4136	B&K 2619	1	2
RISØ* MADE	RISØ MADE	20	7

Table 1. Type and data for pressure recording equipment.

* Piezoelectric ceramic transducers.

The B & K transducers are individually calibrated by means of a standard B & K pistonphone 4220 for acoustic calibration. The piezoelectric transducers are calibrated against the B & K transducers.

The particle velocity-measuring equipment consisted of a Disa 55 D05 anemometer and a Diza 55 P 11 probe. This equipment has a frequency range from 0 to 100 kHz and a noise level of approximately 0.8 mV_{Rms}.

The analogue-measuring signals are recorded on a 14-channel Ampex tape recorder. The frequency range is 0 - 10 kHz with a tape speed of 30 inch./sec.

The tape is then replayed and the signals are digitalized channel by channel through an 8-bit transient recorder (Datalab. DL 902) with a frequency range of 0 - 500 kHz. For a first check the digitized signal is shown on a oscilloscope (Tektronix T 912). Finally, the digitized signals are stored on floppy discs by means of a microcomputer system including a Commodore 8032 and a Commodore 8050.

A few of the experiments have been surveyed by a 16-mm Fastax high-speed camera.

3.2. Data analysing facilities.

The microcomputer system is connected to Risø's central computer installation, where the programs for the data processing are implemented. These programs will deliver one or more of the possibilities mentioned below

- plot of the pressure profile (pressure versus time)
- plot of the particle velocity profile (particle velocity versus time)
- plot of the impulse profile (the pressure integrated with respect to time versus time)
- plot of frequency spectra (amplitude spectrum, power spectrum, phase spectrum).

In the present analysis, the first option is most commonly used.

3.3. Preliminary experimental studies.

The modelling of the unconfined gas cloud is of course essential in experiments of this type. However, for practical reasons, it is necessary to introduce a weak confinement in order to obtain a well-defined source (size, composition, point of ignition).

Two different types of membranes have been considered in this context, partly a standard toy balloon and partly a meteorological latex balloon.

A number of pilot tests have been carried out in order to clarify the choice of the confinement. In these experiments the explosion process has been surveyed by a high-speed camera, and the pressure signal has been measured in two different directions, both located 1.90 m from the center of the charge. The experimental setup appears from Figs. 4a and 4 b.

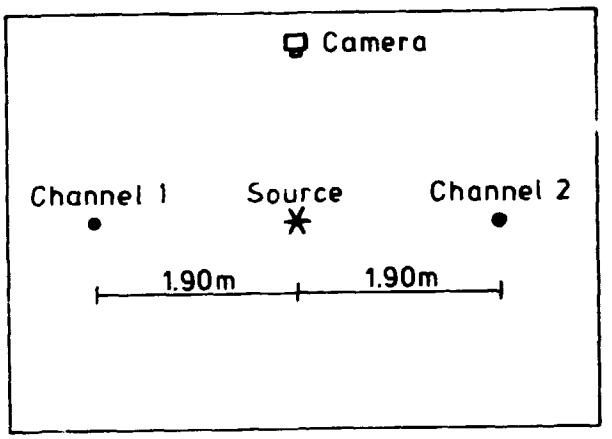

Fig. 4a. Ground plane of the experimental setup.

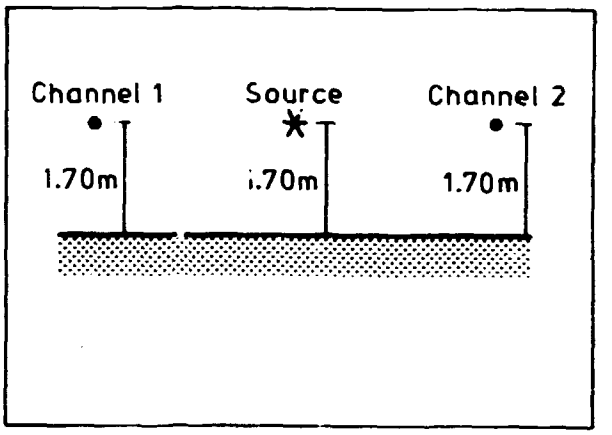

Fig. 4b. Cross section of the experimental setup.

The pressure measurements showed that the toy balloon membrane, compared to the meteorological balloons, introduced some high-frequency fluctuations in the pressure signals. Furthermore, the symmetry of the blast waves arising from the toy balloon explosions showed up to be rather poor, in contradiction to the blast waves arising from the explosions where the meteorological balloons had been used as a membrane.

The explanation of these results may be found in the high-speed films (further described in section 3.4), which showed that the behaviour of the two types of confinement was quite different in nature. The toy balloons fractured after a small increase in diameter, and consequently just in the beginning of the combustion process. This resulted in an extremely asymmetric explosion pattern probably due to the formation of an uncontrolled swirling layer in the reaction zone. The meteorological balloons expanded almost spherically-symmetric during the entire burning process, and the membrane did not fracture until it was reached by the flame front, and the combustion thus had finished.

Typical examples of the pressure profiles arising from the toy balloon explosions and the meteorological balloon explosions are shown in Figs. 5a and 5b, respectively.

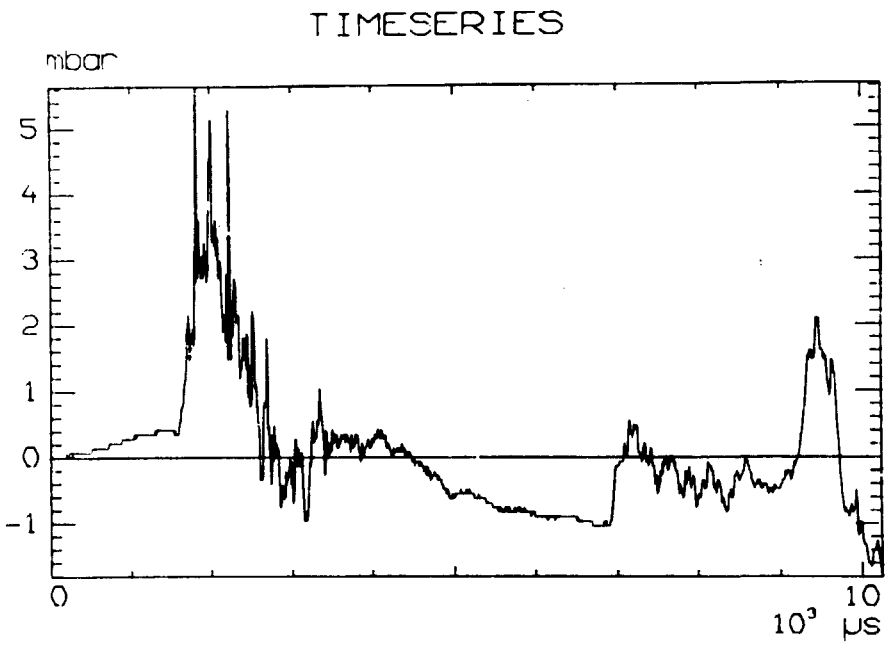

Fig. 5a. Typical pressure signal from a "toy balloon explosion".

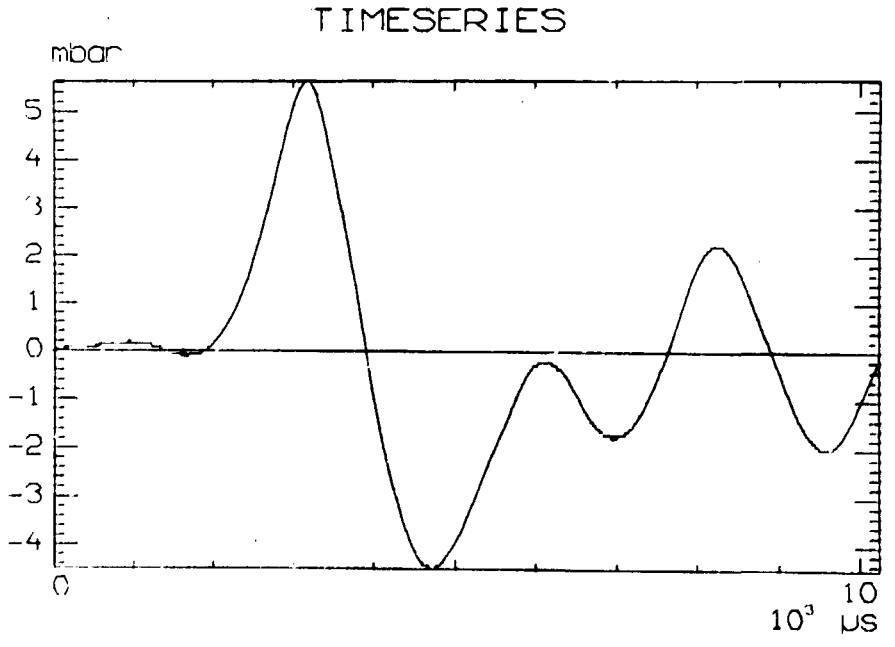

Fig. 5b. Typical pressure signal from a "meteorological balloon explosion".

In order to obtain spherical-symmetric blast waves it was decided to use meteorological balloons throughout the rest of the experiments. These were manufactured by Phillips Rubber LTD., and the relevant product data appears from Table 2 below.

BALLOON SIZE (g)	APPLIED UNSTRECHED DIAMETER (mm)	MINIMUM BURSTING DIAMETER (AT GROUND LEVEL) (m)
30	220	1.067

Table 2. Balloon data.

In relation to the reproducibility of the experiments the most reasonable choice of mixture is a stochiometric one, as the burning velocity (and thus the energy transformation) for these are relatively insensitive for small changes in the mixture composition (1). It has been decided to operate with a mixture consisting of 15.8% methane, 31.6% oxygen and 52.6% nitrogen, which appeared to produce peak pressures of suitable levels.

However, in spite of the use of a stochiometric mixture, the reproducibility of the source strength showed up to be unsatisfactory, and consequently it was decided to operate with fixed pressure reference measuring points in the future experiments. The recorded pressure signals will then be normalized with respect to the reference measurements, which is characteristic of a particular experiment. Having eliminated the variations in the strength of the explosion, it is thus possible to compare the experiments mutually.

3.4. Source characteristics.

A total of 8 experiments, surveyed by the Fastax 16-mm high-speed camera, have been carried out in order to investigate the source characteristics, i.e. the deformation of the meteorological balloons during the explosion process.

Two parameters have been varied in this series of experiments - the diameter of the source and composition of the gas-

mixture. The specific data for each experiment appears from Table 3.

EXPERIMENT NO.	MIXTURE (Vol.%) CH_4	O_2	N_2	INITIAL CHARGE DIAMETER (cm)	PICTURES/SEC.
69	16	32	52	25	2400
70	16	32	52	25	2500
71	16	32	52	25	2600
73	16	32	52	30	2500
74	16	32	52	35	2600
75	15	35	50	25	2500
76	14	39	47	25	6000
77	13	45	42	25	5500

Table. 3. Experimental data.

A sequence from one of the films (corresponding to experiment no. 71) is shown in Fig. 6.

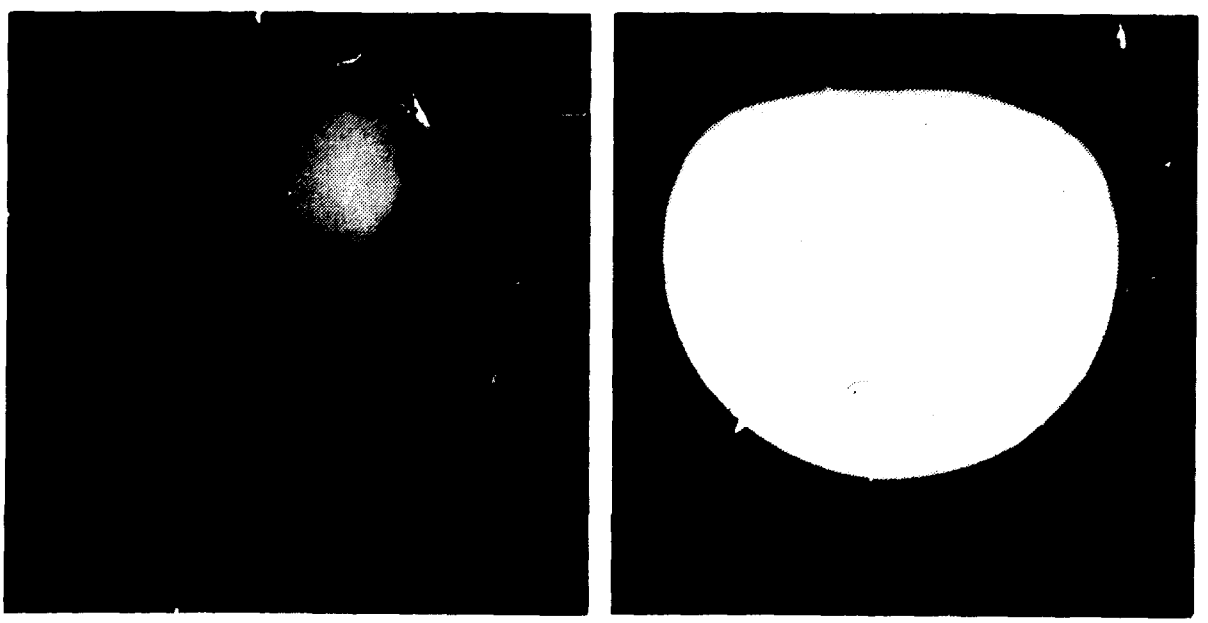

t = 0

t = 6.9 ms

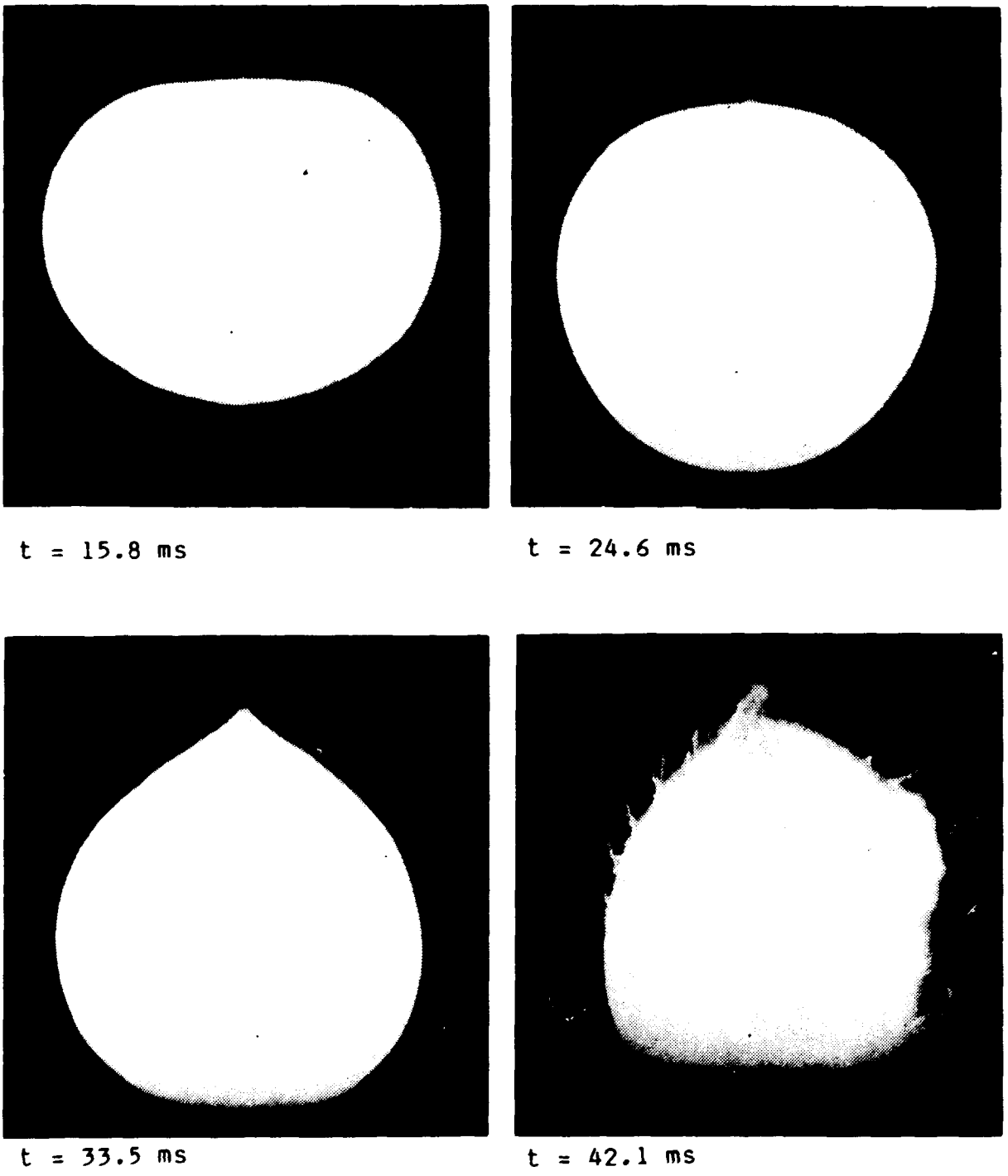

Fig. 6. High-speed photographies of the balloon deformation process.

The balloon has a fixed point on the circumference during the expansion, and as a consequence the balloon deformation is not perfectly spherically symmetric. The resulting deformation is a spherically symmetric expansion superimposed by vertical oscillations as shown in Fig. 6. On the basis of the high-speed films the vertical and horizontal "diameter" of the balloons have been plotted as functions of time.

These curves are shown in Figs. 7-14.

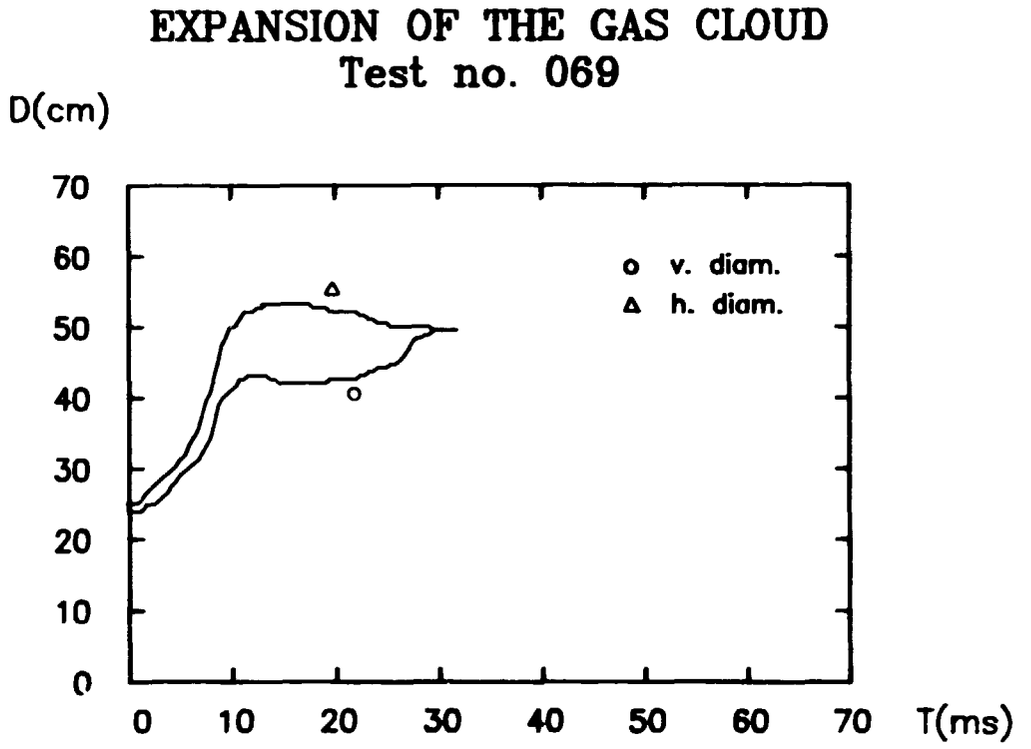

Fig. 7. Expansion of the gas cloud.

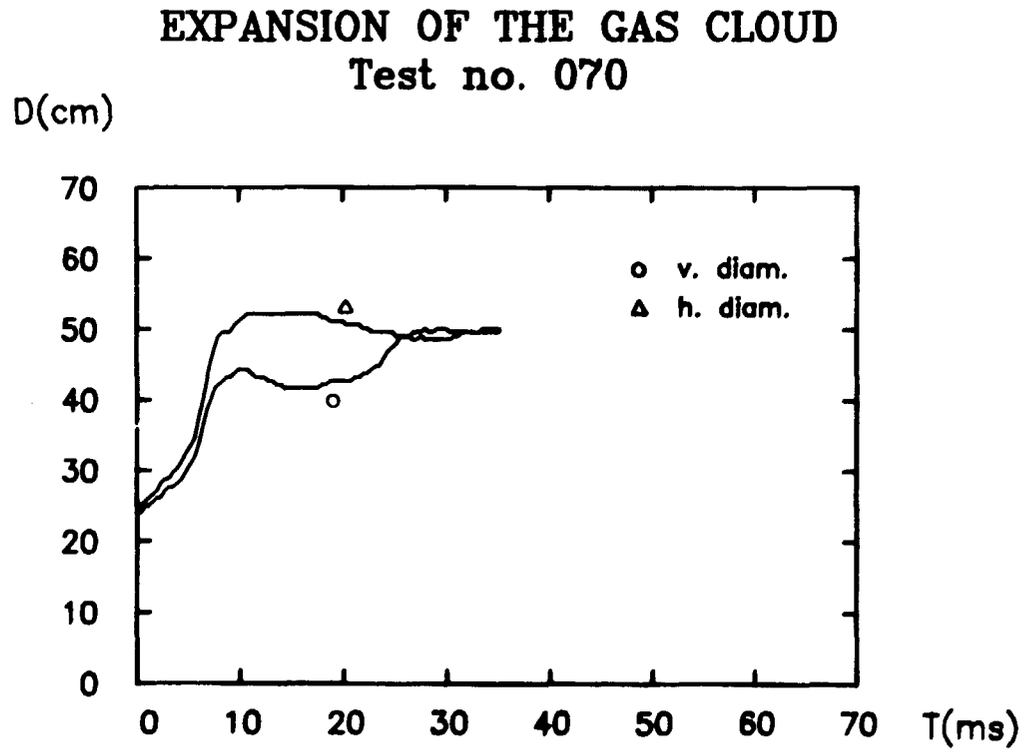

Fig. 8. Expansion of the gas cloud.

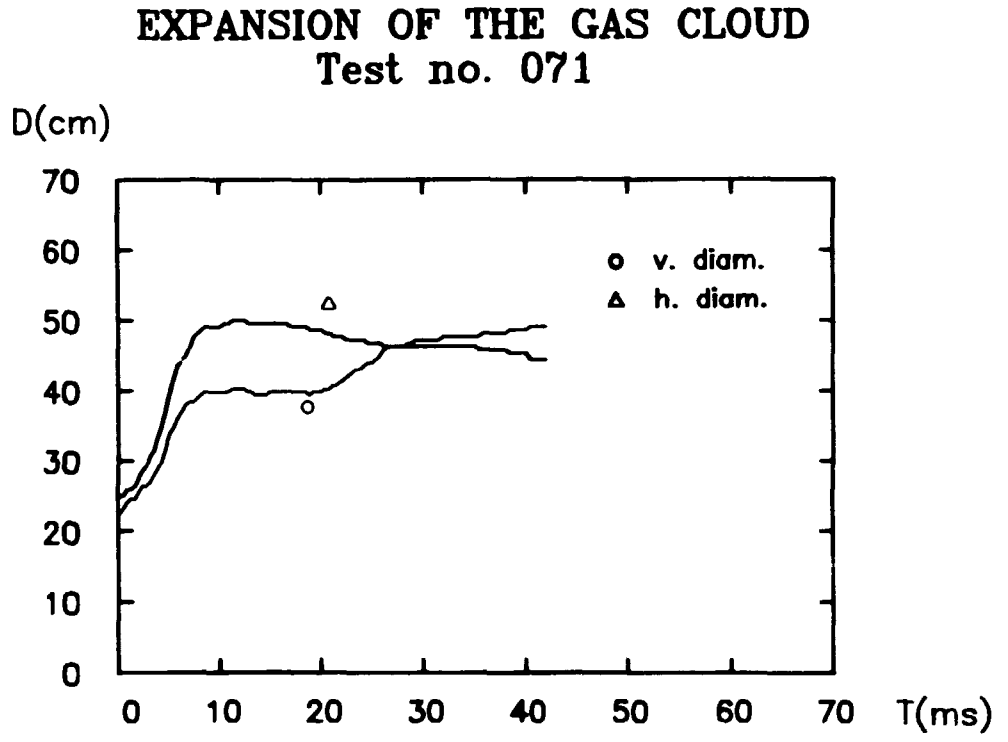

Fig. 9. Expansion of the gas cloud.

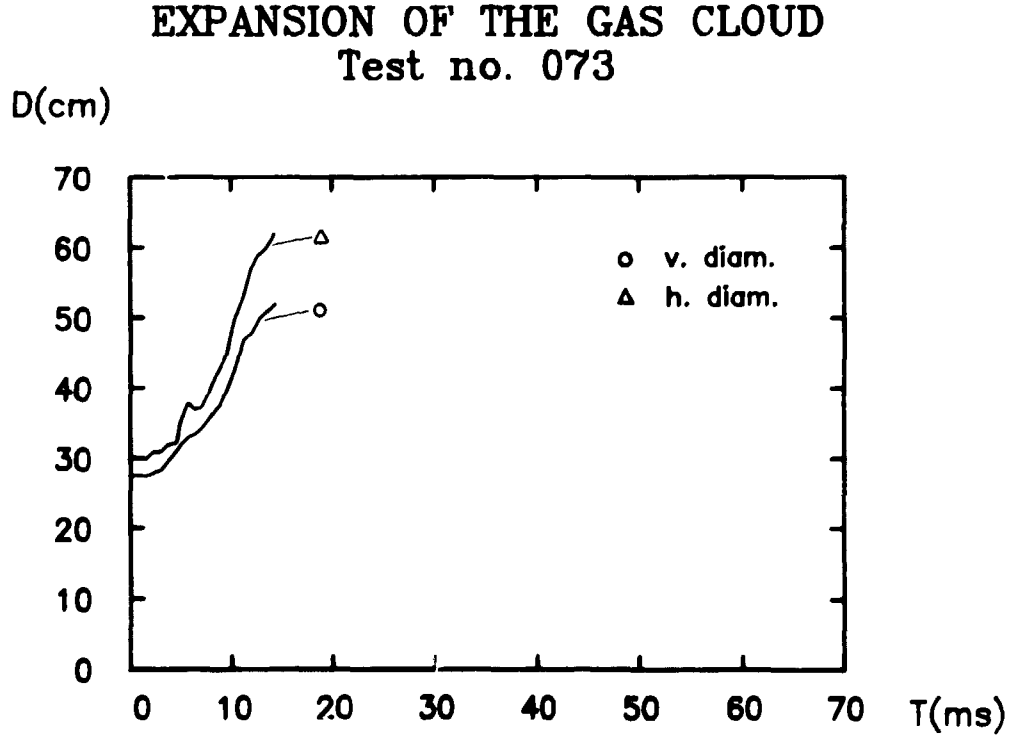

Fig. 10. Expansion of the gas cloud.

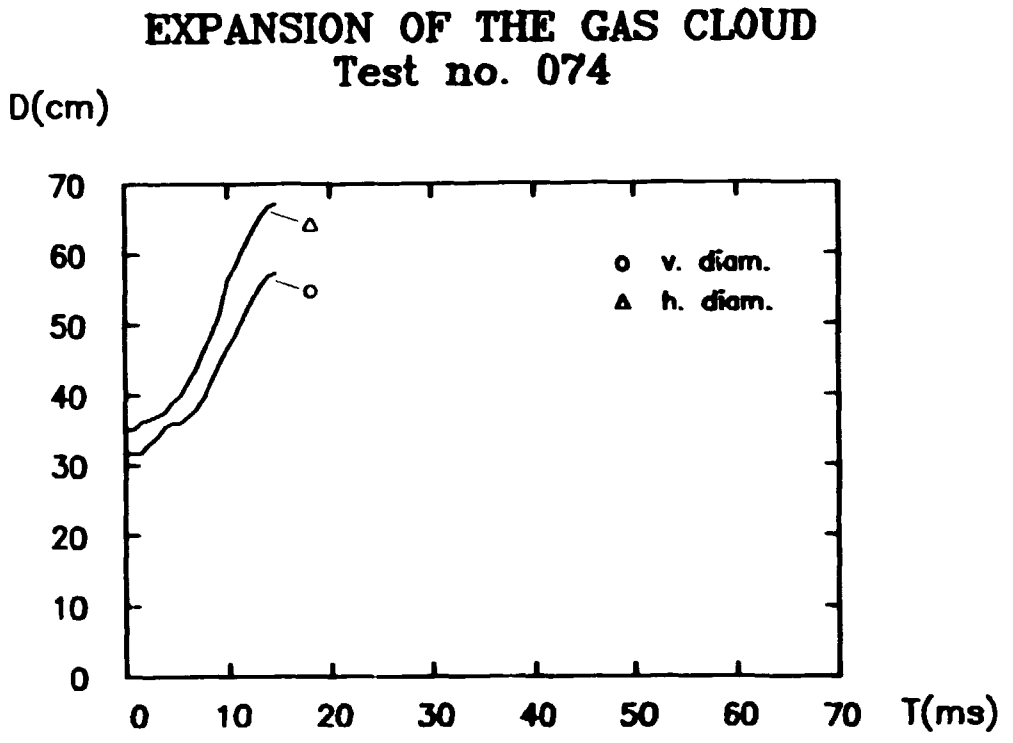

Fig. 11. Expansion of the gas cloud.

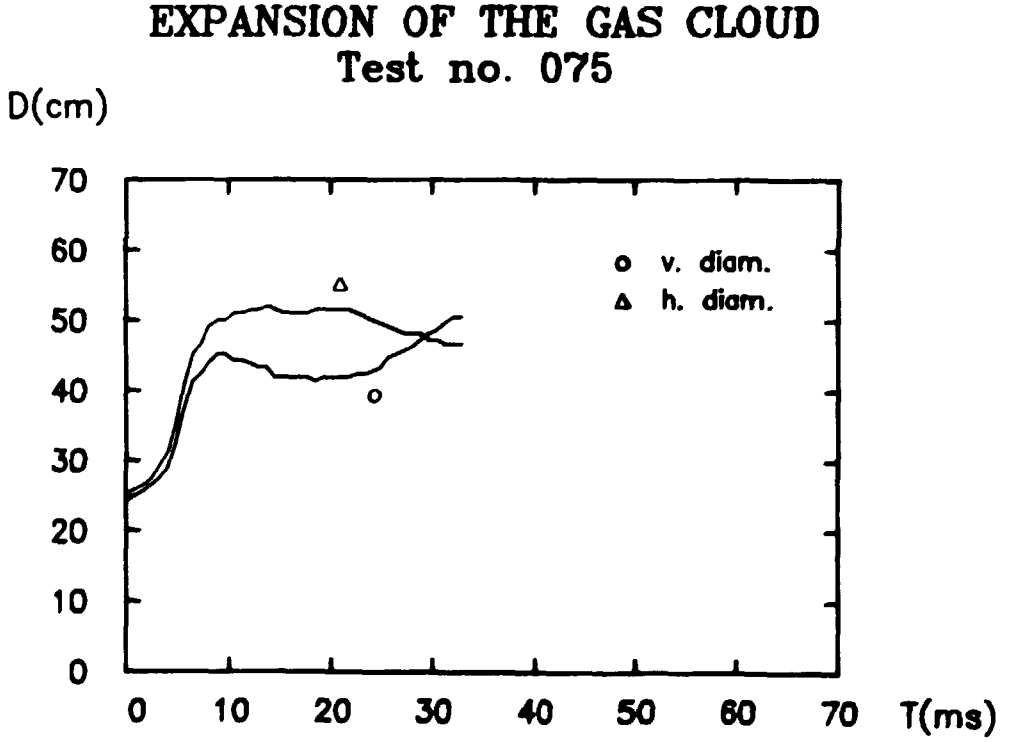

Fig. 12. Expansion of the gas cloud.

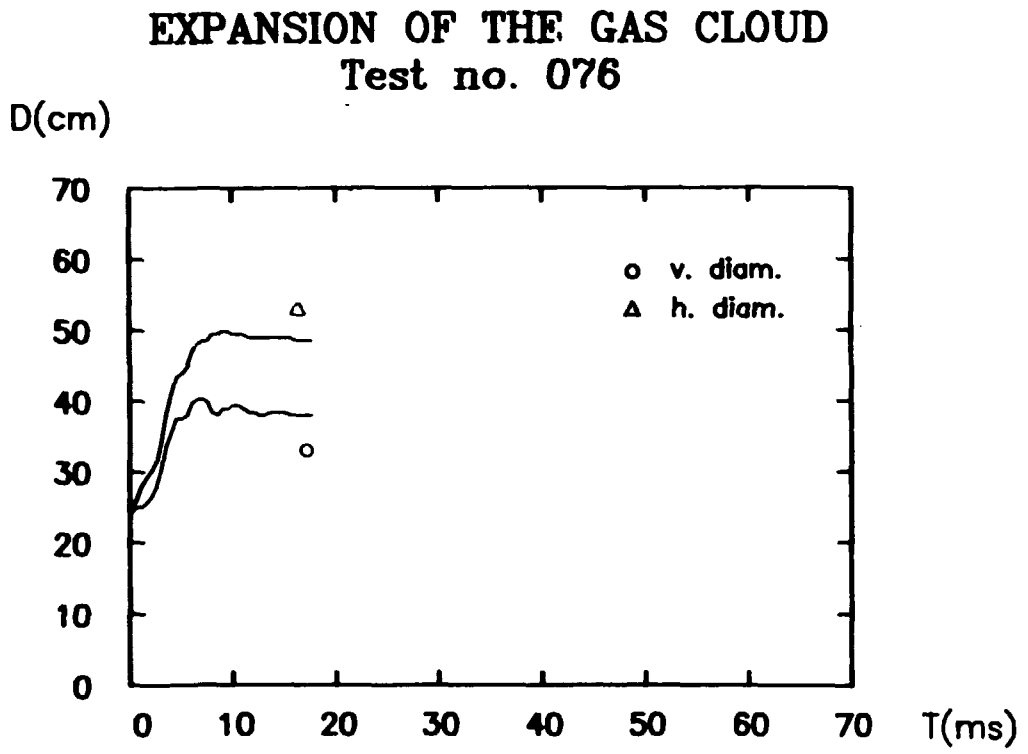

Fig. 13. Expansion of the gas cloud.

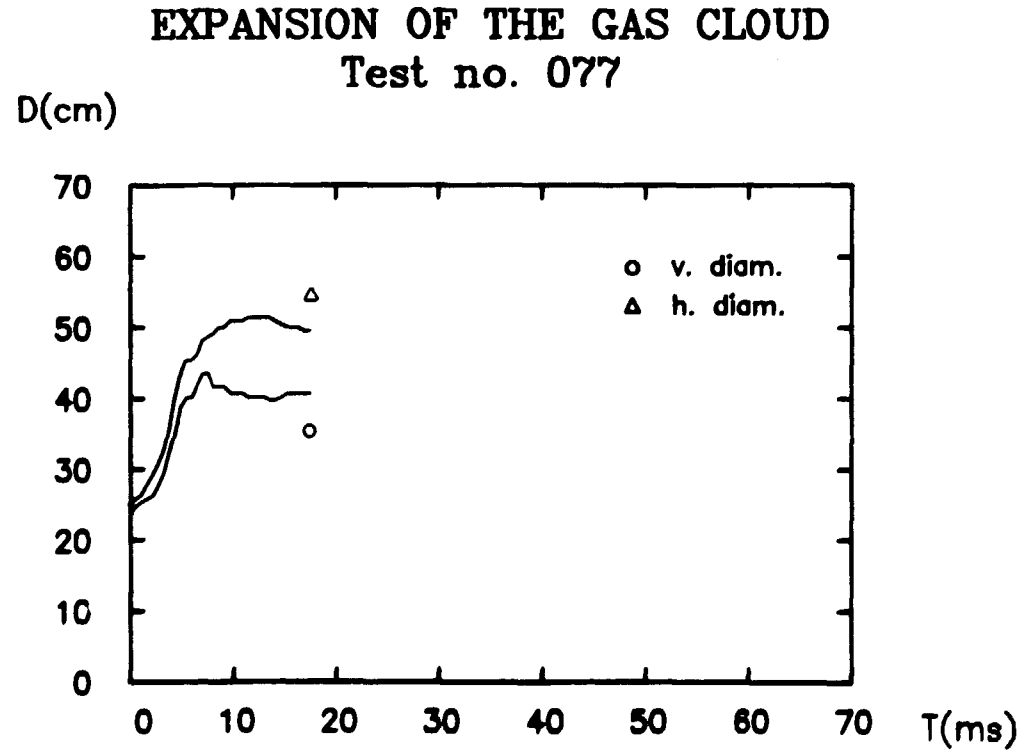

Fig. 14. Expansion of the gas cloud.

An average of the horizontal and the vertical "diameters" given above has been used as input for the simple acoustical piston model described in section 4.

The effect of a change in the mixture composition is primarily a change in the time scale, whereas the effect of a change in the initial size of the charge is a change in both deformation scale and time scale.

Regarding the final stage of the balloon deformation process, it appears that the theoretical expansion factor for the stochiometric mixture (cf. Appendix 1) shows excellent agreement with the expansion factor calculated from the ratio of the initial diameter to the diameter just before breakup of the balloon (under the assumption that the burnt gas is in a homogeneous state when the balloon breaks up). This indicates that all the gas is burnt when the rupture of the balloon takes place, and that, in the present experiments, the combustion process consequently cannot be disturbed by swirling layers introduced by the collapse of the balloon.

3.5. Characteristics of the primary pressure wave.

The characteristics of the primary (or clean) pressure wave - i.e. the blast wave without influence from reflected waves - are investigated in this section. A total of 11 experiments have been carried out in this context.

The first part of this series of tests, consisting of 7 experiments, is devoted to the question of symmetry of the blast wave in relation to the frequency content and the peak pressure level. The second part treats the change in the pressure characteristics when the distance from the source to the measuring point is increased.

3.5.1. Symmetry measurements.

3.5.1.1. Experimental setup.

In order to investigate the blast symmetry, the pressure profile has been recorded in 8 different directions from the source. The experimental setup for these experiments are outlined in Fig. 15 below,

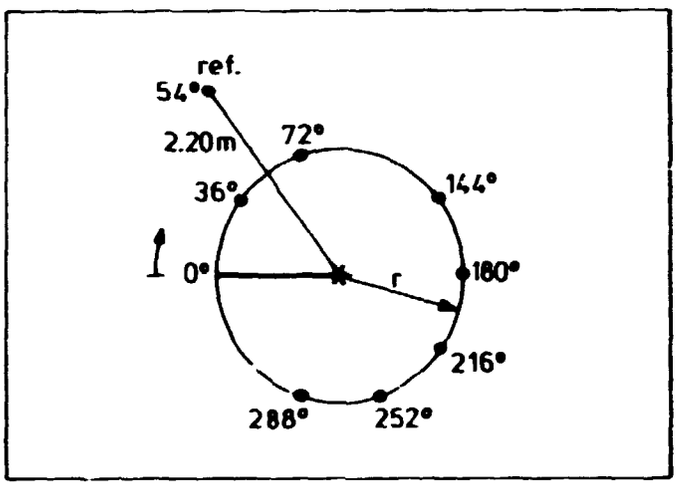

Fig. 15. The experimental setup.

where "*" symbolizes the source and "·" symbolizes a measuring point. Each measuring point is characterized by a number indicating the position in degrees. For the reference measurement (marked "ref.") the distance to the source is furthermore specified. The source as well as the measuring points were placed at a height of 1.88 cm above the ground in order to avoid any influence from ground-reflected waves on the peak pressures. The specific data for each of these experiments appears from Table 4.

EXPERIMENT NO.	MIXTURE (vol%) CH_4	O_2	N_2	SOURCE DIAMETER (m)	r (m)
119	16	32	52	0.25	1.00
120	16	32	52	0.30	1.00
121	16	32	52	0.30	1.00
122	16	32	52	0.30	1.60
123	16	32	52	0.30	1.60
124	16	32	52	0.30	2.20
125	16	32	52	0.30	2.20

Table 4. Data for the symmetry tests.

3.5.1.2. Results.

The measured data are presented in the following figures and tables.

In Fig. 16 ar example is given of a typical pressure pulse recorded at a distance of 1.00 m from the center of the source.

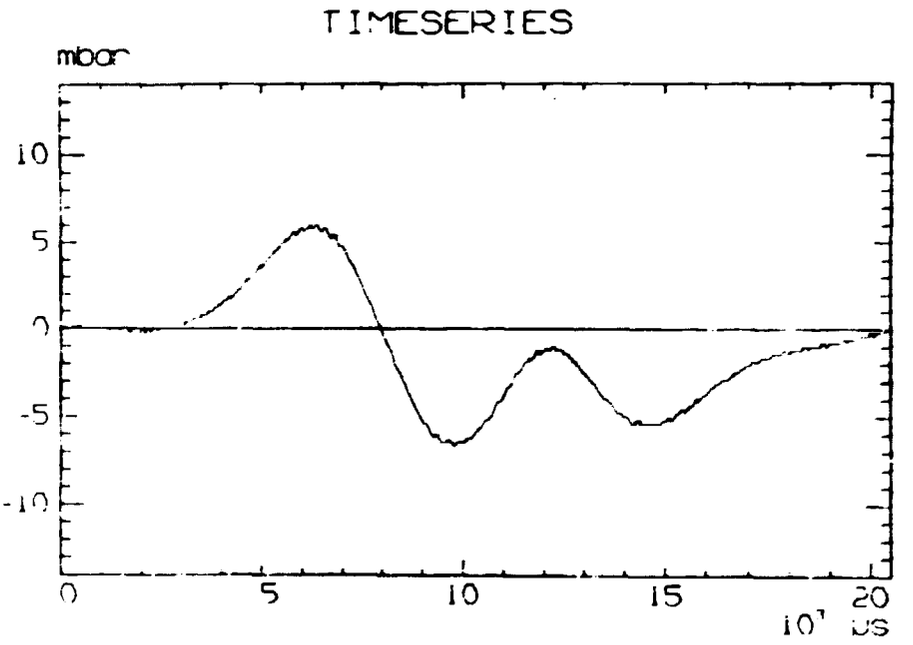

Fig. 16. Pressure profile recorded at 1 m from the source.

From curves of this type the normalized peak and the normalized peak-to-peak pressures have been evaluated. In Figs. 17 - 30 these are given as a function of the position of the measuring point. In these curves and throughout the rest of the report $P_M/P_{M,ref.}$ denotes the normalized peak pressure and $P_{p-p}/P_{p-p,ref.}$ denotes the normalized peak-to-peak pressure.

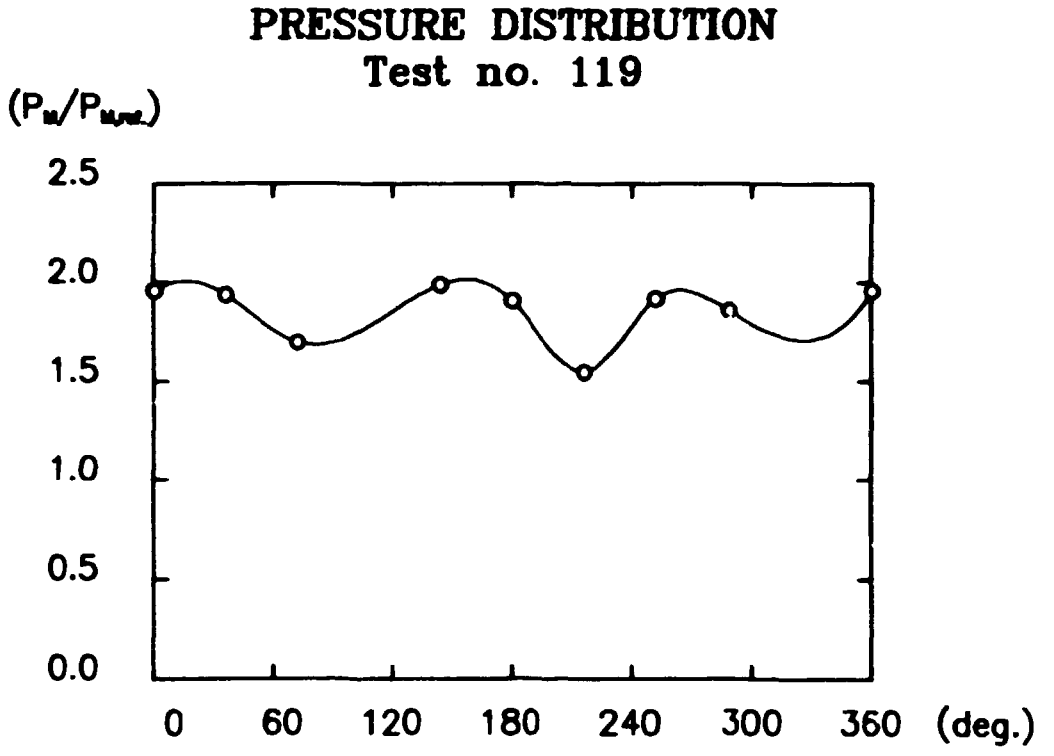

Fig. 17. Normalized peak pressure distribution.

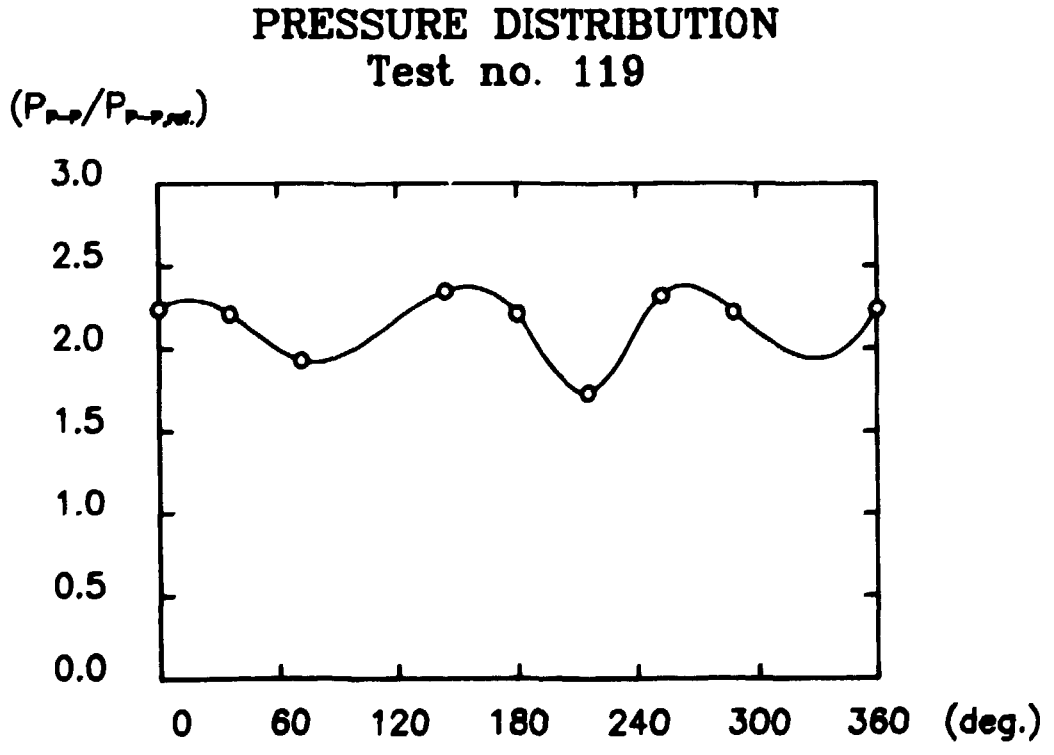

Fig. 18. Normalized peak-to-peak pressure distribution.

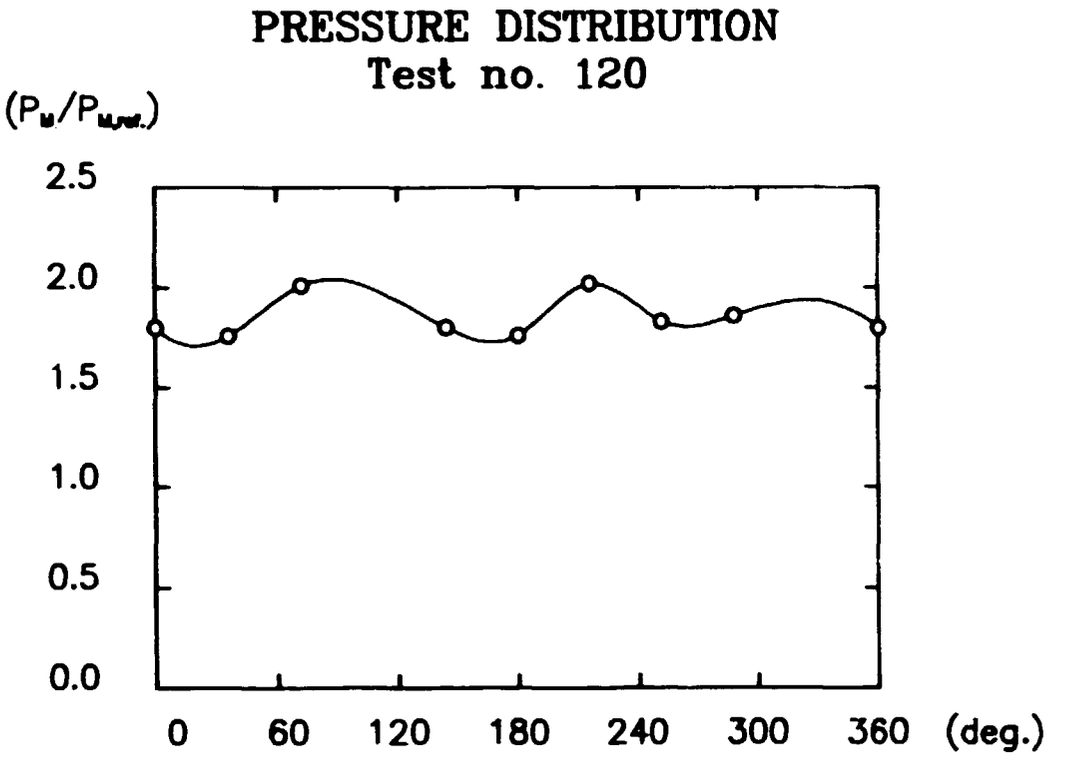

Fig. 19. Normalized peak pressure distribution.

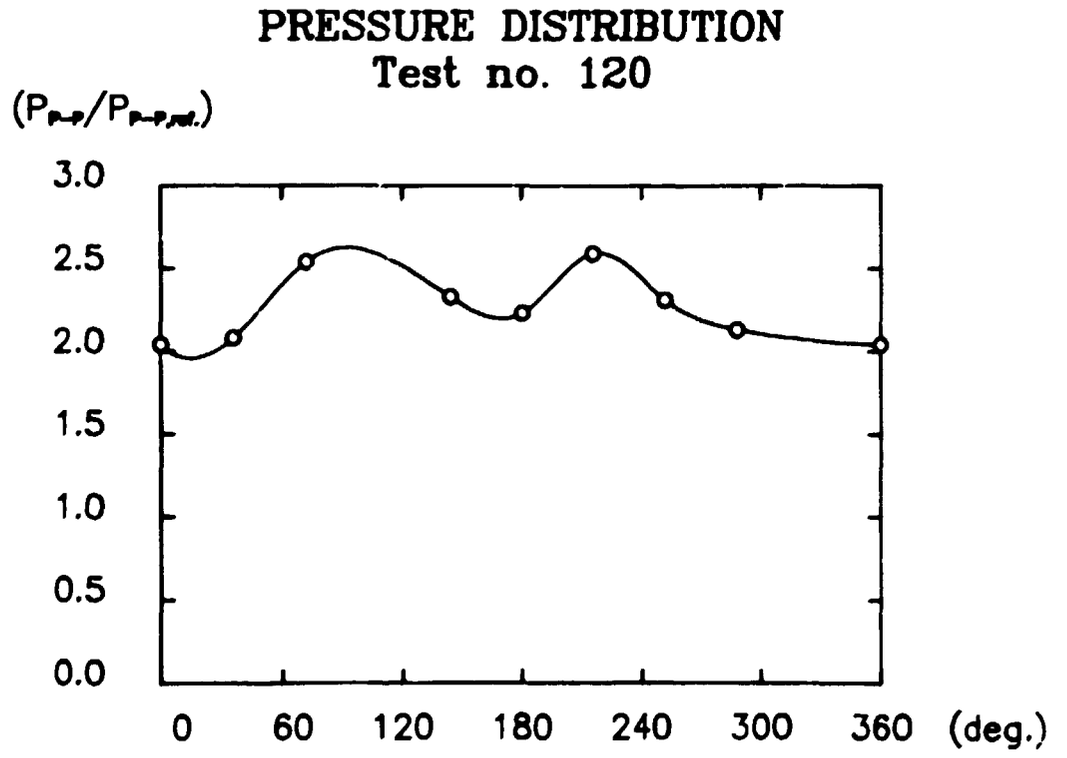

Fig. 20. Normalized peak-to-peak pressure distribution.

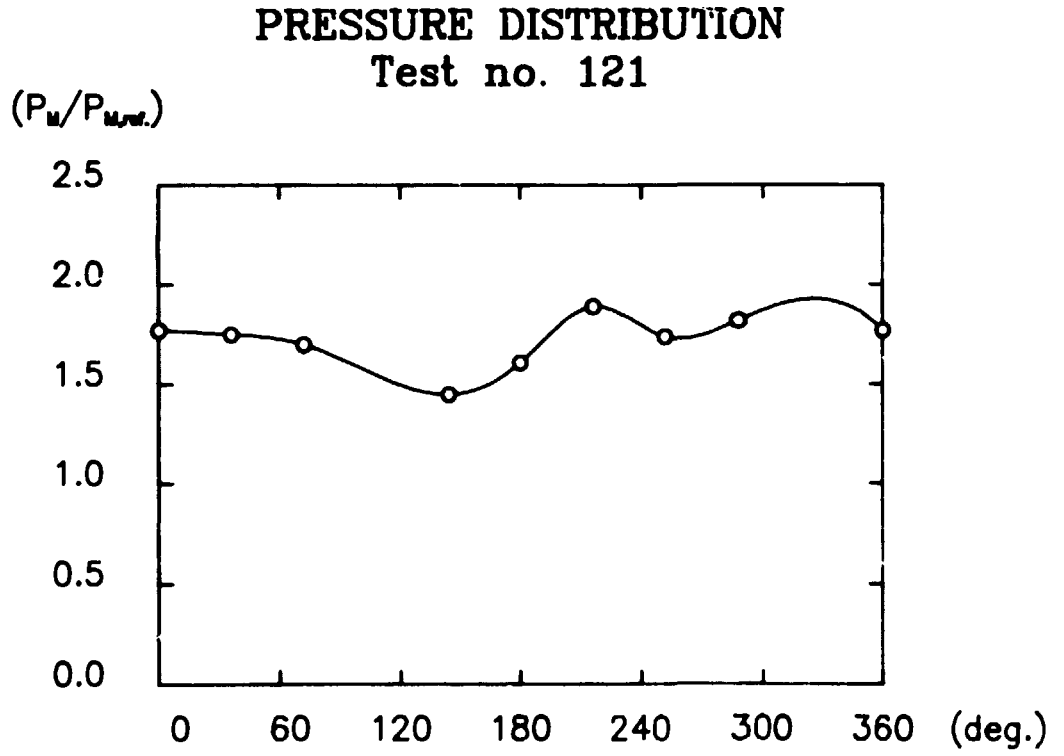

Fig. 21. Normalized peak pressure distribution.

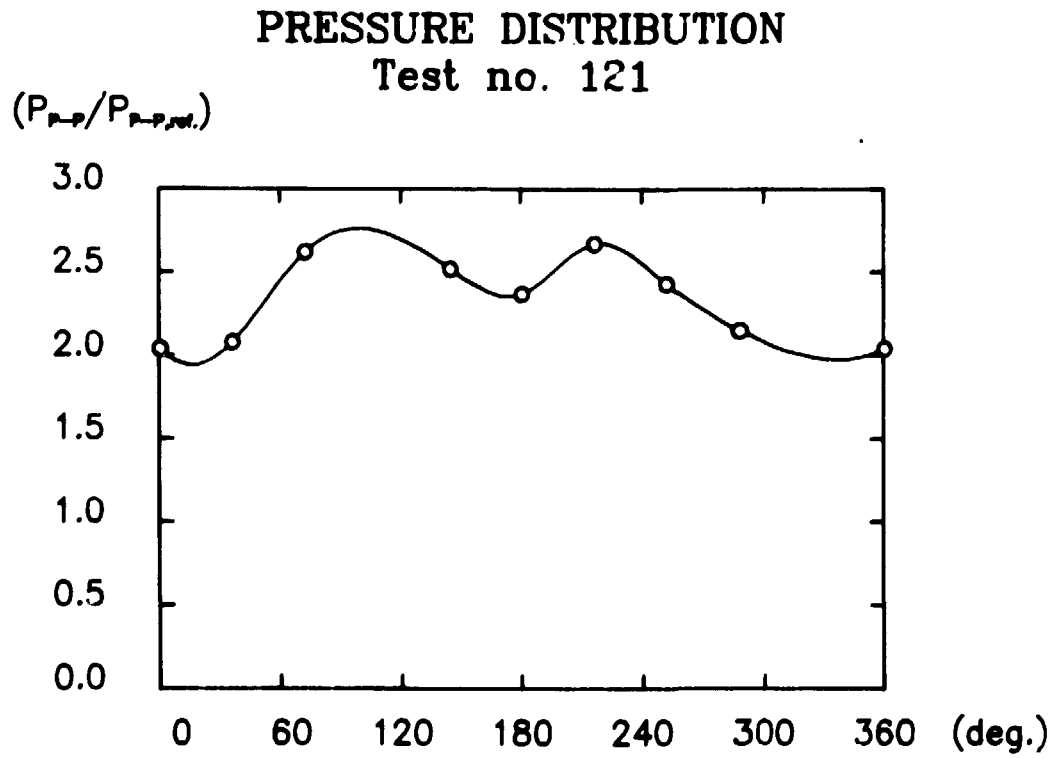

Fig. 22. Normalized peak-to-peak pressure distribution.

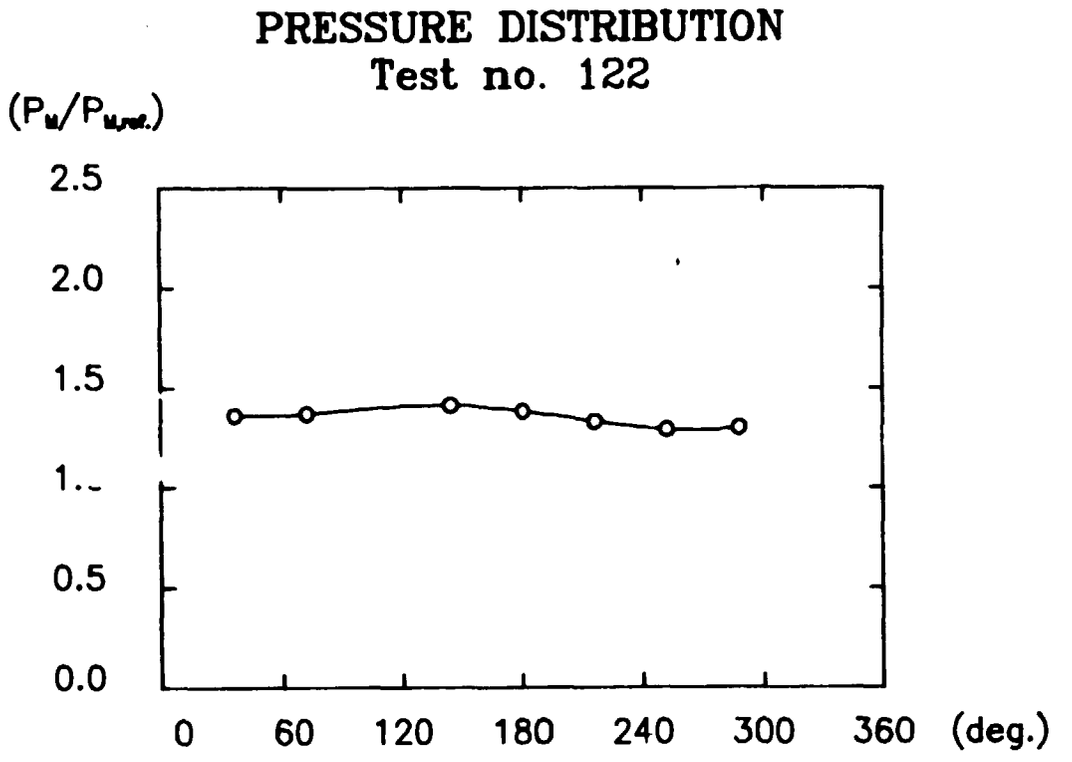

Fig. 23. Normalized peak pressure distribution.

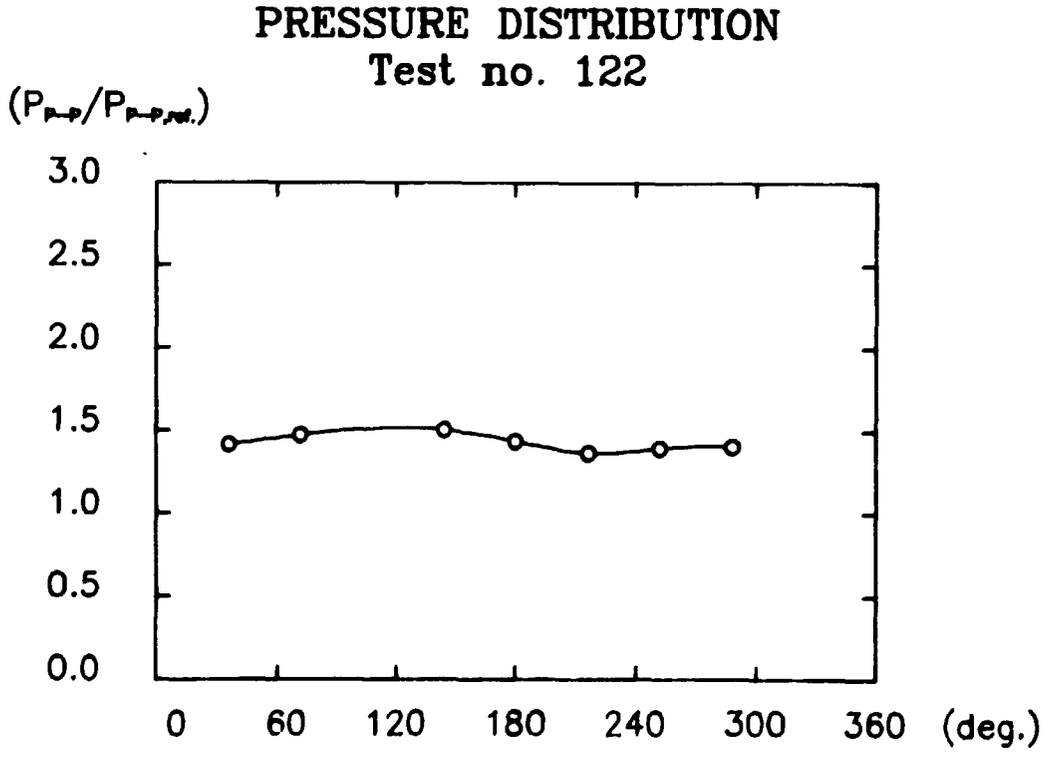

Fig. 24. Normalized peak-to-peak pressure distribution.

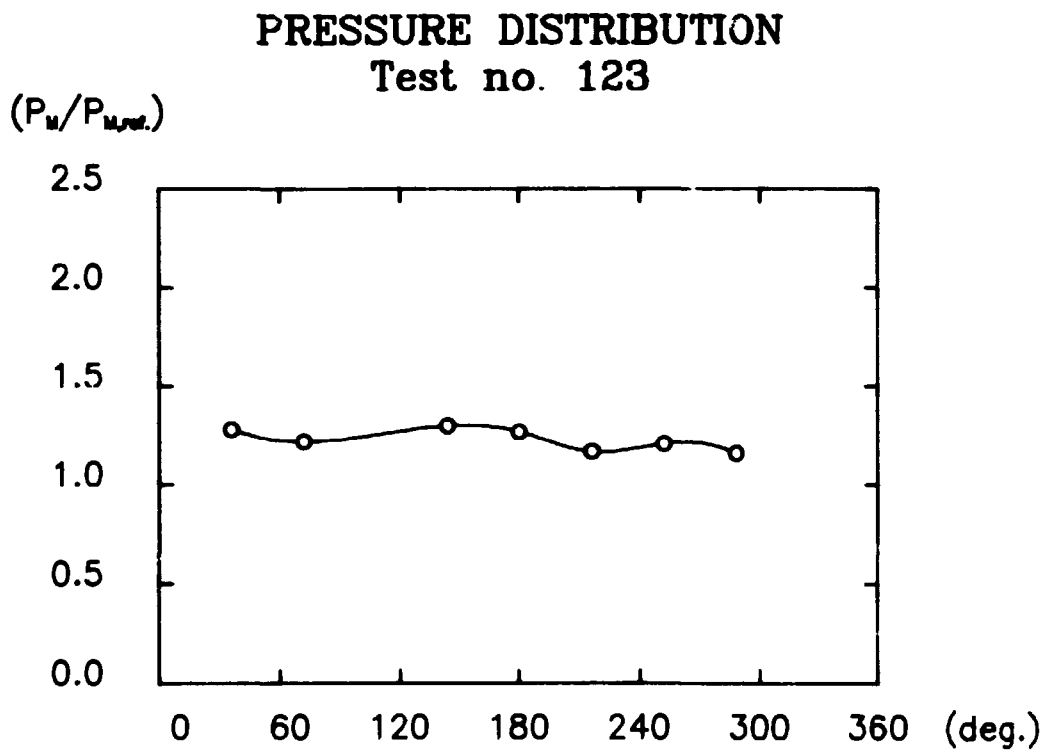

Fig. 25. Normalized peak pressure distribution.

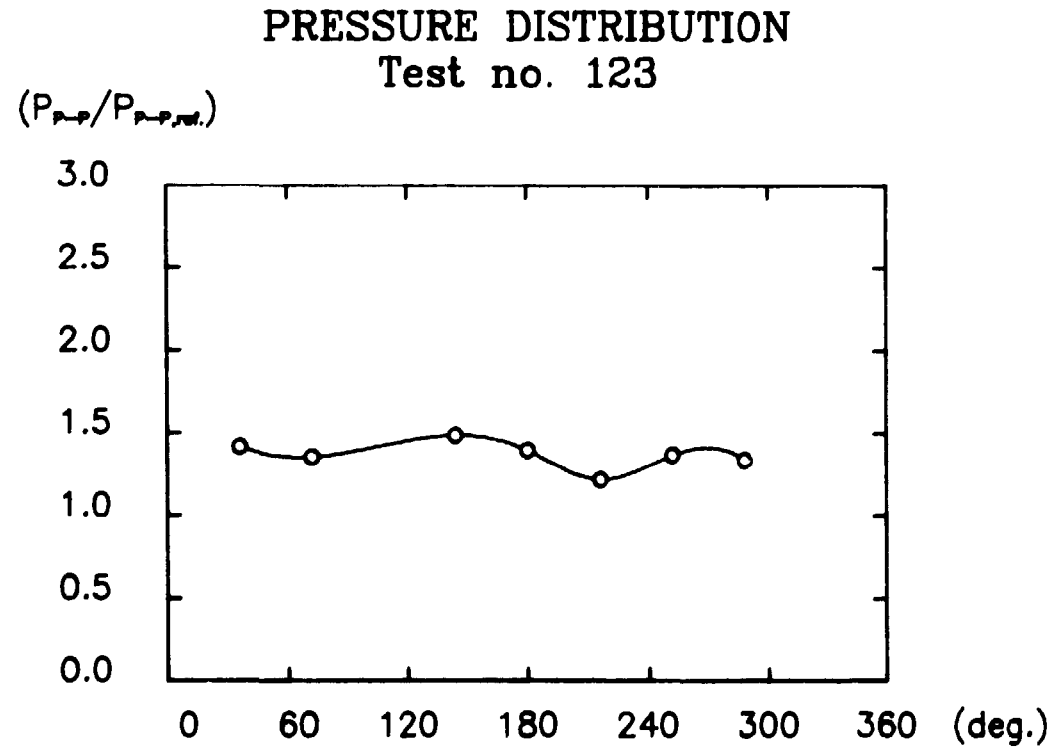

Fig. 26. Normalized peak-to-peak pressure distribution.

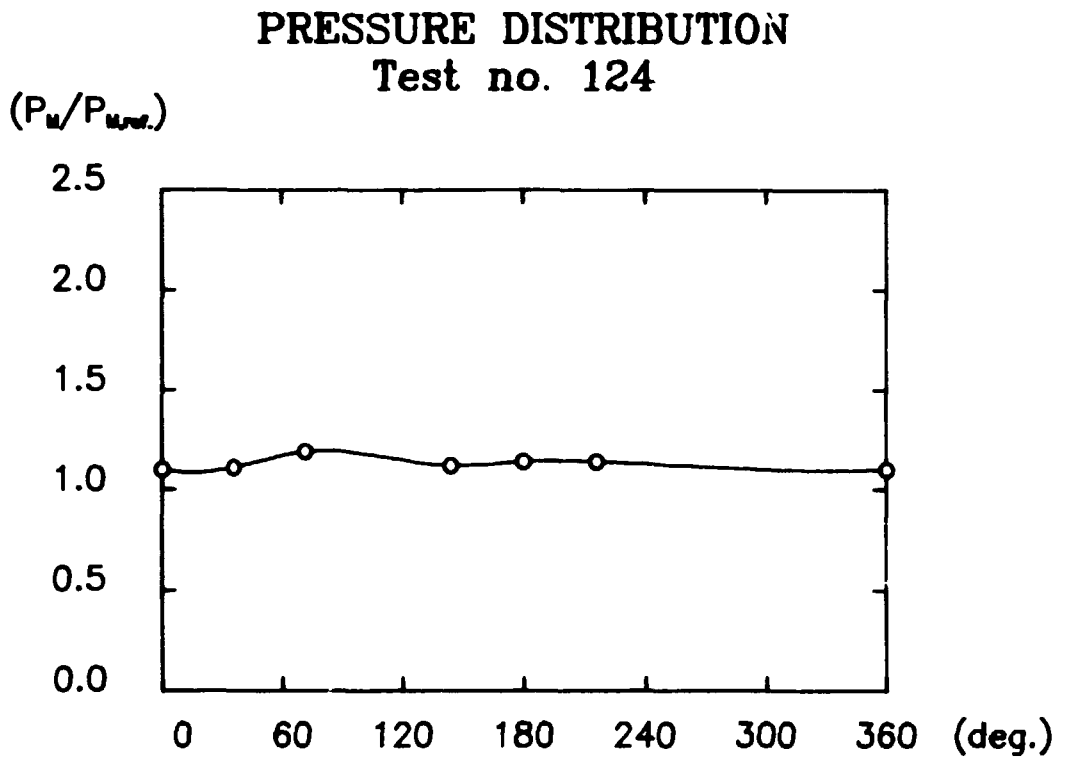

Fig. 27. Normalized peak pressure distribution.

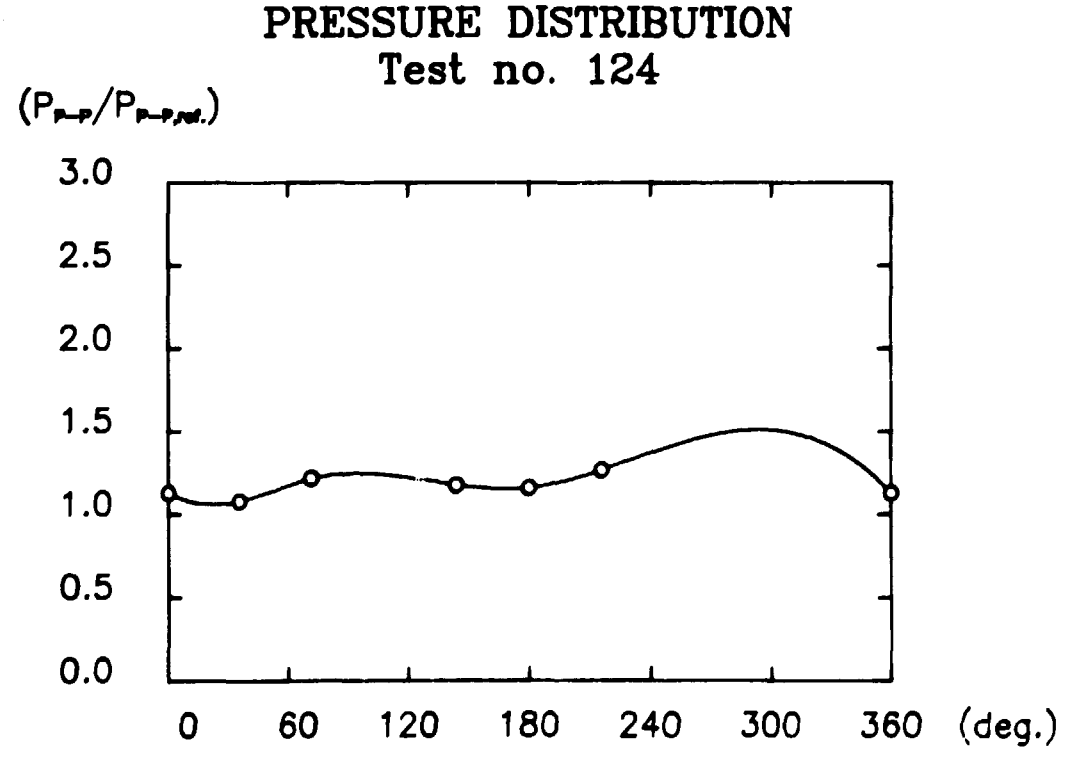

Fig. 28. Normalized peak-to-peak pressure distribution.

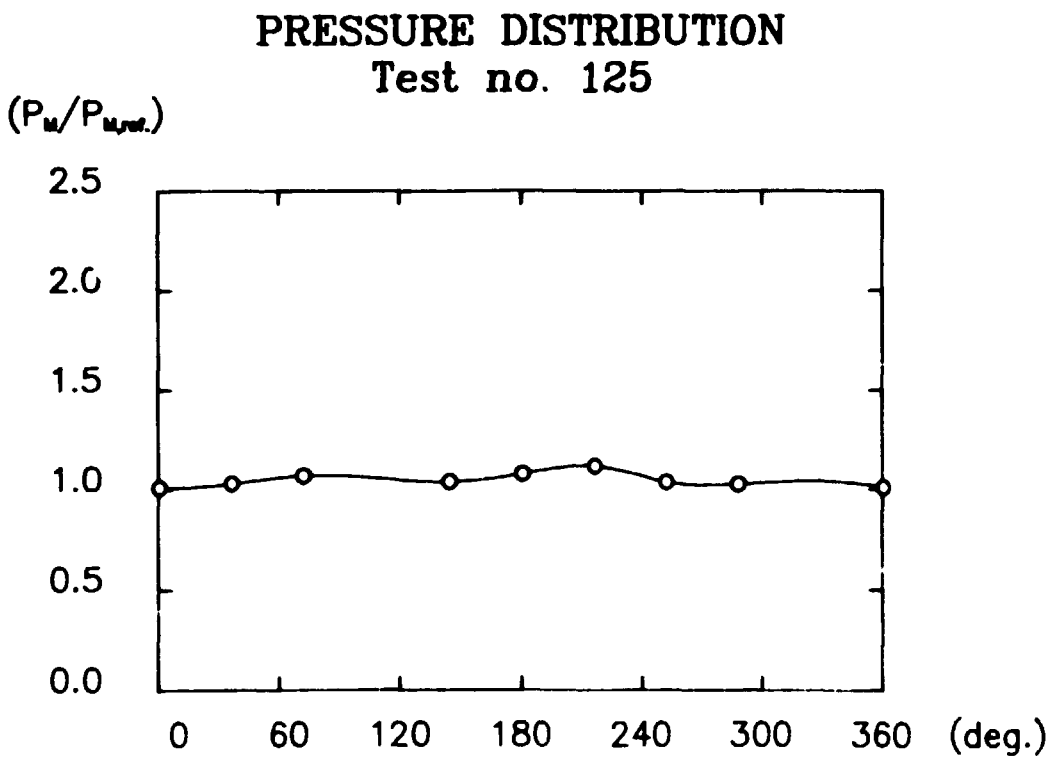

Fig. 29. Normalized peak pressure distribution.

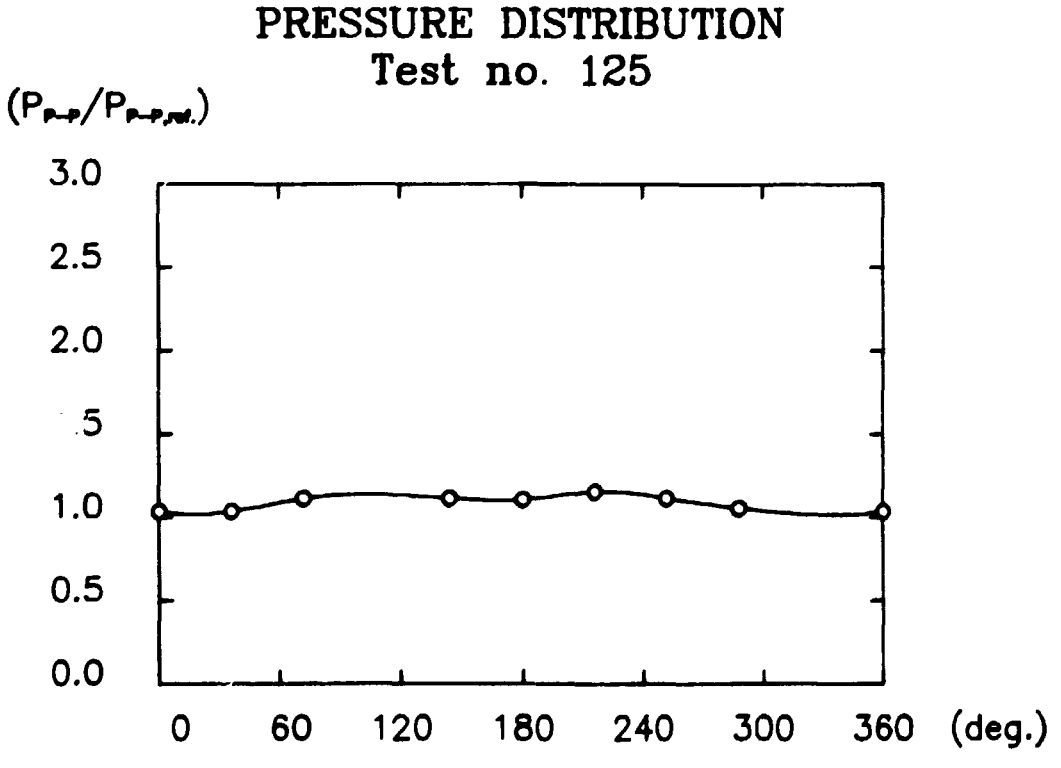

Fig. 30. Normalized peak-to-peak pressure distribution.

The reference measurements corresponding to the results presented in Figs. 17-30 are given in Table 5 below.

TEST NO.	119	120	121	122	123	124	125
$P_{M,ref.}$ (mbar)	3.1	2.9	1.2	3.3	2.5	2.8	3.8
$P_{p-p,ref.}$ (mbar)	5.7	5.0	1.2	6.9	5.7	6.0	7.2

Table 5. Reference values corresponding to the experiments 119-125.

Finally Table 6 below gives the mean value of the dominant frequency for each experiment, <f>, together with the corresponding coefficient of variation $\sigma_{\%}$.

TEST NO.	119	120	121	122	123	124	125
<f>(Hz)	105	155	210	170	159	148	172
$\sigma_{\%}$ (%)	4	2	6	1	1	2	1

Table 6. Frequencies corresponding to the experiments 119-125.

3.5.1.3. Evaluation of the results.

The results presented in the Figures 17-30 indicate, that the pressure level varies considerably in the circumferical direction near the source, probably due to instabilities in the combustion zone. These pressure variations are apparently damped with increasing distance from the center of the explosion. The blast wave becomes consequently symmetric with increasing distance from the source. This behaviour is confirmed by the Tables 7-8 below, where the mean values of the normalized pressures together with the corresponding coefficient of variation are computed for each particular experimental type.

DISTANCE (m)	1.0	1.6	2.2
$\langle P_M/P_{M,ref} \rangle$	1.81	1.29	1.09
$\sigma_{\%}$ (%)	8	6	5

Table 7. Mean normalized pressures corresponding to specific test types.

DISTANCE (m)	1.0	1.6	2.2
$\langle P_{p-p}/P_{p-p,ref} \rangle$	2.26	1.40	1.12
$\sigma_{\%}$ (%)	10	5	6

Table 8. Mean normalized pressures corresponding to specific test types.

Acording to Lighthill (6), p. 35, the radiation from an irregular combustion can be modelled as that from a compact source region, where the sum of all monopole source strengths is not especially small compared to the individual source strengths. A compact source region is defined in this context as a region containing acoustic sources, and with a characteristic dimension that is small compared with a typical wavelength of the sound generated. A compact source region generally generates waves close to monopole source character (with the strength of the monopole equal to the sum of all individual monopole strengths) in the far field, whereas the near field normally is of a more complicated nature.

This principal difference between the near field and the far field is in close agreement with present observations.

Concerning the frequencies, it is seen from Table 6 that the mean frequency varies considerably from experiment to experiment, whereas no significant variations of the frequency as a function of the circumferential direction (expressed by the

$\sigma_{\%}$ value) is observed for any of the experiments. This also indicates source symmetry. The change in frequency content from experiment to experiment is supposed to be due primarily to deviations in the combustion rate as no correlation between the mean frequency and the actual measuring distance is observed.

3.5.2 Distance measurements.

3.5.2.1. Experimental setup.

The pressure attenuation with increasing distance from the source is examined by recording the pressure pulse in 8 different distances from the center of the source. The experimental setup for these experiments is roughly outlined in Fig. 31 below.

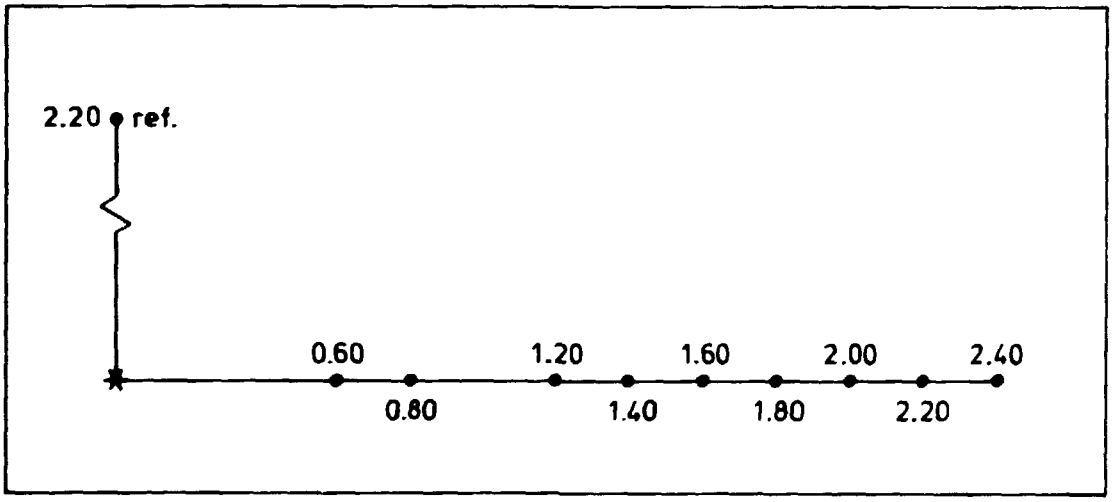

Fig. 31. The experimental setup.

As previously stated "*" symbolizes the source and the "." symbolizes a measuring point. Each measuring point is characterized by a number indicating the distance to the center of the source in meters. The reference measurement is marked with a "ref.". The source as well as the measuring points were placed at a height of 1.88 m above the ground. The specific data for each of the these experiments appears from Table 9.

EXPERIMENT NO.	MIXTURE (vol%) CH_4	O_2	N_2	SOURCE DIAMETER(m)
126	16	32	52	0.30
127	16	32	52	0.30
128	16	32	52	0.30
129	16	32	52	0.30

Table 9. Data for the distance tests.

3.5.2.2. Results.

The measured data are presented in the following figures and tables.

In the Figs. 32-33 typical examples of pressure pulses recorded in 0.60 m and 2.20 m distances, respectively, are presented.

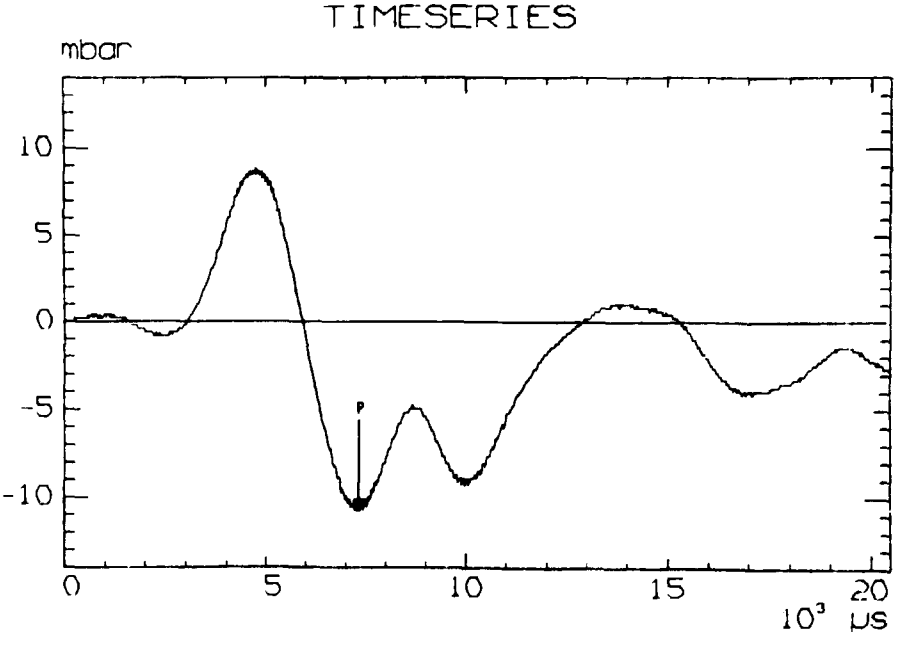

Fig. 32. Pressure pulse recorded in 0.60 m distance from the source.

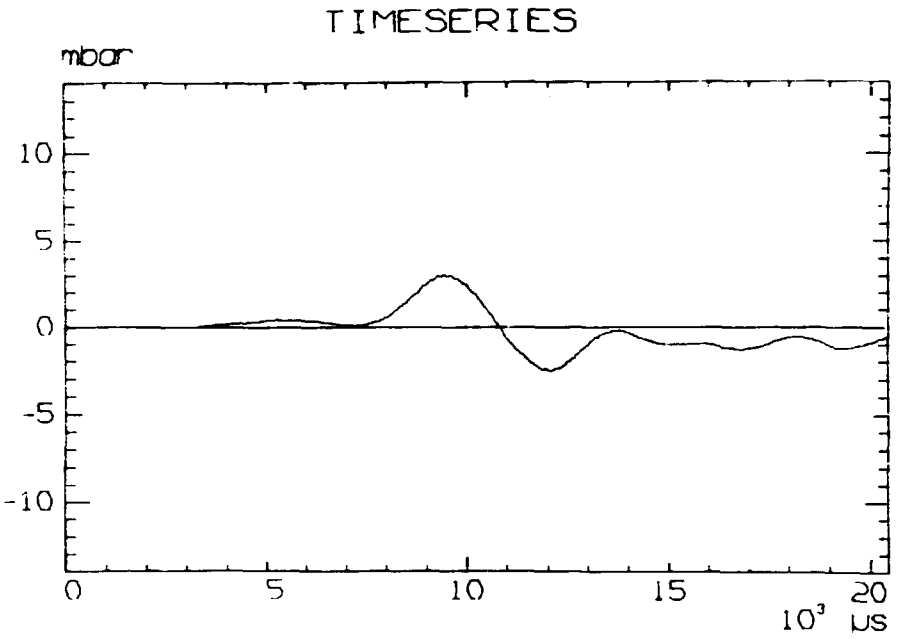

Fig. 33. Pressure pulse recorded in 2.20 m distance from the source.

From curves of this type the normalized peak and the normalized peak-to-peak pressures have been evaluated. These are given in the Figs. 34-41 as a function of the distance from the center of the source.

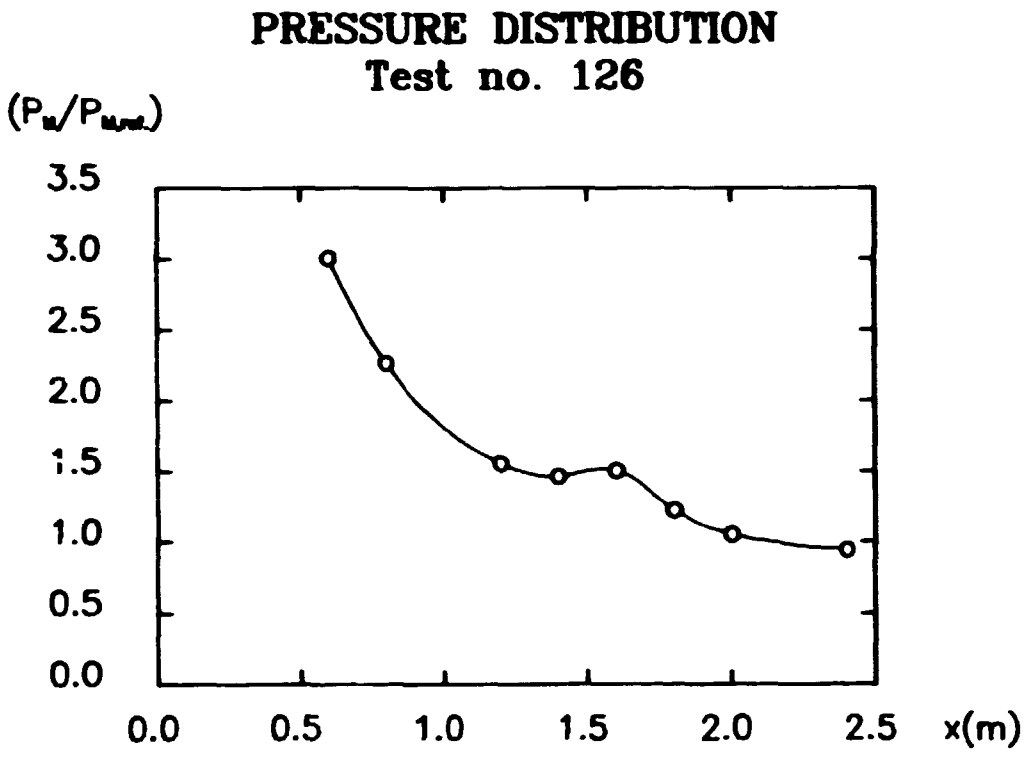

Fig. 34. Normalized peak pressure distribution.

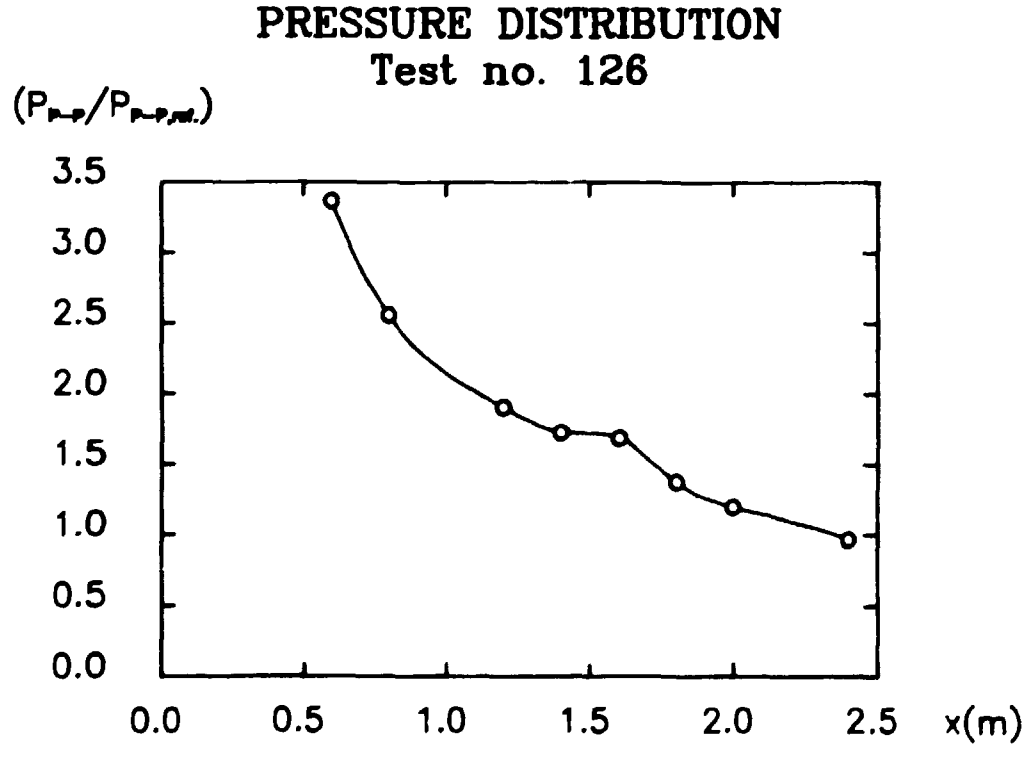

Fig. 35. Normalized peak-to-peak pressure distribution.

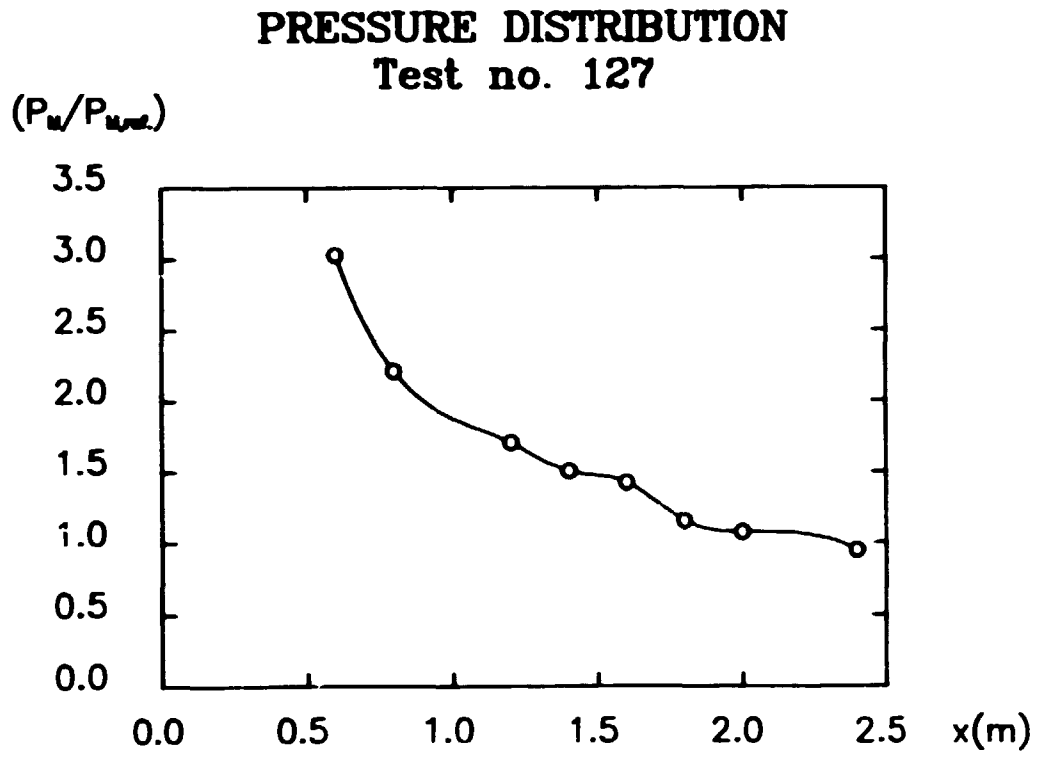

Fig. 36. Normalized peak pressure distribution.

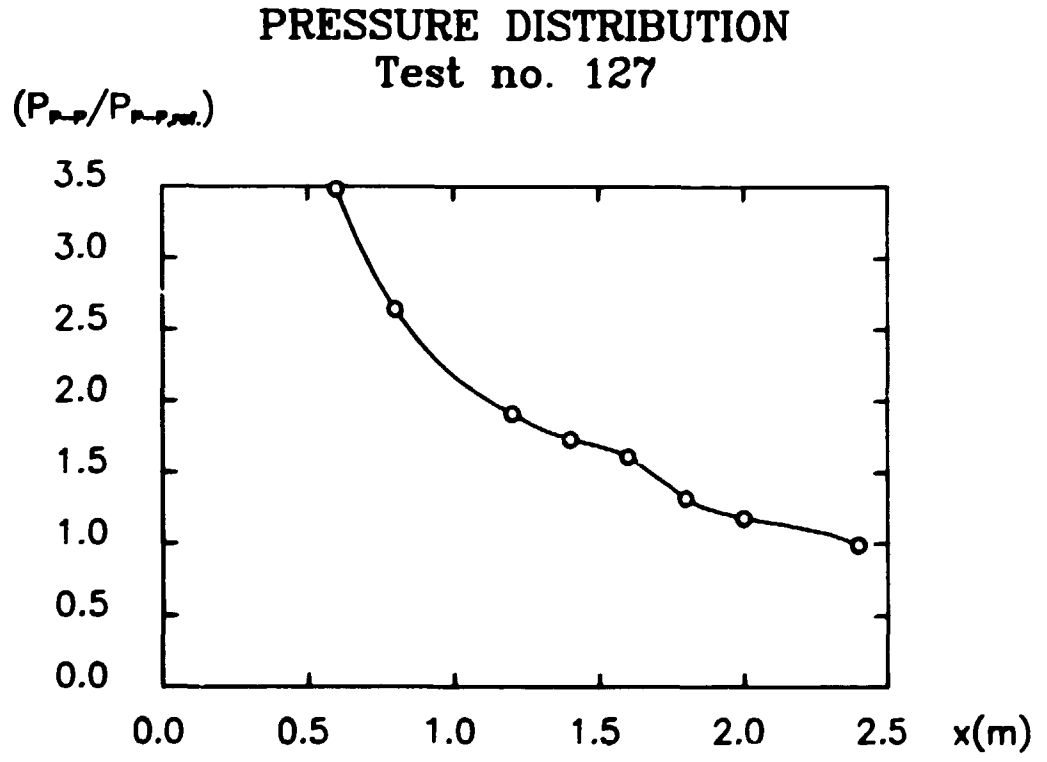

Fig. 37. Normalized peak-to-peak pressure distribution.

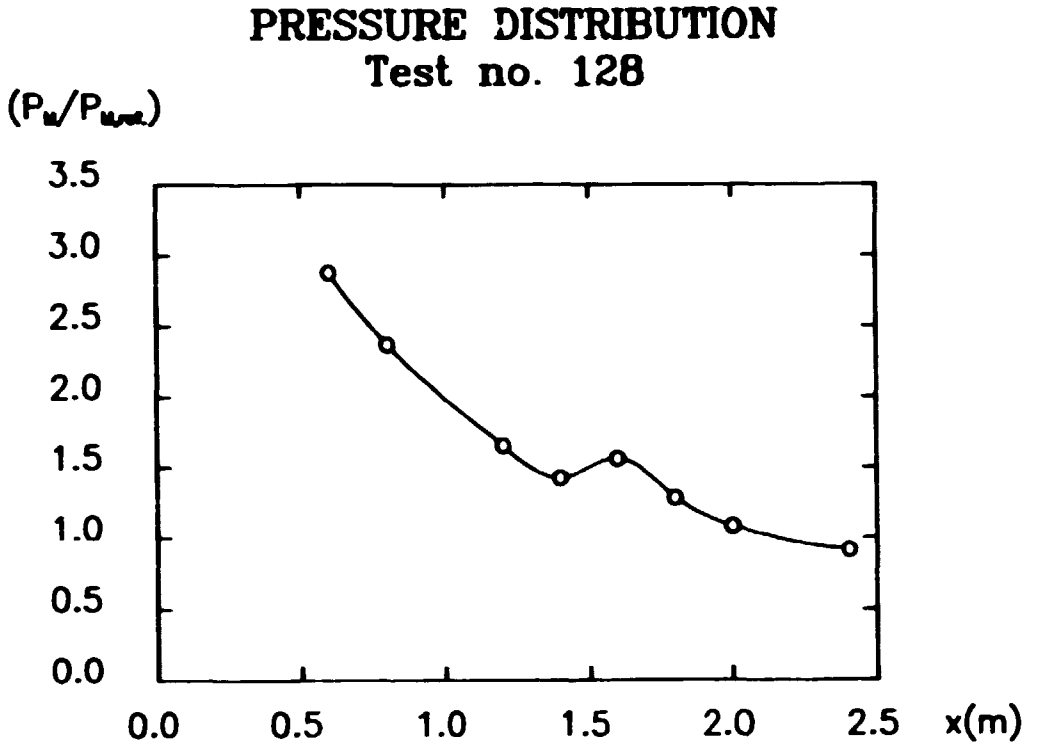

Fig. 38. Normalized peak pressure distribution.

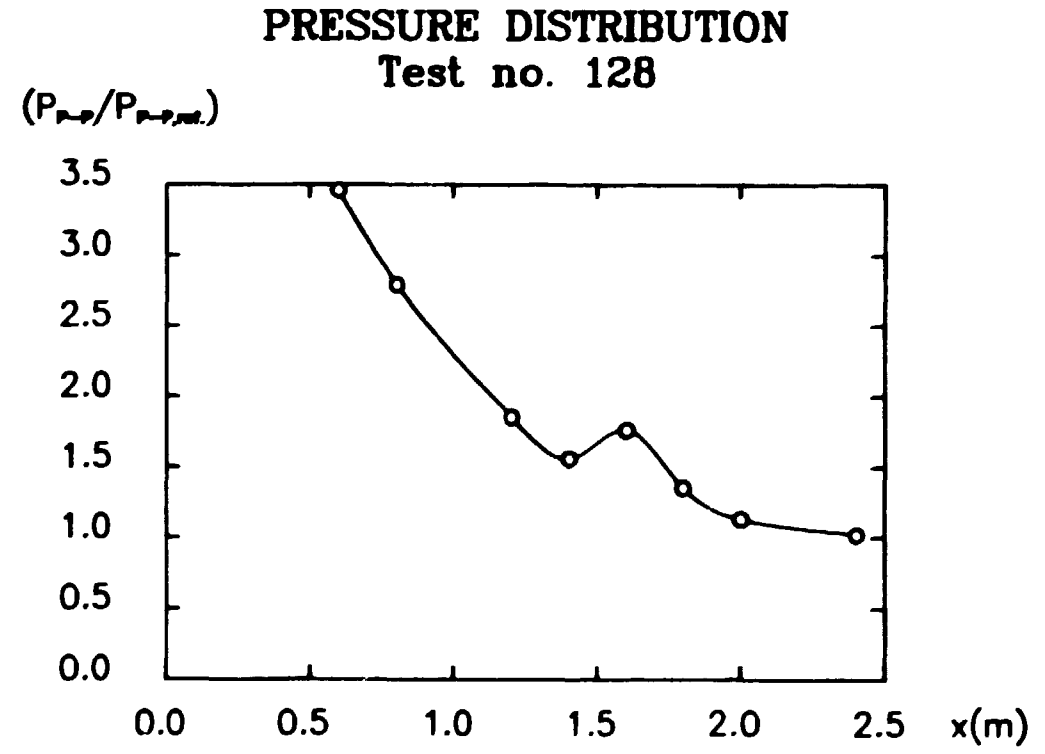

Fig. 39. Normalized peak-to-peak pressure distribution.

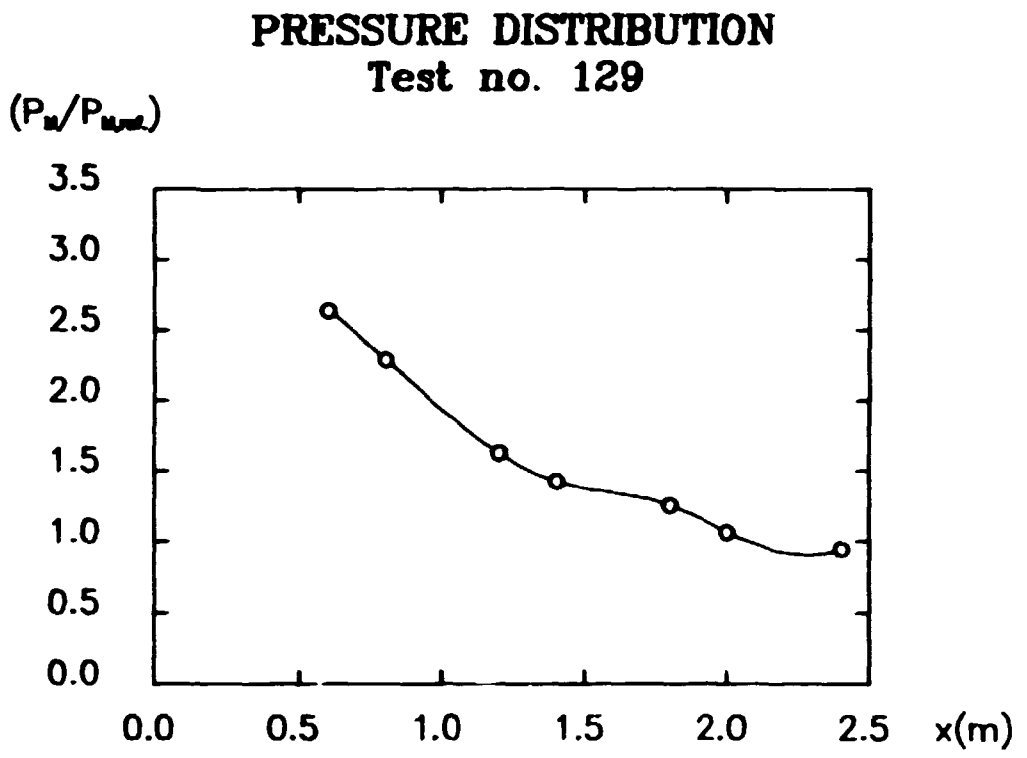

Fig. 40. Normalized peak pressure distribution.

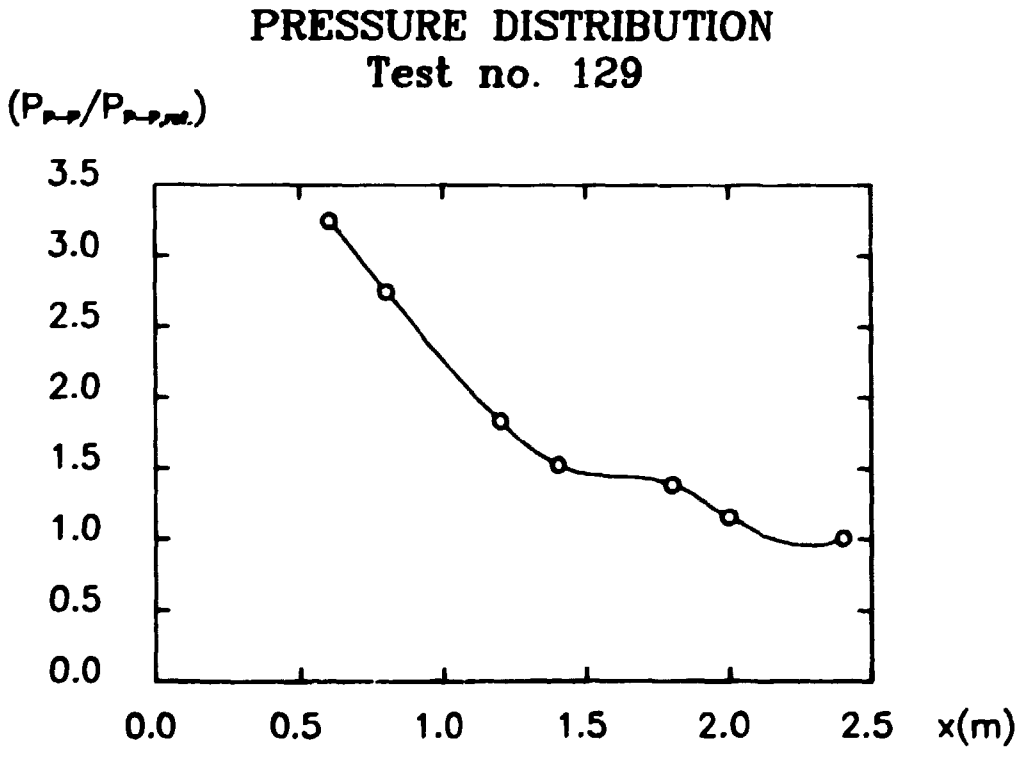

Fig. 41. Normalized peak-to-peak pressure distribution.

The reference measurements corresponding to the results presented in Figures 34-41 are given in Table 10 below.

TEST NO.	126	127	128	129
$P_{M,ref.}$ (mbar)	2.6	2.6	3.1	3.5
$P_{p-p,ref.}$ (mbar)	5.9	5.6	5.7	6.8

Table 10. Reference values corresponding to experiments 126-129.

3.5.2.3. Evaluation of the results.

A comparison of the Figs. 32 and 33 shows that the shape of the positive pressure phase is preserved with increasing distance between the source and measuring point, whereas the shape of the negative pressure phase has changed. Concerning the negative phase, it is noted that only the part following the point marked P in Fig. 32 is modified. This modification is expected to be due to ground reflection. In order to test this assumption the time between the direct and reflected signals is evaluated and compared with the time between the beginning of the positive pulse and point P. The actual situation appears from Fig. 42 below,

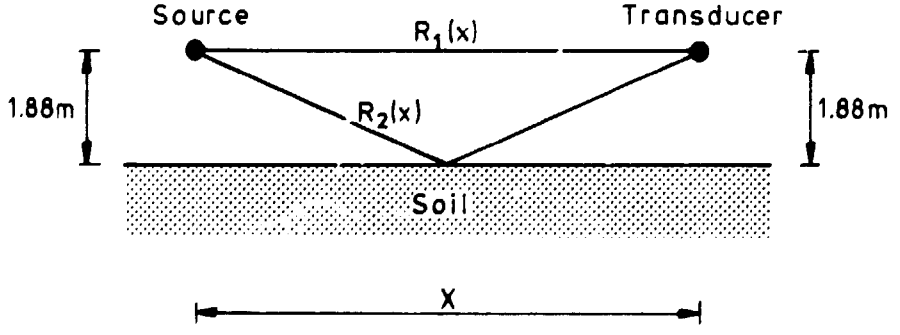

Fig. 42. Sketch of the situation.

where

$R_1(X)$ denotes the distance travelled by the "direct" signal,

$R_2(X)$ denotes the distance travelled by the "reflected" signal, and

X denotes the horizontal distance between the source and transducer.

Provided that the speed of sound, c_0, is constant the distance considered (and equals 340 m/s), the following result can be obtained

$$\Delta R = R_2(X) - R_1(X)$$

$$= 2((1.88m)^2 + \frac{X^2}{4})^{\frac{1}{2}} - X$$

$$\Delta t_C = \frac{\Delta R}{c_0}$$

where Δt_C denotes the computed time interval between the arrival of the direct and the reflected signal. In Fig. 43 below Δt_C is given as a function of the horizontal distance X.

Inspection of the curves corresponding to different measuring distances shows that the time between the beginning of the positive pulse and the point where the "modifications" begin is closely related to the computed time Δt_C. This indicate that the shape of the negative pressure phase is changed due to reflections from the ground. The above-described phenomenon, is true for experiments 126-129, but as the Δt_C values for the actual measuring distances are greater than the time between the beginning of the positive phase and the fully developed negative pressure, the maximum and minimum peak pressures are unaffected of ground reflections.

As expected, Figs. 34-41 show decreasing pressure level with increasing distance from the source. This is true for all the measurements except for those performed in a distance of 1.60 m from the center of the source. This behaviour is believed to be due to a measuring error. The attenuation generally is not so

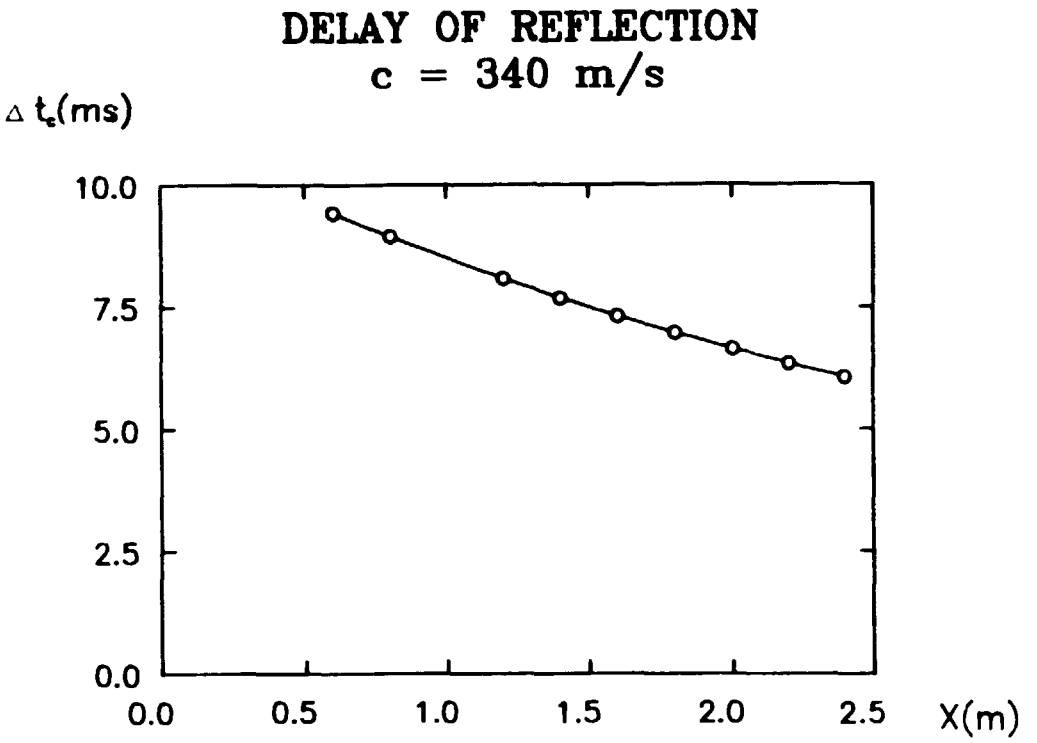

Fig. 43. Computed time delay as a function of the horizontal distance between the source and transducer.

strong as that of the acoustic 1/R point source. The neglecting of non-linear effects obviously does not explain this for they should increase the attenuation; but it is rather due to the complex character of the near field where the compactness condition is unfulfilled.

3.6. Pressure propagation over a hard plane surface.

The characteristics of pressure propagation over a hard surface, where reflections from the ground cannot be neglected, have been investigated in 4 experiments described below. In these experiments the pressure as a function of the distance from the center of the source and the pressure as a function of the level over the hard surface have been investigated. Moreover, the question of rotational symmetry has been treated.

3.6.1. Experimental setup.

The pressure signal has been recorded in two diametrically op-

posite directions in order to evaluate the degree of symmetry. In one of these directions (marked pos. 1 in the following) the pressure has been recorded in four levels and in the other (marked pos. 2 in the following) the pressure has been recorded in three levels. Additionally two reference measurements have been performed, one in the pos. 2 direction, and the other in a direction perpendicular to this. The experimental setup is schematically shown in Figs. 44a and 44b below.

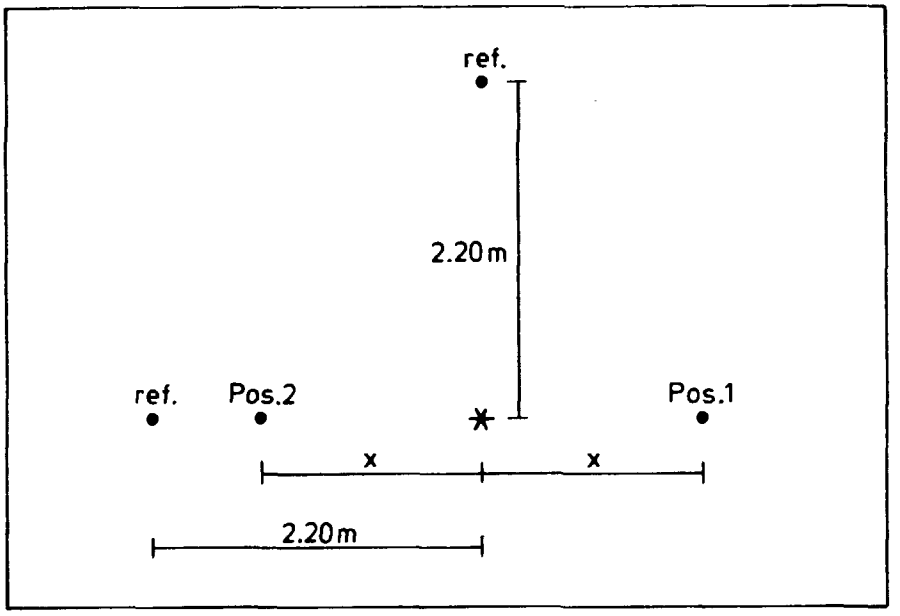

Fig. 44a. Ground plane of the experimental setup.

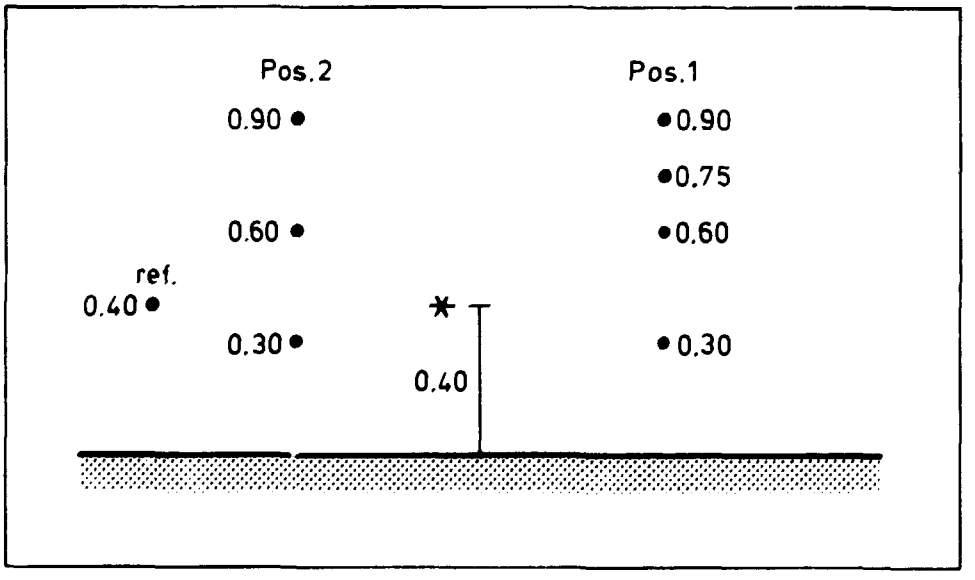

Fig. 44b. Cross section of the experimental setup.

The symbolism is the same as used previously. The numbers attached to the measuring points in Fig. 44b indicate the level over the surface in meters. The specific data for each of the four experiments appear from Table 11.

EXPERIMENT NO.	MIXTURE(Vol.%) CH_4	O_2	N_2	DIAMETER (m)	X (m)
176	16	32	52	0.30	2.20
177	16	32	52	0.30	1.90
178	16	32	52	0.30	1.55
179	16	32	52	0.30	1.20

Table 11. Experimental data.

3.6.2. Results

The measured data are presented in the following figures and tables.

Examples of pressure pulses recorded in 2.20 m distance from the source are presented in Figs. 45-46.

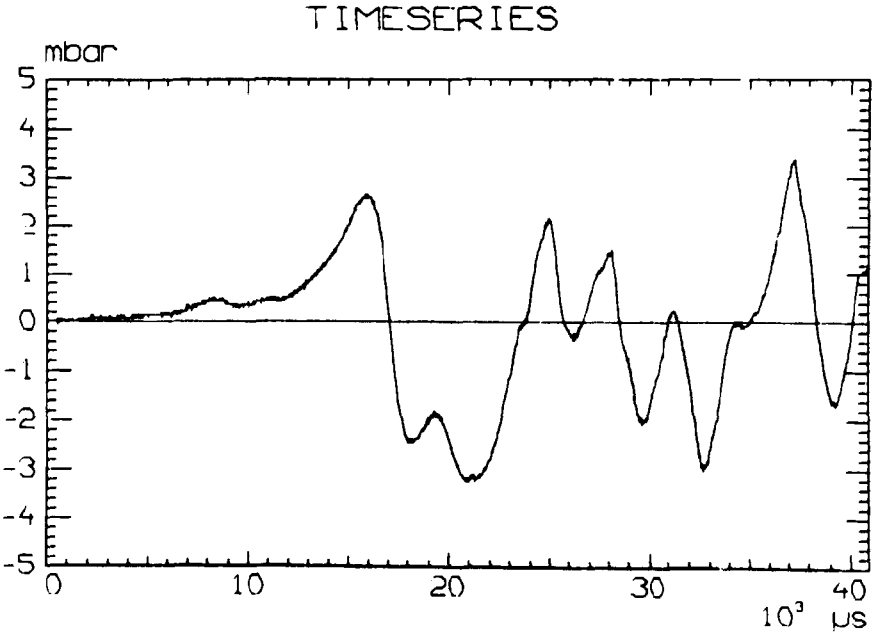

Fig. 45. Pressure pulse recorded 0.30 m above the ground.

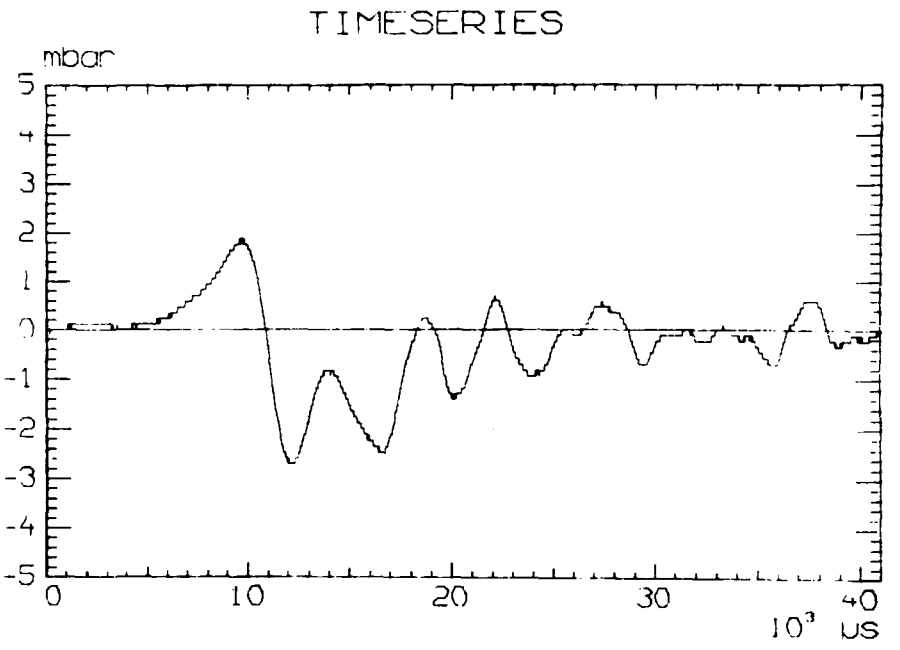

Fig. 46. Pressure pulse recorded 0.90 m above the ground.

Likewise, two examples of pressure pulses recorded in 1.20 m distance from the center of the source are presented in Figs. 47-48.

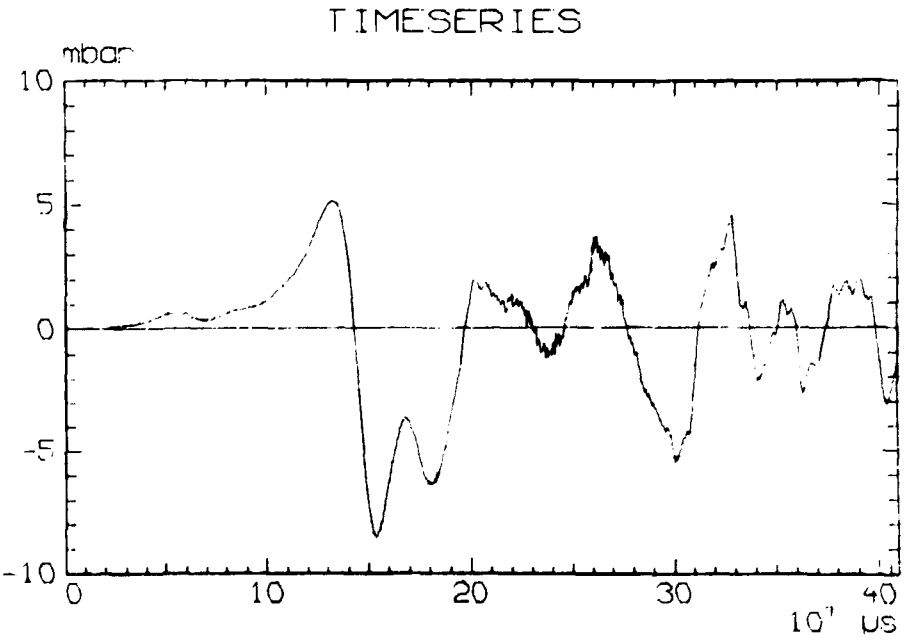

Fig. 47. Pressure pulse recorded 0.30 m above the ground.

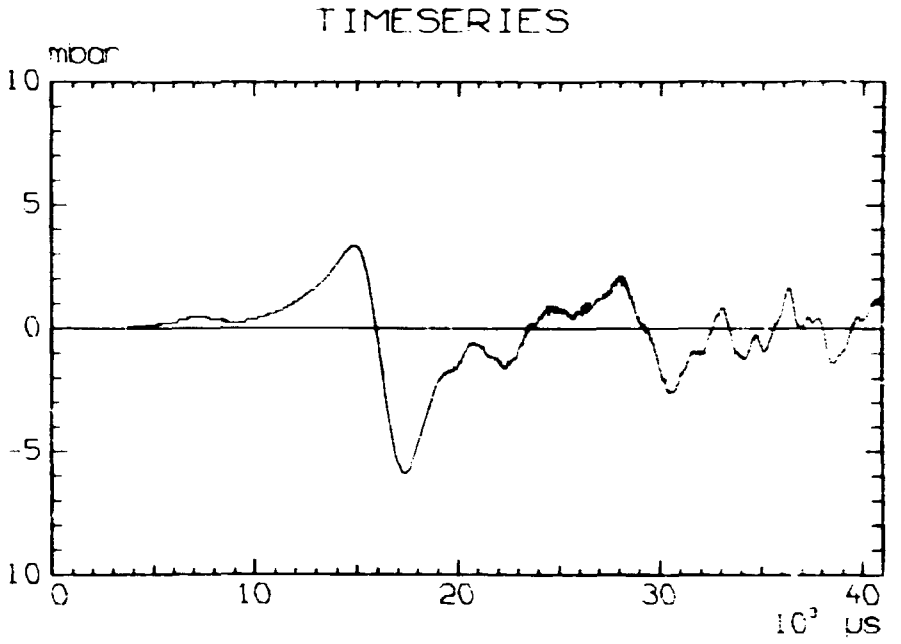

Fig. 48. Pressure pulse recorded 0.90 m above the ground.

On the basis of curves of this type the normalized peak and the normalized peak-to-peak pressure have been evaluated. The mean of the two reference measurements have been used in the normalization of the pressures. The normalized pressures are given in Figs. 49-56 as a function of the measuring level, h, given in meters. Each figure includes a sketch illustrating the situation.

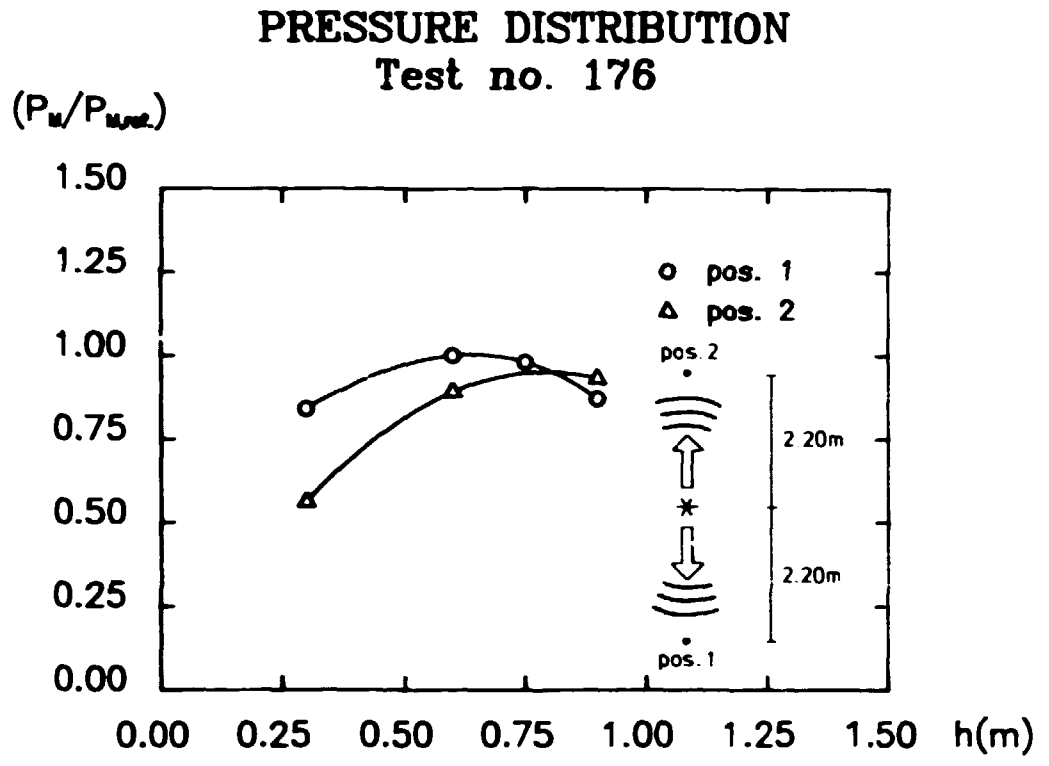

Fig. 49. Normalized peak pressure distribution.

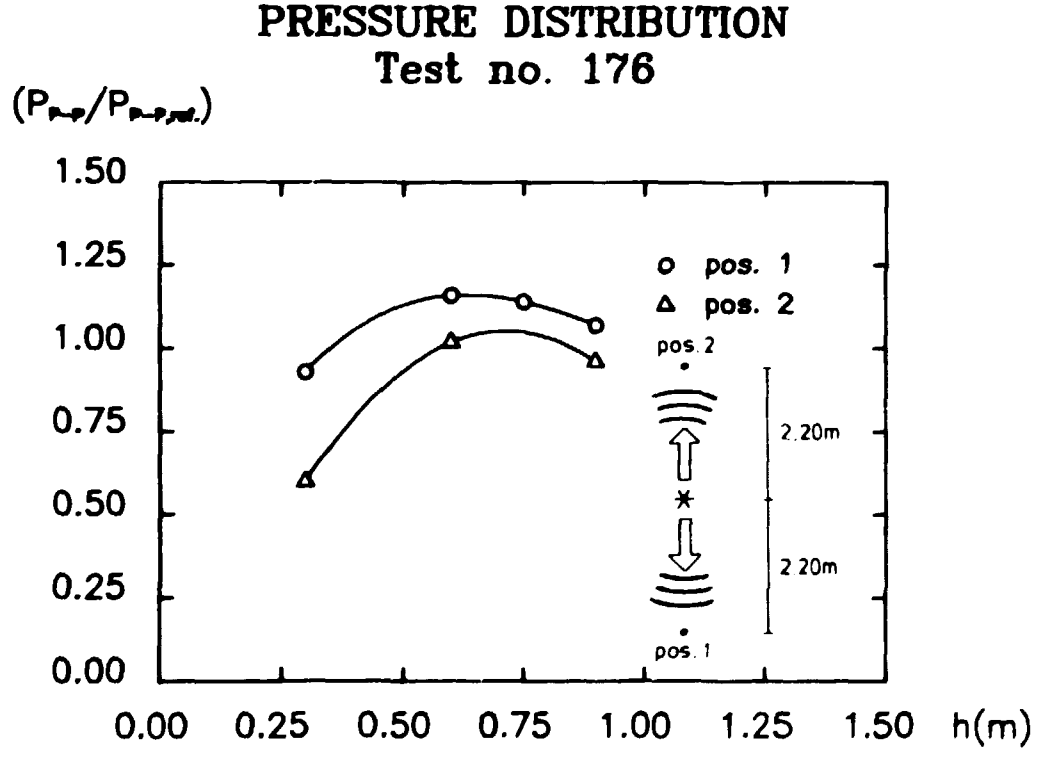

Fig. 50. Normalized peak-to-peak pressure distribution.

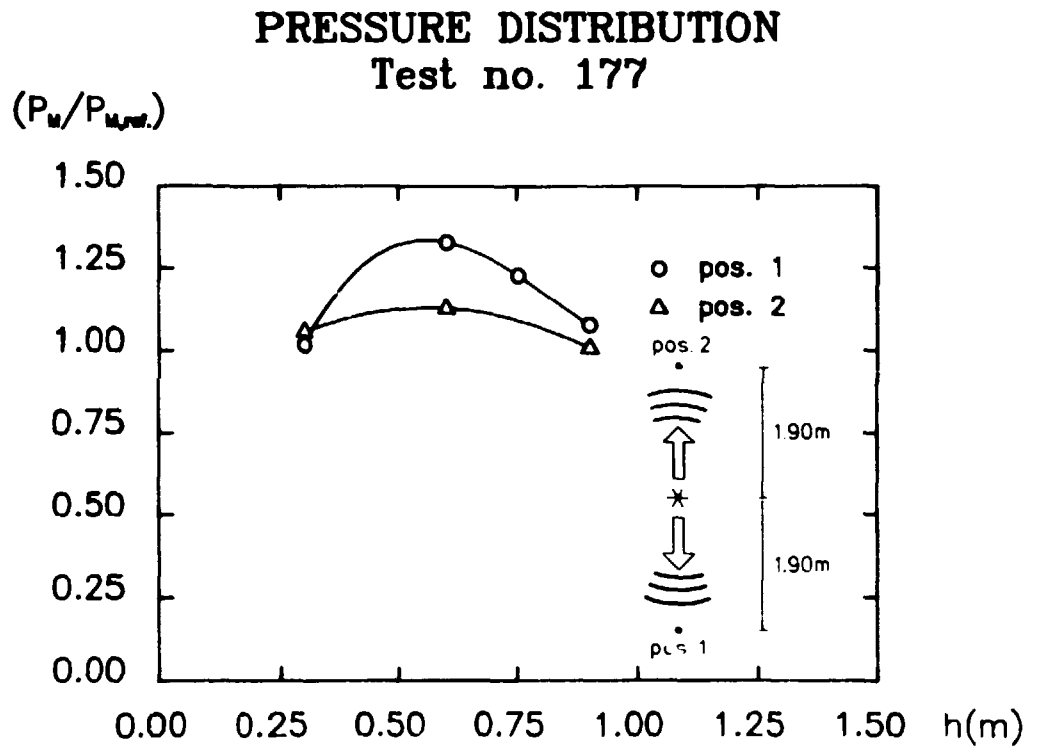

Fig. 51. Normalized peak pressure distribution.

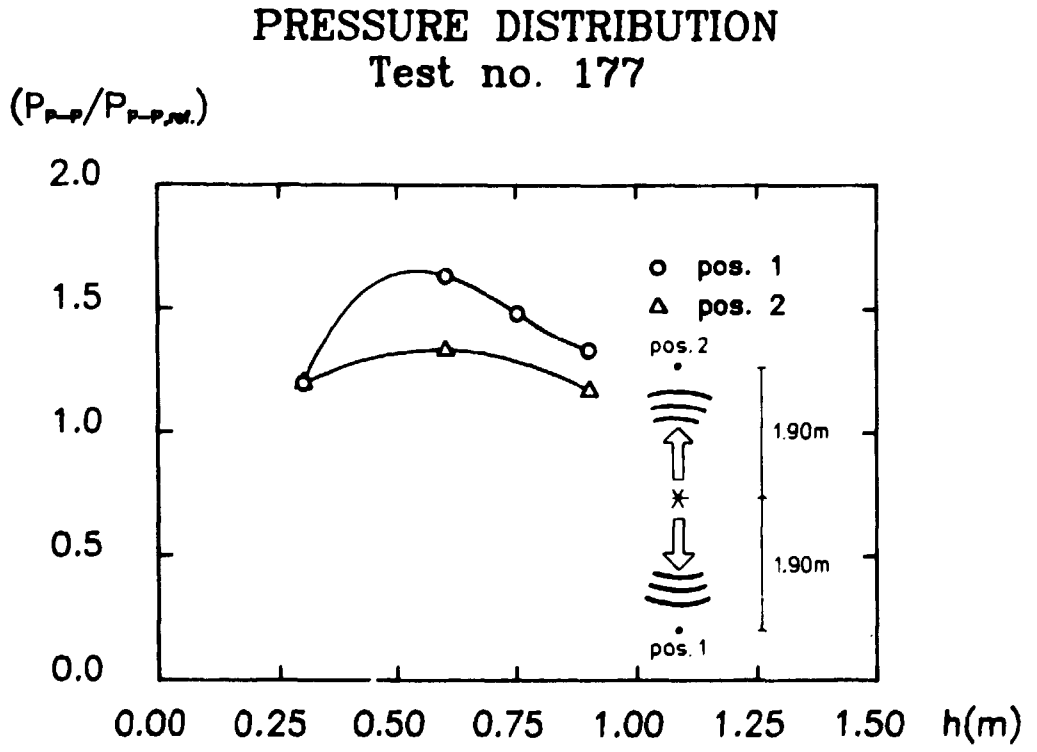

Fig. 52. Normalized peak-to-peak pressure distribution.

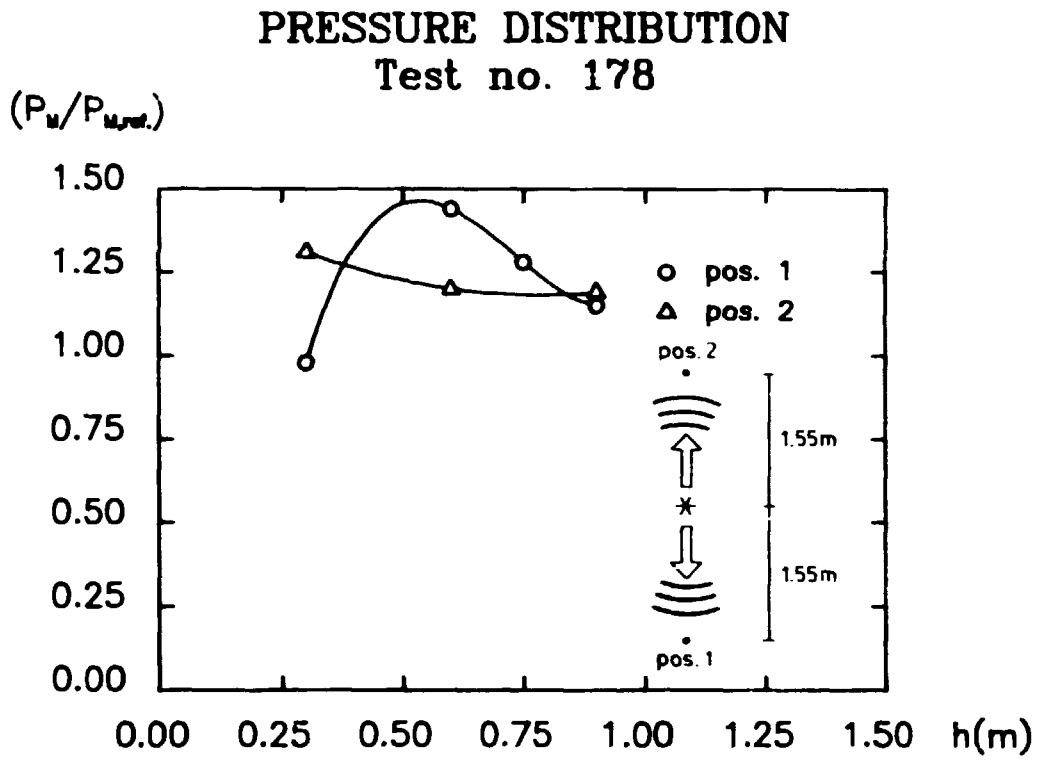

Fig. 53. Normalized peak pressure distribution.

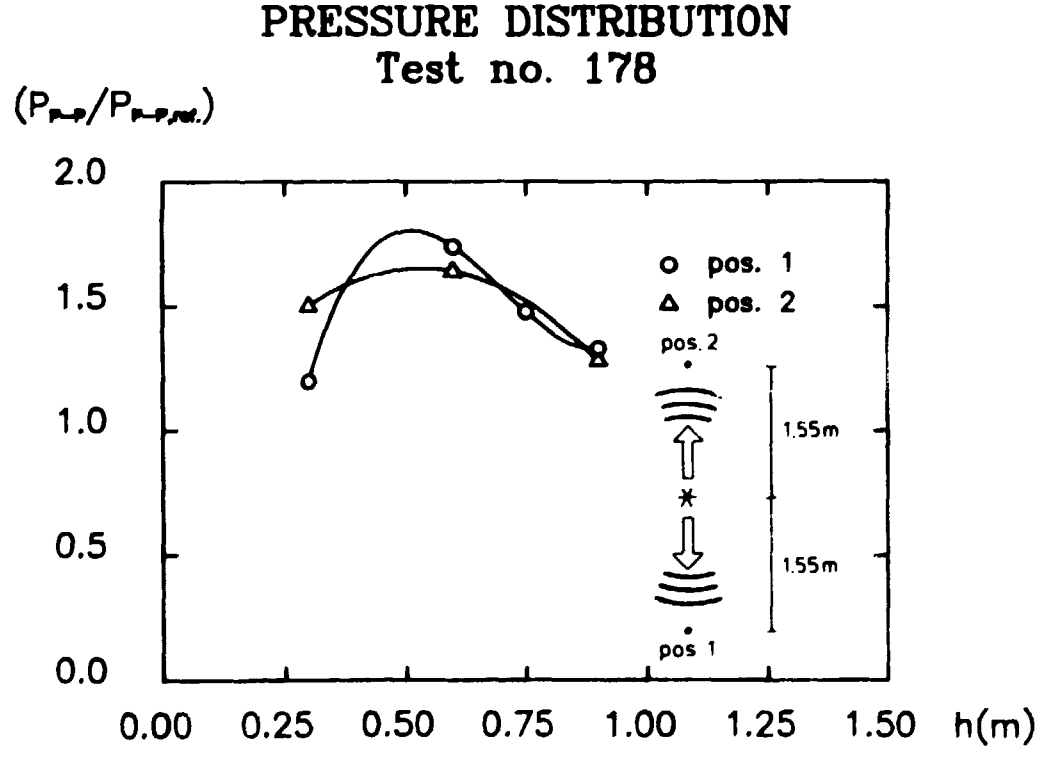

Fig. 54. Normalized peak-to-peak pressure distribution.

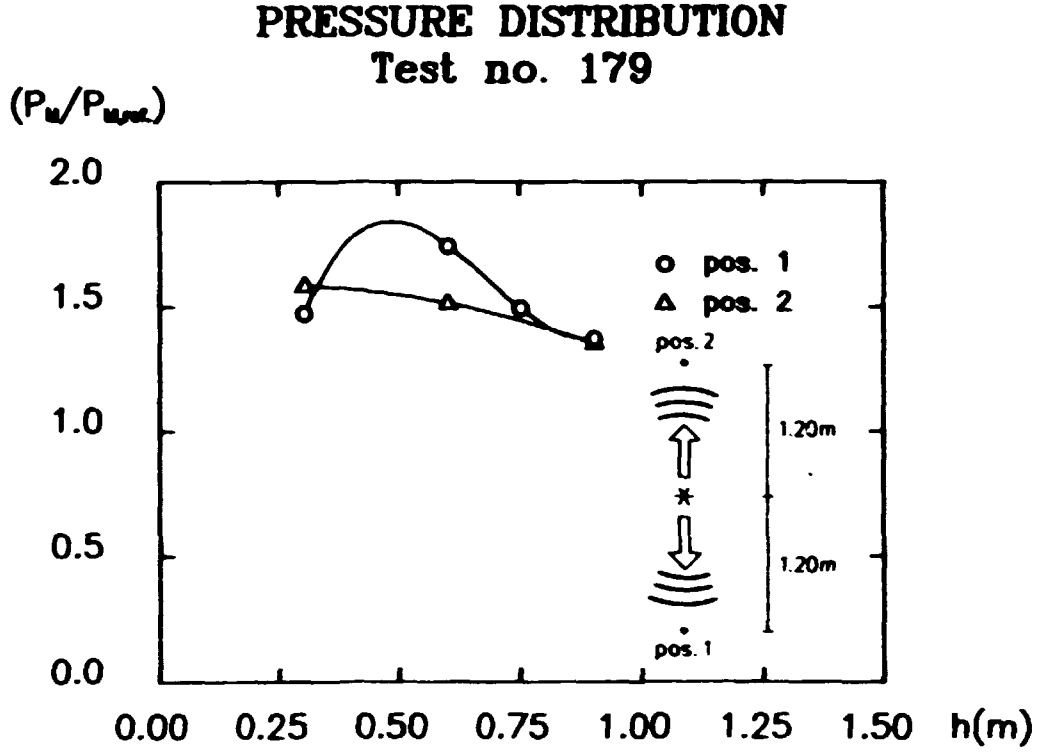

Fig. 55. Normalized peak pressure distribution.

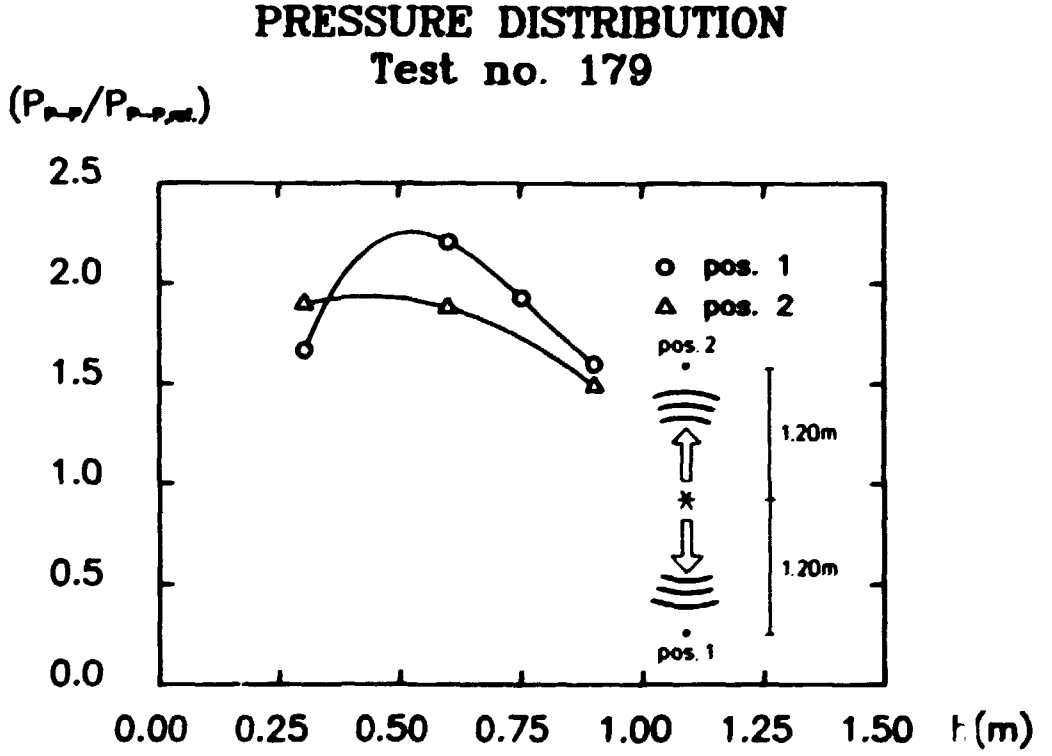

Fig. 56. Normalized peak-to-peak pressure distribution.

In Figs. 57-64 the normalized pressures are given as functions of the distance from the center of the source for a specific measuring level.

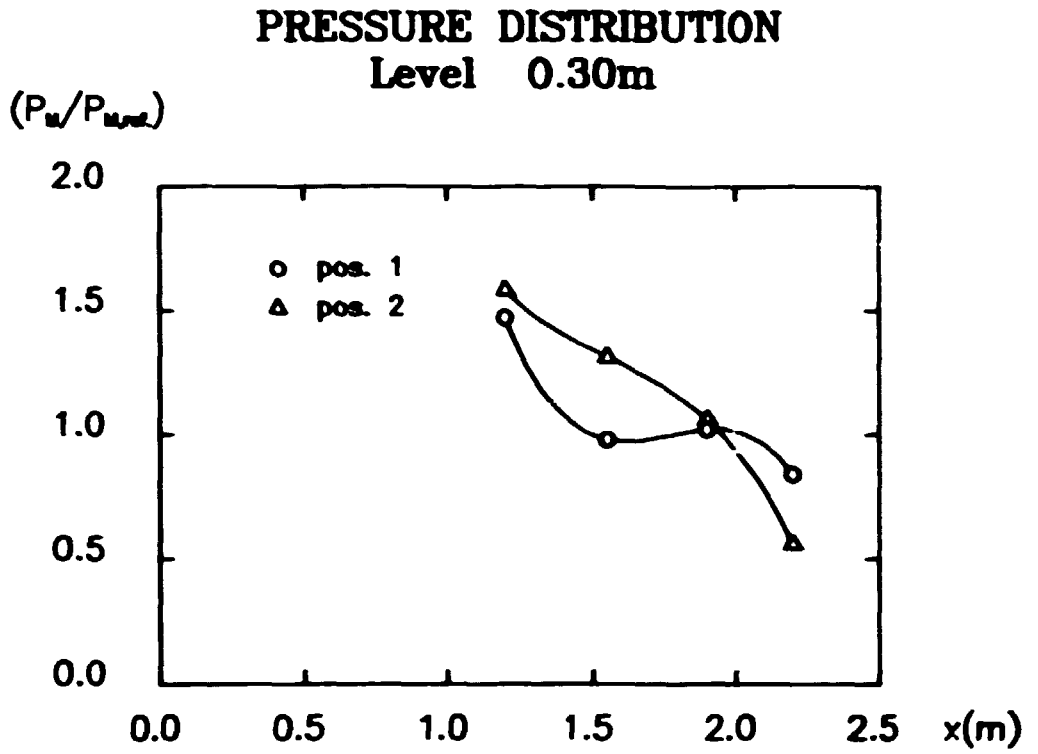

Fig. 57. Normalized peak pressure distribution.

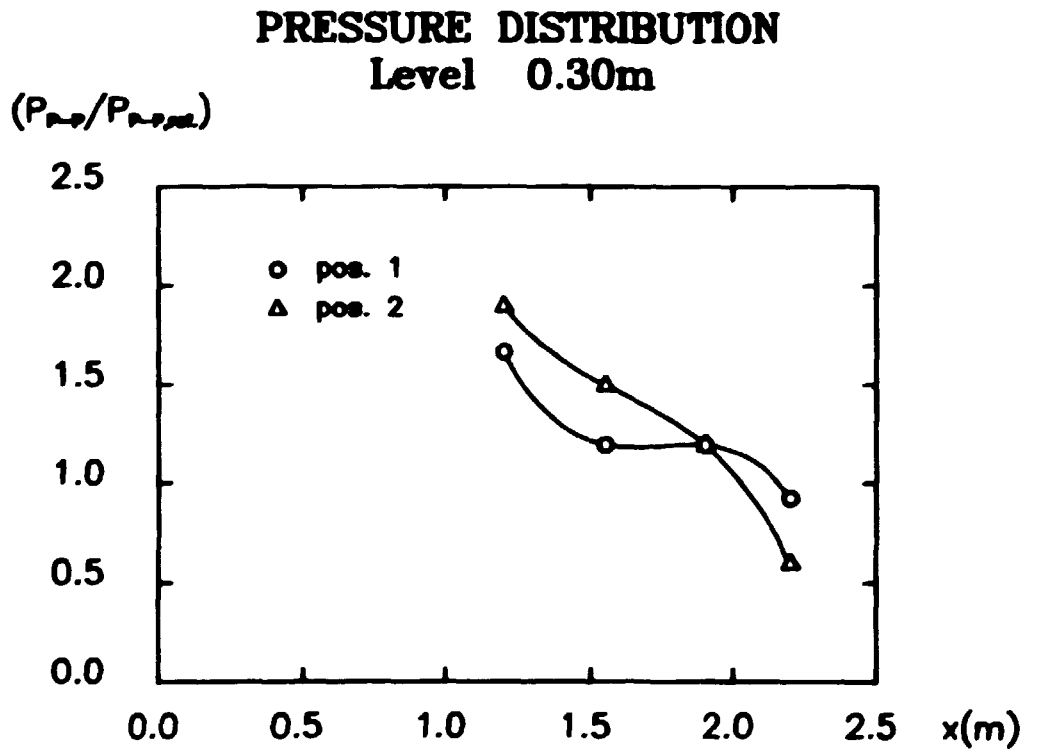

Fig. 58. Normalized peak-to-peak pressure distribution.

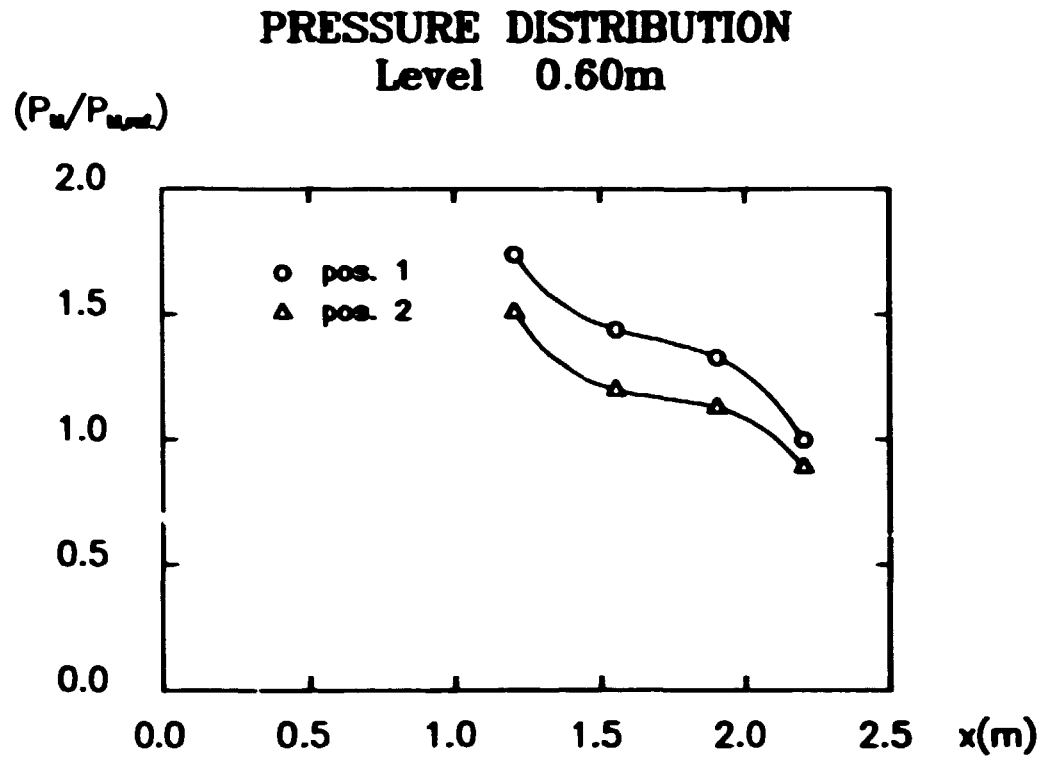

Fig. 59. Normalized peak pressure distribution.

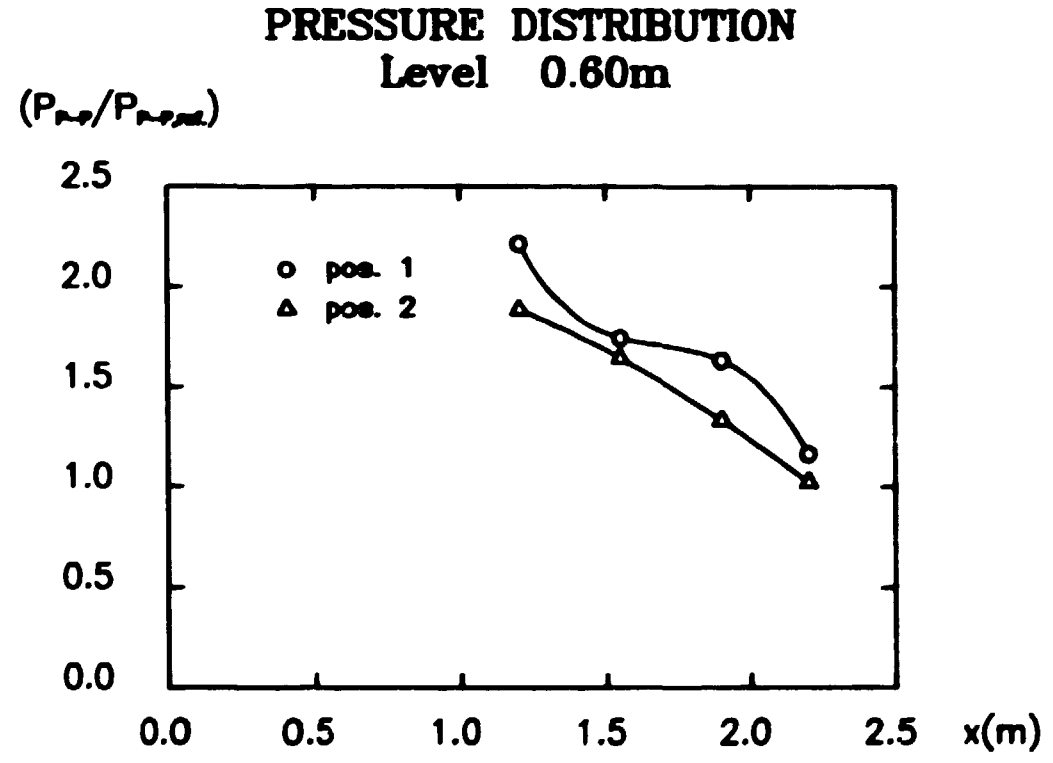

Fig. 60. Normalized peak-to-peak pressure distribution.

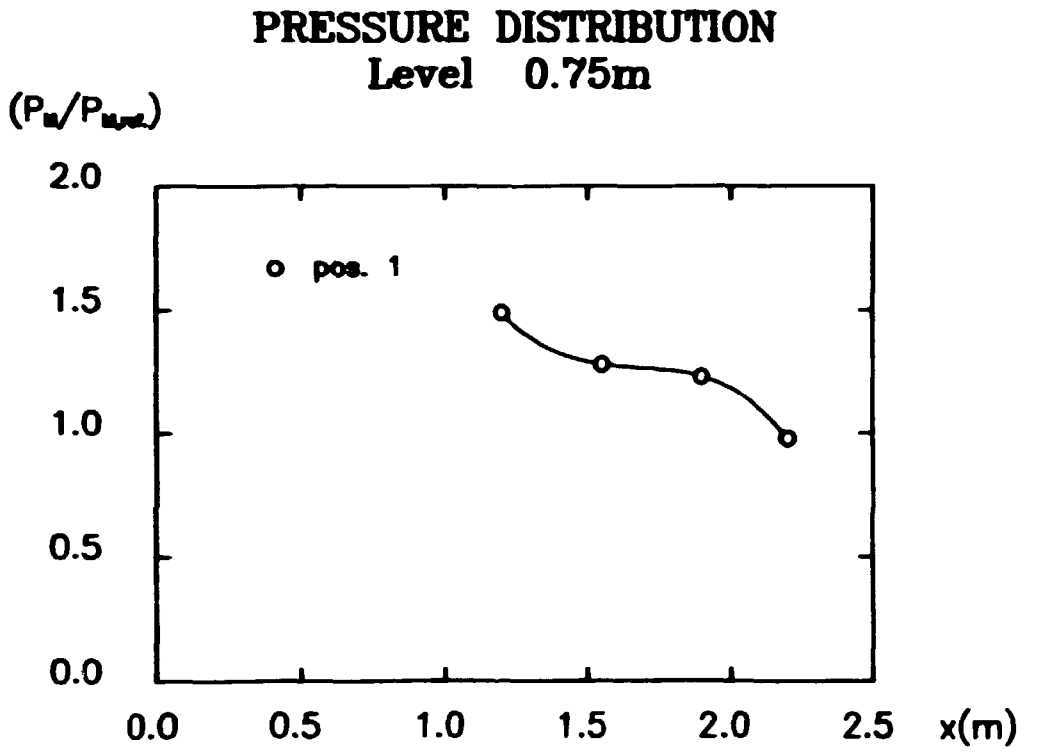

Fig. 61. Normalized peak pressure distribution.

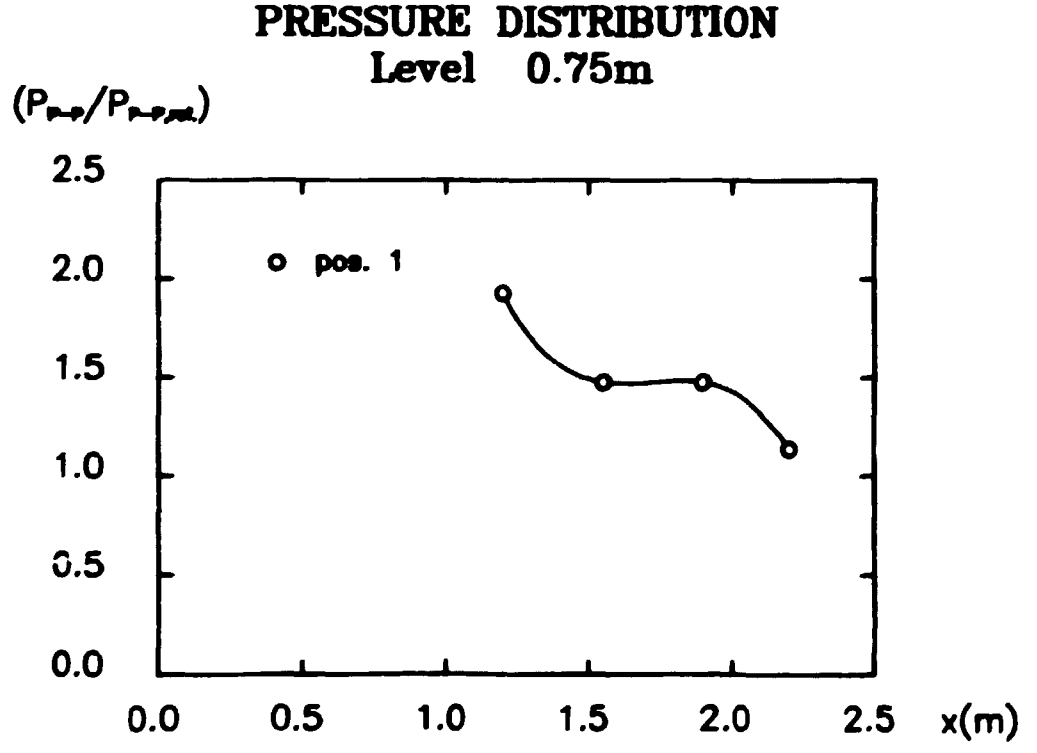

Fig. 62. Normalized peak-to-peak pressure distribution.

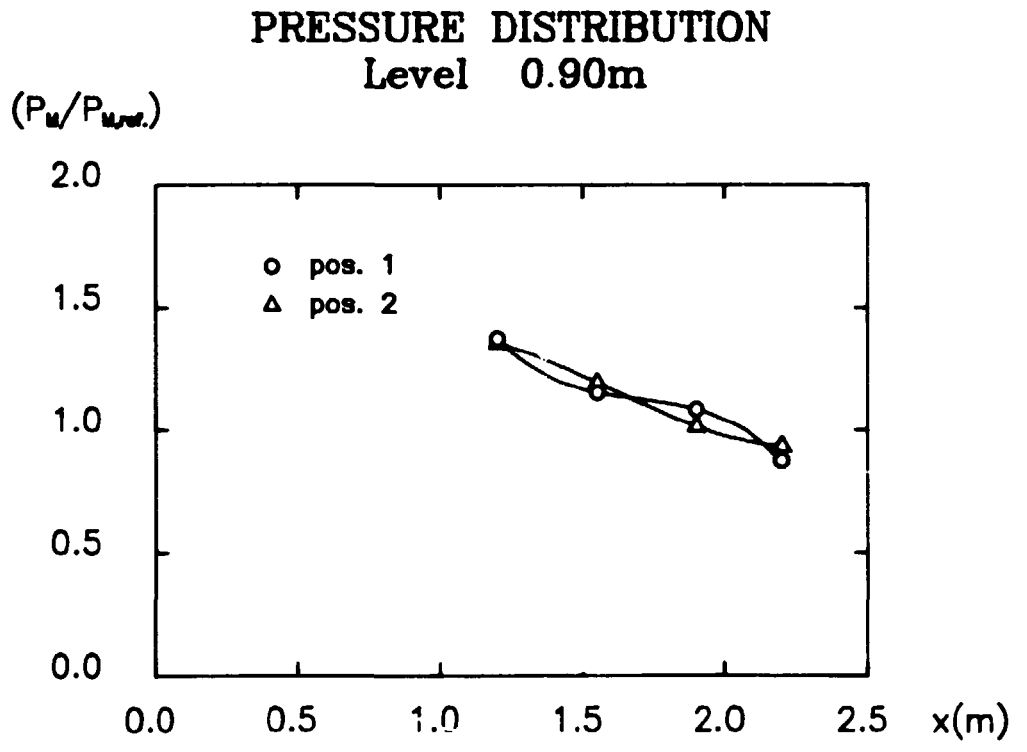

Fig. 63. Normalized peak pressure distribution.

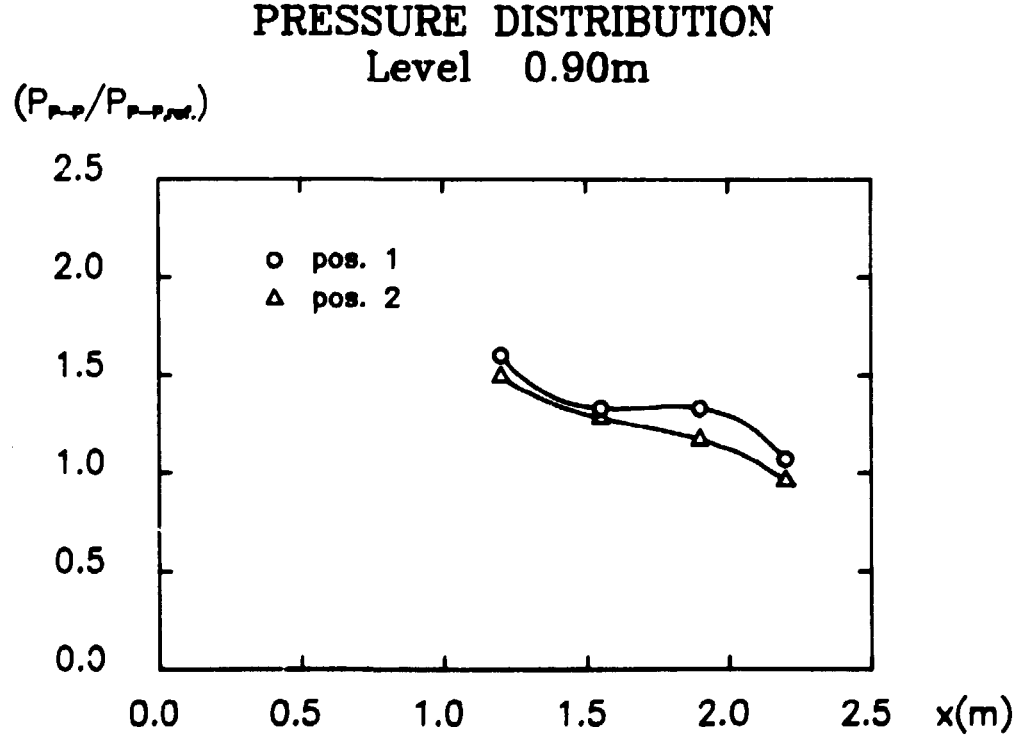

Fig. 64. Normalized peak-to-peak pressure distribution.

The means of the reference measurements corresponding to the results presented in the above Figures are given in Table 12 below, where <·> denotes the mean value operator.

TEST NO.	176	177	178	179
$\langle P_{M,ref} \rangle$ (mbar)	2.9	4.5	4.0	3.2
$\langle P_{P-P,ref} \rangle$(mbar)	6.1	10.0	8.8	7.5

Table 12. Mean of reference values corresponding to experiments 175-179.

3.6.3. Evaluation of the results.

A comparison of the Figs. 45 and 46, and Figs. 47 and 48 show that the shape of the positive pressure phase is preserved with increasing distance between the measuring point and ground, whereas the shape of the negative pressure phase is changed. This tendency is also valid for the rest of the measurements. The change is supposed to be due to a phase shift between the "reflected signal" and the "direct signal". The difference in behaviour of the positive and negative phases can be due to a different frequency content in those two phases.

For an ideal symmetric situation the curves corresponding to positions 1 and 2, respectively, in Figs. 49-56 should coincide. This is obviously not the case - in fact, a considerable deviation is observed. The explanation might be found in the graphs presented in Figs. 57-64, where it is seen that the degree of agreement between the measurements at positions 1 and 2 are increased with increasing distance from the ground. In other words, it is seen that near the reflecting surface a boundary layer is formed where considerable scatter is introduced and the symmetry properties are destroyed, whereas the symmetry is preserved at larger distances from the surface.

Again referring to Figs. 57-64, it is noted that the acoustic 1/R attenuation is reasonably reproduced by the measurements performed not too close to the ground.

Finally, it is noted that the overall pressure level corresponding to these experiments is slightly increased compared with the pressure level corresponding to the situation without reflection superimposed. This is what should be expected.

3.7. Pressure field around obstacles placed on an acoustically hard surface.

In this section the boundary conditions have been made further complicated compared to the situation in the previous sections. The setup is as described in section 3.6 except that a number of geometrical well-defined obstacles have been placed on the hard surface.

Three different types of obstacles have been used: all are wooden prisms with a cross section of .25m x .25m. The length of the three were .25m, .50m and .80m. The boxes have been supplied with holes; thus the tranducers could be placed in level with the surface. The position of the holes on the box sides appears from Fig. 65 below, where "•" denotes a hole and all dimensions are given in meters.

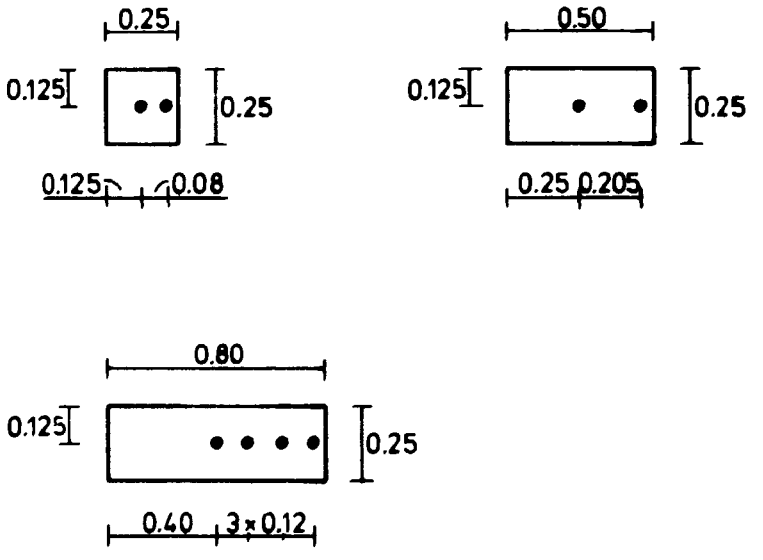

Fig. 65. Position of the "measuring holes".

The plan of the experiments was to investigate various aspects of the boundary/blast-wave interaction. A total of 34 experiments have been performed in this context. In 14 of these tests only a single box has been placed in the flow field; in the remaining 20 two boxes have been used. These two test series shall be handled separately below.

3.7.1. Single box experiments

The pressure distribution on a single box has been investigated in order to highlight

- the pressure load on a geometric simple obstacle,
- the extension of end-effects, which is essential in the evaluation of a two-dimensional mathematical model as approach to the physical three-dimensional phenomena, and
- the scattering and diffraction effects due to such obstacles.

3.7.1.1. Experimental setup

All the experiments have been performed with an 80 cm long box. The box has been placed in different positions and measurements have been performed at various points. This shall not be described in detail here, but is for the sake of clarity illustrated on the figures giving the results from each particular experiment (in section 3.7.1.2). An example of such an illustration is given in Fig. 66.

The sides on the box have been named and a parameter, x, has been introduced in order to specify the actual pressure measusuring points. Moreover, the figure has been provided with a "|||" which symbolizes the pressure wave, and an arrow giving the direction of the pressure propagation.

The distance between the center of the explosion and the front of the box has been constant (and equal to 2.20 m) throughout these tests. The center of the explosion was placed 0.40 m above the ground.

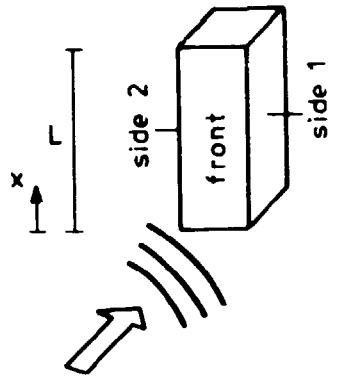

Fig. 66. Example of an illustration of the experimental setup.

Apart from the pressure measurements on the box, two reference measurements have been performed - one in the diametrically opposite direction of the box and one in a direction perpendicular to this. The distance from the reference measurements to the center of the source was 2.20 m.

Specific data for each experiment are given in Table 13.

EXPERIMENT NO.	MIXTURE (Vol.%) CH_4	O_2	N_2	SOURCE DIAMETER (m)	L (m)
142	16	32	52	0.25	0.80
143	16	32	52	0.30	0.80
144	16	32	52	0.30	0.80
145	16	32	52	0.30	0.80
146	16	32	52	0.30	0.80
147	16	32	52	0.30	0.80
148	16	32	52	0.30	0.80
149	16	32	52	0.30	0.80
150	16	32	52	0.30	0.80
151	16	32	52	0.30	0.80
152	16	32	52	0.30	0.80
153	16	32	52	0.30	0.80
154	16	32	52	0.30	0.80
155	16	32	52	0.30	0.80

Table 13. Experimental data.

3.7.1.2. Results.

The measured pressure signals are presented in the figures and tables below.

In Fig. 67 an example of a pressure pulse recorded at the same level as the surface of the box and with a setup as illustrated in Fig. 66, has been presented.

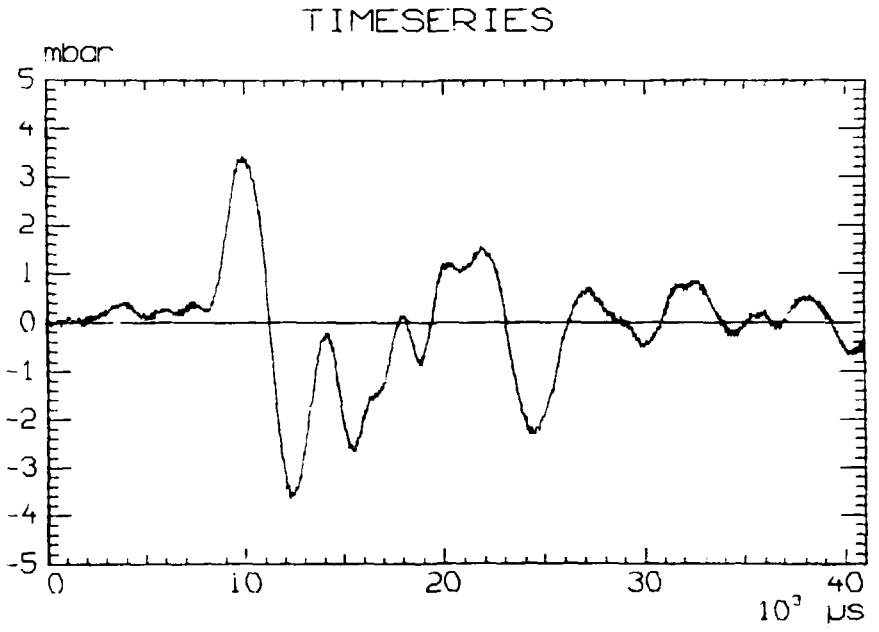

Fig. 67. Pressure pulse recorded in the front of the box 0.52 m

As in the previous sections the normalized peak and the normalized peak-to-peak pressures have been evaluated on the basis of curves of this type. The mean value of the reference measurements has been used in the normalization of the pressures. The normalized pressures are presented in Figs. 68-95. Cubic spline interpolation has been used for curves containing 3 measuring points, whereas curves with only two measuring points have been constructed by use of linear interpolation. In a few of the measurements the negative phase has overloaded the equipment. These measurements are consequently not represented in the peak-to-peak plots, but only in the positive peak plots. The tests have not been presented in chronological order, but are organised such that the experiments with a box "on end" are

presented first and then subsequently the experiments with a "laying" box.

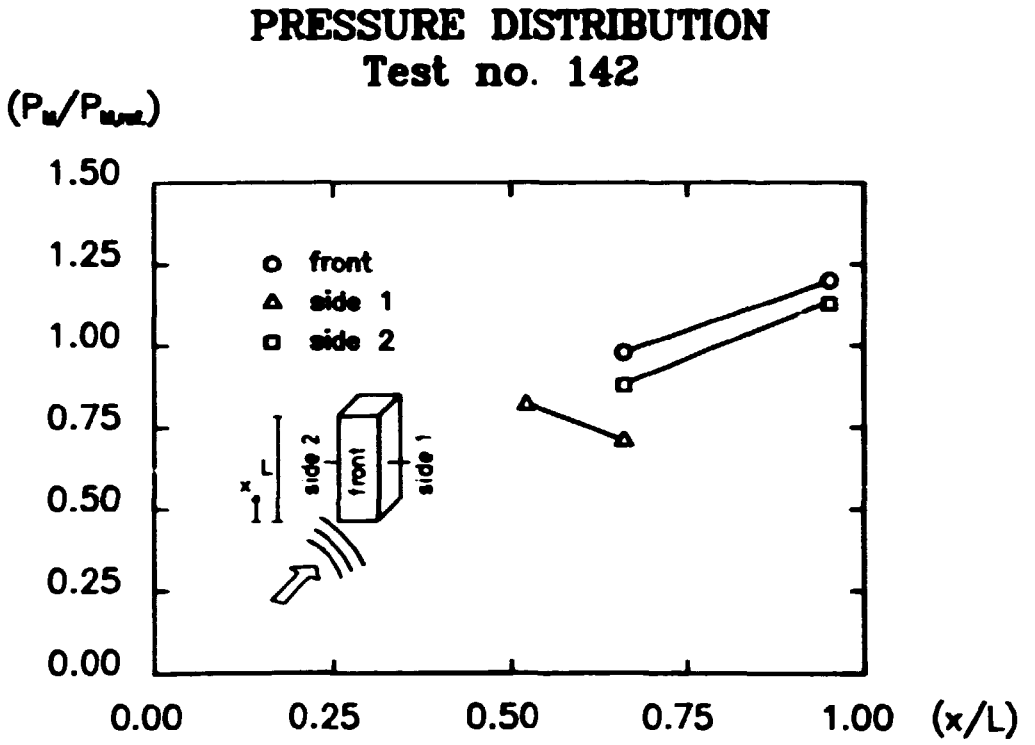

Fig. 68. Normalized peak pressure distribution.

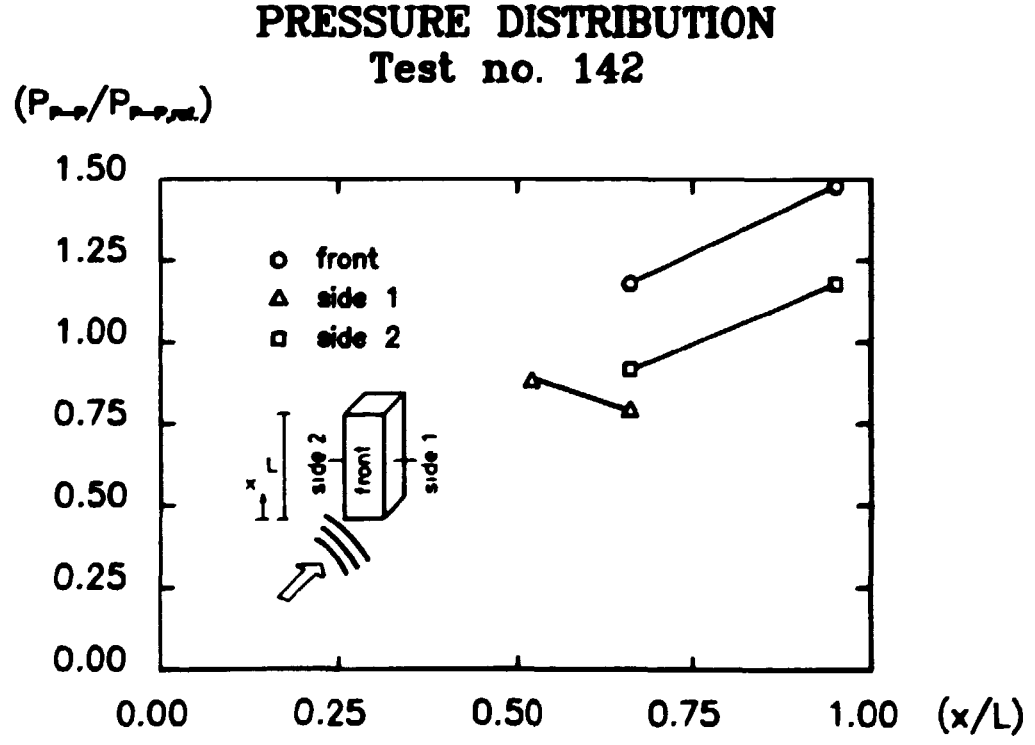

Fig. 69. Normalized peak-to-peak pressure distribution.

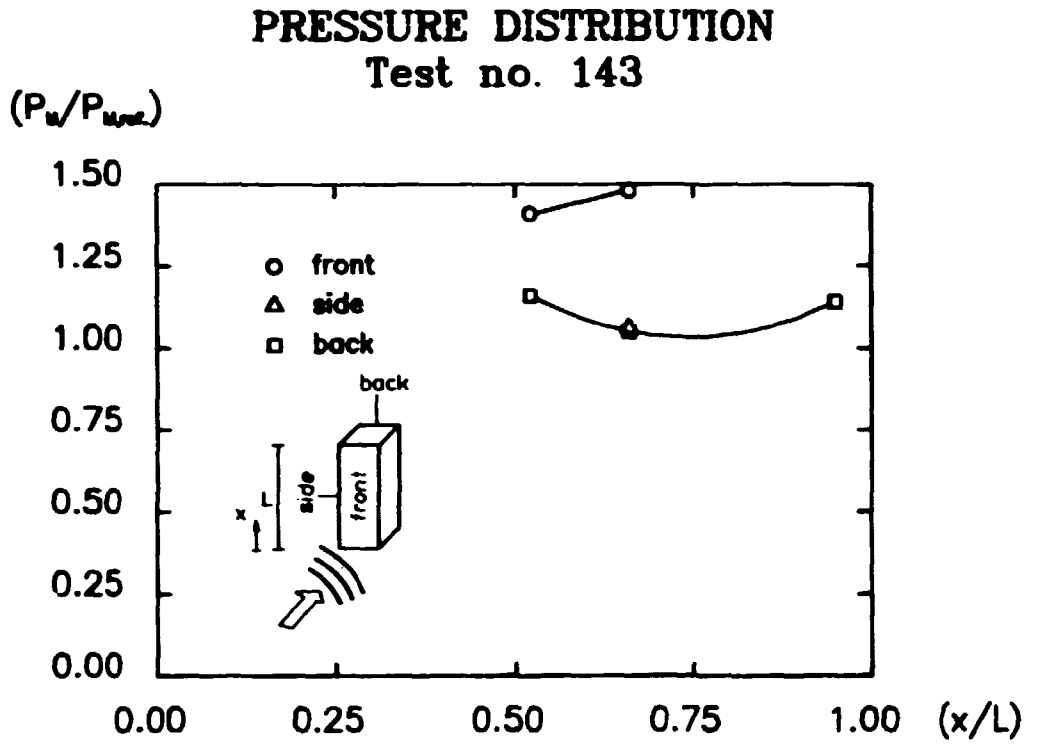

Fig. 70. Normalized peak pressure distribution.

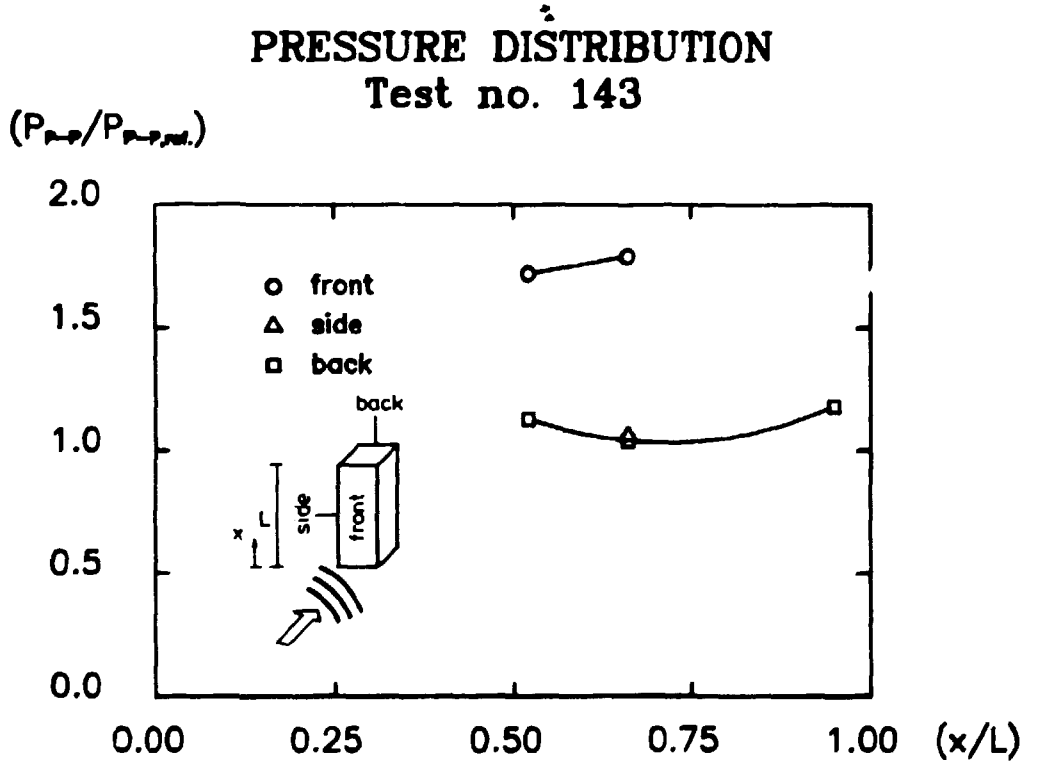

Fig. 71. Normalized peak-to-peak pressure distribution.

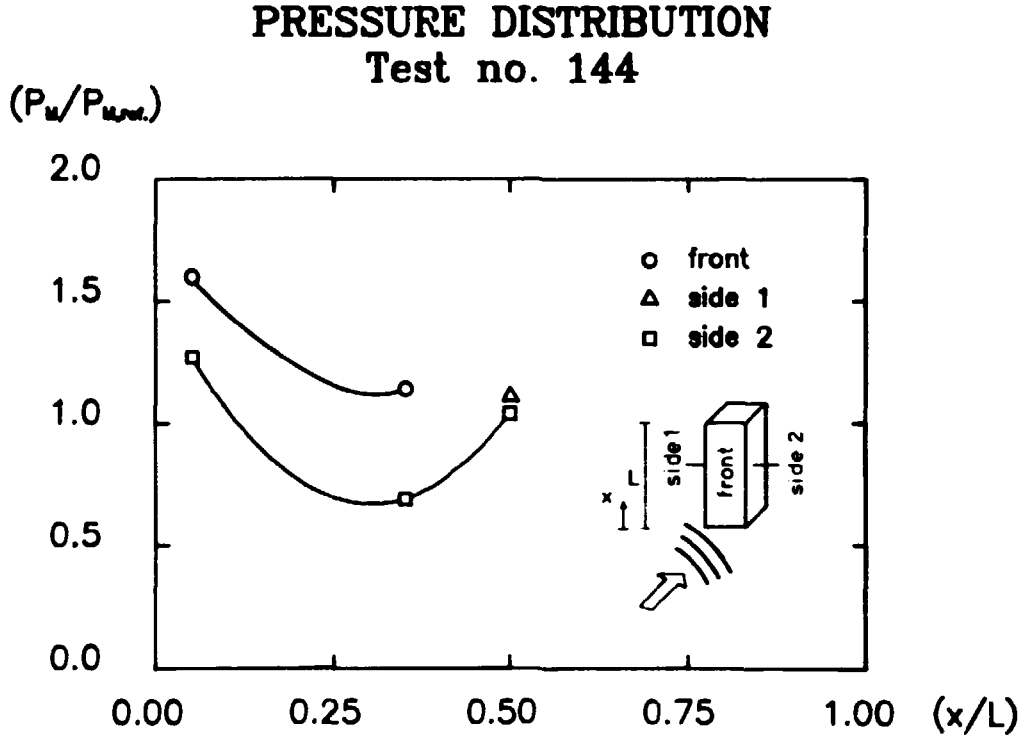

Fig. 72. Normalized peak pressure distribution.

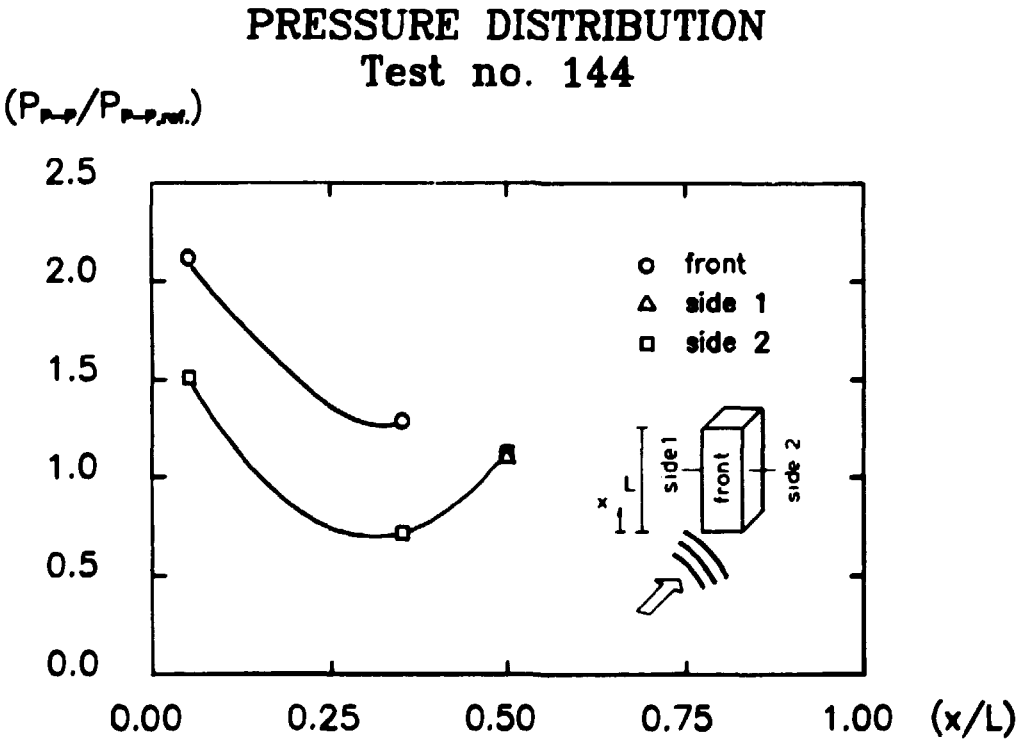

Fig. 73. Normalized peak-to-peak pressure distribution.

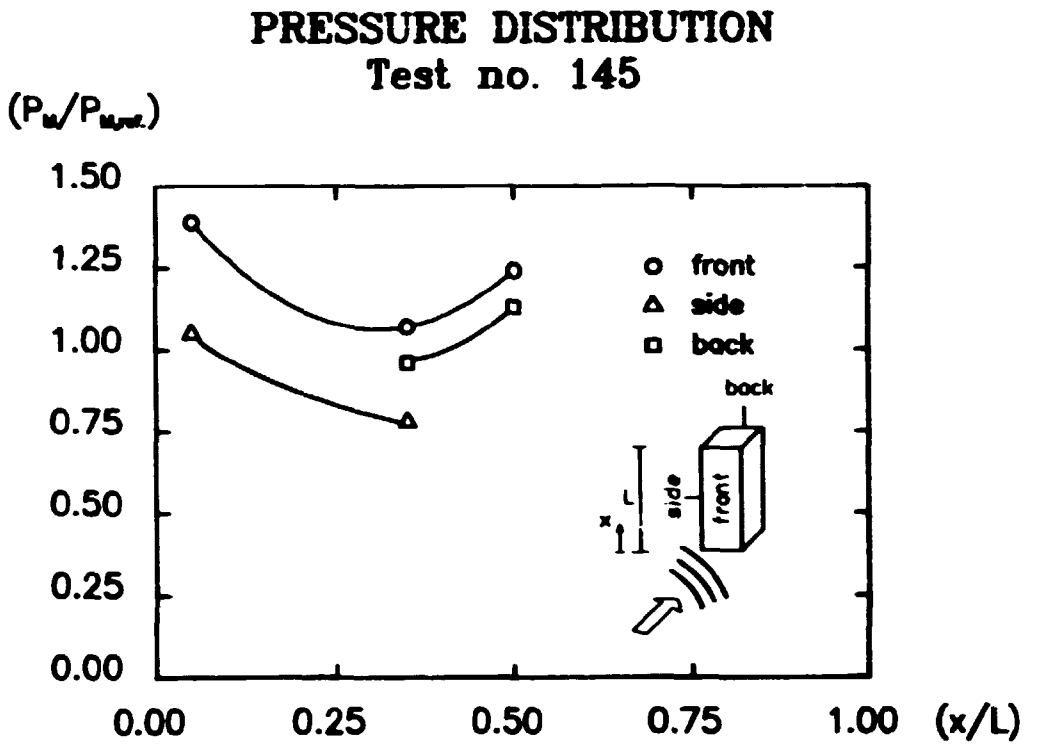

Fig. 75. Normalized peak-to-peak pressure distribution.

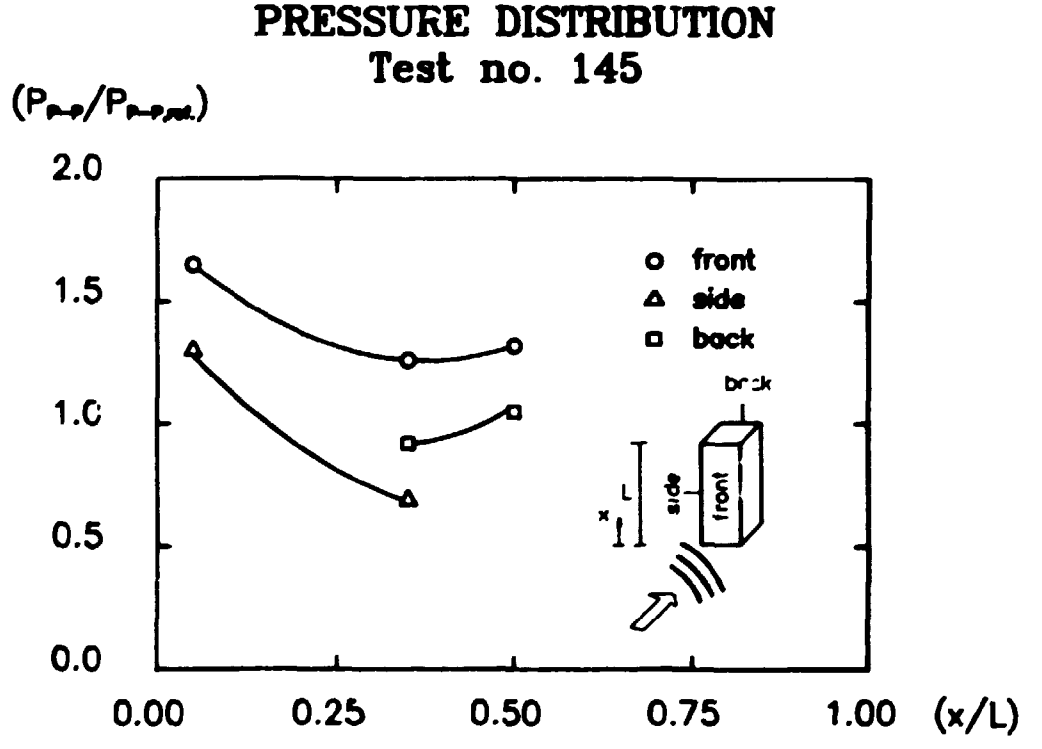

Fig. 74. Normalized peak pressure distribution.

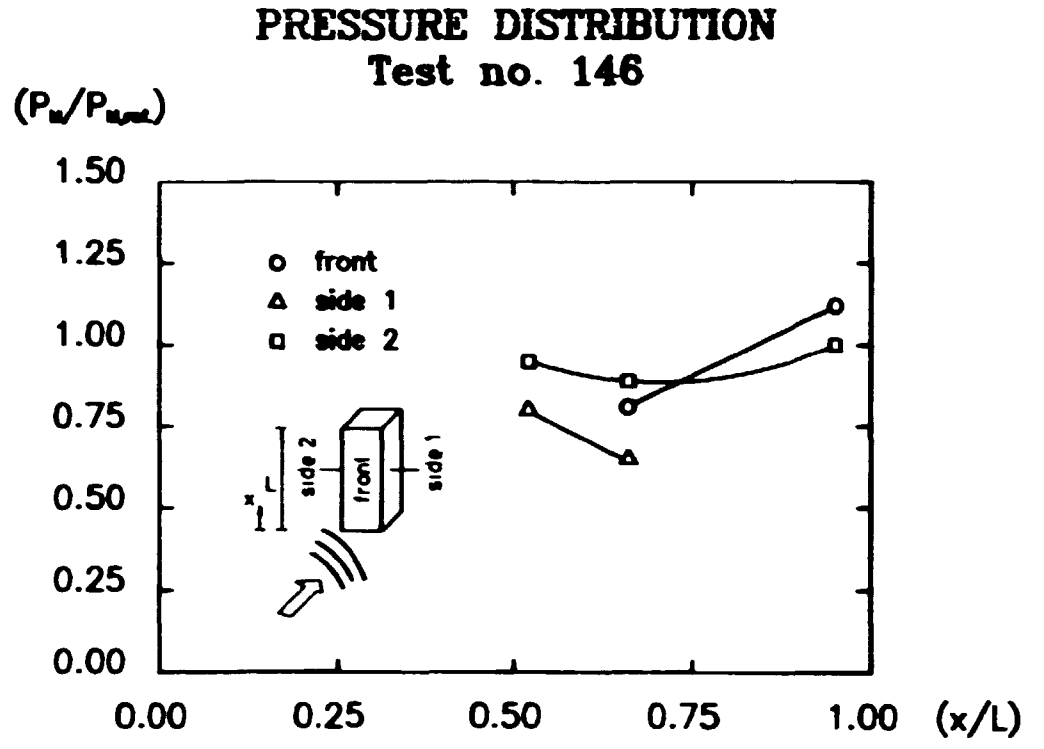

Fig. 76. Normalized peak pressure distribution.

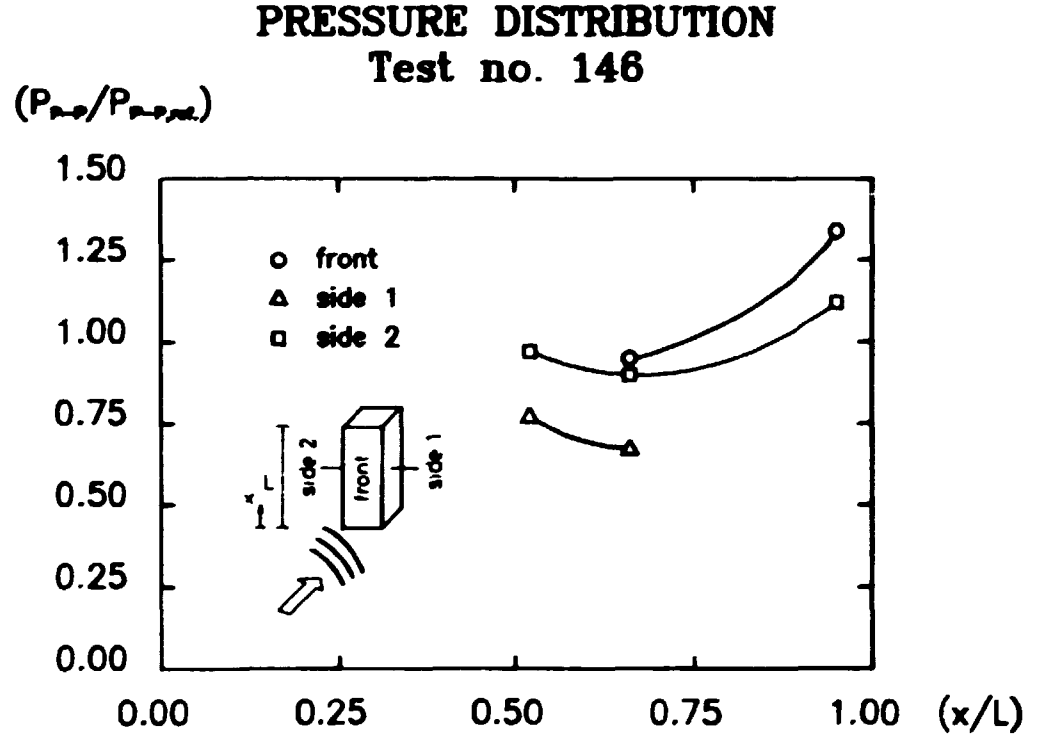

Fig. 77. Normalized peak-to-peak pressure distribution.

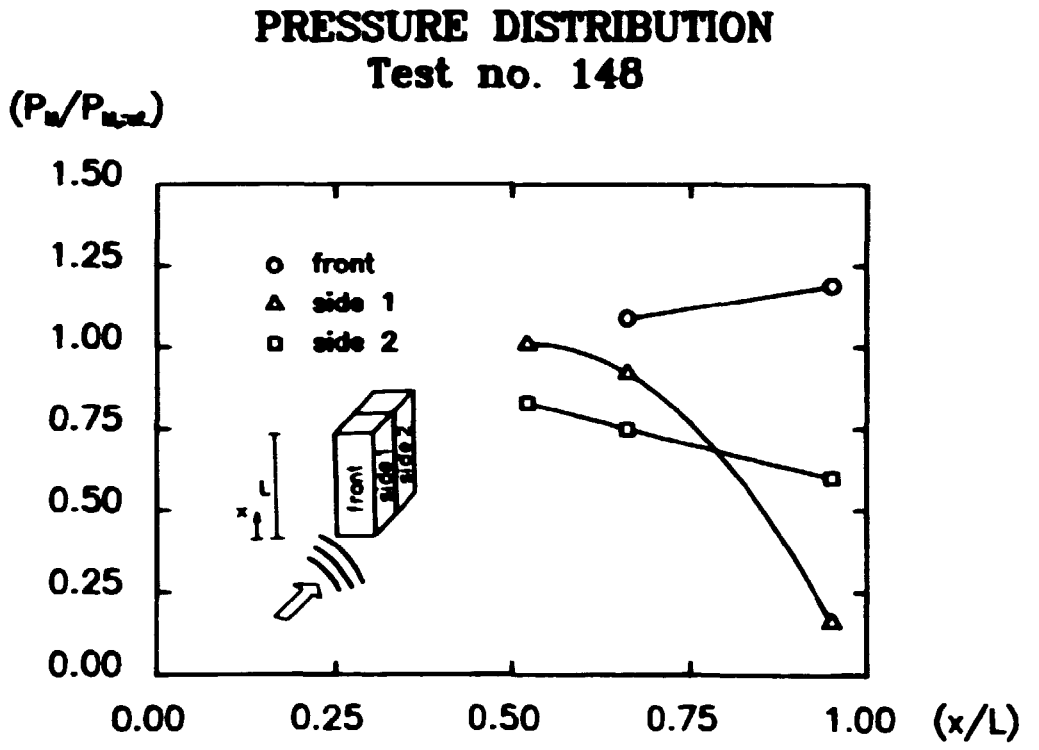

Fig. 78. Normalized peak pressure distribution.

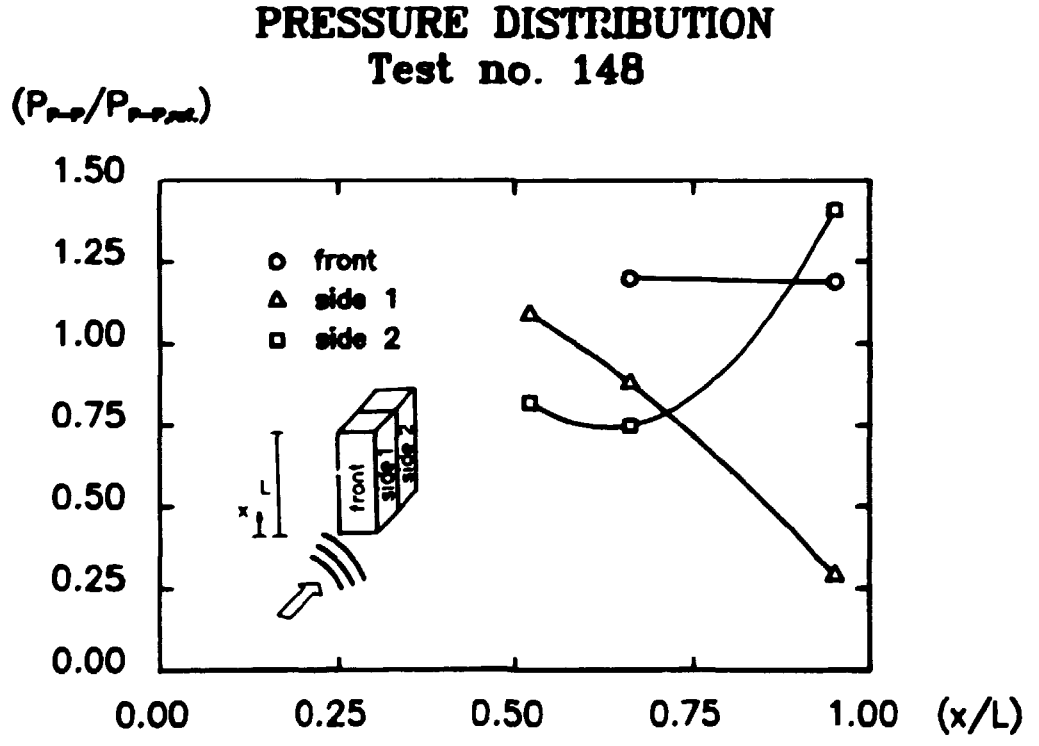

Fig. 79. Normalized peak-to-peak pressure distribution.

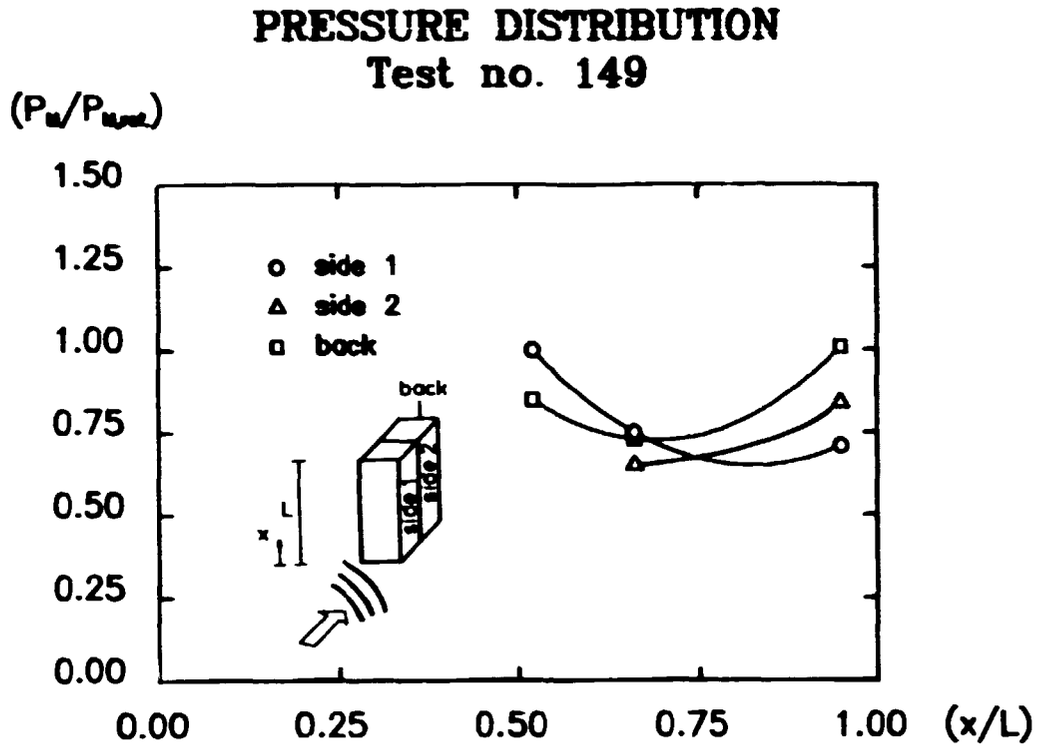

Fig. 80. Normalized peak pressure distribution.

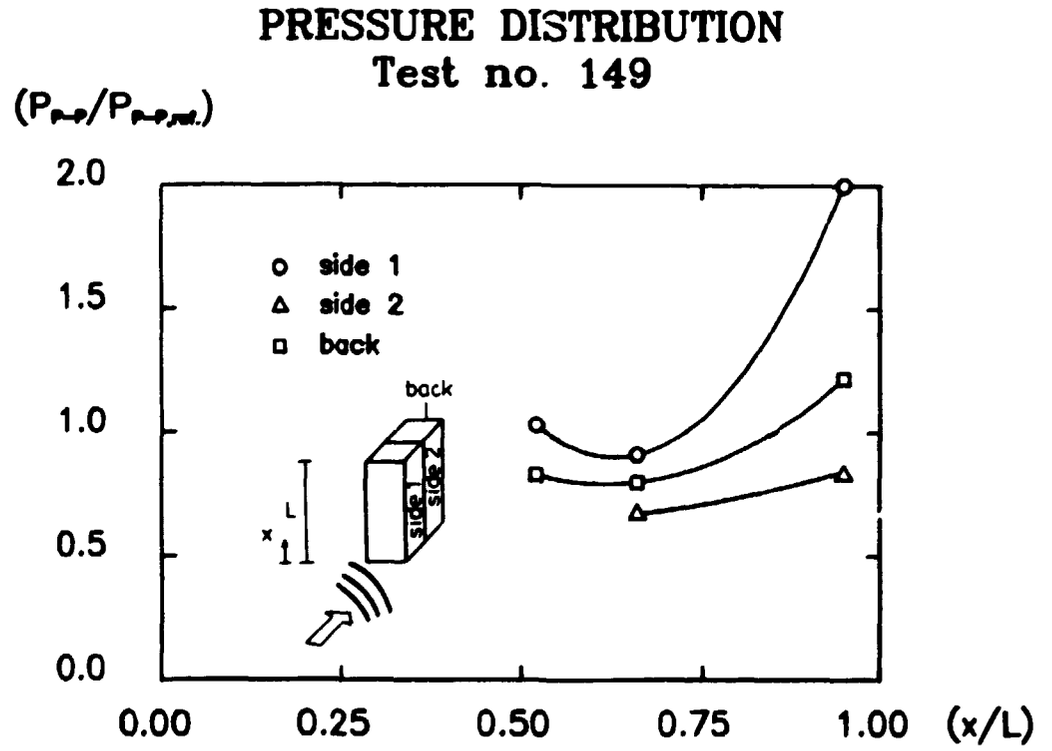

Fig. 81. Normalized peak-to-peak pressure distribution.

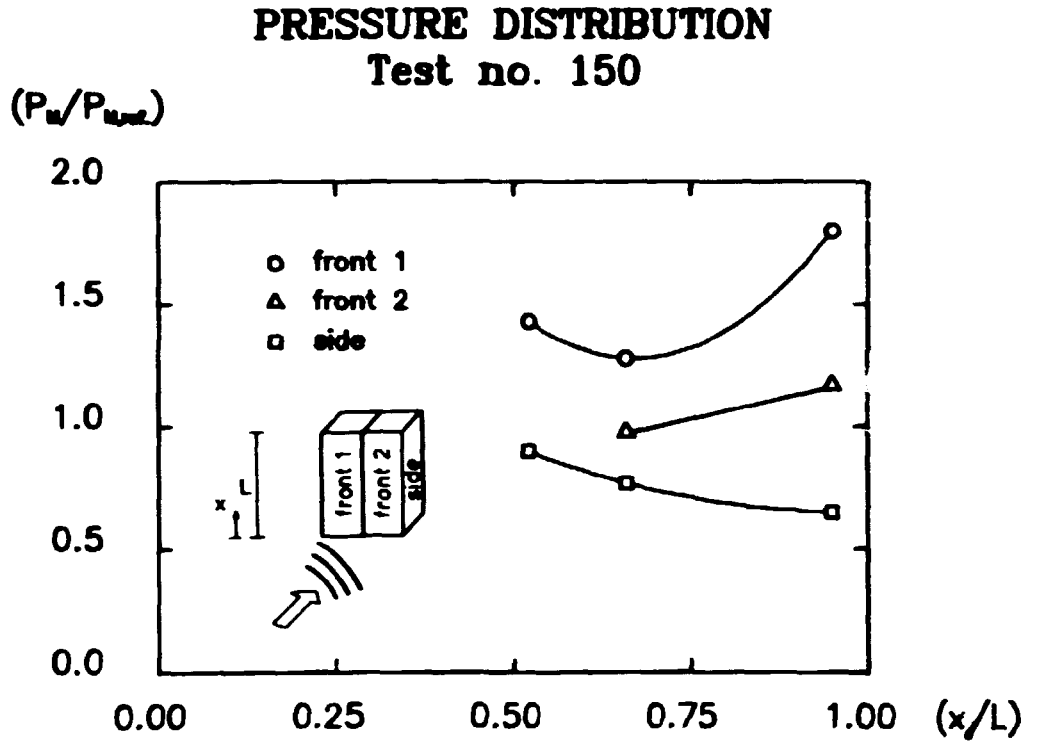

Fig. 82. Normalized peak pressure distribution.

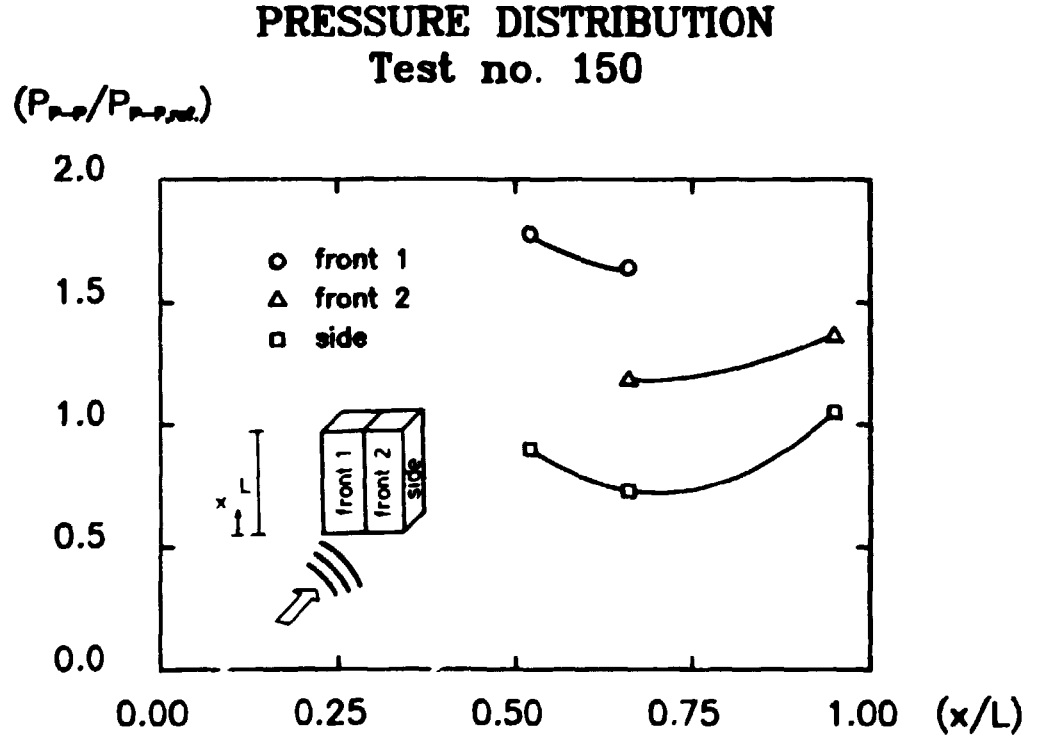

Fig. 83. Normalized peak-to-peak pressure distribution.

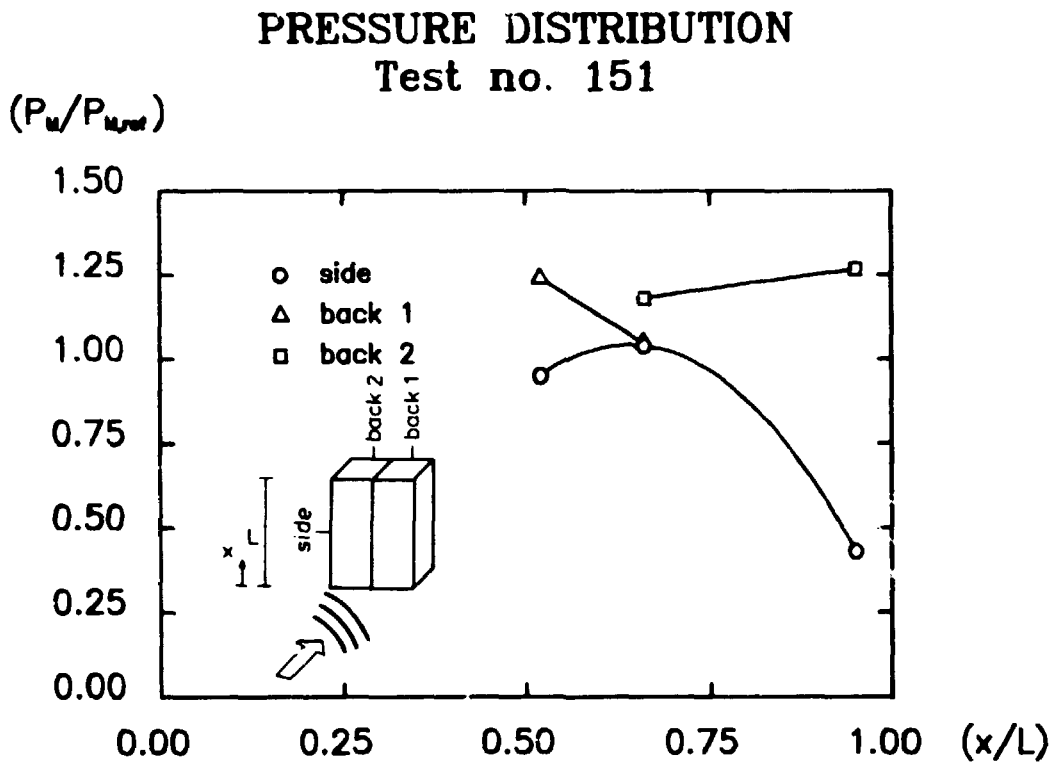

Fig. 84. Normalized peak pressure distribution.

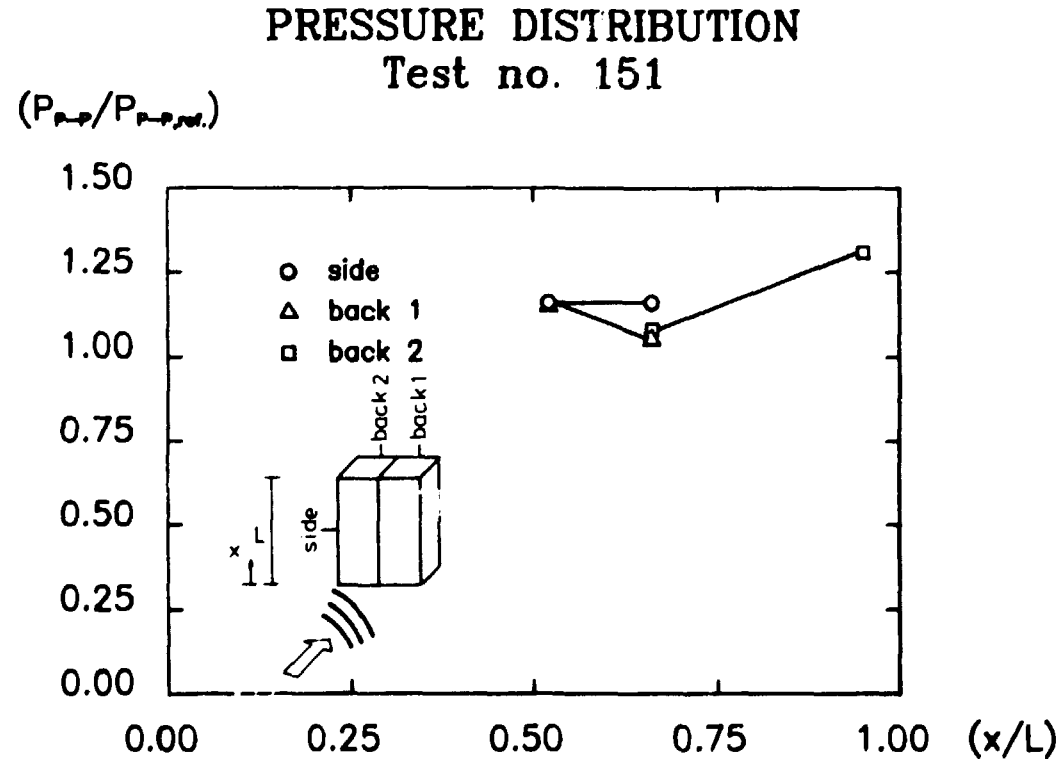

Fig. 85. Normalized peak-to-peak pressure distribution.

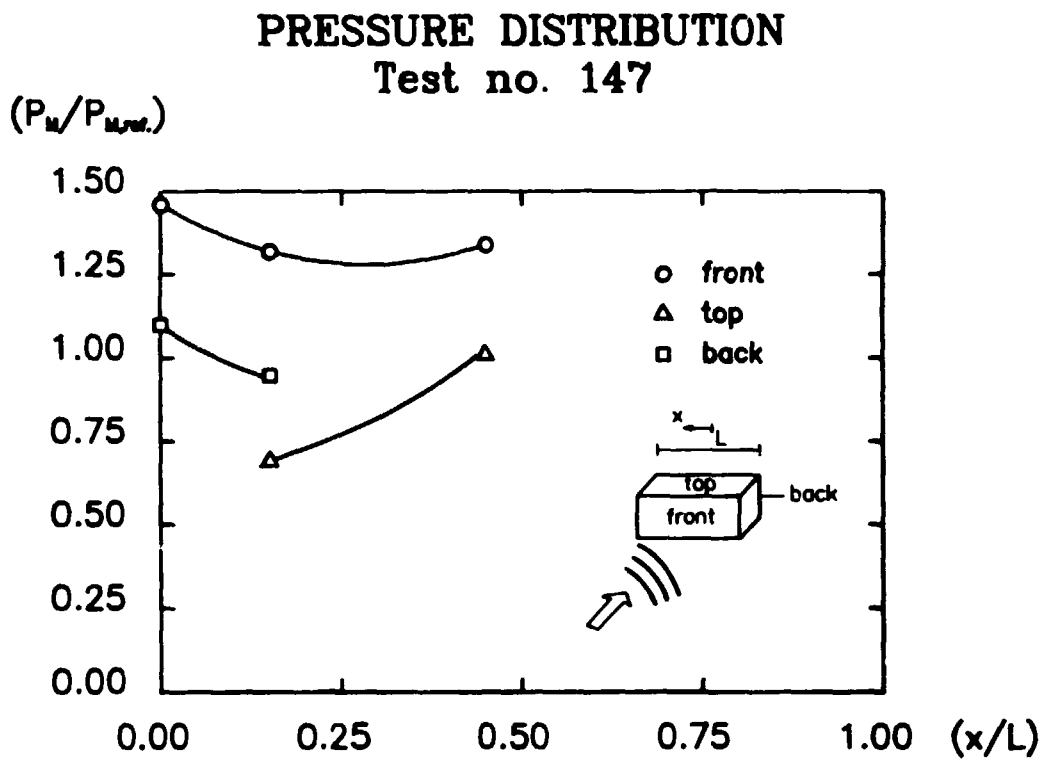

Fig. 86. Normalized peak pressure distribution.

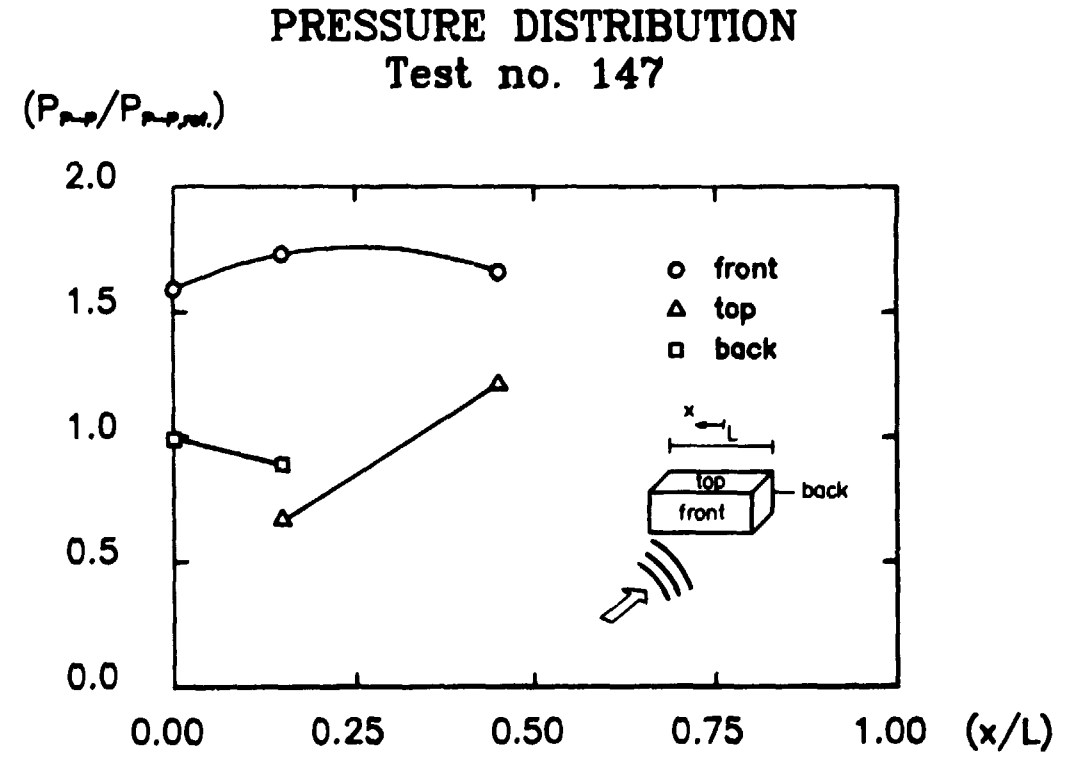

Fig. 87. Normalized peak-to-peak pressure distribution.

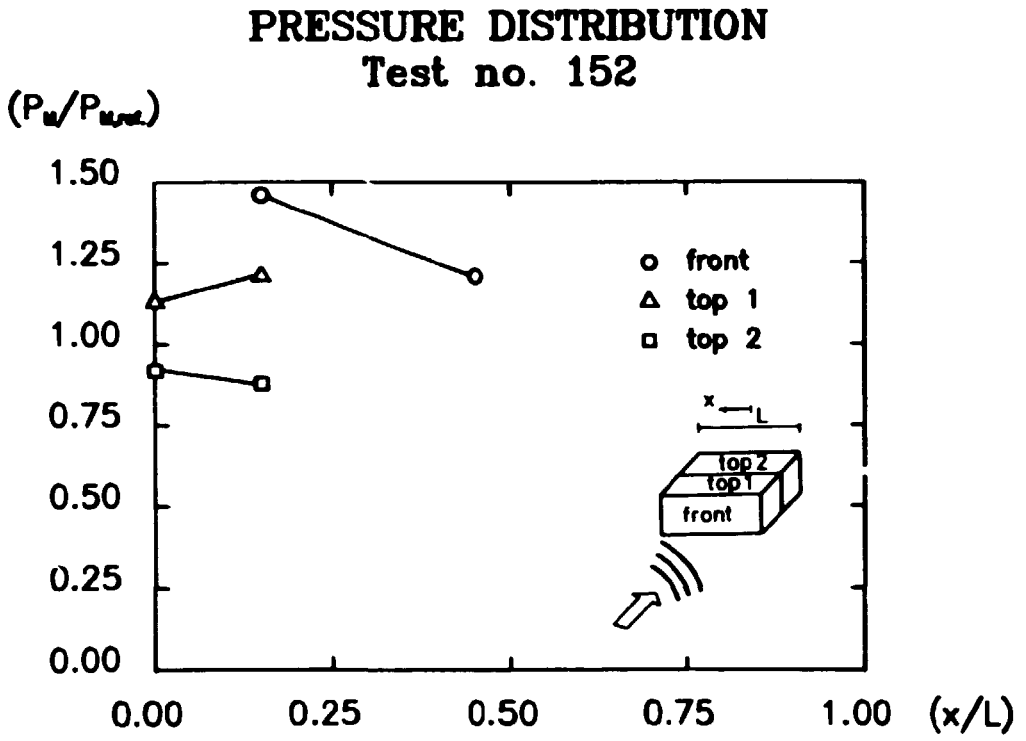

Fig. 88. Normalized peak pressure distribution.

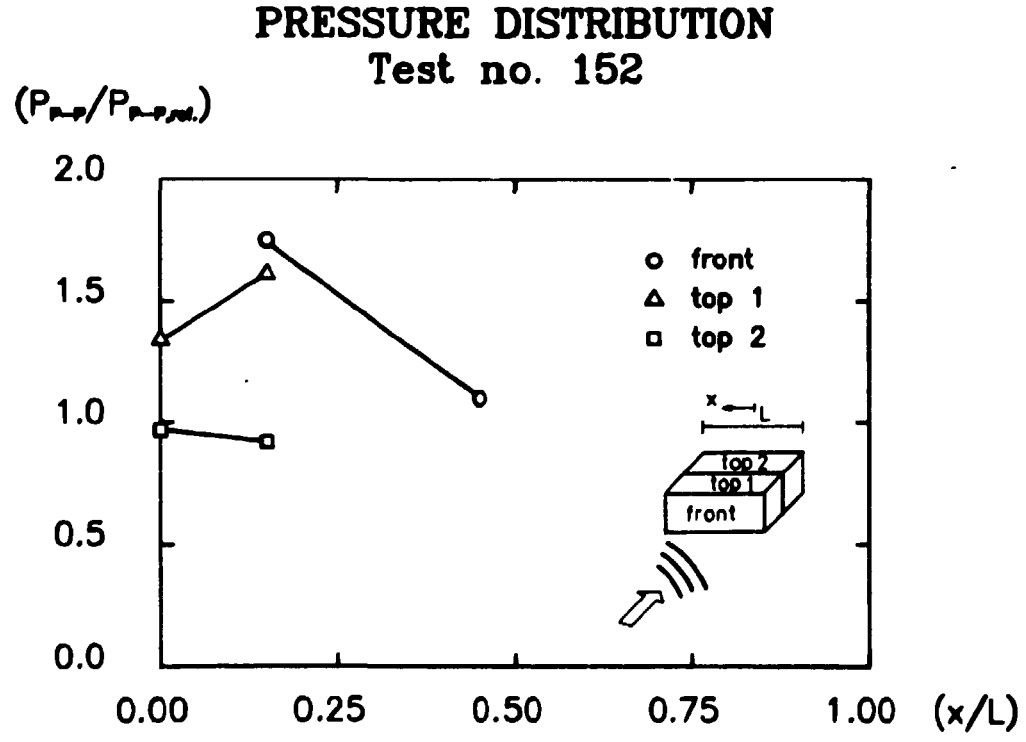

Fig. 89. Normalized peak-to-peak pressure distribution.

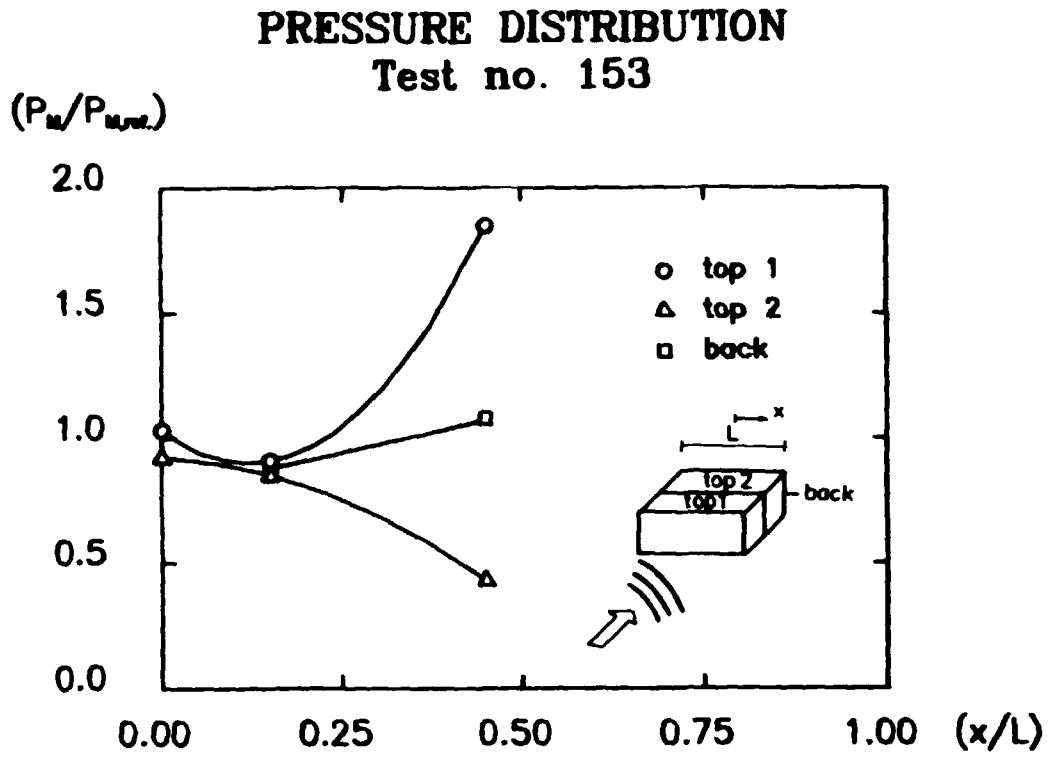

Fig. 90. Normalized peak pressure distribution.

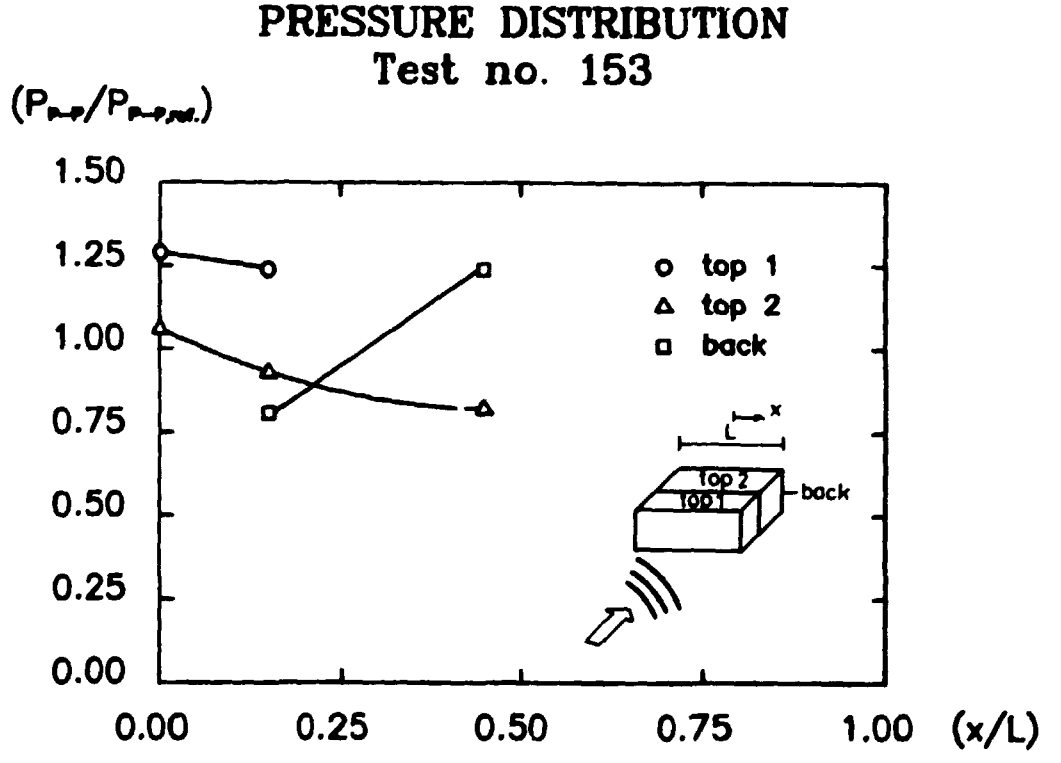

Fig. 91. Normalized peak-to-peak pressure distribution.

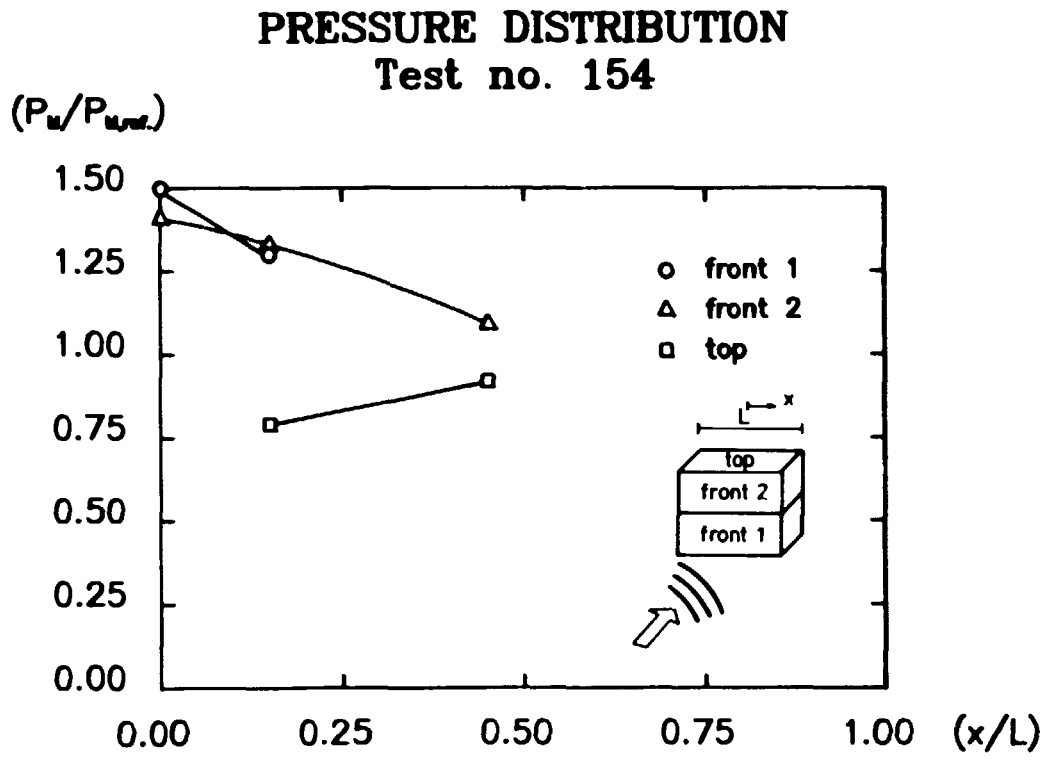

Fig. 92. Normalized peak pressure distribution.

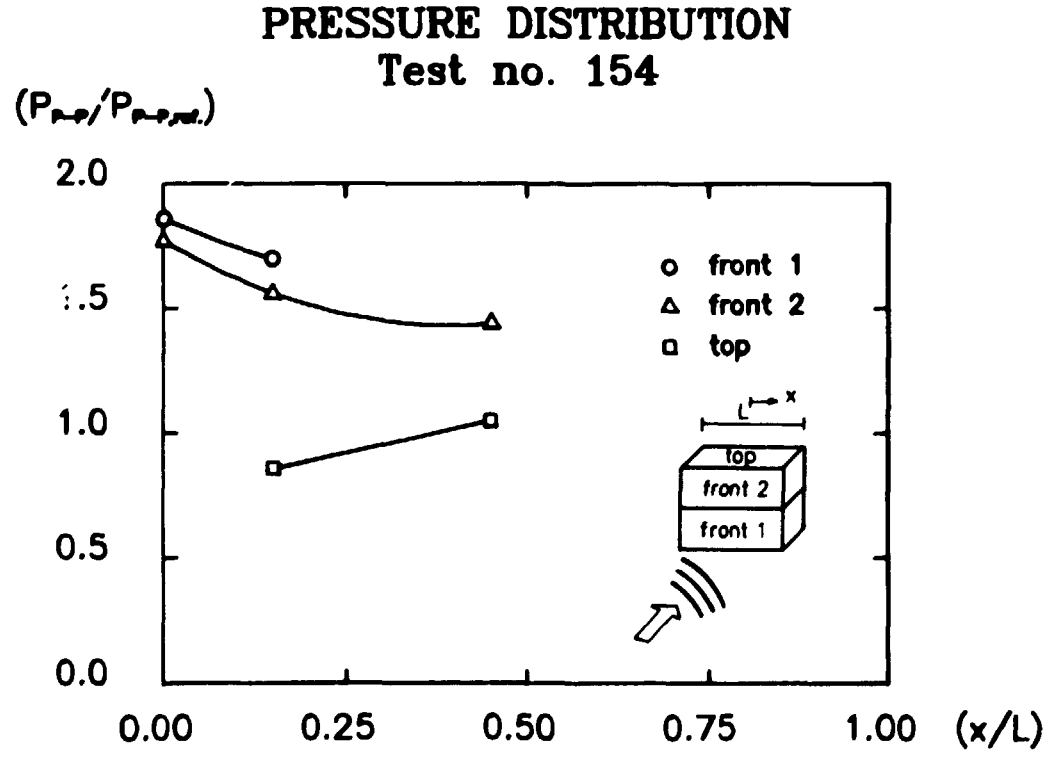

Fig. 93. Normalized peak-to-peak pressure distribution.

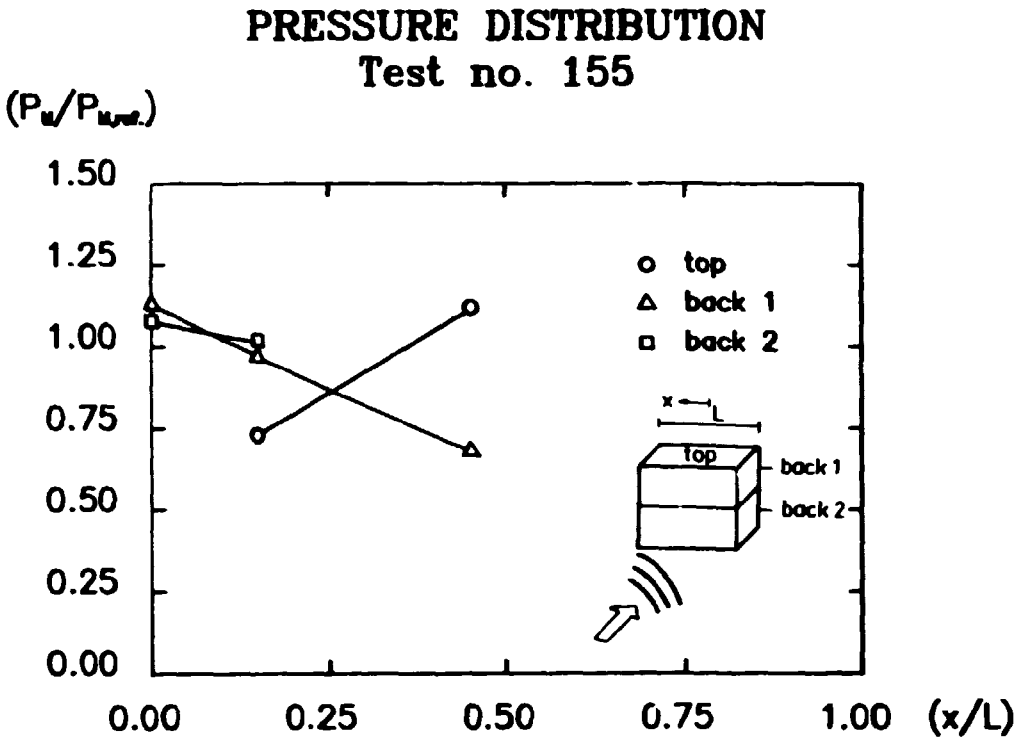

Fig. 94. Normalized peak pressure distribution.

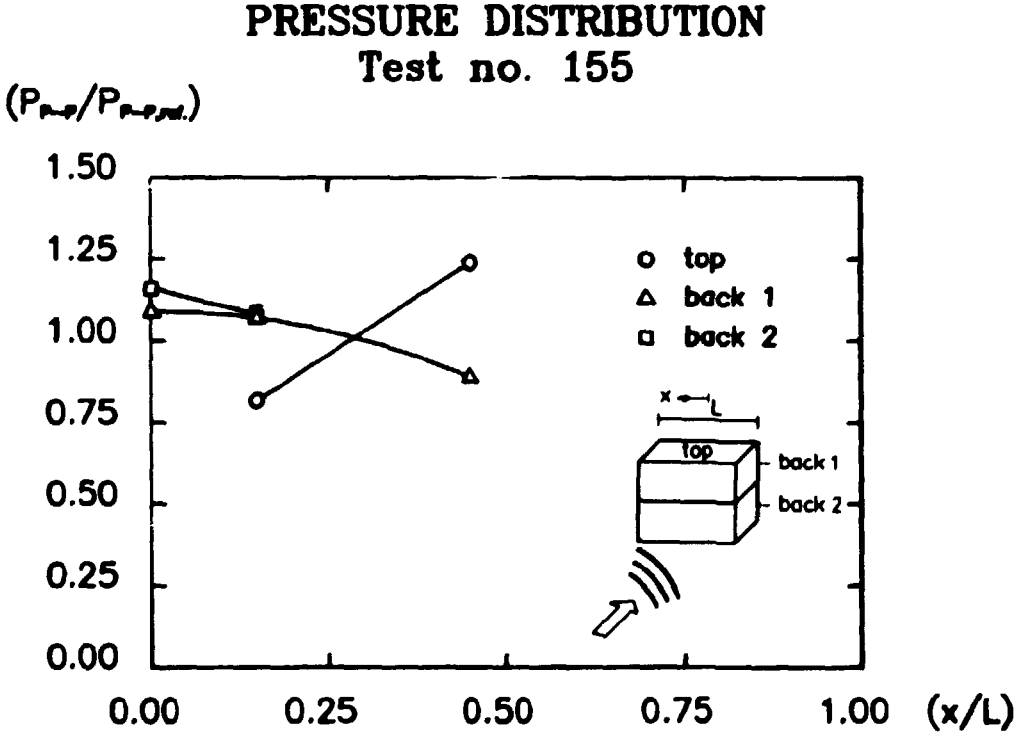

Fig. 95. Normalized peak-to-peak pressure distribution.

The mean of the reference measurements corresponding to the data presented in the above figures are given in Table 14, where, as previously, <·> denotes the mean value operator.

TEST NO.	$\langle P_{M,ref.} \rangle$ (mbar)	$\langle P_{P-P,ref.} \rangle$ (mbar)
142	3.3	5.9
143	4.6	9.0
144	4.8	10.05
145	3.45	6.95
146	3.7	7.8
147	4.35	8.35
148	4.5	9.0
149	3.45	7.35
150	4.15	8.75
151	3.95	9.20
152	3.85	8.45
153	3.45	7.85
154	3.4	7.0
155	3.55	7.5

Table 14. Mean of reference values corresponding to experiments 142-155.

3.7.1.3. Evaluation of the results.

An inspection of curves of the type illustrated in Fig. 67 indicated that the form of the pressure pulses are practically insensitive to the position of the measuring point in the present experiments. Moreover, it was recognized that no frequency shift took place comparing the "box measurements" with the reference measurements. The dominant frequency was of the order of 150 Hz in all cases.

However, the values of the pressure peaks depends strongly on the position of the measuring point.

A detailed evaluation of each experiment would be meaningless, as the data, probably due to scattering and diffraction

effects, contain certain minor fluctuations (which is most pronounced near the edges). This is in accordance with the results obtained in the half-scale experiments (5) concerning the blast wave propagation around banks and houses.

Instead, the general features shall be commented on, knowing that individual deviations can occur. The following general features have been observed for the experiments with the box "on end" (test no. 142, 143, 144, 145, 146, 148, 149, 150, 151):

- the front pressure is higher than the pressure measured on the top, back and sides. With the expected pressure stem-up on the front in mind, this seems to be a resonable result.

- the maximum pressure on the front is obtained near the bottom, as intuitively expected. The pressure build-up at the bottom is in the range 1.5-2.0 times the pressure which would exist at the actual position in the absence of the obstacle. This is a considerably weaker pressure build-up as observed in the half-scale experiments (5), where reflection factors of the order of magnitude 4 were registered.

- in the case of a wide box (2 boxes placed close together, test no. 150, 151) a considerably pressure fluctuation across the front has been observed, and the pressure load thus seems to lack the symmetry which is possessed by the actual experimental setup.

  This may be due to scattering and diffraction effects.

- the side pressure has a reflection coefficient of the order of magnitude 1 with a tendency of increasing pressure with decreasing distance to the bottom.

- A comparison of the two side pressures on a particular box has shown that in most cases they do not possess the symmetry which could be expected based on the symmetry of the experimental setup. The phenomenon is,

as in the previous case, supposed to be caused by diffraction effects. Again this is in accordance with the results obtained in the half-scale experiments (5).

- in case of a deep box (2 boxes placed close together, test no. 148, 149) the front part of the side shows a higher pressure level than the back part.

- the back pressure is generally of the same order of magnitude as the side pressure also with a tendency of increasing pressure with decreasing distance to the bottom.

- in case of a deep box (test no. 148,149) the pressure level on the back showed up to be in between the pressure level at the front part of the sides and the pressure level at the back part.

- in case of a wide box (test no. 150, 151) the back pressure level showed up to be larger than the side pressure level. Moreover, the expected symmetry of the back pressure around the middle of the back was fulfilled.

To sum up, it has been demonstrated that the pressure level on the front, side and back is different. However, the qualitative distribution on the surfaces is on the whole equal to a distribution with the maximum pressure at the bottom and a peak pressure in the middle and at the top of the surface. These two later peaks were not intuitively expected. Finally, no clear demarcation of the end effects could be stated.

The observed general features of the experiments with a "laying" box (test no. 147, 152, 153, 154, 155) are as follows:

- the pressure level on the front is larger than that on the back which again is larger than the pressure level on the top. On the front it is of the order of magnitude 1.5 times the pressure which would exist on the actual position without the obstacle present.

- in case of a deep box (test no. 152, 153) it is observed that the front region of the top is exposed to a higher pressure level than the back region of the top, and that the pressure level on the back of the box is at a value in between.

- in case of a high box (test no. 154, 155) it is seen, that the vertical variation of the pressure, both on the front and on the back of the box, is insignificant.

- the pressure distribution on the front and on the back shows the same tendency as the pressure decrease with increasing distance from the middle of the box. The picture is quite the opposite for the top pressure distribution, where the pressure increases with increasing distance from the middle of the obstacle.

- as was the case with the box "on end", no clear demarcation of the end effects in the tests with a "laying" box has been found.

To sum up, it has been demonstrated that the qualitative pressure distribution as well as the pressure level vary with the actual surfaces on the box, and that no demarcation of the end effects present can be stated.

3.7.2. Multiple box experiments.

In these tests the pressure distribution on two boxes placed in various configurations has been discussed. The purpose of the experiments was to investigate the wave-wave interaction caused by these obstacles and to study scattering and diffraction effects.

3.7.2.1. Experimental setup.

All three types of boxes (described in section 3.7) have been used in these experiments. The position and orientation of the

EXPERIMENT NO.	MIXTURE (Vol.%) CH_4	O_2	N_2	SOURCE DIAMETER (m)	L (m)
156	16	32	52	0.30	0.80
157	16	32	52	0.30	0.80
159	16	32	52	0.30	0.80
160	16	32	52	0.30	0.80
161	16	32	52	0.30	0.80
162	16	32	52	0.30	0.80
163	16	32	52	0.30	0.80
164	16	32	52	0.30	0.80
165	16	32	52	0.30	0.80
166	16	32	52	0.30	0.80
167	16	32	52	0.30	0.80
168	16	32	52	0.30	0.80
169	16	32	52	0.30	0.80
170	16	32	52	0.30	0.80
171	16	32	52	0.30	0.80
172	16	32	52	0.30	0.80
173	16	32	52	0.30	0.80
174	16	32	52	0.30	0.80
175	16	32	52	0.30	0.50(box1) 0.25(box2)

Table 15. Experimental data

boxes have been varied, and pressure measurements have been performed in various positions on the surfaces of the obstacles. As in section 3.7.1.1 the specific experimental setup appears from sketches attached to the figures presenting the results (given in section 3.7.2.2). These sketches follow the idea outlined in section 3.7.1.1.

The distance between the center of the explosive source and the front of the obstacle, which was placed at the largest distance, had been kept constant and equal to 2.20 m. The center of the explosion was placed 0.40 m above the ground.

Two reference measurements have been performed at a distance of 2.20 m from the source - one in the diametrically opposite direction of the boxes and one in a direction perpendicular on this.

Specific data for each particular experiment are given in Table 15.

3.7.2.2. Results

The measured pressure signals are presented in the following figures and tables. A typical pressure pulse originating from these experiments is similar to the one illustrated in Fig. 67 in section 3.7.2.1.

The normalized peak and the normalized peak-to-peak pressures have been evaluated on the basis of the measured pressure pulses. As previously, the mean of the reference measurements have been used in the normalization of the pressures.

The normalized pressures are presentated in Figs. 96-163. Cubic spline interpolation has been used for drawing curves containing three measuring points, whereas linear interpolation have been used for curves containing two points.

In a few of the measurements the negative phase has overloaded the equipment. These measurements are consequently not represented in the peak-to-peak plots, but only in the positive peak plots.

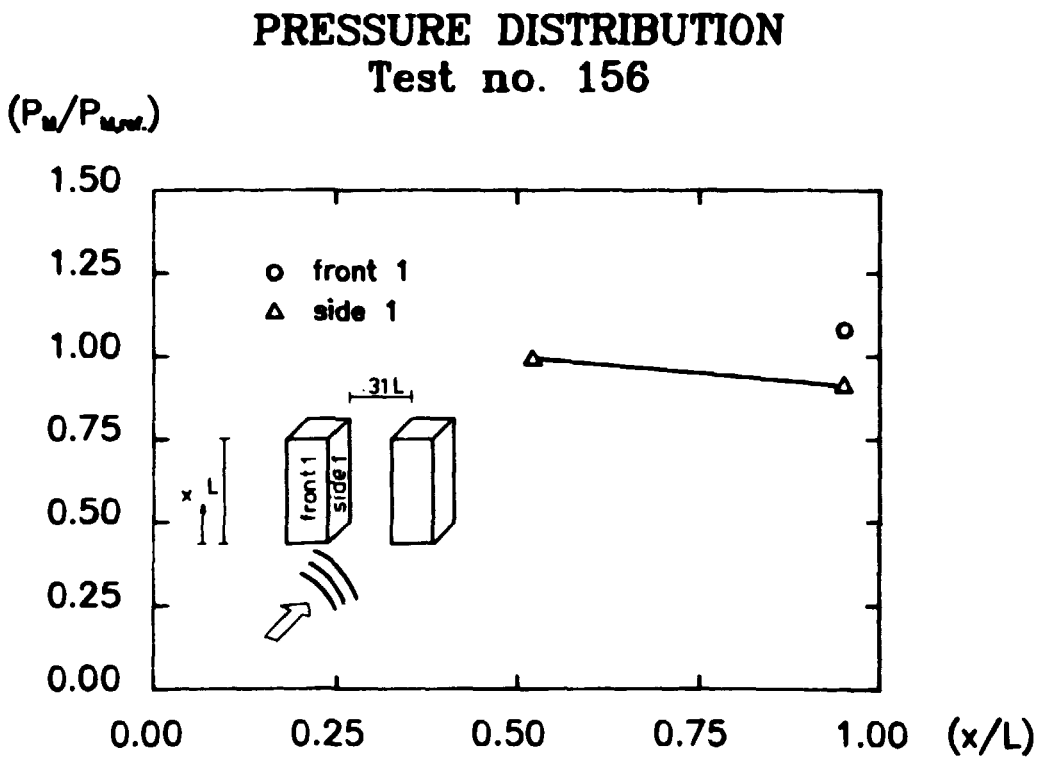

Fig. 96. Normalized peak pressure distribution.

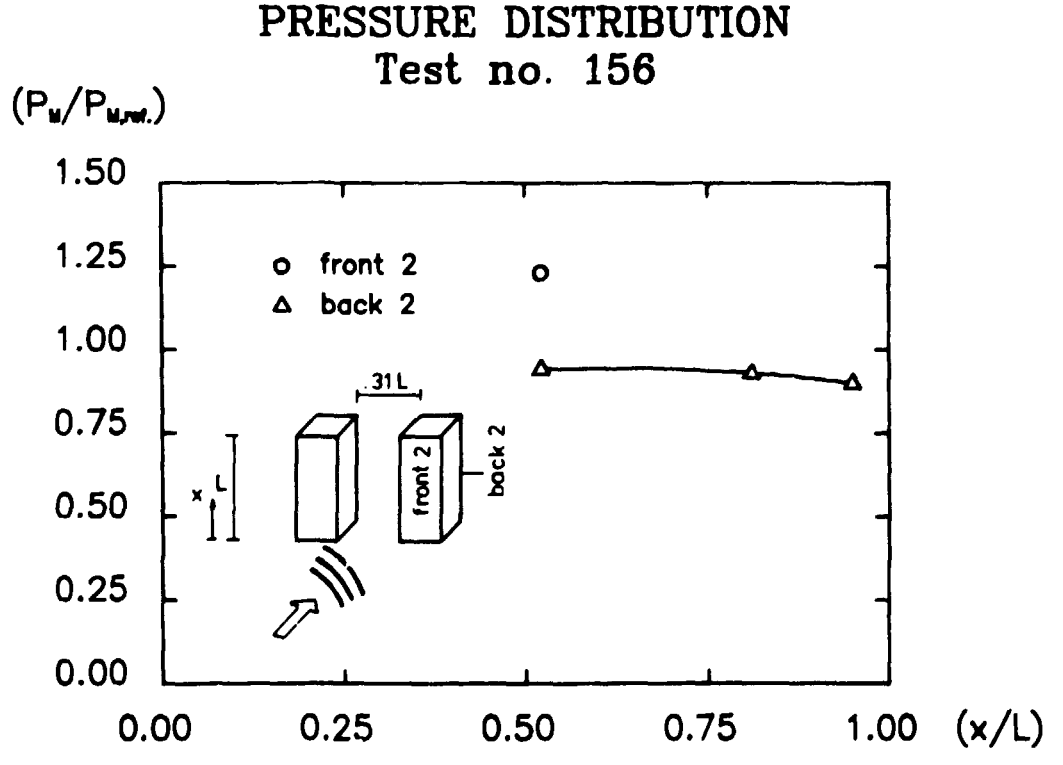

Fig. 97. Normalized peak pressure distribution.

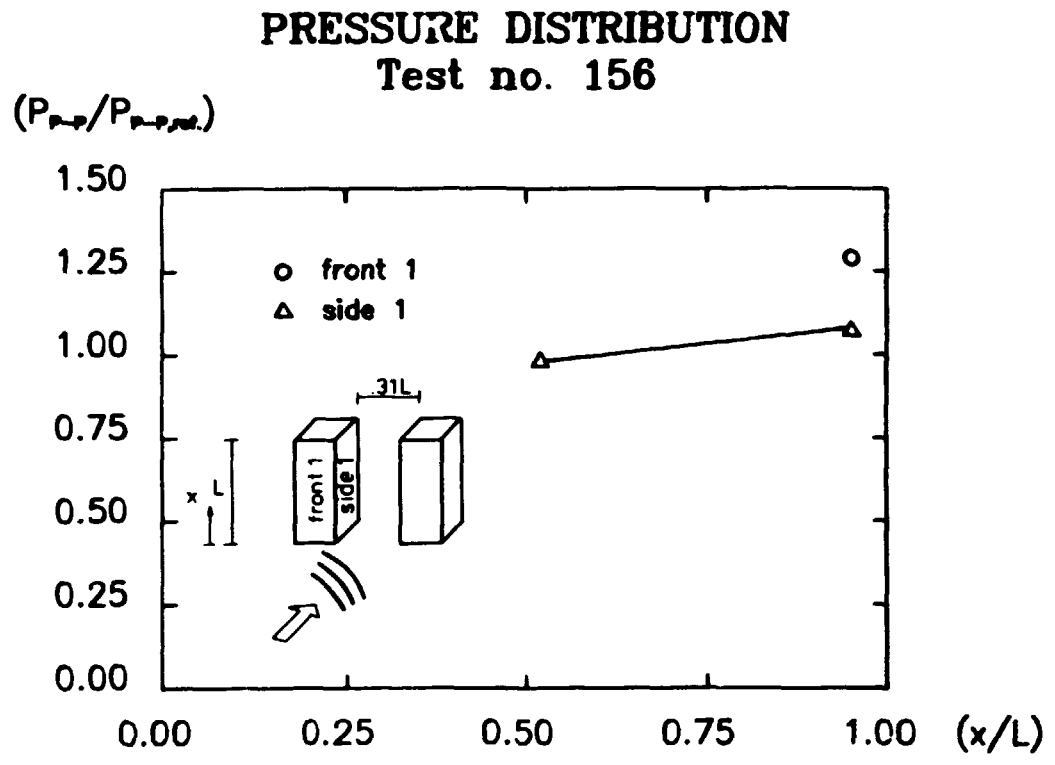

Fig. 98. Normalized peak-to-peak pressure distribution.

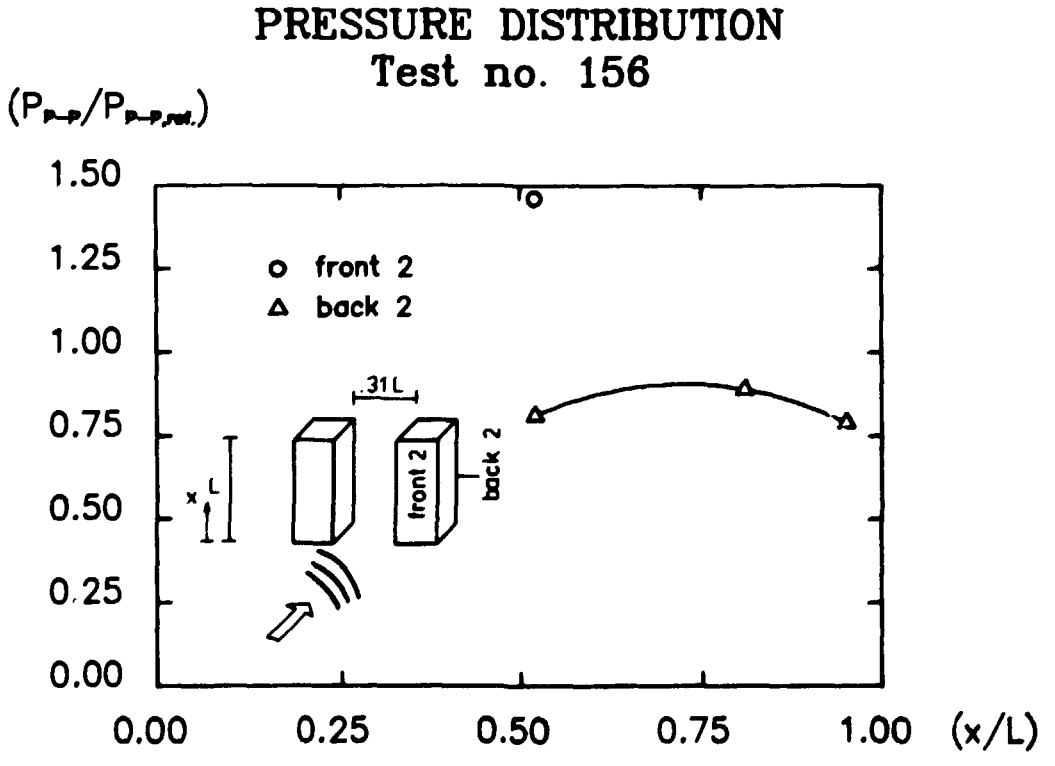

Fig. 99. Normalized peak-to-peak pressure distribution.

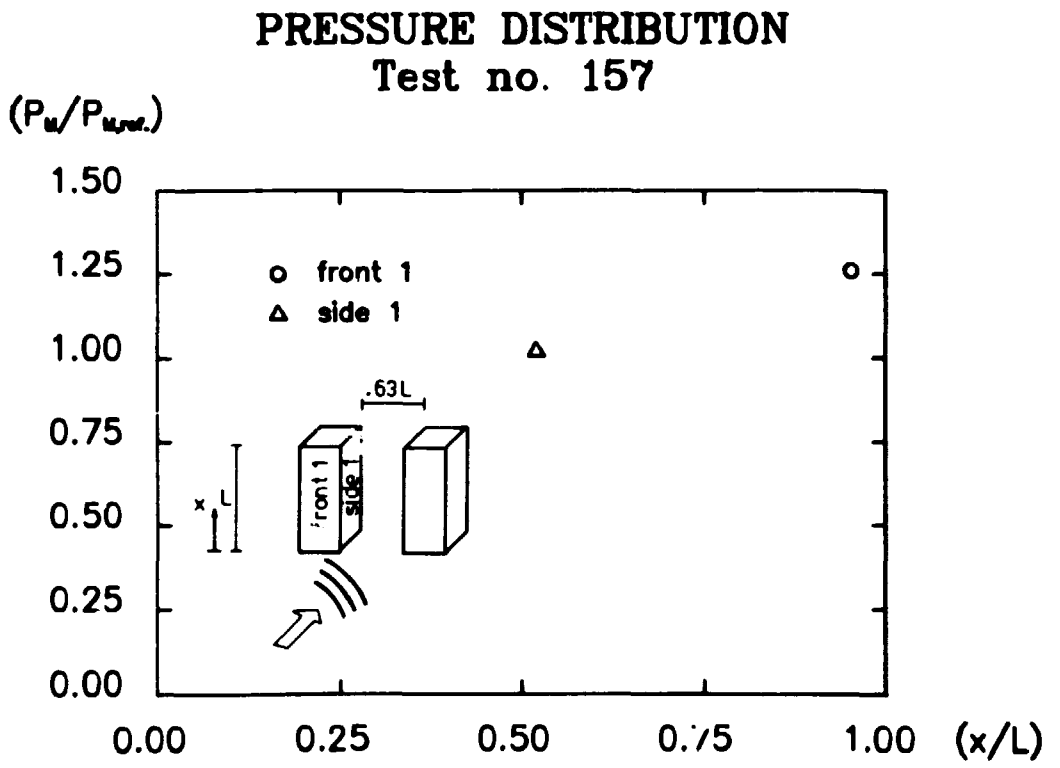

Fig. 100. Normalized peak pressure distribution.

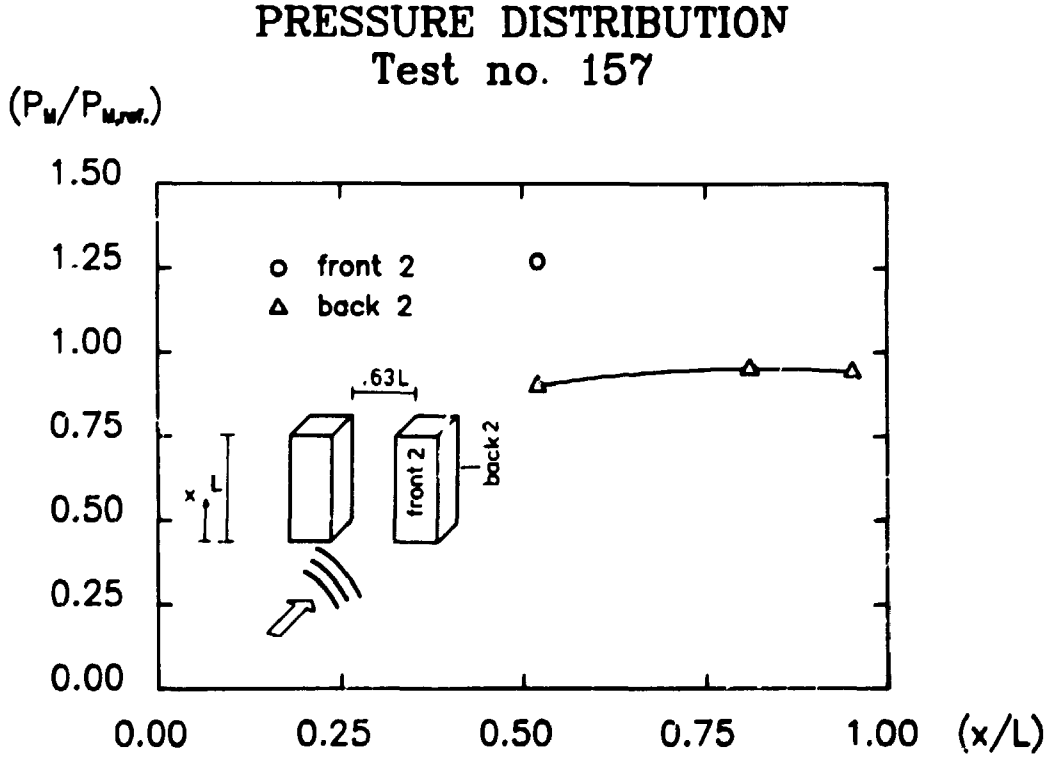

Fig. 101. Normalized peak pressure distribution.

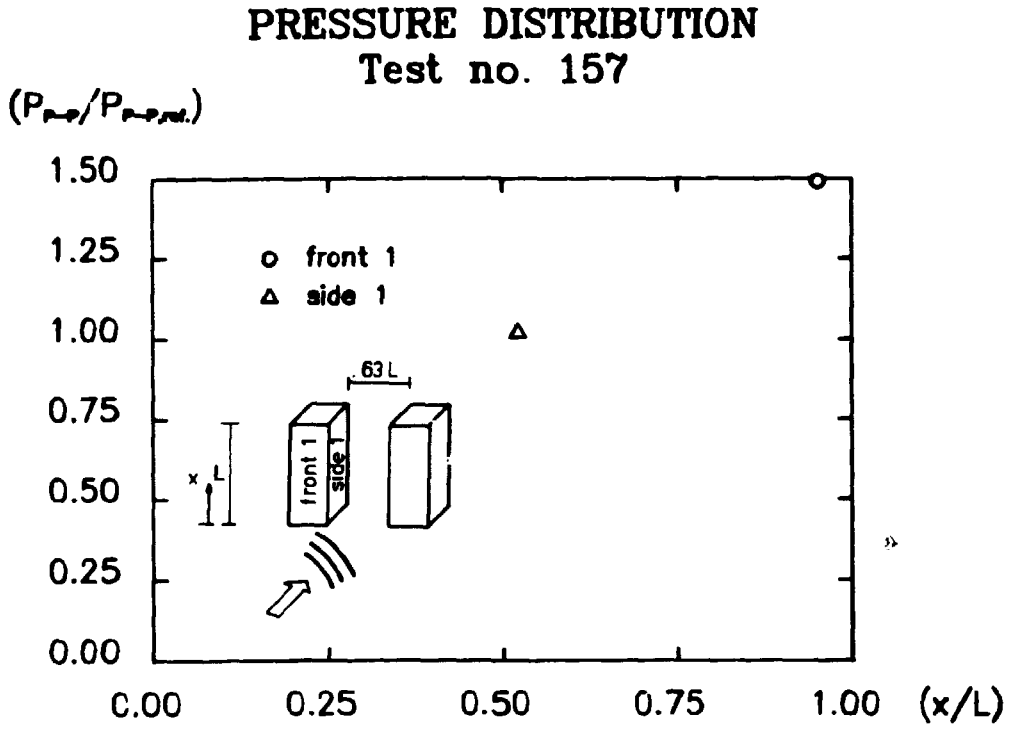

Fig. 102. Normalized peak-to-peak pressure distribution.

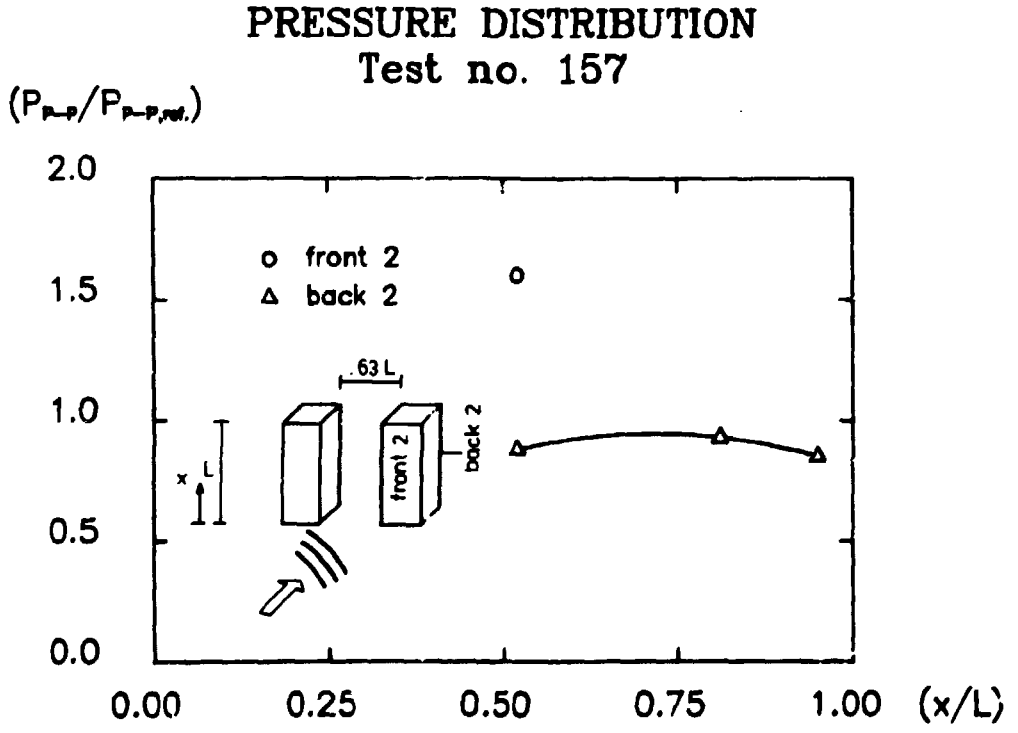

Fig. 103. Normalized peak-to-peak pressure distribution.

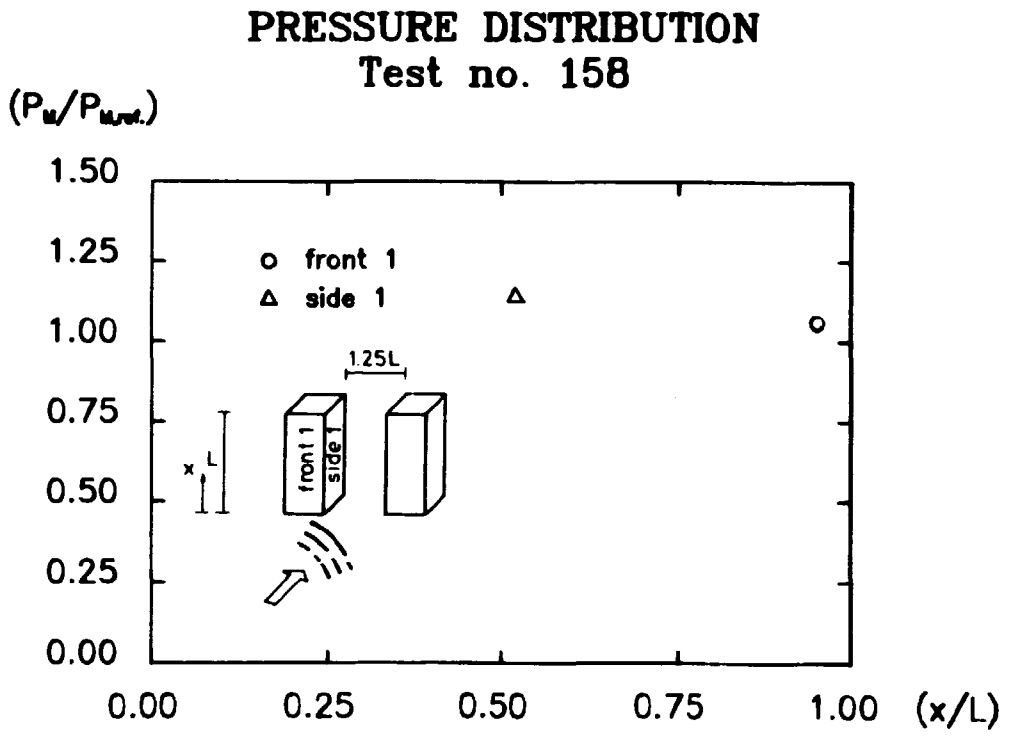

Fig. 104. Normalized peak pressure distribution.

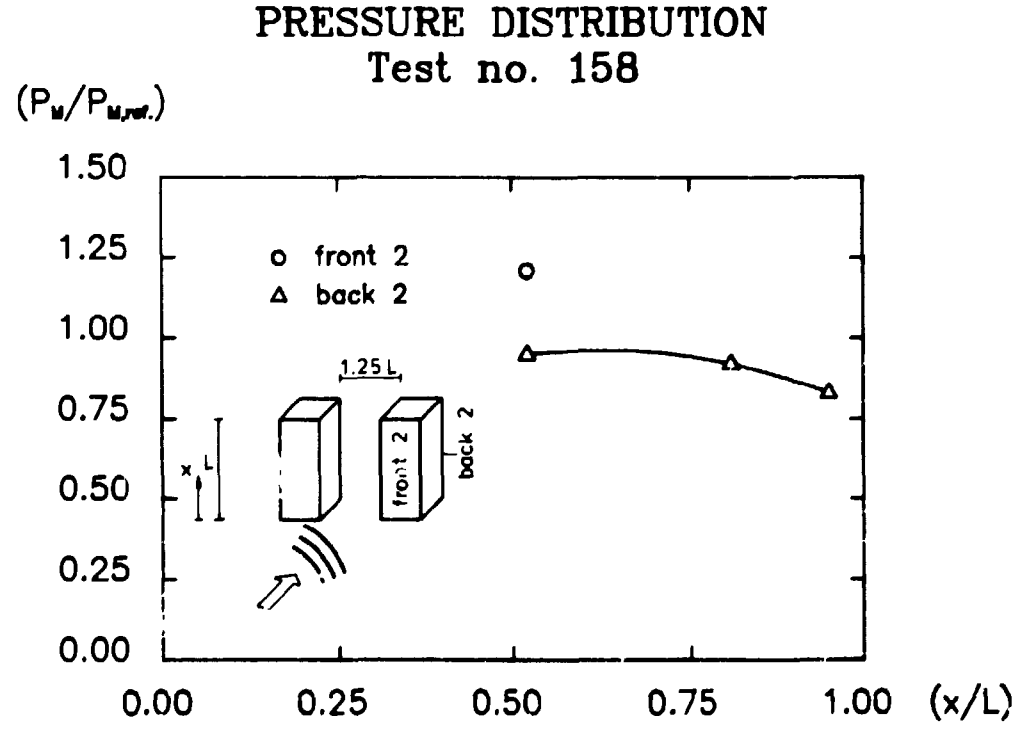

Fig. 105. Normalized peak pressure distribution.

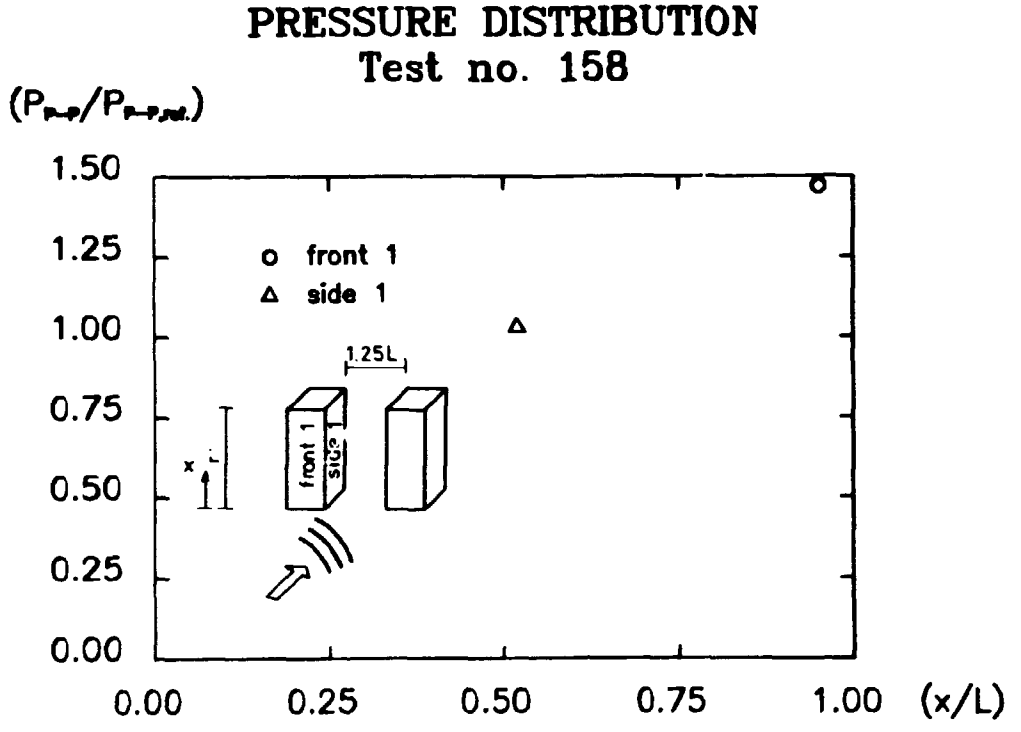

Fig. 106. Normalized peak-to-peak pressure distribution.

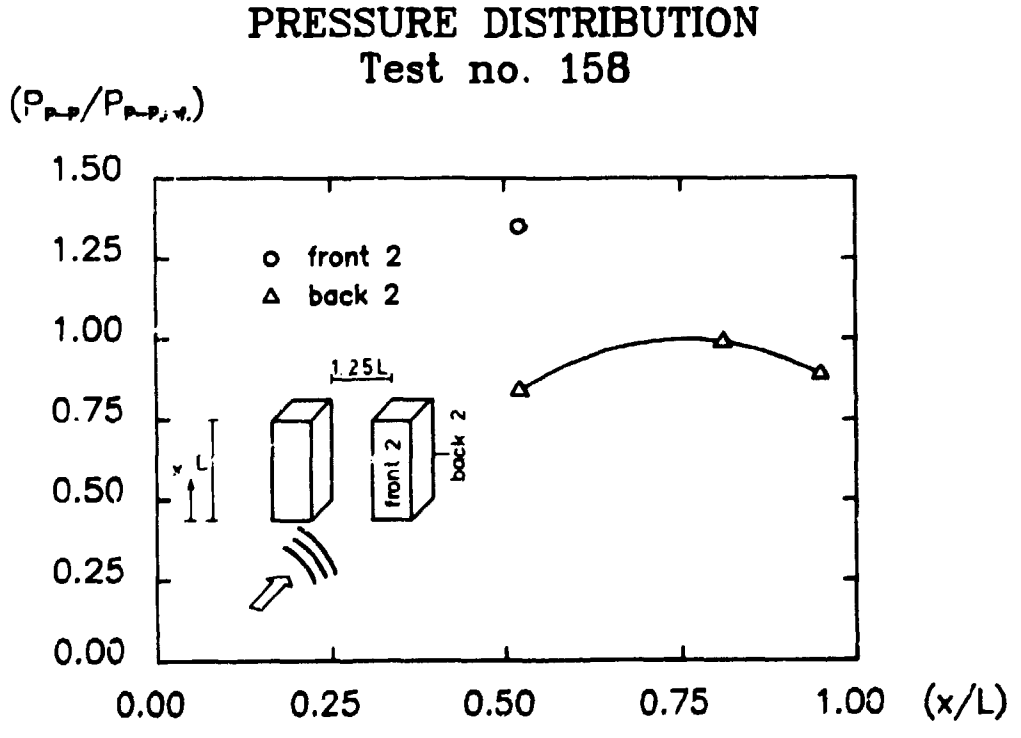

Fig. 107. Normalized peak-to-peak pressure distribution.

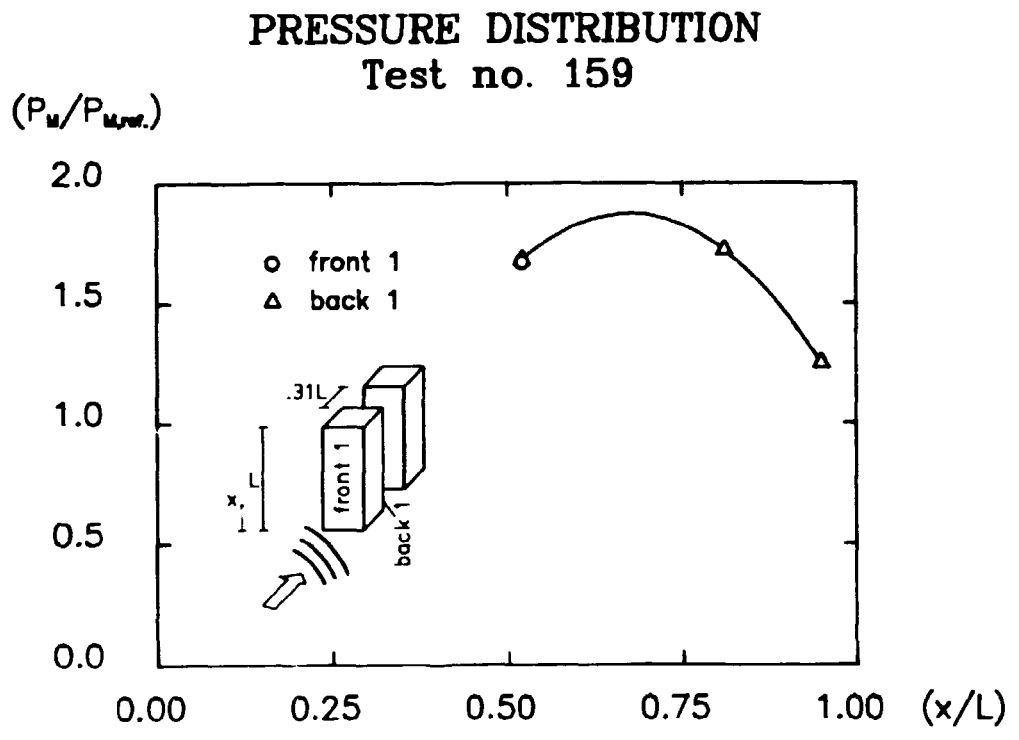

Fig. 108. Normalized peak pressure distribution.

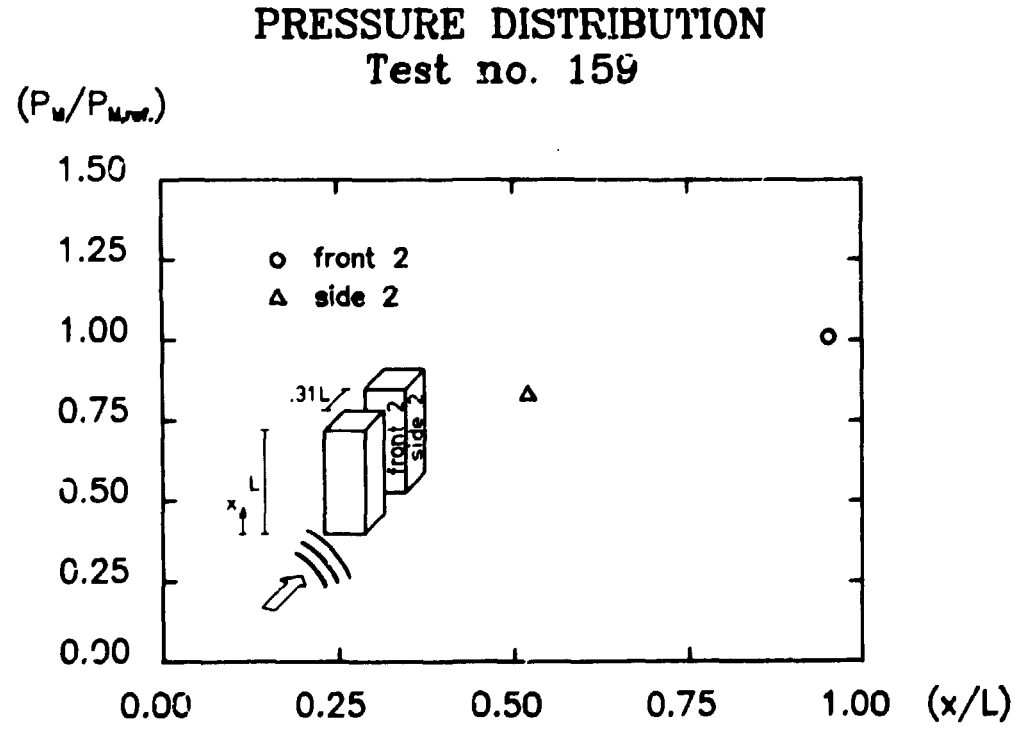

Fig. 109. Normalized peak pressure distribution.

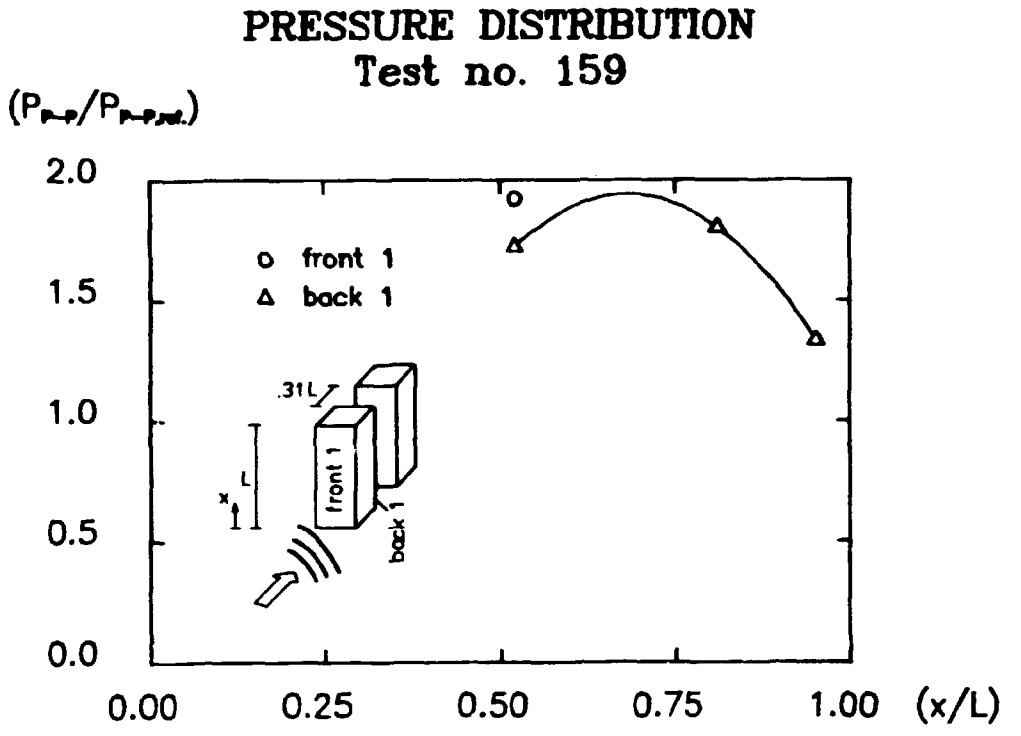

Fig. 110. Normalized peak-to-peak pressure distribution.

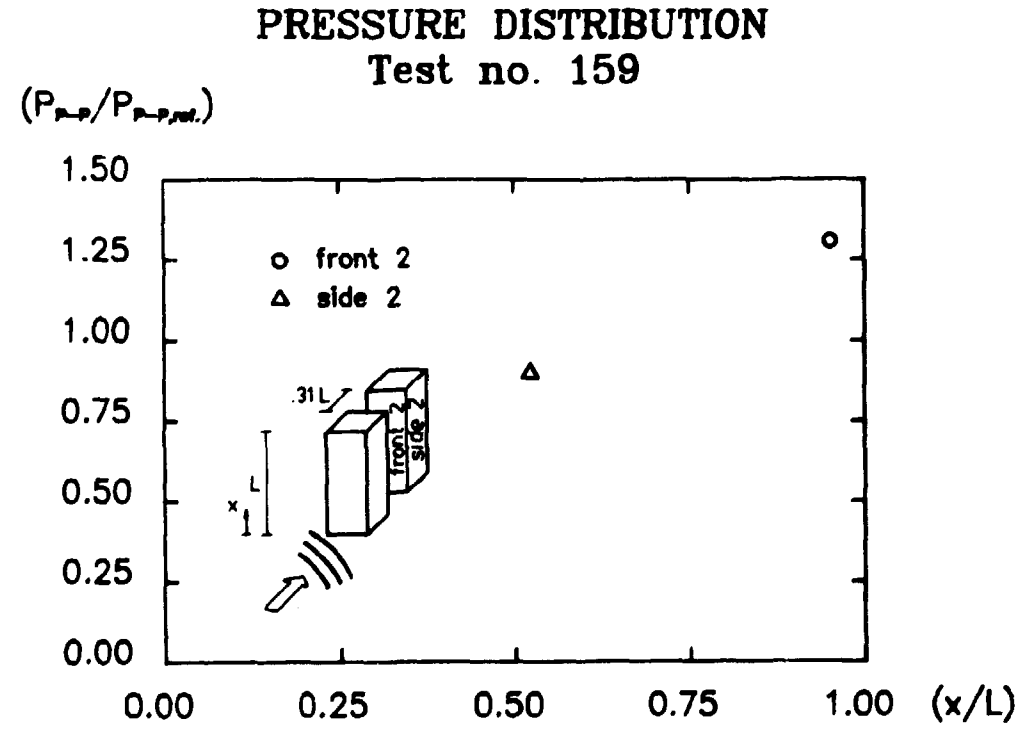

Fig. 111. Normalized peak-to-peak pressure distribution.

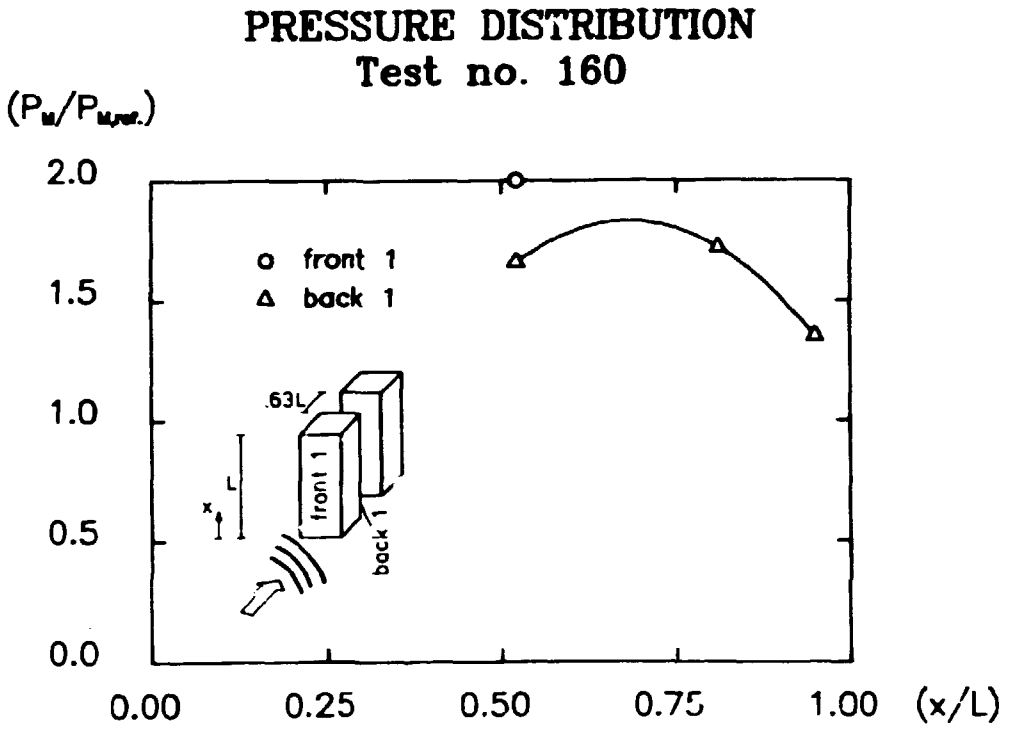

Fig. 112. Normalized peak pressure distribution.

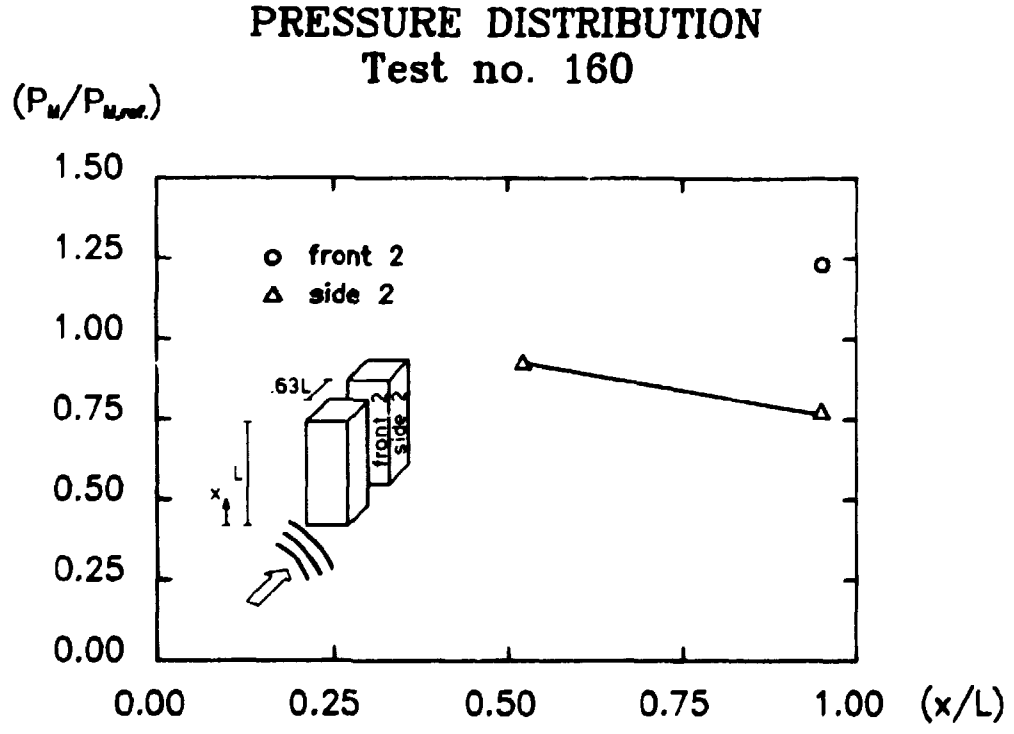

Fig. 113. Normalized peak pressure distribution.

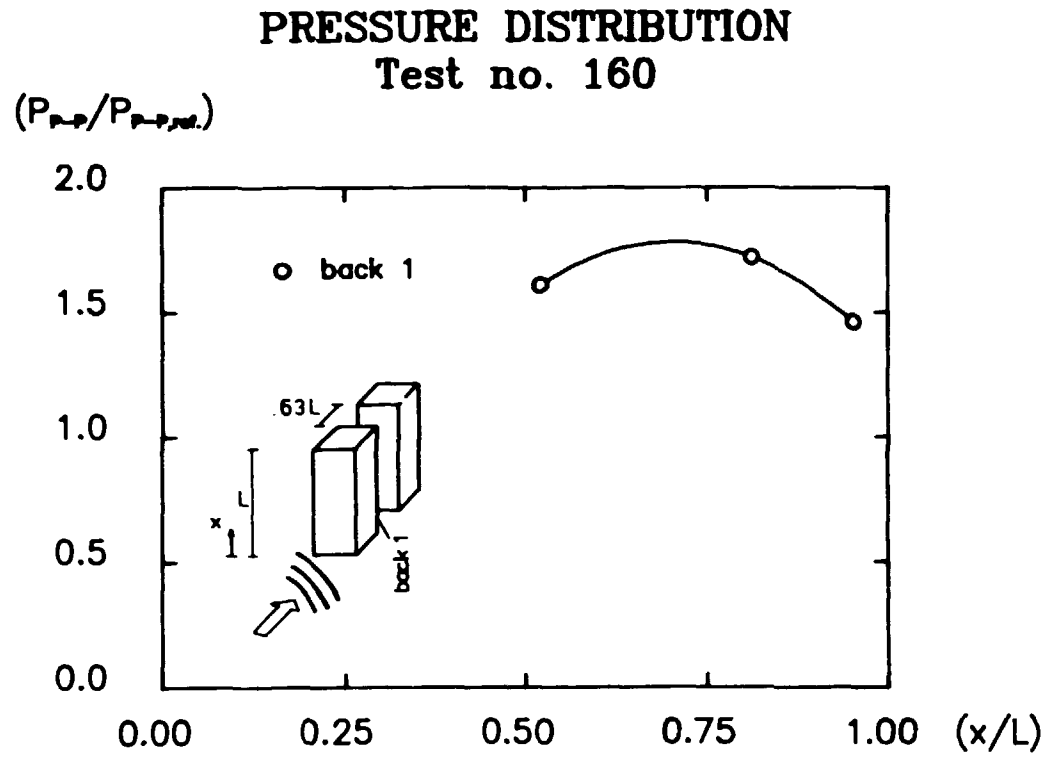

Fig. 114. Normalized peak-to-peak pressure distribution.

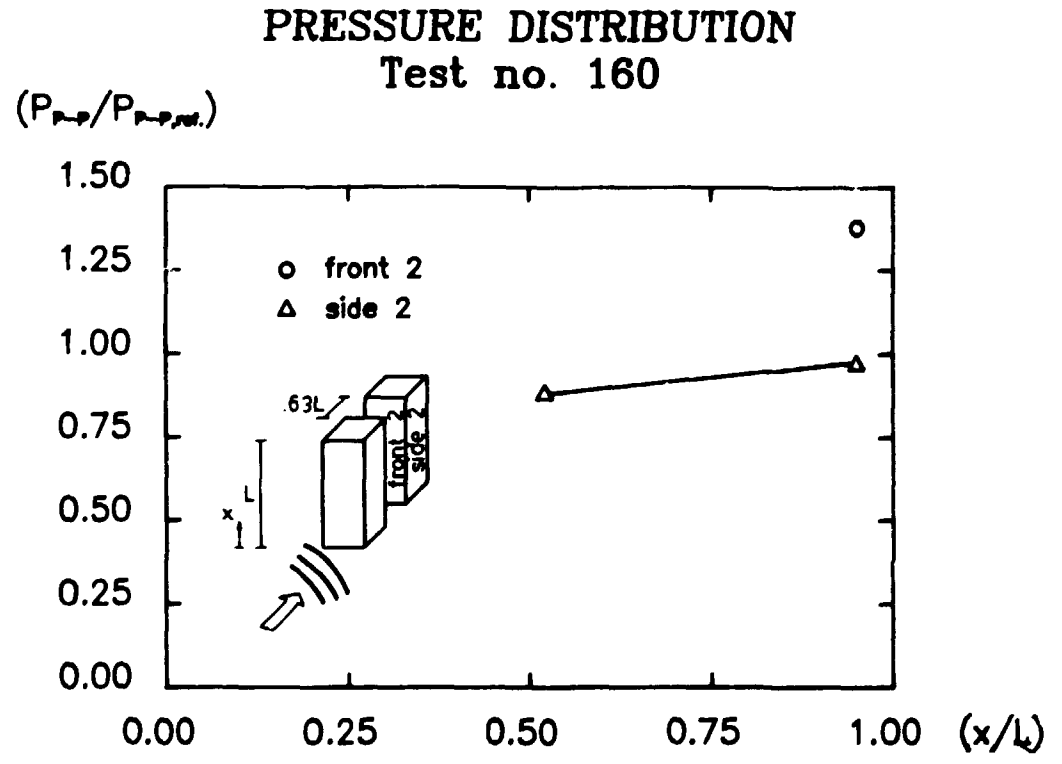

Fig. 115. Normalized peak-to-peak pressure distribution.

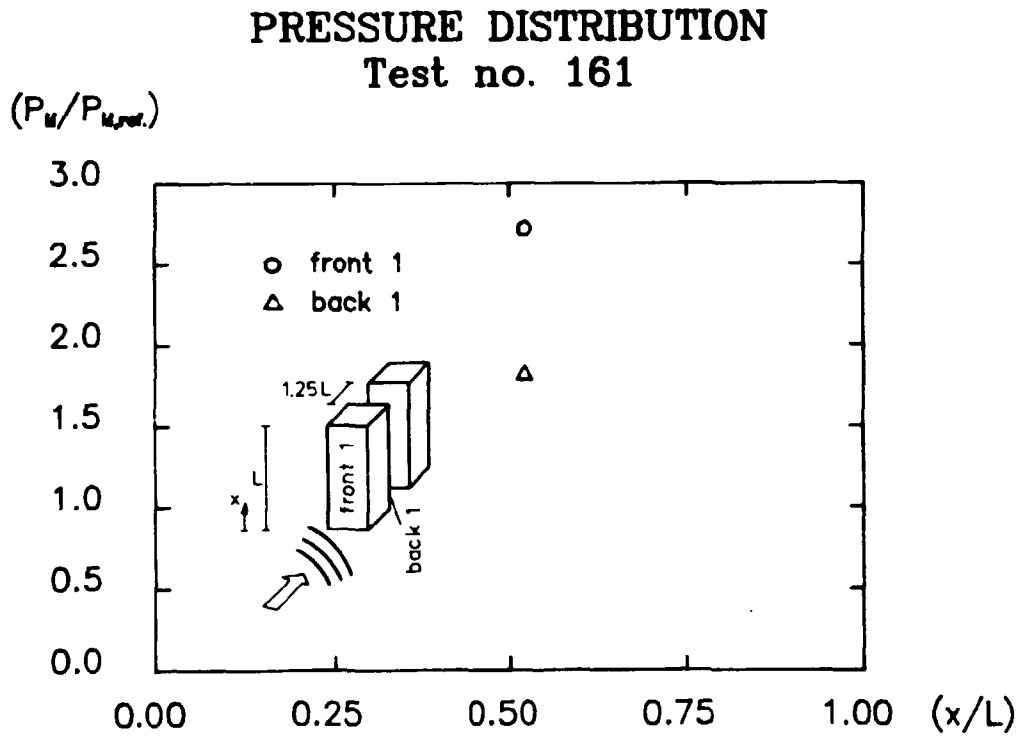

Fig. 116. Normalized peak pressure distribution.

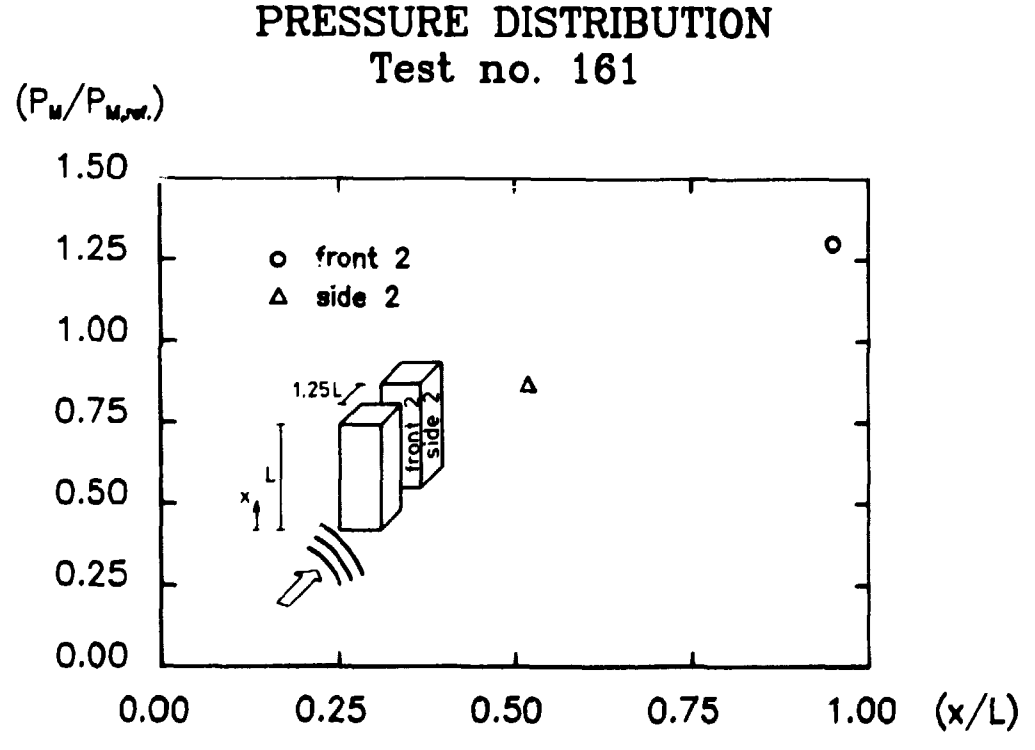

Fig. 117. Normalized peak pressure distribution.

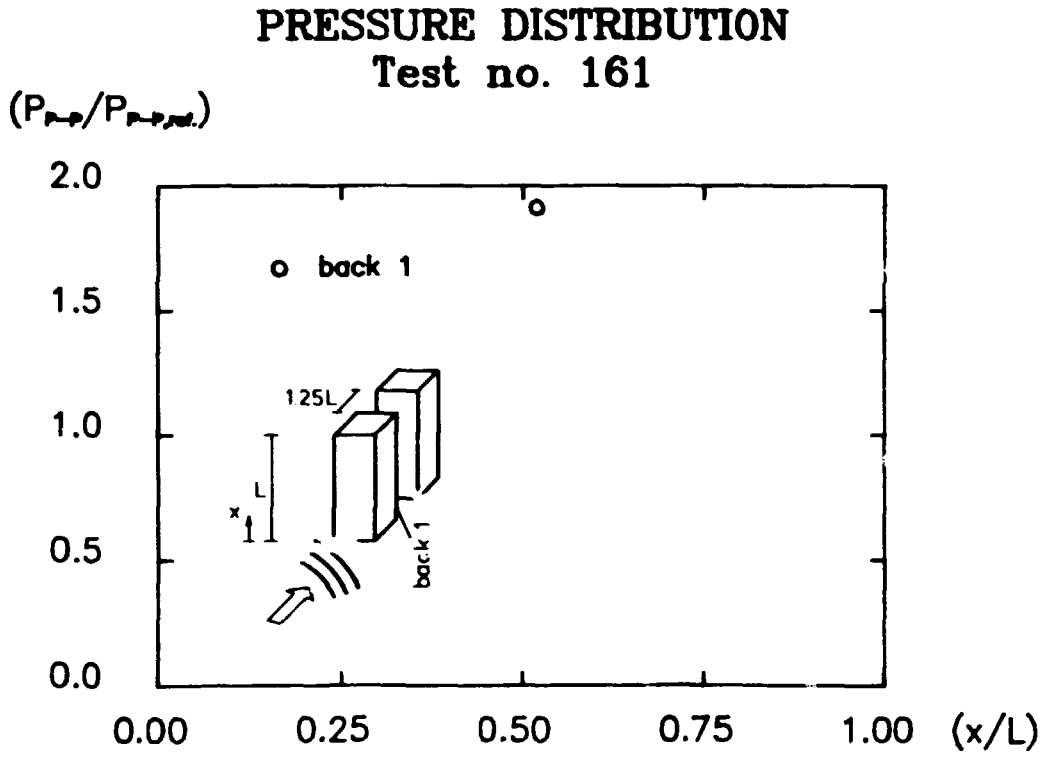

Fig. 118. Normalized peak-to-peak pressure distribution.

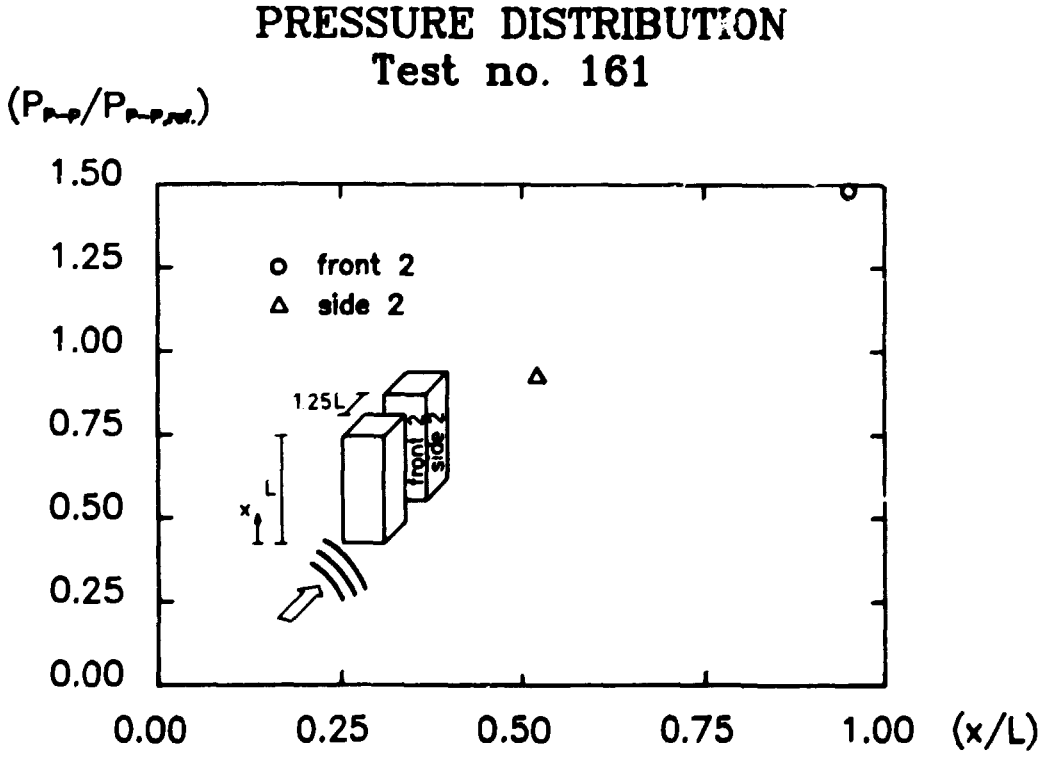

Fig. 119. Normalized peak-to-peak pressure distribution.

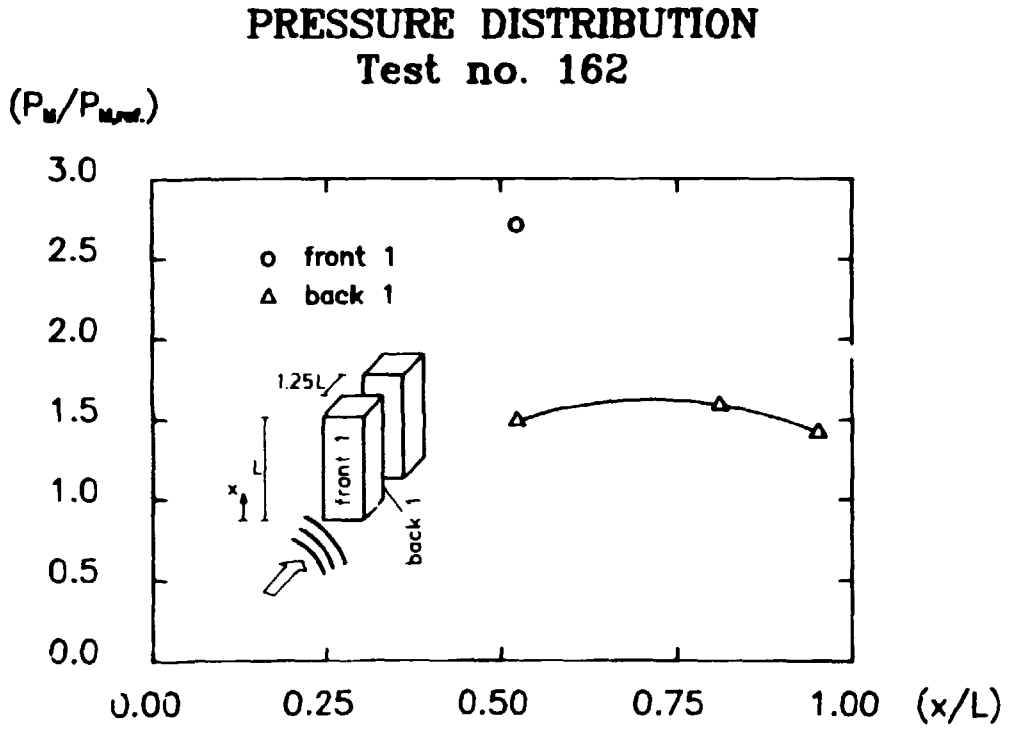

Fig. 120. Normalized peak pressure distribution.

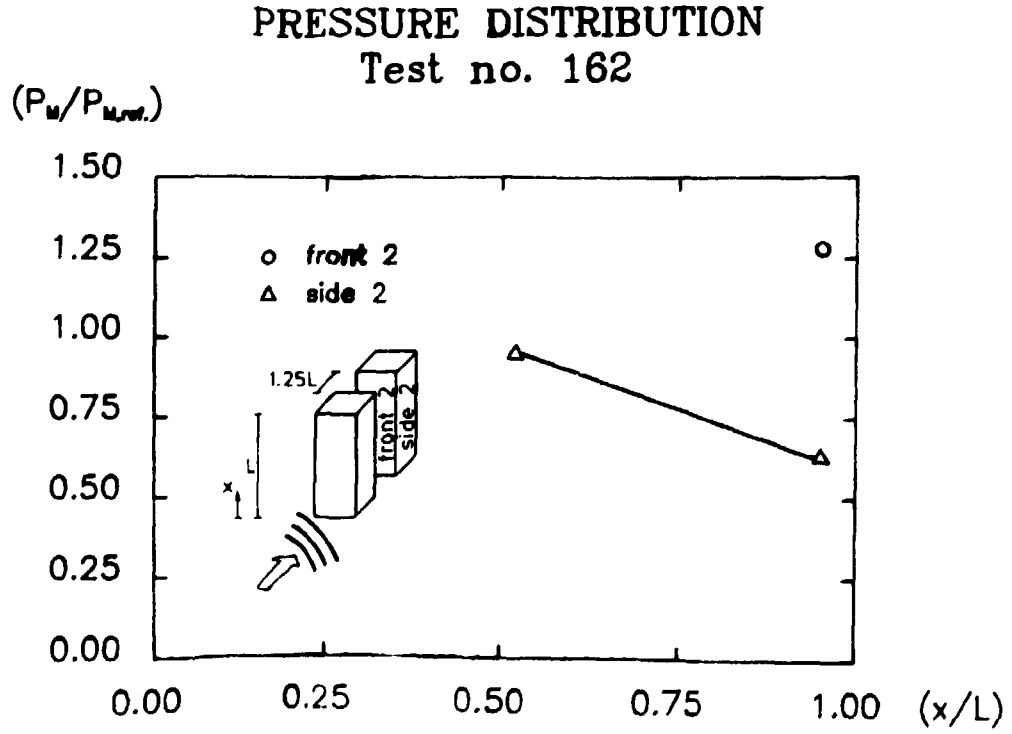

Fig. 121. Normalized peak pressure distribution.

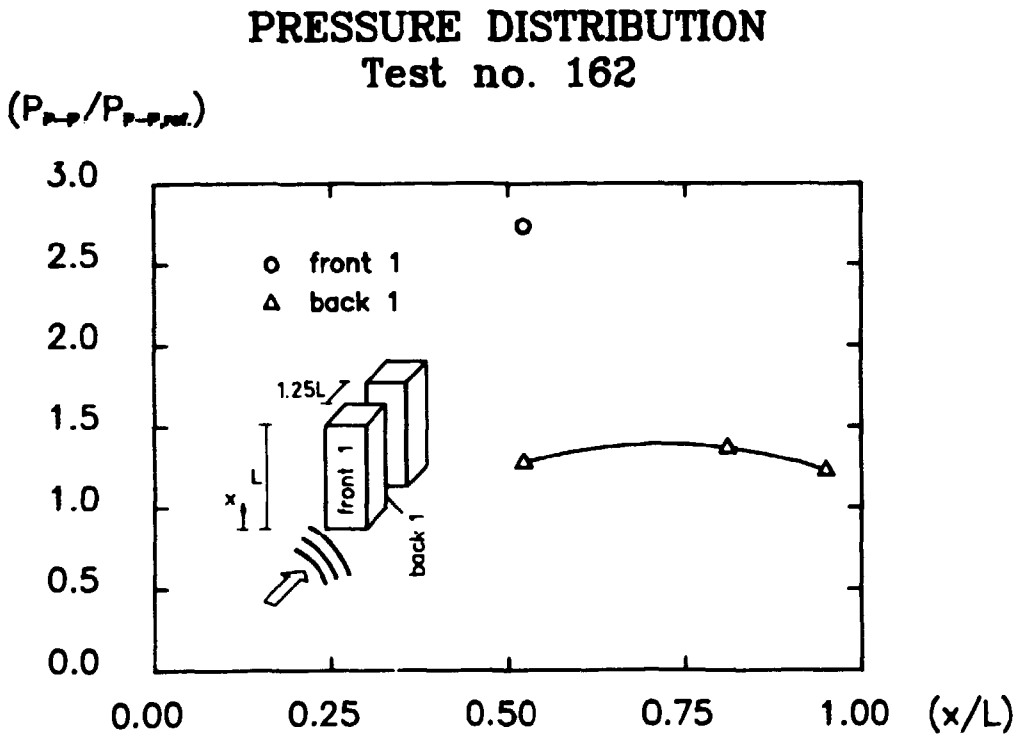

Fig. 122. Normalized peak-to-peak pressure distribution.

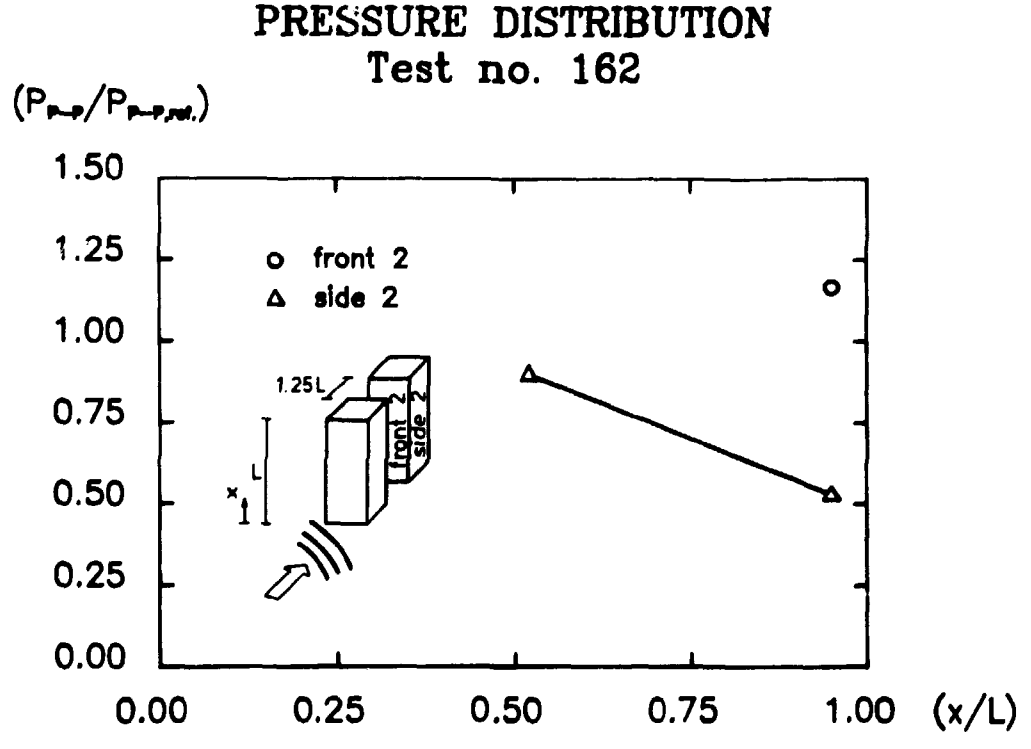

Fig. 123. Normalized peak-to-peak pressure distribution.

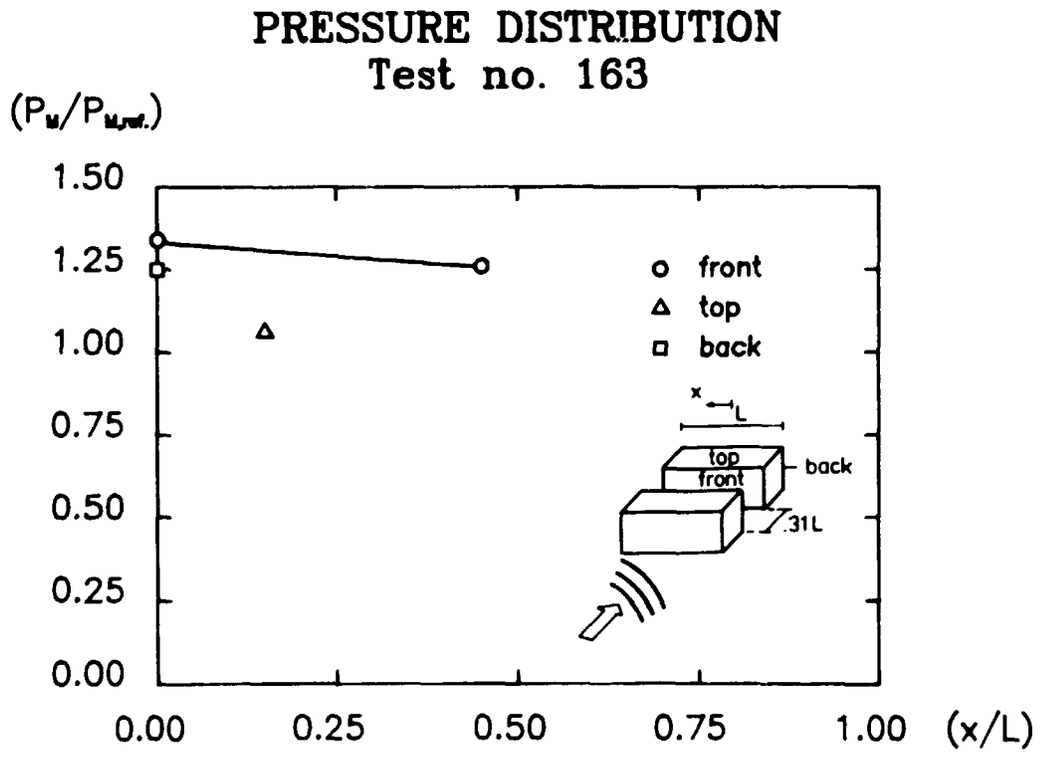

Fig. 124. Normalized peak pressure distribution.

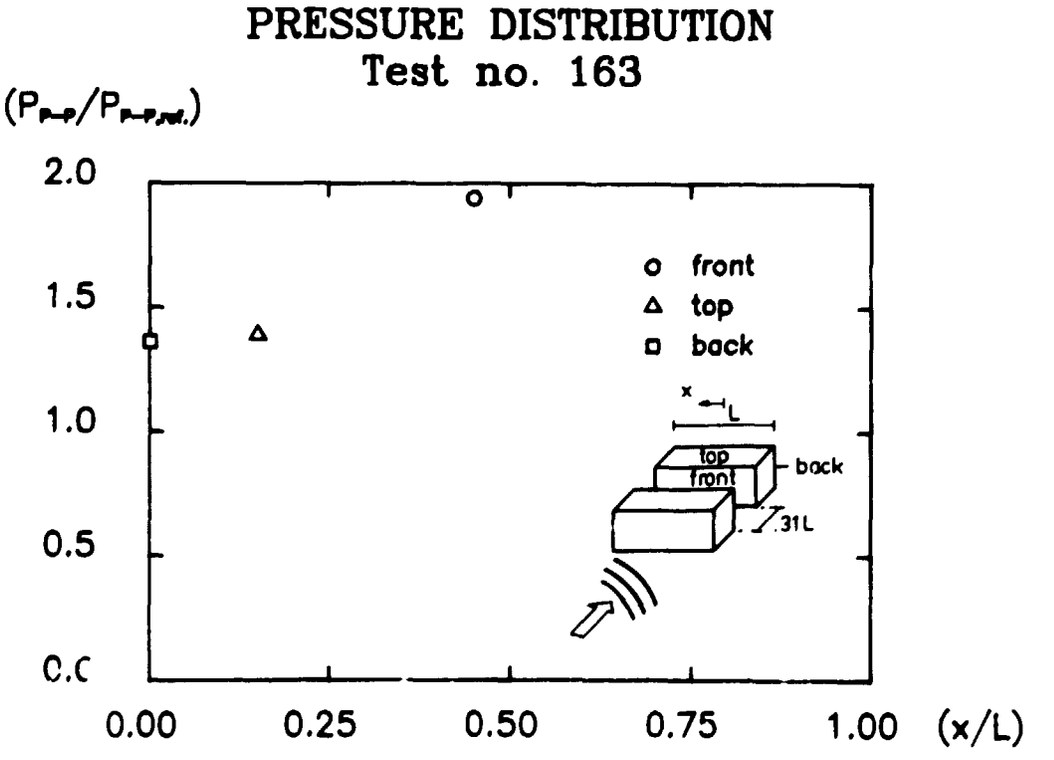

Fig. 125. Normalized peak-to-peak pressure distribution.

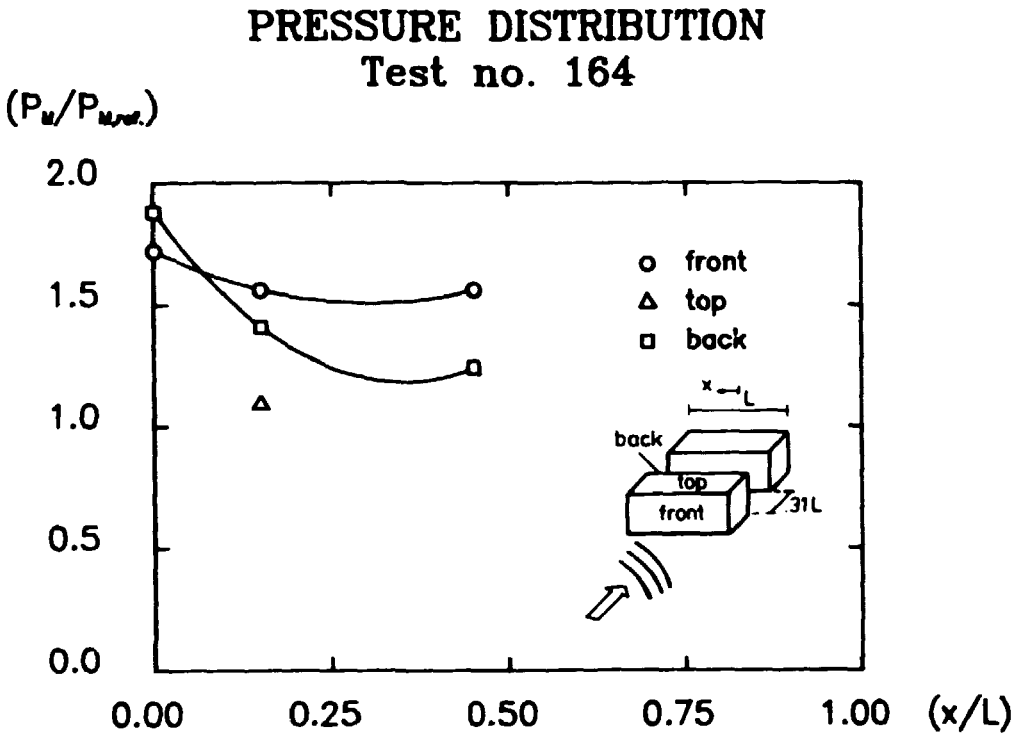

Fig. 126. Normalized peak pressure distribution.

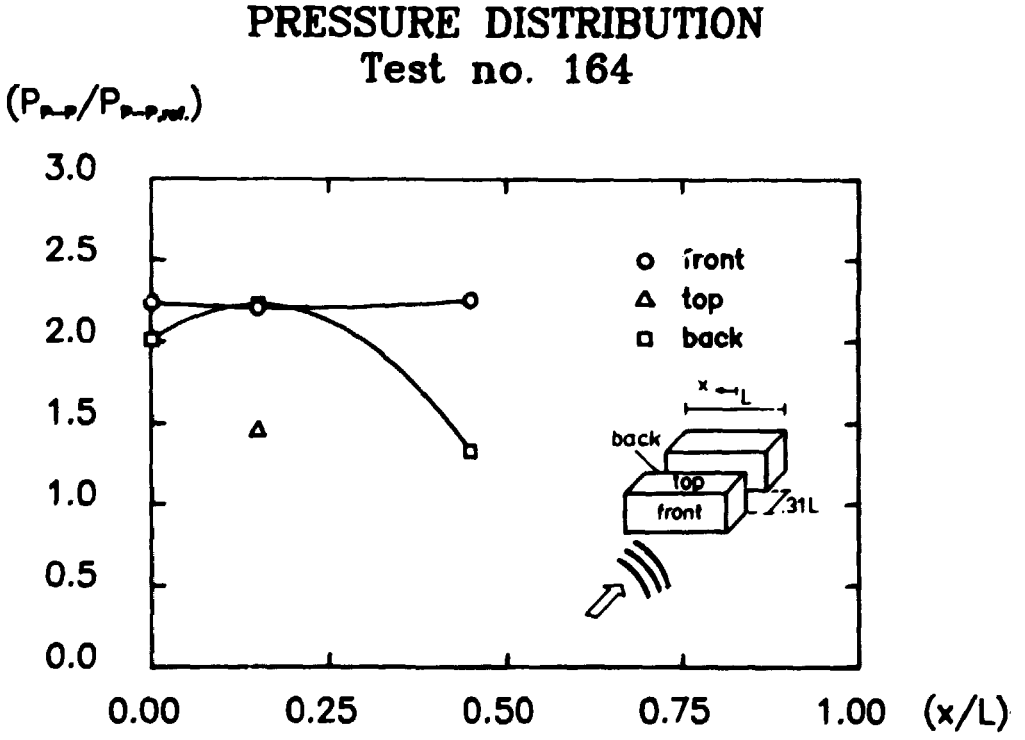

Fig. 127. Normalized peak-to-peak pressure distribution.

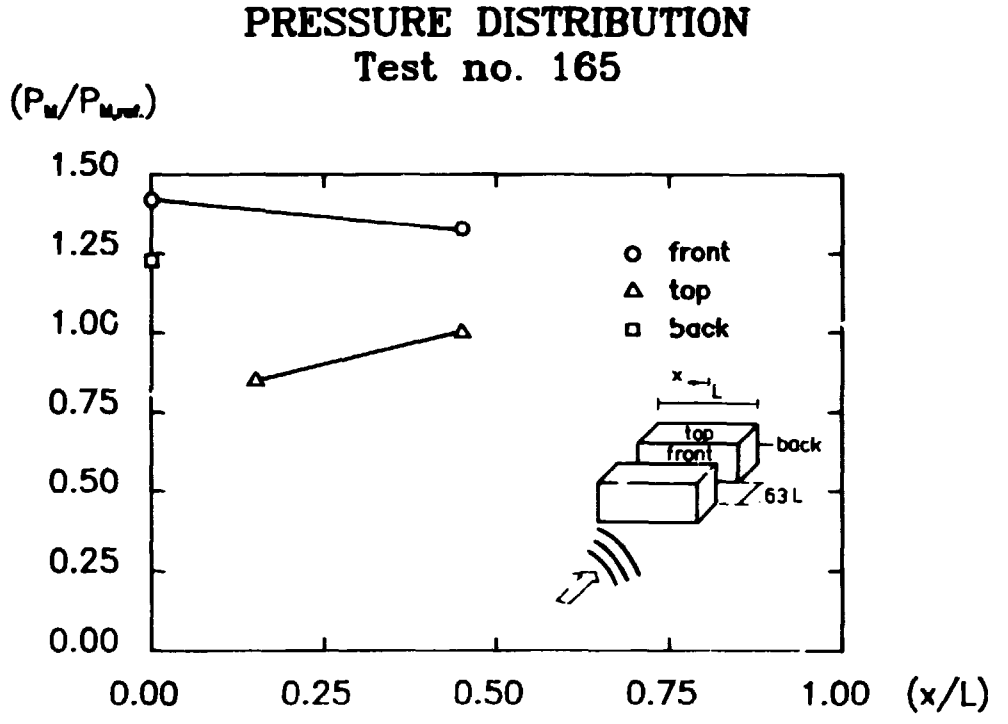

Fig. 128. Normalized peak pressure distribution.

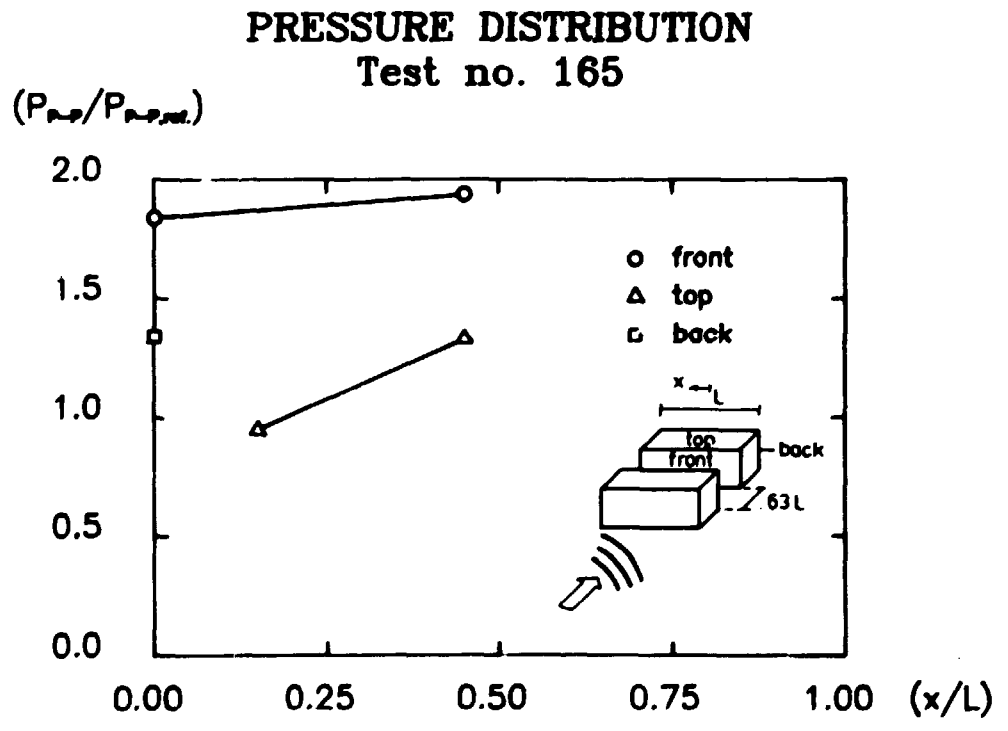

Fig. 129. Normalized peak-to-peak pressure distribution.

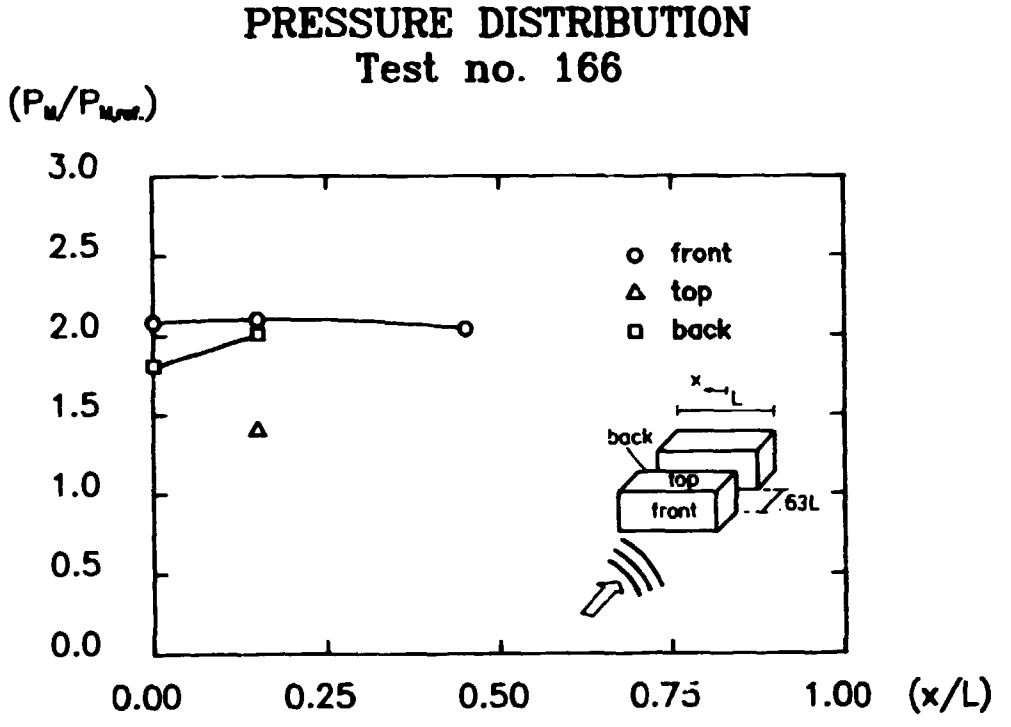

Fig. 130. Normalized peak pressure distribution.

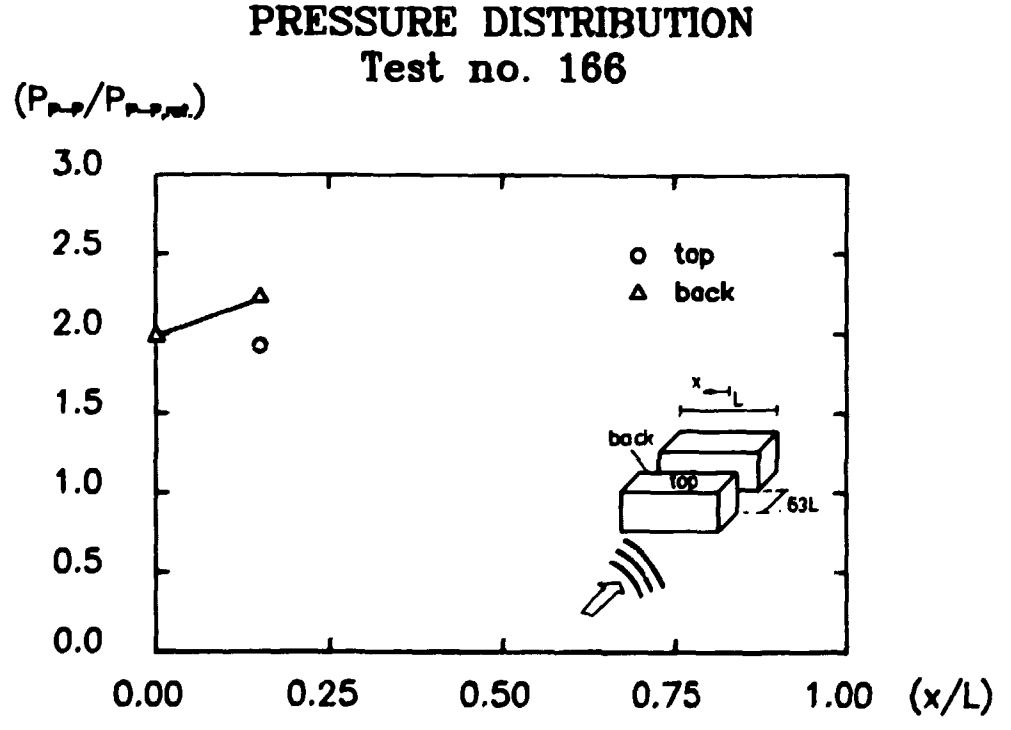

Fig. 131. Normalized peak-to-peak pressure distribution.

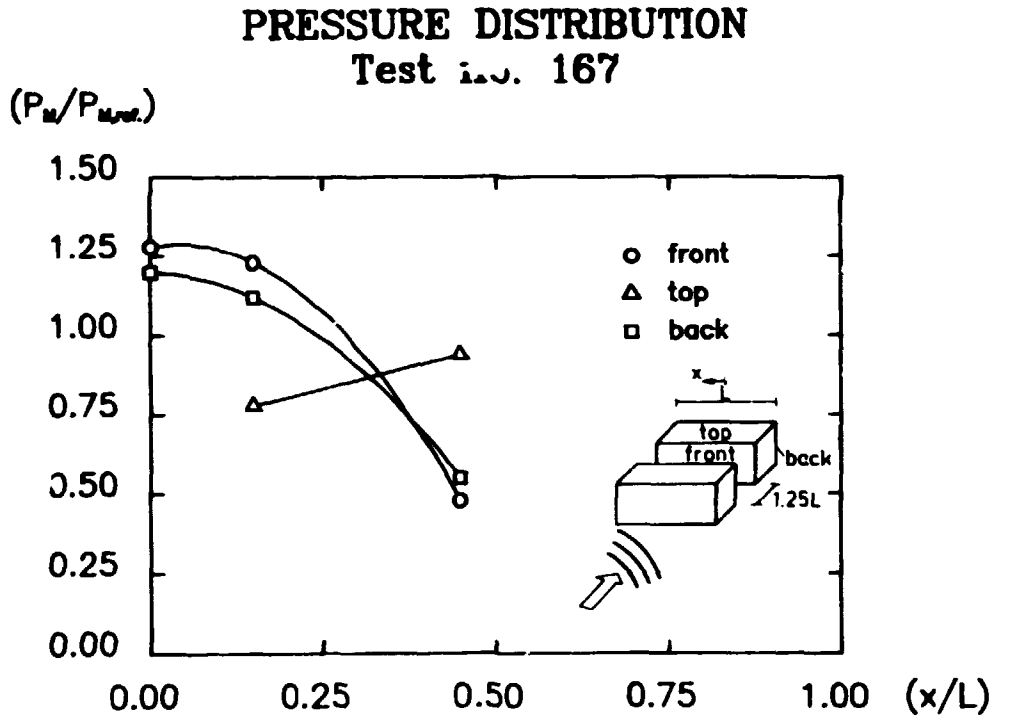

Fig. 132. Normalized peak pressure distribution.

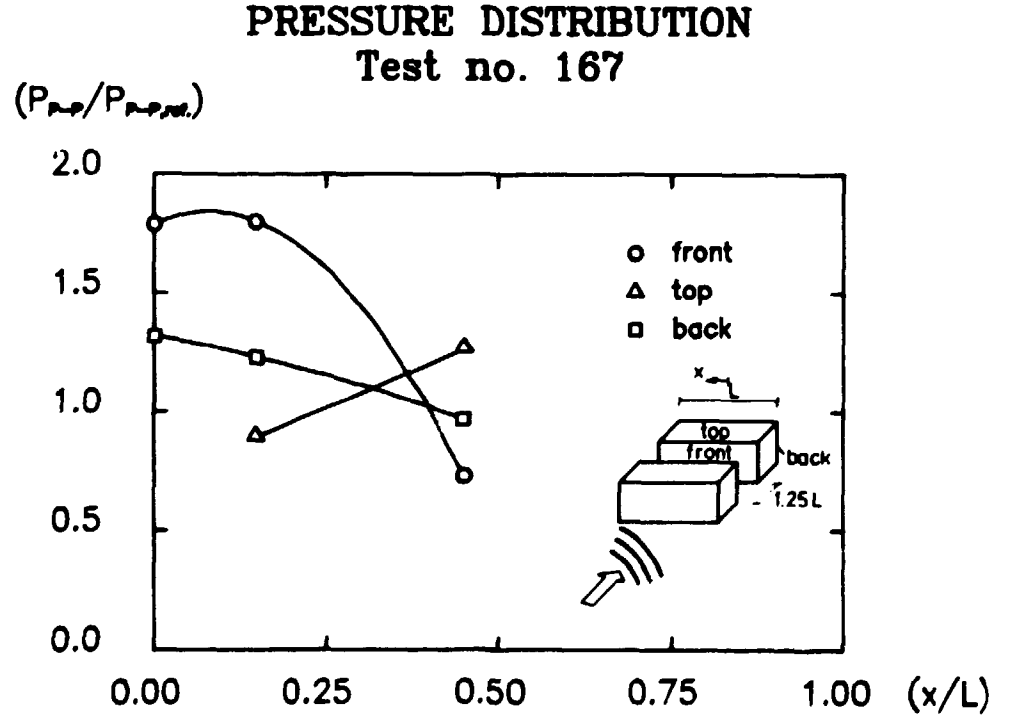

Fig. 133. Normalized peak-to-peak pressure distribution.

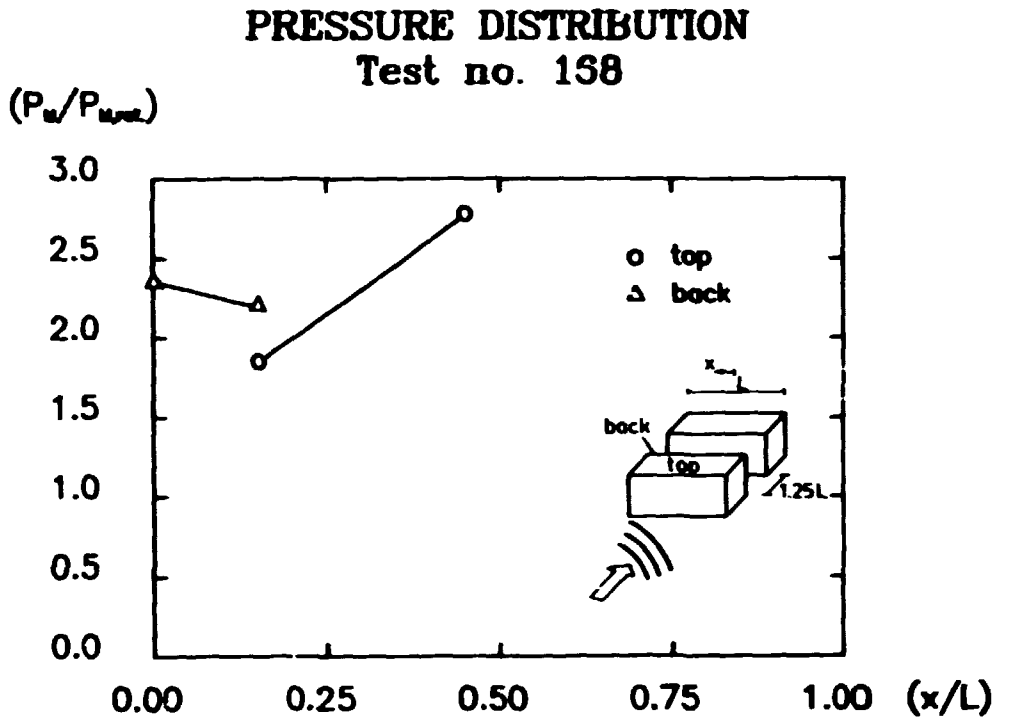

Fig. 134. Normalized peak pressure distribution.

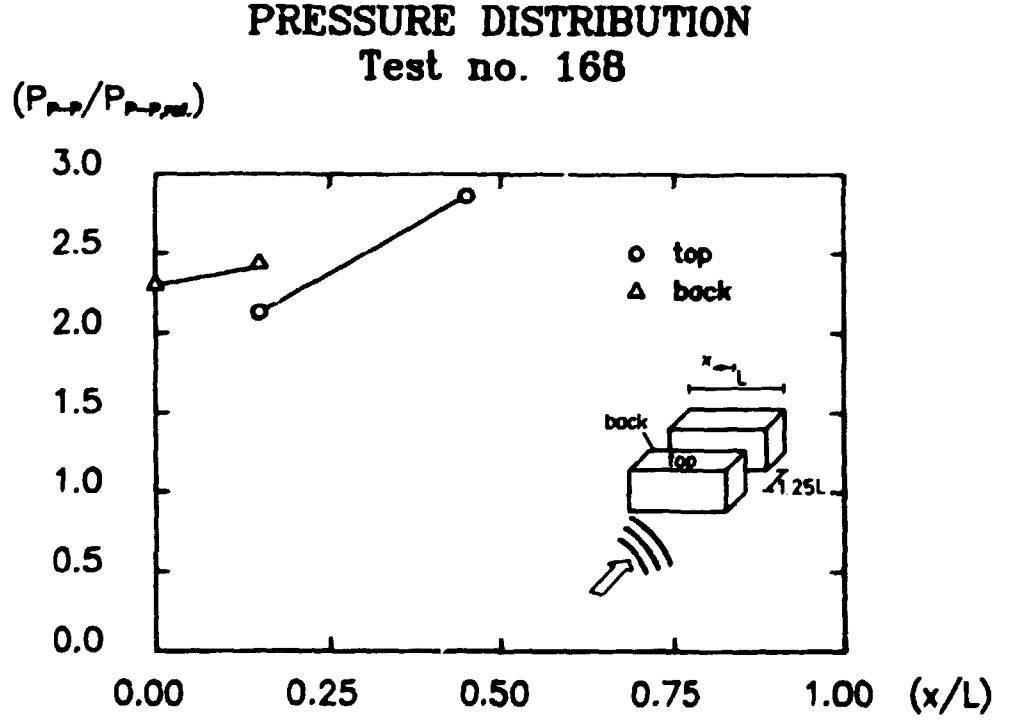

Fig. 135. Normalized peak-to-peak pressure distribution.

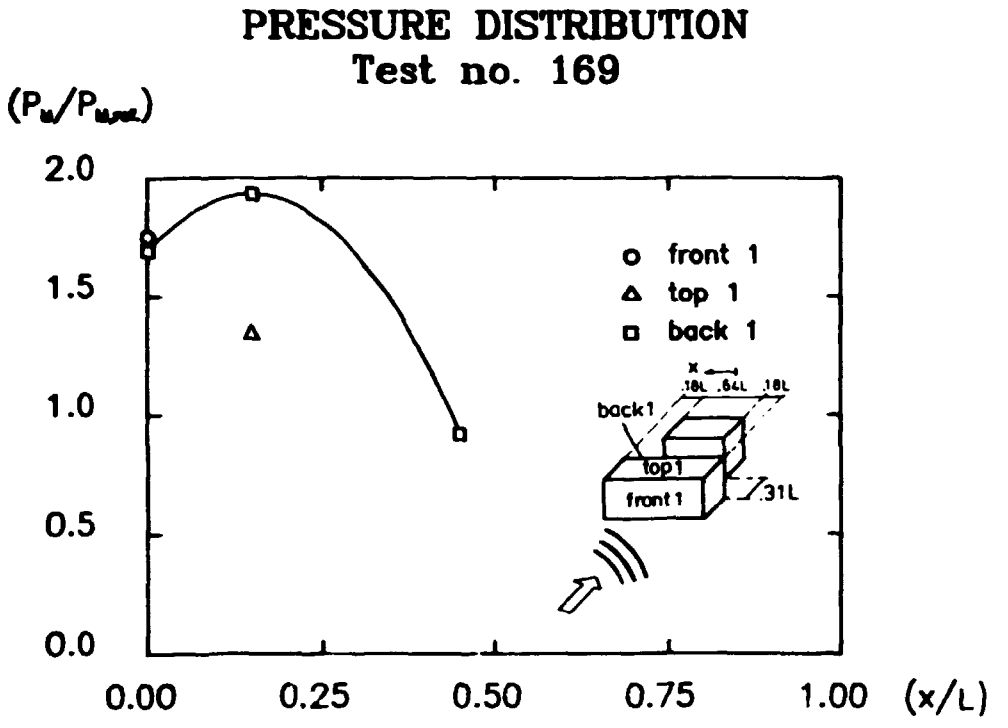

Fig. 136. Normalized peak pressure distribution.

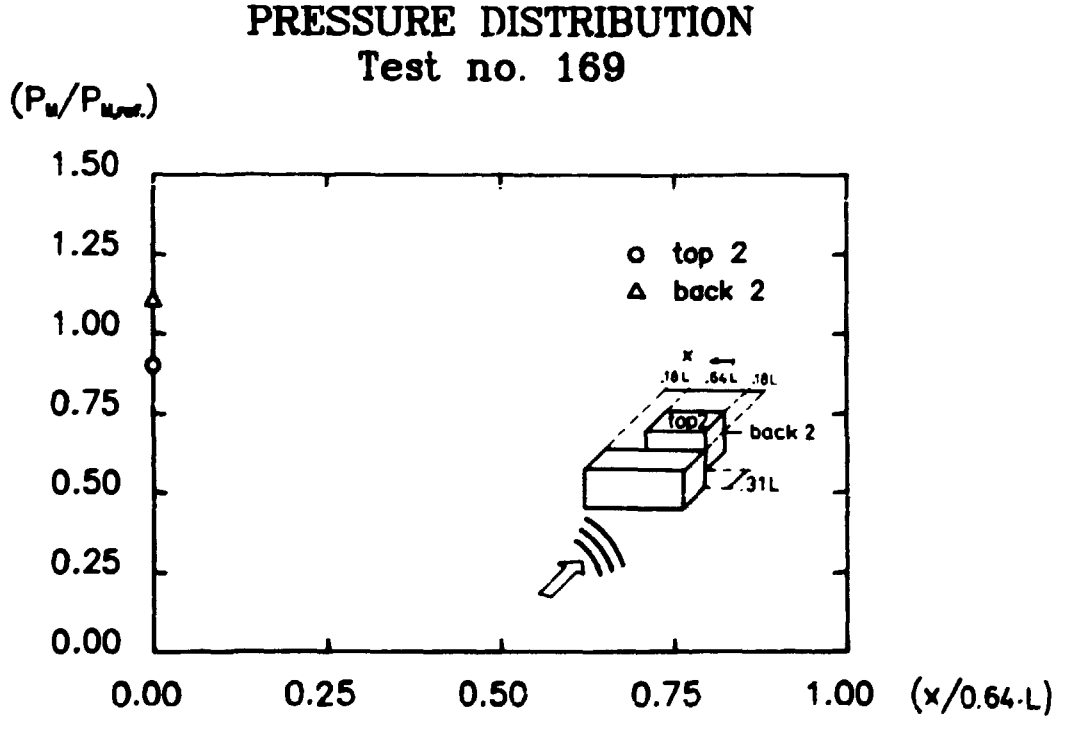

Fig. 137. Normalized peak pressure distribution.

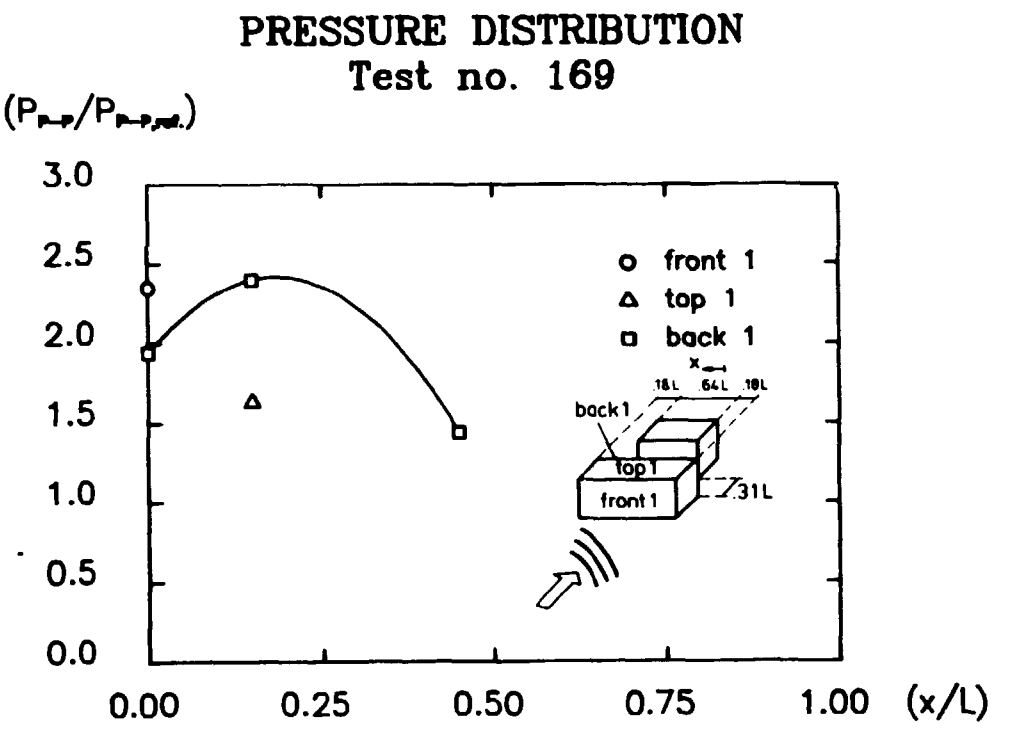

Fig. 138. Normalized peak-to-peak pressure distribution.

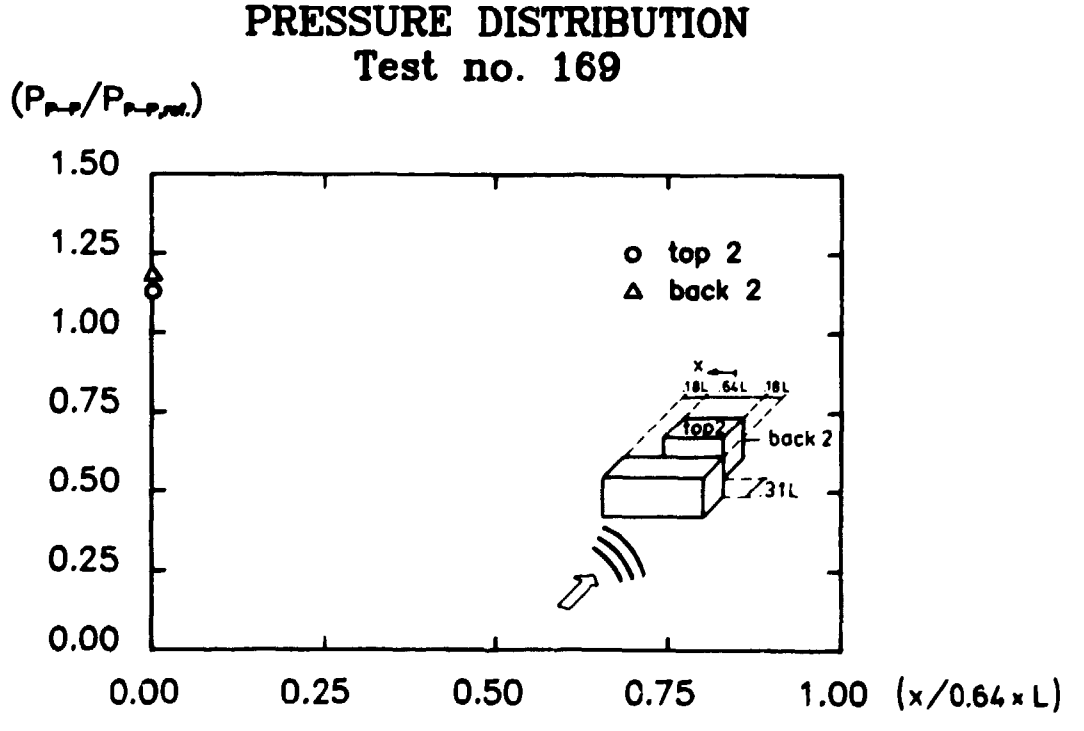

Fig. 139. Normalized peak-to-peak pressure distribution.

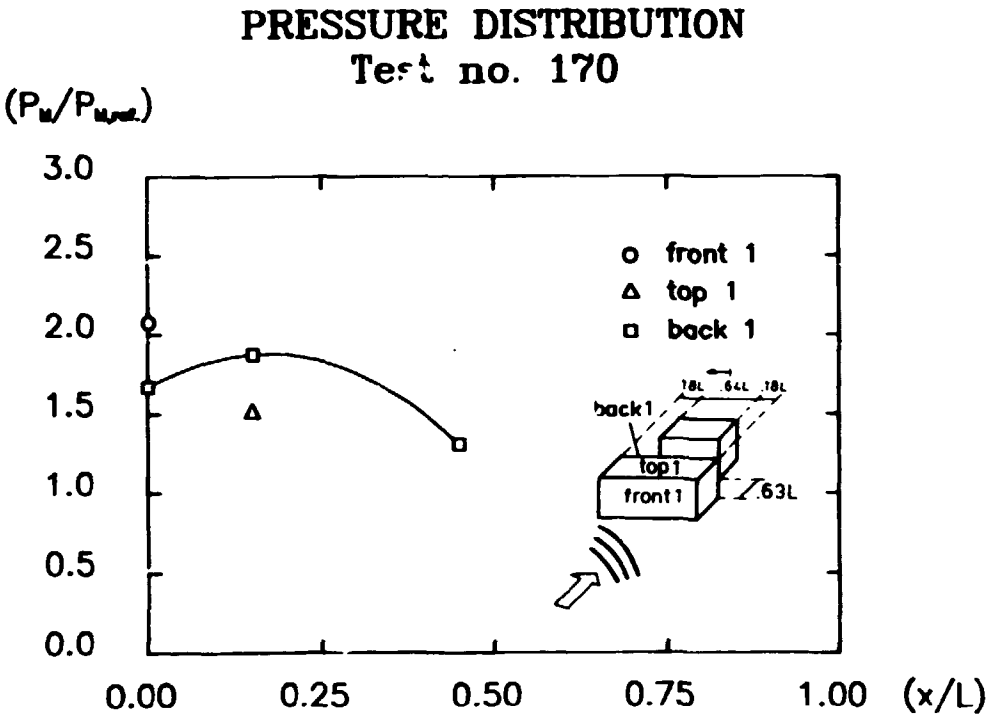

Fig. 140. Normalized peak pressure distribution.

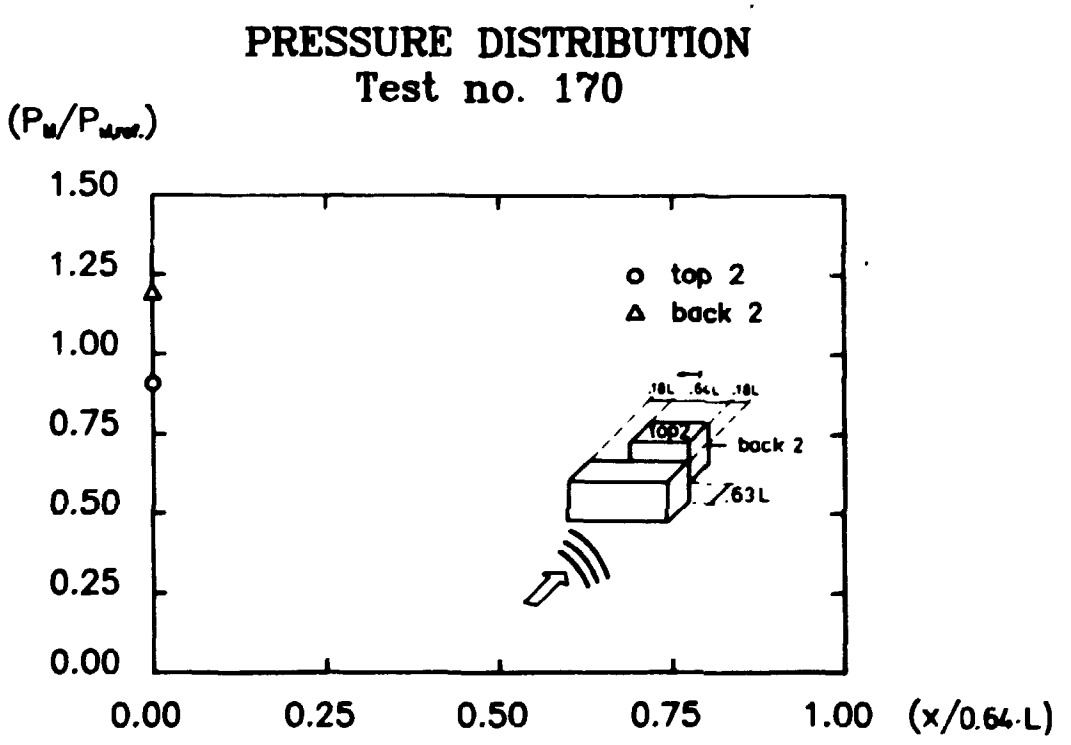

Fig. 141. Normalized peak pressure distribution.

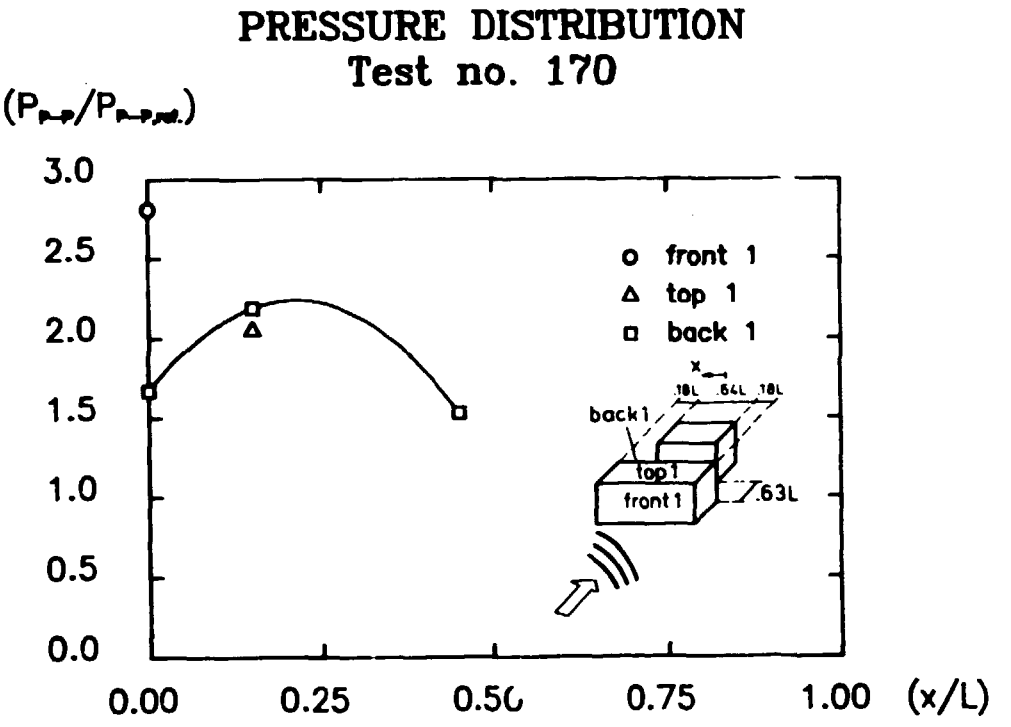

Fig. 142. Normalized peak-to-peak pressure distribution.

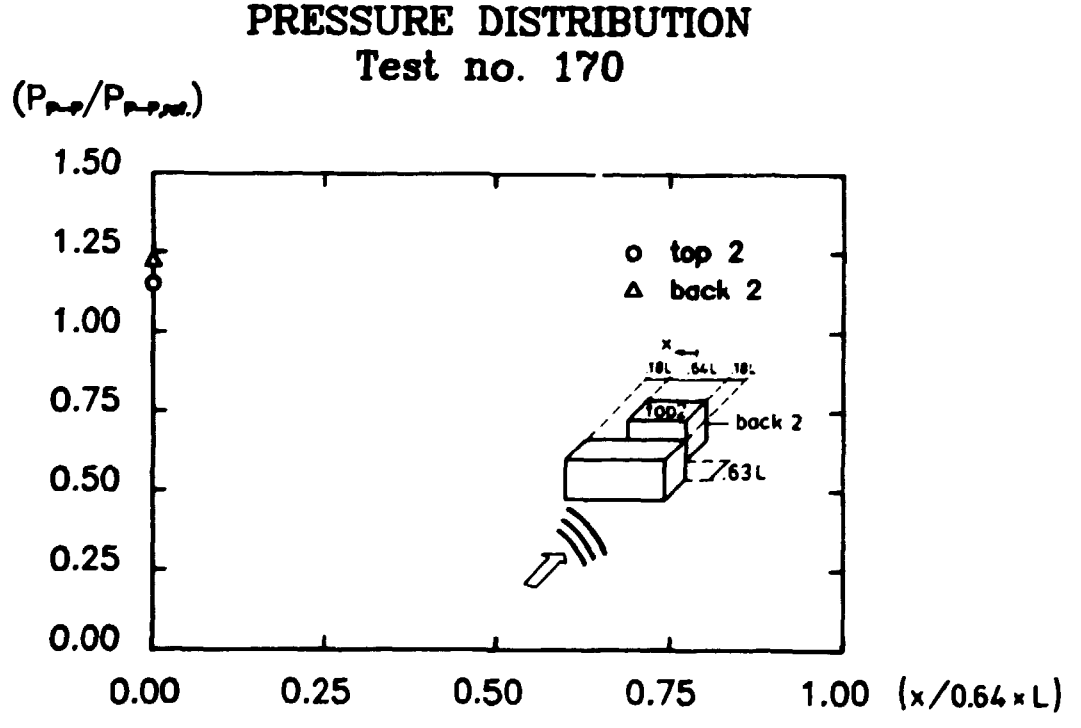

Fig. 143. Normalized peak-to-peak pressure distribution.

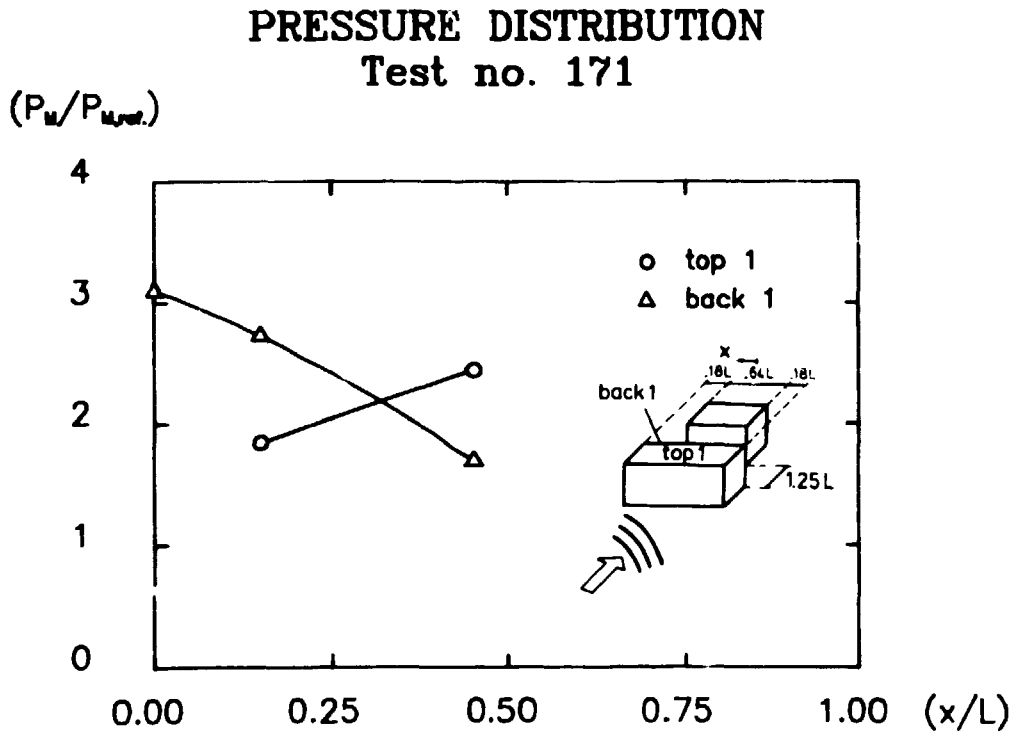

Fig. 144. Normalized peak pressure distribution.

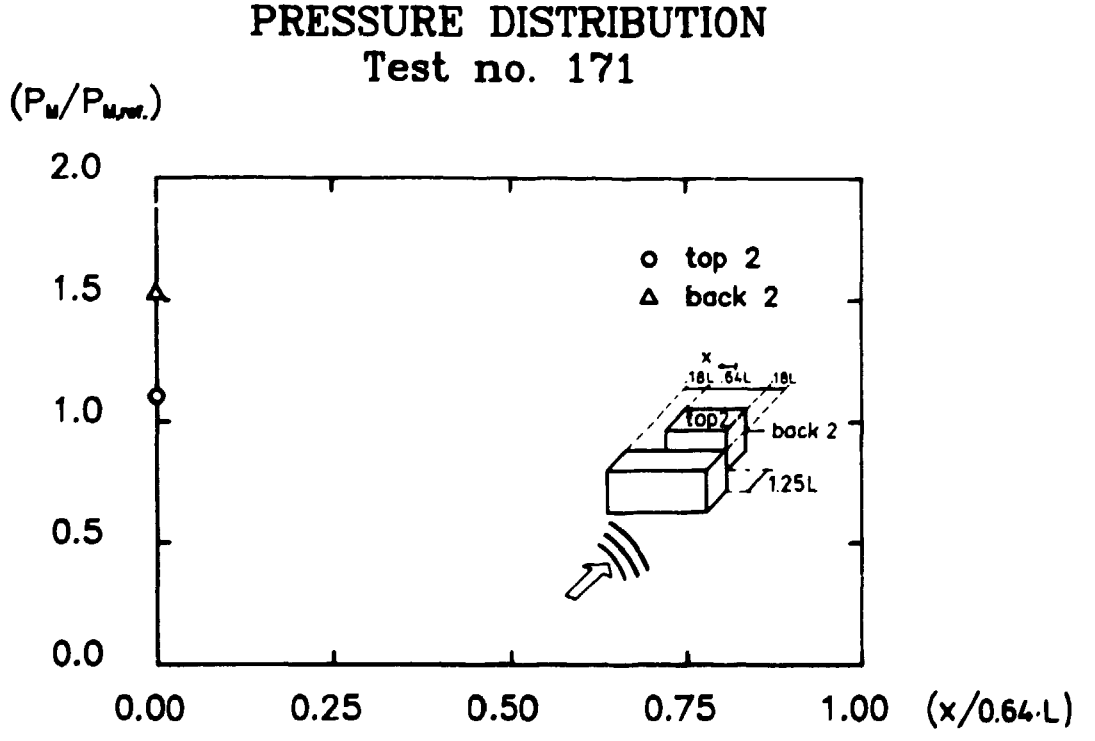

Fig. 145. Normalized peak pressure distribution.

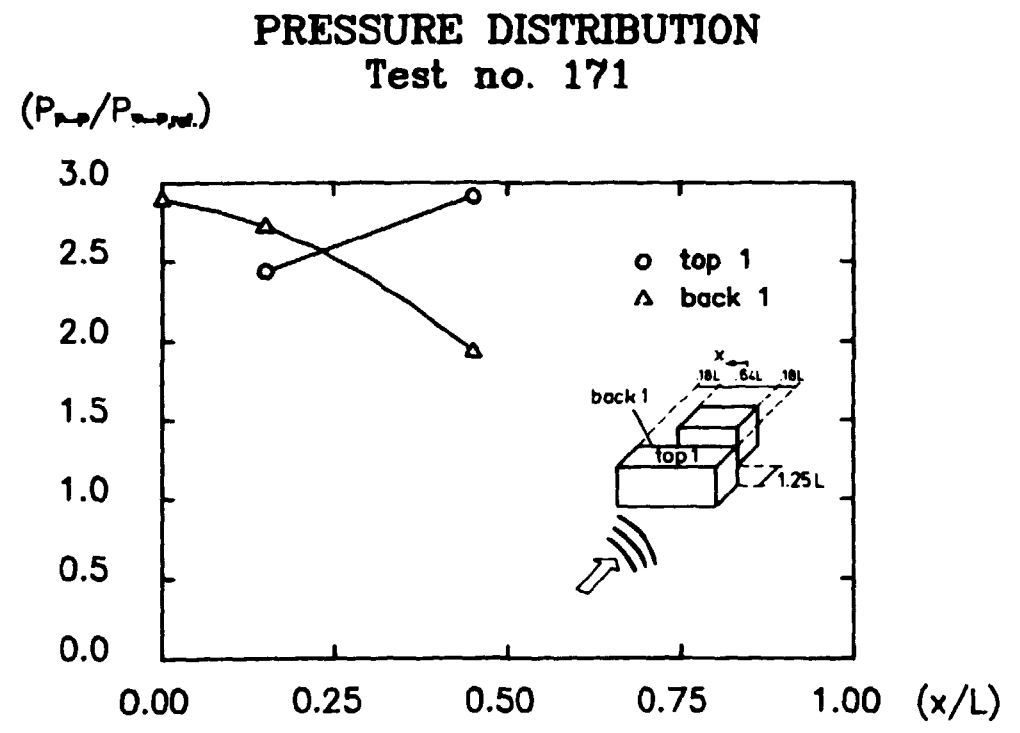

Fig. 146. Normalized peak-to-peak pressure distribution.

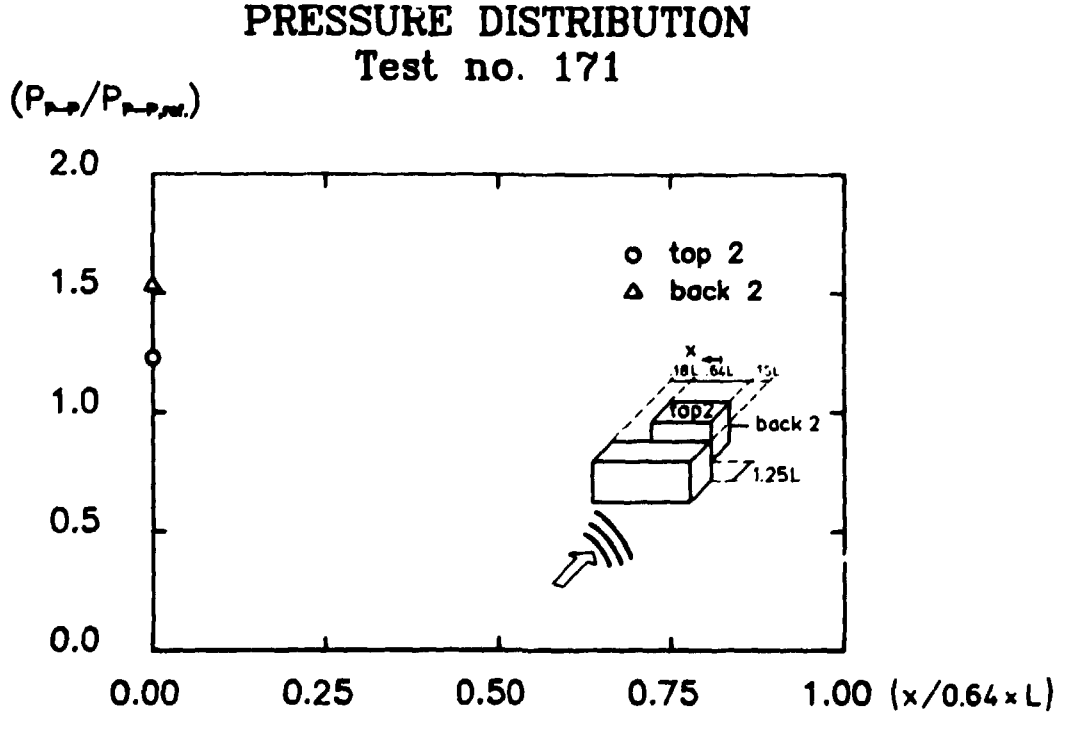

Fig. 147. Normalized peak-to-peak pressure distribution.

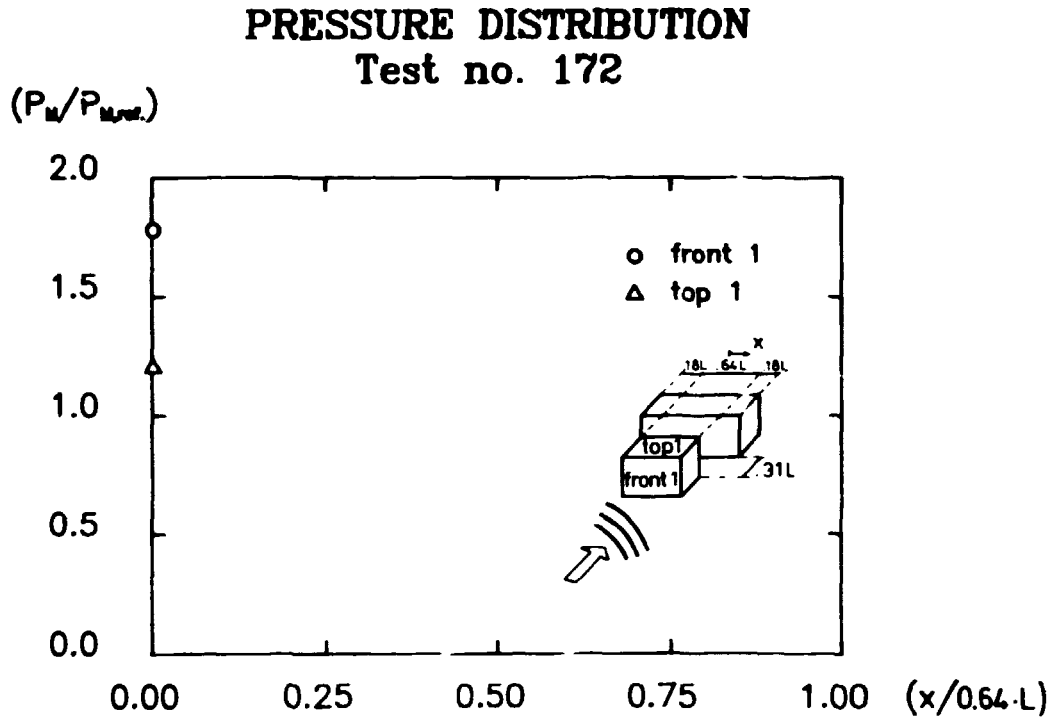

Fig. 148. Normalized peak pressure distribution.

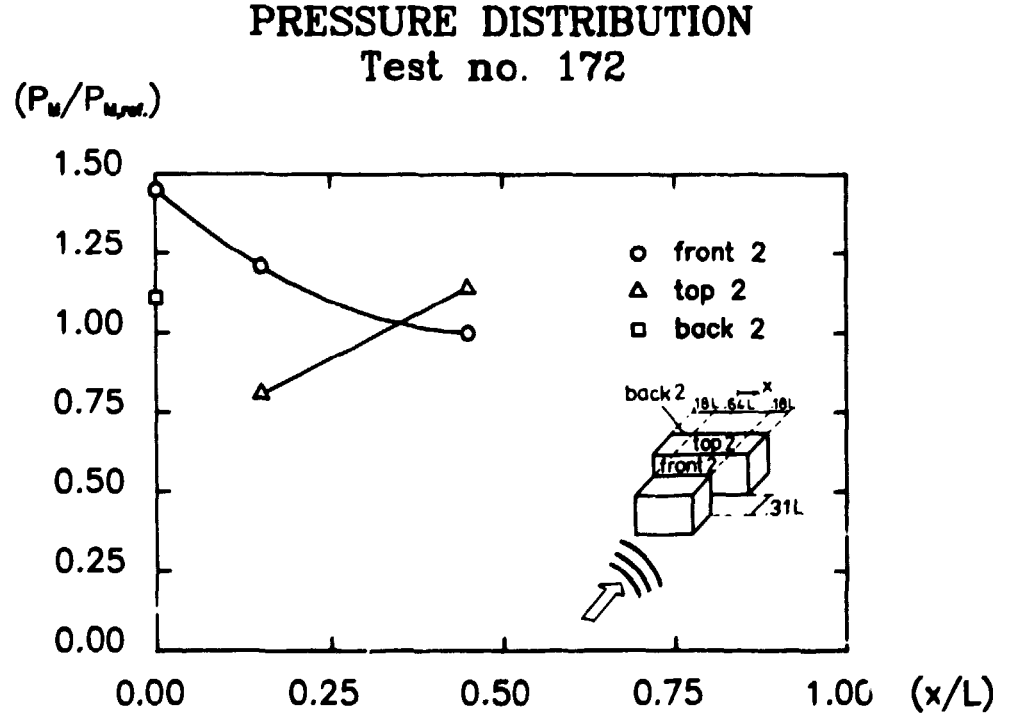

Fig. 149. Normalized peak pressure distribution.

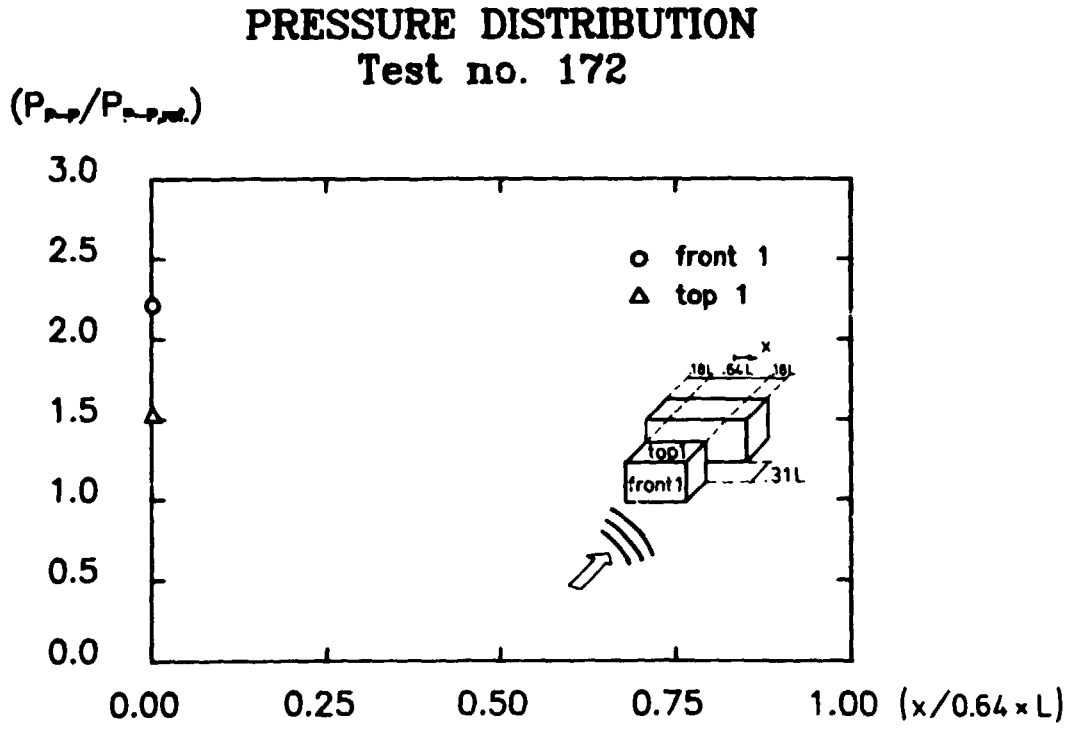

Fig. 150. Normalized peak-to-peak pressure distribution.

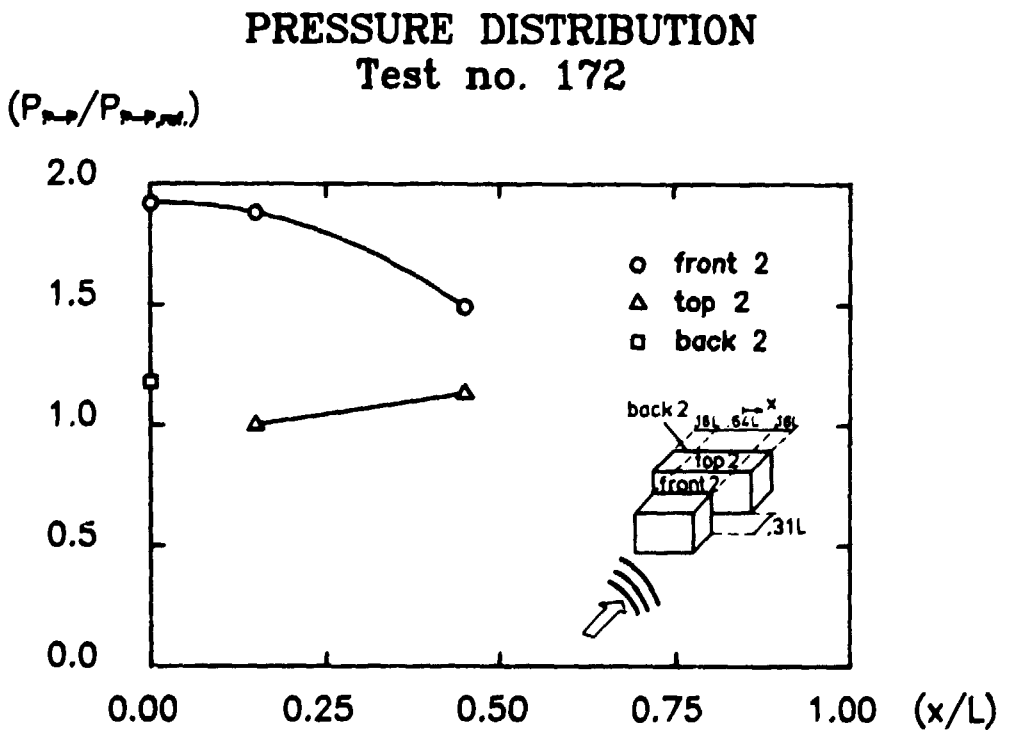

Fig. 151. Normalized peak-to-peak pressure distribution.

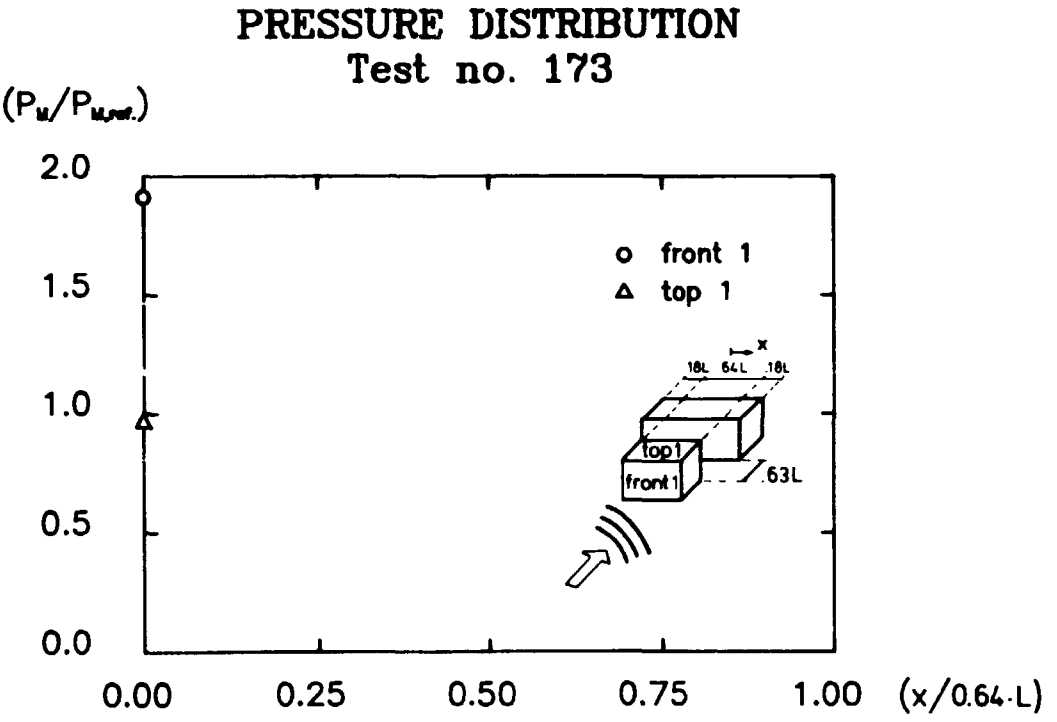

Fig. 152. Normalized peak pressure distribution.

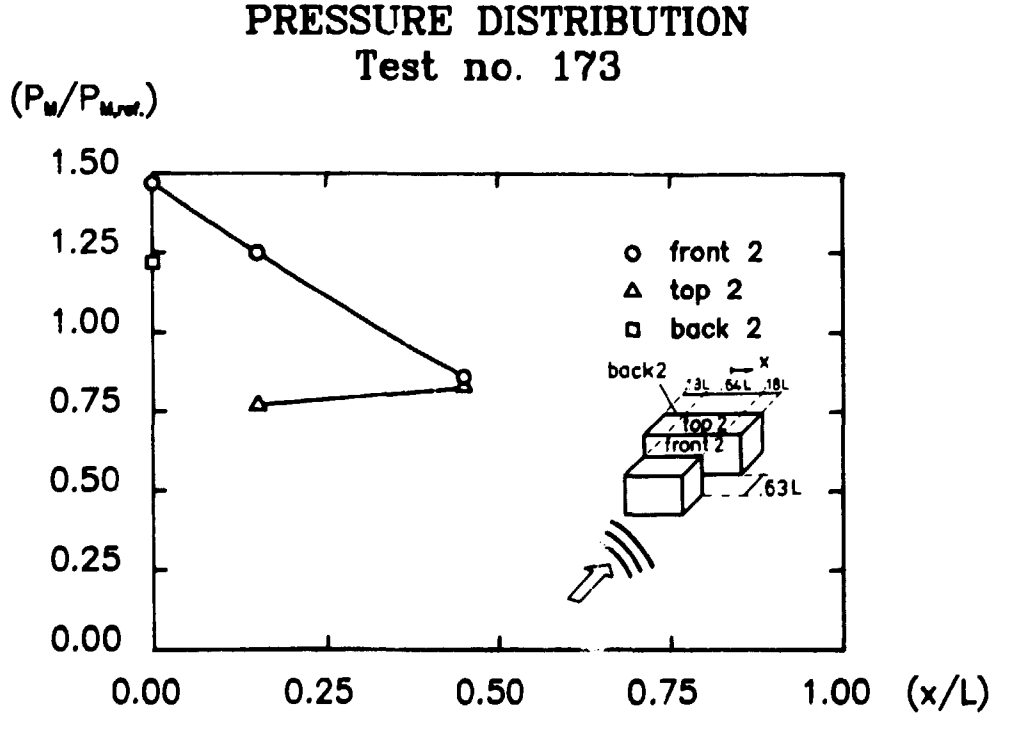

Fig. 153. Normalized peak pressure distribution.

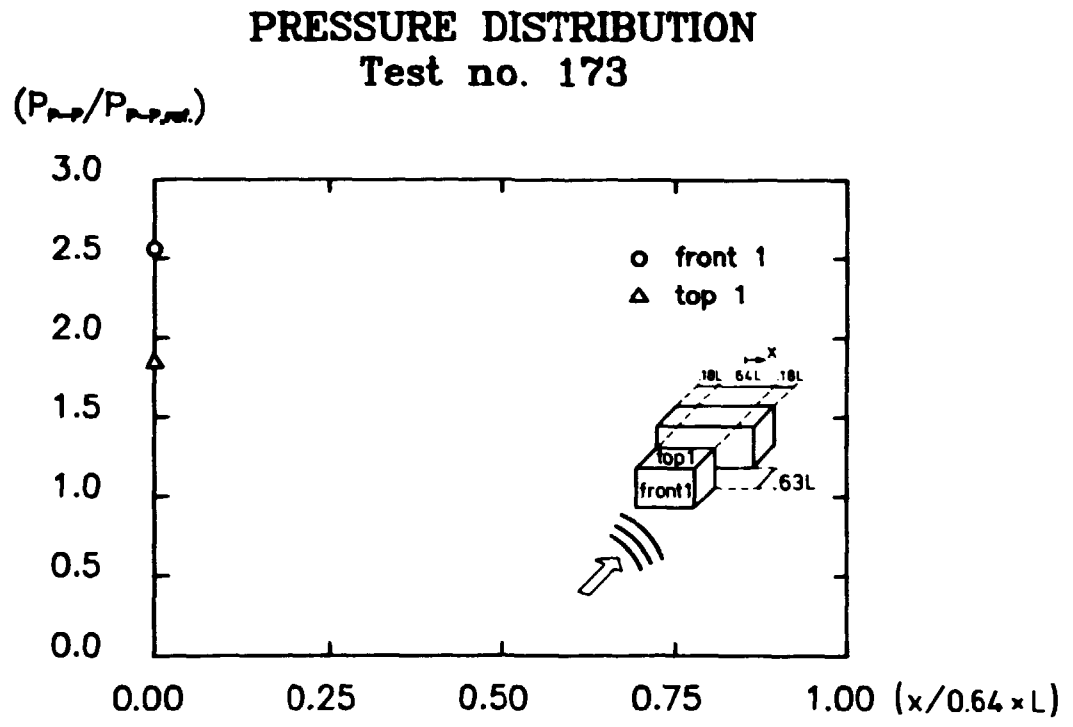

Fig. 154. Normalized peak-to-peak pressure distribution.

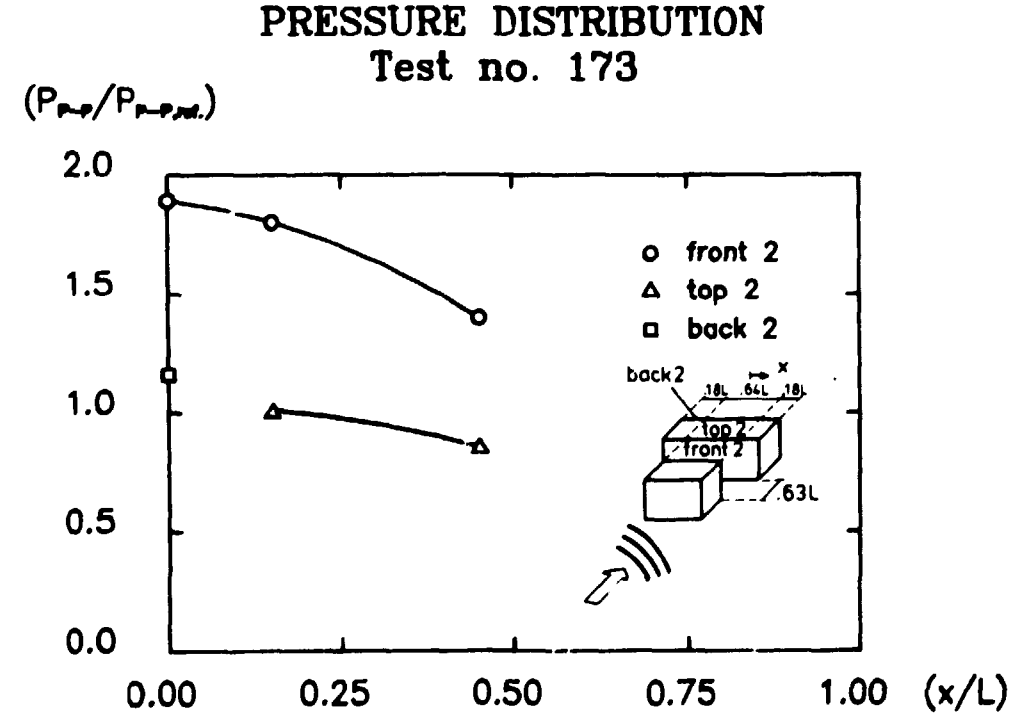

Fig. 155. Normalized peak-to-peak pressure distribution.

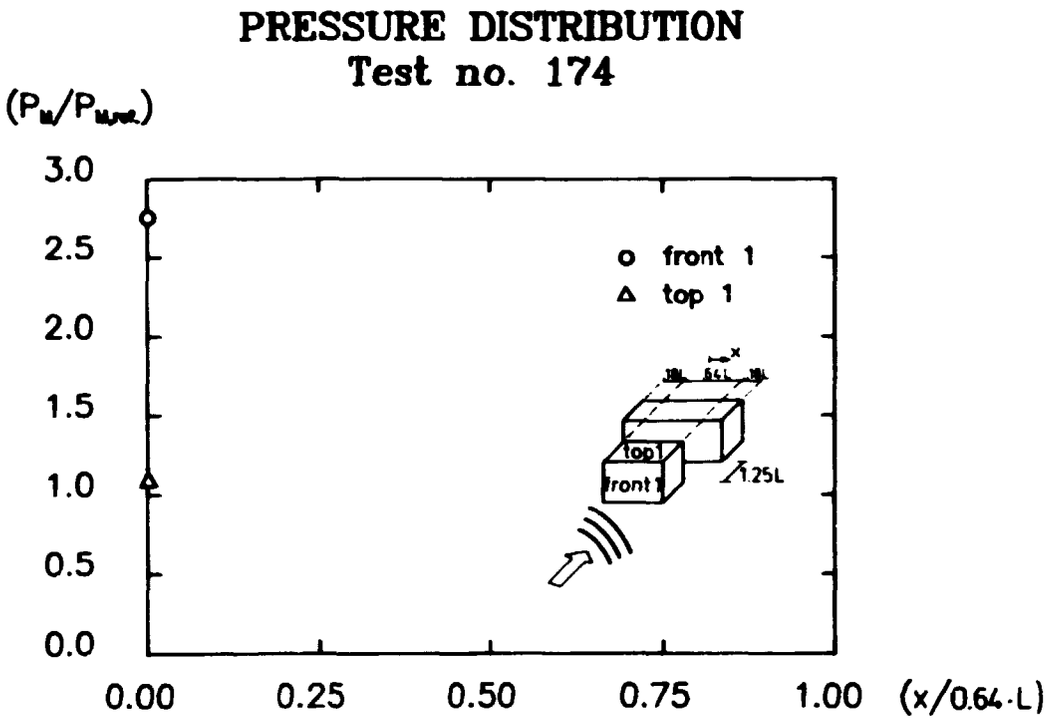

Fig. 156. Normalized peak pressure distribution.

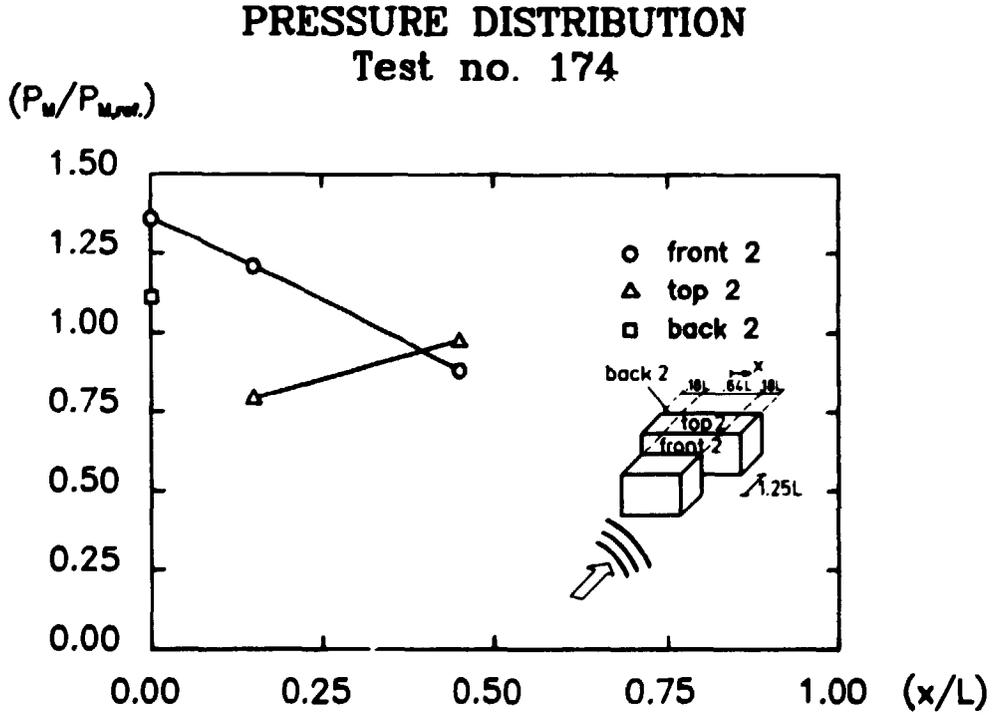

Fig. 157. Normalized peak pressure distribution.

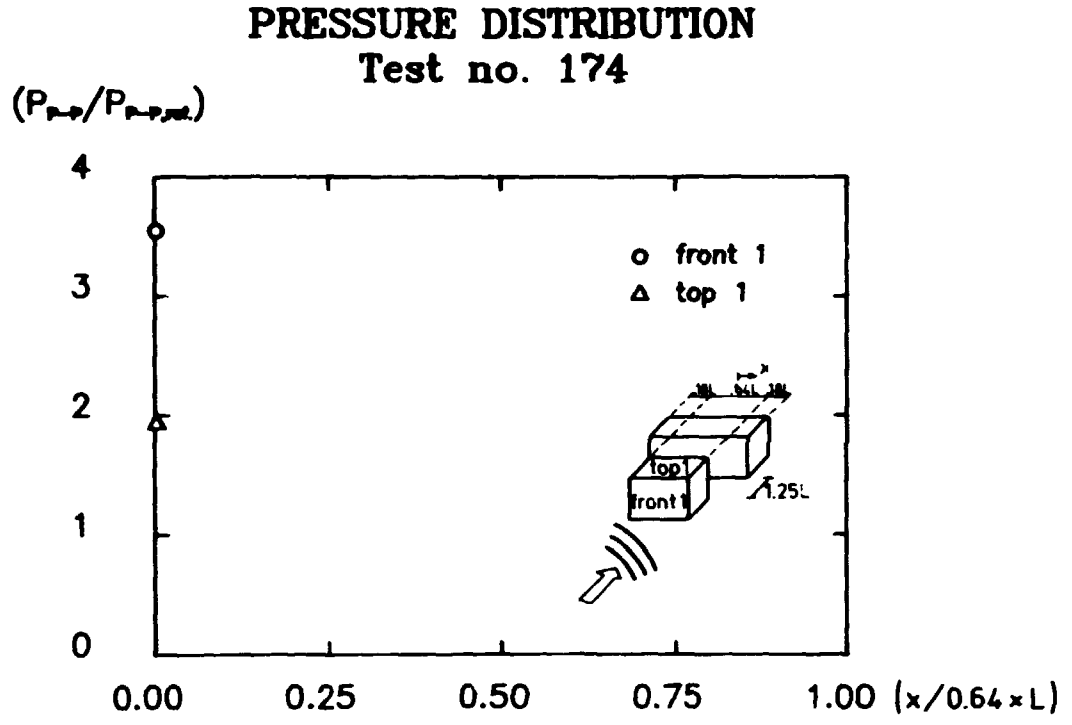

Fig. 158. Normalized peak-to-peak pressure distribution.

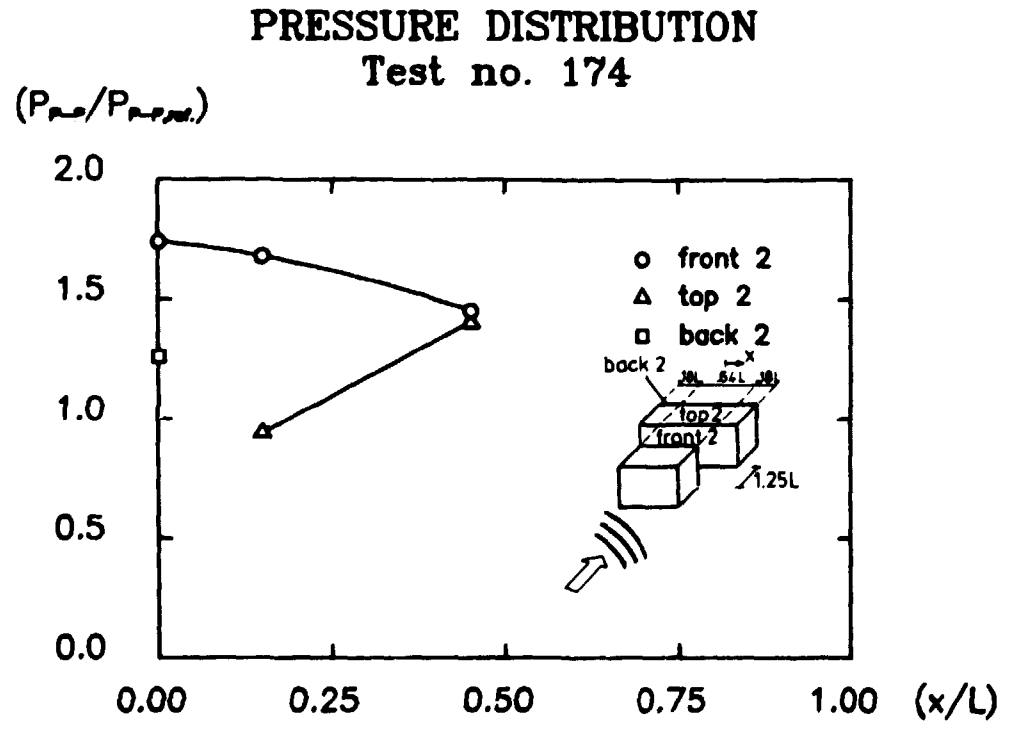

Fig. 159. Normalized peak-to-peak pressure distribution.

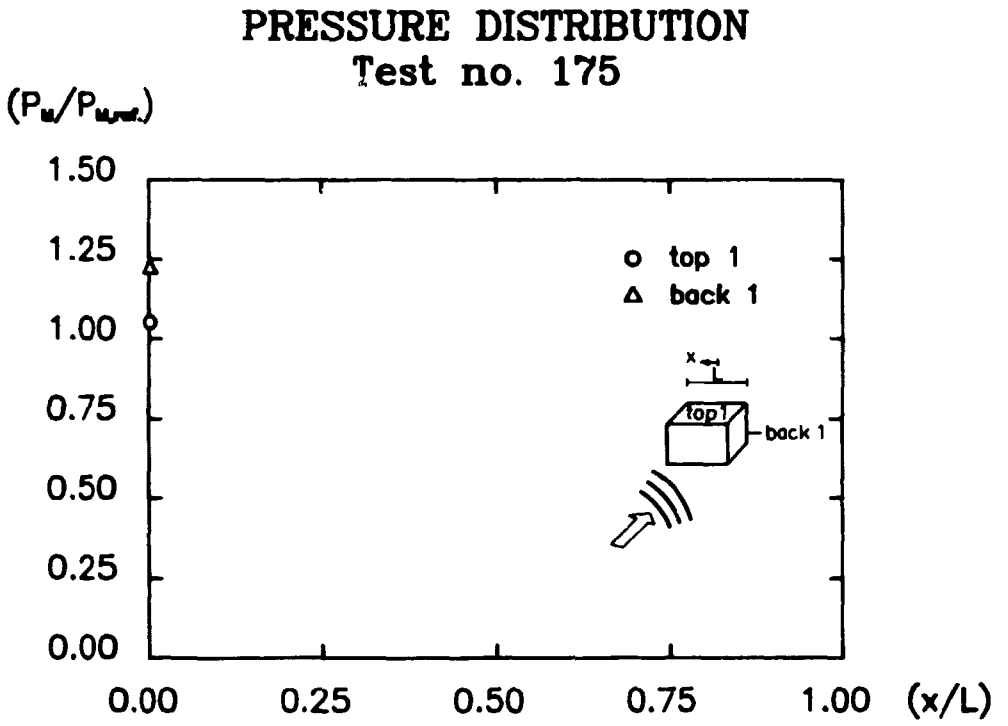

Fig. 160. Normalized peak pressure distribution.

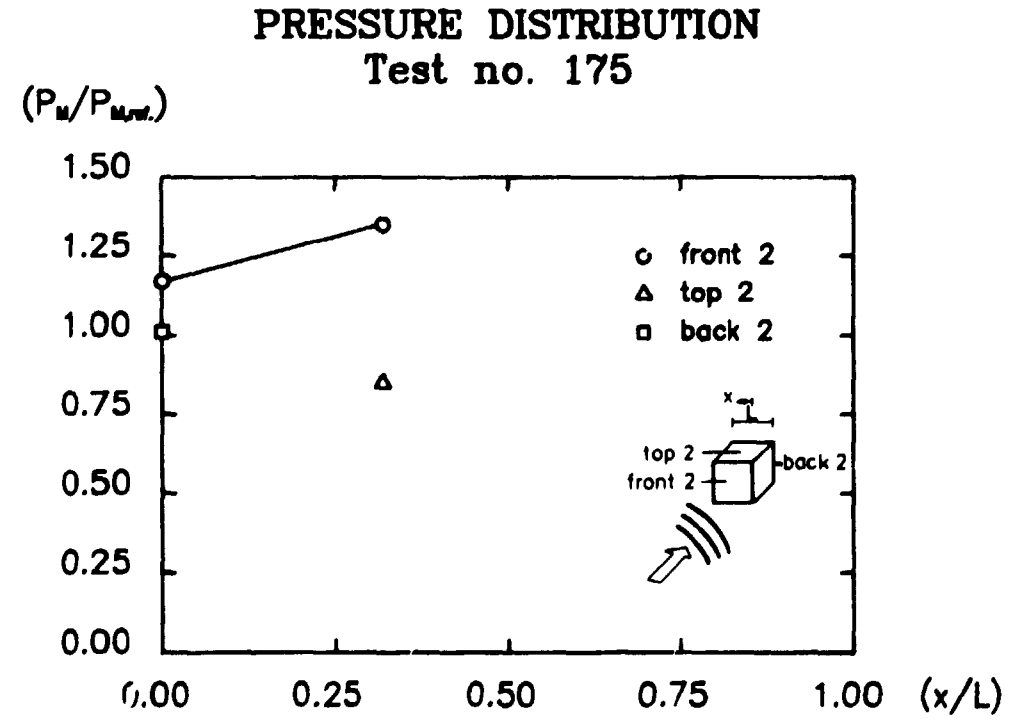

Fig. 161. Normalized peak pressure distribution.

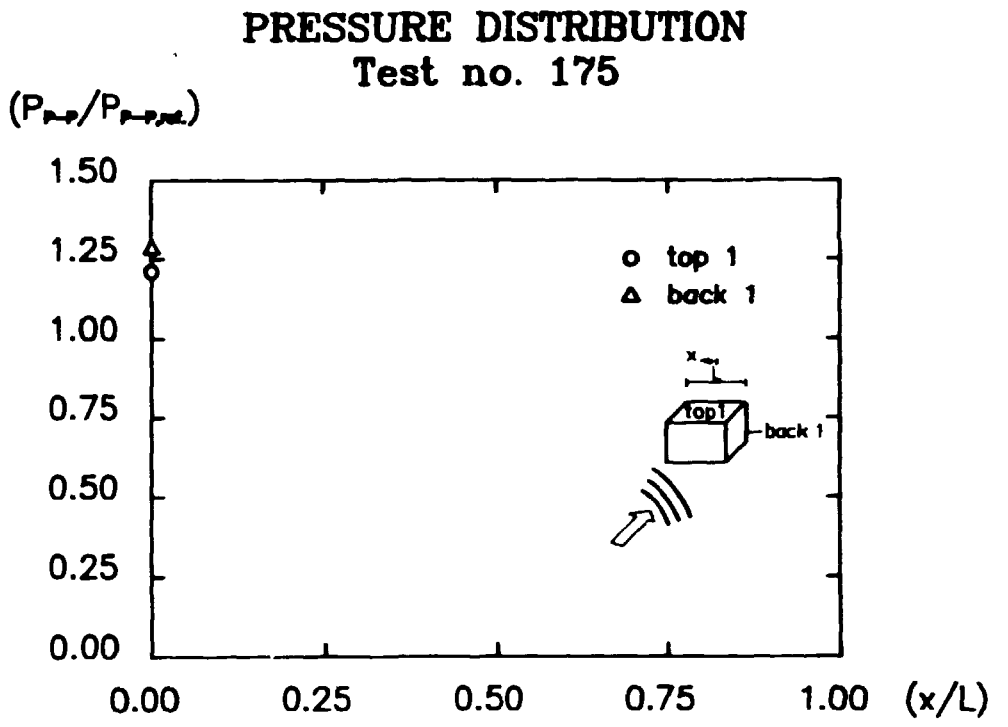

Fig. 162. Normalized peak-to-peak pressure distribution.

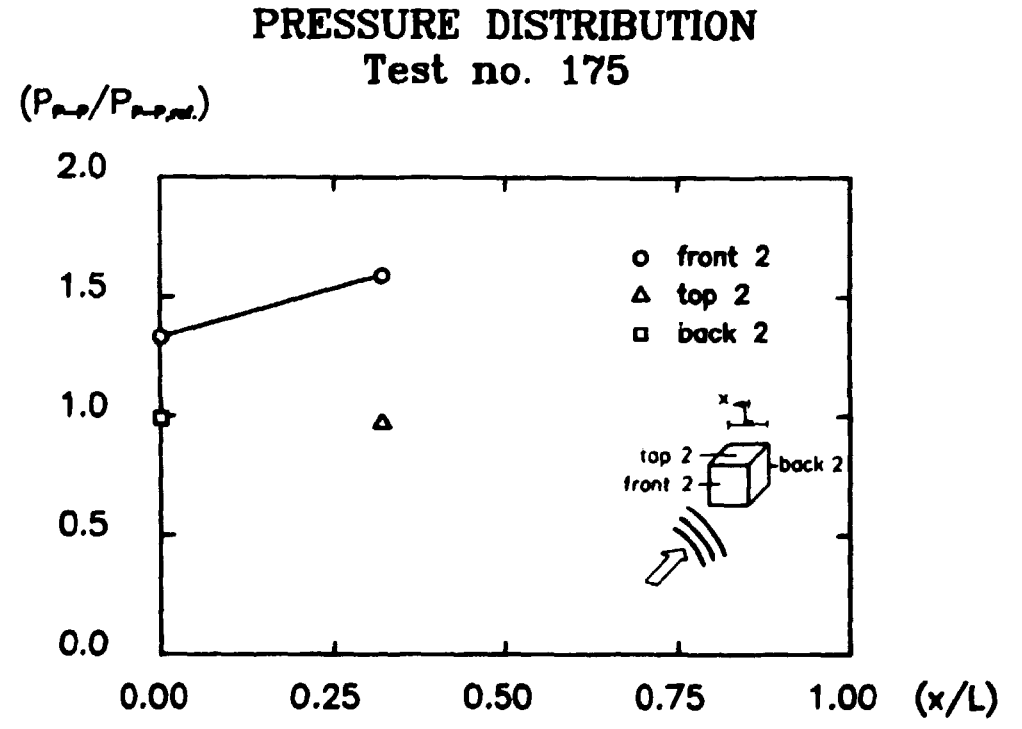

Fig. 163. Normalized peak-to-peak pressure distribution.

The mean of the reference measurements corresponding to the data presented in the above figures are given in Table 16.

EXPERIMENT NO.	$\langle P_{M,ref.} \rangle$ (mbar)	$\langle P_{p-p,ref.} \rangle$ (mbar)
156	4.85	10.95
157	5.75	11.45
158	3.2	7.4
159	5.2	9.95
160	5.2	11.35
161	3.3	7.15
162	3.35	7.3
163	5.1	10.1
164	1.7	6.0
165	3.6	7.4
166	3.9	7.85
167	3.1	7.25
168	5.7	11.65
169	4.35	9.4
170	3.75	8.45
171	3.7	8.2
172	4.3	8.7
173	3.5	8.95
174	3.75	7.6
175	4.45	9.2

Table 16. Mean of reference values corresponding to experiments 156-175.

3.7.2.3. Evaluation of results.

An inspection of the pressure pulse curves has shown that changes in the wave form from one measuring point to another can occur, but that the dominating frequency in all cases was of the order of magnitude 150 Hz.

The measured peak pressures depends strongly on the position of the measuring point. However, as in section 3.7.1.3, a detailed

description of each particular experiment would be meaningless due to turbulence and diffraction phenomena. Instead the general features of the data shall be accentuated. Each of the characteristic configurations have been commented on separately.

Identical boxes "on end" and at equal distance from the explosion (experiments no. 156-158):

- no significant effect of varying distance between the obstacles is observed, and the pressure distribution on the obstacles approaches the pressure distribution obtained in the corresponding single-box experiment.

- the front pressure is higher than the pressure measured on the back, and the reflection coefficient for the front is of the order of magnitude 1.25. The back pressure is again larger than that on the side.

- the two obstacles do not possess full symmetry as could be expected; this is apparently due to diffraction and scattering phenomena.

In conclusion there is no significant interaction between the two boxes present, with regard to the pressure build-up.

Identical boxes "on end" and placed along a line from the source experiments no. 159-162):

- in these experiments a significant dependence of the distance between the boxes has been demonstrated, in the sense that the back pressure of the box in front is considerably higher, relatively, than the corresponding pressure on a single box (~ 40%) for a small distance between the boxes (0.31 L). This effect disappears with increasing distance between boxes, and is supposed to be due to reflections from the box behind. Moreover, the front pressure on the box behind showed up to be considerably less than the correspon-

ding pressure on a single box (~ 40%), again for small distances between the boxes. This effect is also weakened with increasing distance between them, and is supposed to be due to some shade effect behind the first obstacle.

- the pressure distribution on the remaining surfaces is approximately the same as the pressure distribution registered on the corresponding single-box experiment.

In conclusion, a significant wave interaction has been demonstrated in the sense that the back pressure of the box in front is increased and the front pressure of the box behind is decreased - all for small distances between the boxes.

Identical "laying" boxes placed on a line from the source (experiments no. 163-168):

- in the case of a long distance between obstacles (0.63L, 1.25L) no significant wave interaction has been observed and qualitatively the situation is as in the corresponding single-box experiment (no. 147). However, for the greatest distance (1.25 L) a rather complicated pressure field is registered probably due to the short distance between the source and the obstacle in front.

- in the case of a small distance between obstacles (0.31 L) a significant pressure wave interaction is observed. The front pressure of the box behind is decreased some 20% compared to the corresponding single-box experiment, whereas the top and back pressures of this particular box are unaffected. This phenomenon is probably due to a shadow zone behind the obstacle in front. Furthermore, it is seen that the back pressure of the box in front is increased some 40% at the middle of the surface and some 10% at the ends. This behaviour is supposed to be caused by reflections from the box behind. The pressure distribution on the remaining surfaces is unaffected and qualitatively as registered in the corresponding single-box experiment.

In conclusion, a wave-wave interaction has been demonstrated for boxes placed close together.

Different "laying" boxes placed on a line from the source (experiments no. 169-174):

The features to be emphasized in these experiments are exactly the same as those corresponding to experiments 163-168 when the box in front is the large box. When the small box is placed in front no wave interaction of the previously described type has been demonstrated, and the situation is thus similar to that in corresponding single-box experiments.

Two small "laying" boxes placed with large distance (experiment 175):

These two boxes do not interact of course, and the experiment replaces in this sense two single-box experiments with the smallest box types.

- the pressure distribution on the medium box shows the same general picture as the pressure distribution on a large box exposed to a similar load.

- the pressure distribution on the smallest box is also qualitatively as that on a large box, except that the front pressure is increased near the end. This latter observation may be due to boundary effects.

In conclusion the pressure distribution on small boxes is roughly the same as that on large boxes exposed to the same pressure load.

4. PISTON MODEL

In this section the problem of a sphere expanding at a low Mach number in a gas is treated by means of linear acoustic theory, and a closed form solution is obtained for a sphere expanding as a stepwise linear function of time.

4.1. Differential equation.

In a linear approximation, the propagation of disturbances through a non viscous elastic fluid is governed by the equation of motion (7)

$$\lambda \bar{\nabla}\bar{\nabla} \cdot \bar{u} = \rho \ddot{\bar{u}} \tag{4.1.1}$$

where λ is the Lamé constant, u is the displacement, ρ the density of the fluid and a dot denotes differentiation with respect to the time t.

The vector equation (4.1.1) can be replaced by the scalar equation

$$\nabla^2 \phi = \frac{1}{c^2} \ddot{\phi} \tag{4.1.2}$$

where ϕ is the velocity potential defined by

$$\bar{v} = \dot{\bar{u}} = \bar{\nabla}\phi \tag{4.1.3}$$

and c is the velocity of sound in the fluid given by

$$c = \sqrt{\frac{\lambda}{\rho}} \tag{4.1.4}$$

The pressure is then given by (7)

$$p = -\lambda \bar{\nabla} \cdot u = -\rho \dot{\phi} \tag{4.1.5}$$

For problems with spherical symmetry the wave equation (4.1.2) takes the form

$$\frac{\partial^2 (r\phi)}{\partial r^2} = \frac{1}{c^2} \frac{\partial^2 (r\phi)}{\partial t^2} \tag{4.1.6}$$

yielding solutions of the form

$$r\phi(r,t) = f(t-r/c) + g(t+r/c) \tag{4.1.7}$$

where $f(t-r/c)$ corresponds to diverging waves and $g(t+r/c)$ corresponds to converging waves.

In the case of an expanding sphere in an initially resting fluid only diverging waves are present, and the solution (4.1.7) then takes the form

$$r\phi(r,t) = f(s) \tag{4.1.8}$$

where

$$s = t - r/c \tag{4.1.9}$$

Insertion of (4.1.8) into (4.1.3) and (4.1.5) yields the following expressions for the radial velocity and the pressure

$$v(r,t) = \frac{\partial \phi}{\partial r} = -\frac{1}{rc} f'(s) - \frac{1}{r^2} f(s) \tag{4.1.10}$$

and

$$r \cdot p(r,t) = -\rho \frac{\partial \phi}{\partial t} = -\rho f'(s) \tag{4.1.11}$$

where a prime denotes differentiation with respect to the parameter s.

The condition to be satisfied on the surface is

$$v(R(t),t) = \dot{R}(t) \tag{4.1.12}$$

where

$$R = R(t) \tag{4.1.13}$$

denotes the radius of the sphere.

Equation (4.1.10) and (4.1.12) now yield the following equation for the determination of f(s)

$$f'(s) + \frac{c}{R(t)} f(s) = -cR(t)\dot{R}(t) \tag{4.1.14}$$

where

$$s = t - R(t)/c \tag{4.1 15}$$

In order to obtain a solution to equation (4.1.14) it is necessary to demand, that s is a monotonic function of t. This is the case for subsonic expansion rates, for which

$$\frac{ds}{dt} = 1 - \dot{R}(t)/c > 0 \tag{4.1.16}$$

The radius of the sphere can then be given as a function of s, and the solution of (4.1.14) is straight forward. However, as shown in Fig. 164, the radius is given implicitly as a function of s.

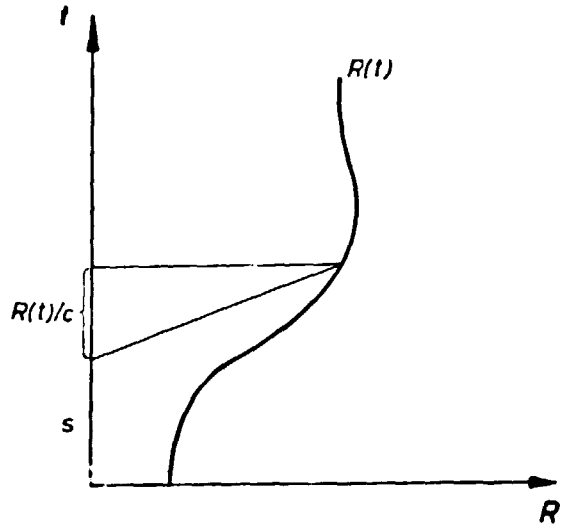

Fig. 164. Determination of the time factor s from t and R(t).

It is therefore more convenient to use the time t as integration variable. The solution then takes the form

$$f(t-R(t)/c) = \exp\left(-\int_{t_o}^{t} \frac{c}{R(\tau_2)} \frac{ds}{d\tau_2}\, d\tau_2\right)$$

$$\times\left\{-c\int_{t_o}^{t} \exp\left(\int_{t_o}^{\tau_1} \frac{c}{R(\tau_2)} \frac{ds}{d\tau_2}\, d\tau_2\right)\dot{R}(\tau_1)R(\tau_1)\frac{ds}{d\tau_1}d\tau_1 + f(t_o-R(t_o)/c)\right\}$$

$$= R(t)\exp\left(-\int_{t_o}^{t} \frac{c}{R(\tau_2)}d\tau_2\right)$$

$$\times\left\{-\int_{t_o}^{t} \exp\left(\int_{t_o}^{\tau_1} \frac{c}{R(\tau_2)}d\tau_2\right)\dot{R}(\tau_1)(c-\dot{R}(\tau_1))d\tau_1 + \frac{f(t_o-R(t_o)/c)}{R(t_o)}\right\}$$

$$, t \geq t_o \qquad (4.1.17)$$

The pressure on the surface of the expanding sphere is then obtained by combination of (4.1.11), (4.1.14) and (4.1.17)

$$Rp(R,t) = \rho c\left[R(t)\dot{R}(t) + \frac{f(t-R(t)/c)}{R(t)}\right]$$

$$= \rho c\left[R(t)\dot{R}(t) + \exp\left(-\int_{t_o}^{t} \frac{c}{R(\tau_2)} d\tau_2\right)\right.$$

$$\left. \times\left\{-\int_{t_o}^{t} \exp\left(\int_{t_o}^{\tau} \frac{c}{R(\tau_2)} d\tau_2\right)\dot{R}(\tau_1)(c-\dot{R}(\tau_1))d\tau_1 + \frac{f(t_o-R(t_o)/c)}{R(t_o)}\right\}\right]$$

$$, t \geq t_o \qquad (4.1.18)$$

From eq. (4.1.11) it is clear, that the product rp(r,t) is a function of s alone. For any combinations of r and t it can be found implicitly by the relation

$$rp(r,t) = R(t^*)p(R(t^*),t^*) \qquad (4.1.19)$$

where

$$t^* - R(t^*)/c = t - r/c \qquad (4.1.20)$$

In general it is not possible to obtain a closed form espression through (4.1.18), but for special forms of R(t) the integrations in (4.1.17) can be performed analytically, as shown in section 4.2.

4.2. Sphere expanding at constant rate.

Assume that the sphere expands with the constant Mach number α in the time interval $t_1 < t < t_2$

$$R(t) = R(t_1) + \alpha c(t-t_1) \tag{4.2.1}$$

The exponential functions in (4.1.17) then take the form

$$\exp\left(-\int_{t_1}^{t} \frac{c}{R(t)}dt\right) = \left(\frac{R(t)}{R(t_1)}\right)^{-\frac{1}{\alpha}}, \tag{4.2.2}$$

and eq. (4.1.17) now directly yields

$$\begin{aligned}\frac{f(s)}{R(t)} &= -R(t)^{-\frac{1}{\alpha}} c^2\alpha(1-\alpha)\int_{t_1}^{t} R(t)^{\frac{1}{\alpha}}dt + \left(\frac{R(t)}{R(t_1)}\right)^{-\frac{1}{\alpha}} \frac{f(s_1)}{R(t_1)} \\ &= -\frac{c\alpha(1-\alpha)}{1+\alpha}\left(R(t)-R(t_1)\left(\frac{R(t)}{R(t_1)}\right)\right)^{-\frac{1}{\alpha}} + \left(\frac{R(t)}{R(t_1)}\right)^{-\frac{1}{\alpha}} \frac{f(s_1)}{R(t_1)}\end{aligned} \tag{4.2.3}$$

It is evident that eq. (4.2.3) can be used directly in connection with (4.1.10) to obtain an exact solution in cases where the expansion of the sphere is a stepwise linear function of time, but due to the first term in (4.1.18) and the continuity of f(s), the pressure history will become discontinous for each change of expansion rate.

4.3. Application to gas explosion experiments.

As already stated by Taylor (8) the influence of the nonlinearrity in the gasdynamics equations is significant for a spherical piston expanding in a gas. However, the effect decreases with distance, and a linear acoustic approximation can be expected to contain some of the important effects in connection with the generation of the pressure wave.

One such effect is the influence of variations in the flame speed during deflagration of gas clouds. This effect was inve-

stigated by Dechaies and Leyer (9), who concluded that even small changes in the expansion rate highly influence the generated pressure pulses.

The acoustic approximation described above is in fact able to illustrate this effect.

As no general analytical solution exist to eq. (4.1.14) it is not straightforward to perform an analytical pertubation analysis, but a numerical example shall be given.

In section 3.4 curves giving the "horizontal" and "vertical" radius of an expanding gascloud have been presented. Taking the mean of "horizontal" and "vertical" radius corresponding to experiment no. 69 the curves given by the dots in Figs. 165 and 166 are obtained. As these types of curves are given with limited resolution, large inaccuracies in the expansion rates and thereby in the calculated pressure can be introduced. Some kind of data smoothing technique is therefore required.

As the rate is very sensitive to the inaccuracies and at the same time of significant importance to the solution (eq. (4.2.3)) a limited Fourier series approximation of the rate rather than the expansion function itself has been chosen. In Figs. 165 and 166 below measured and smoothed data for experiment no. 69 are given for two different numbers of Fourier coefficients.

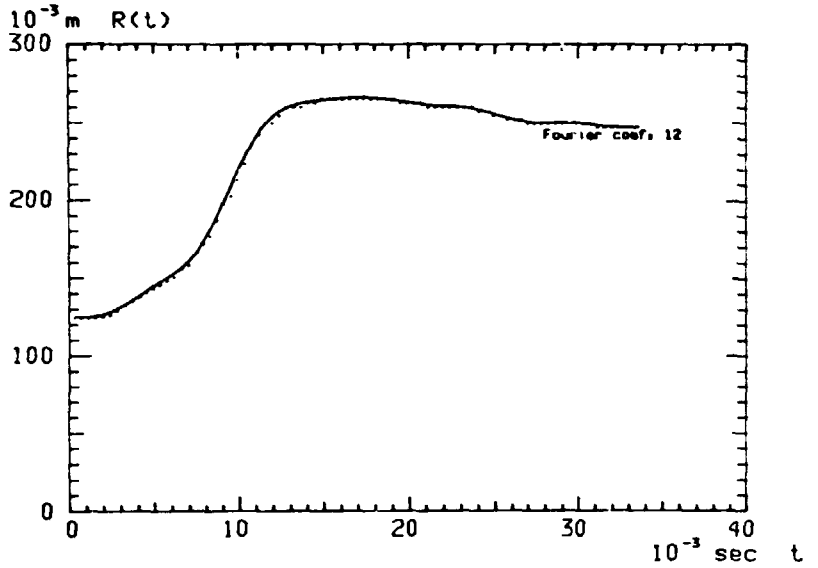

Fig. 165. Expansion of the gas cloud.

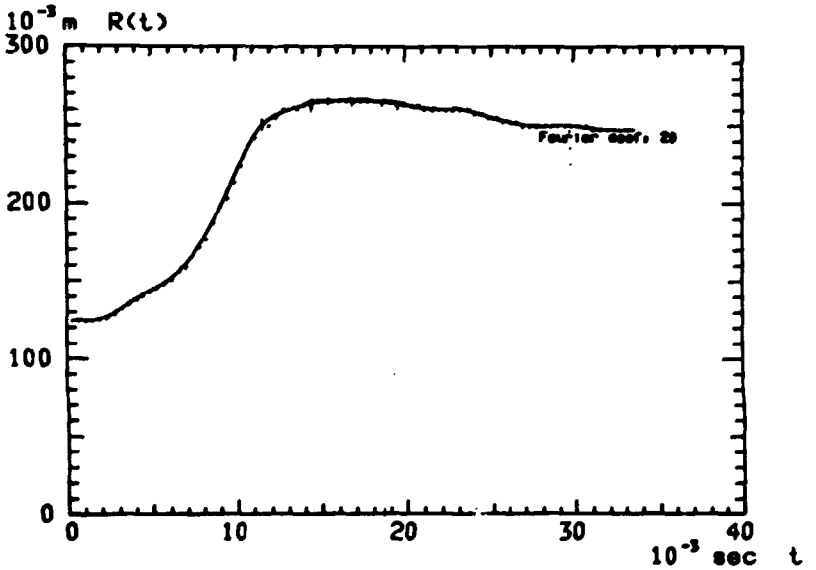

Fig. 166. Expansion of the gas cloud.

As can be observed, the differences between the two approximations are insignificant as concerns the R(t)-values.

In Figs. 167 and 168 below the corresponding calculated pressures are given at a distance of 1.9 m from the center of the expanding cloud.

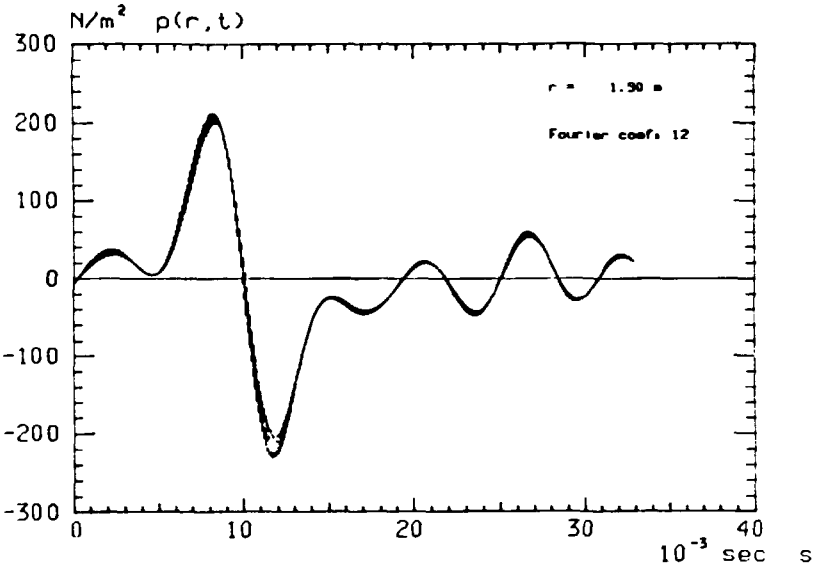

Fig. 167. Calculated pressure pulse.

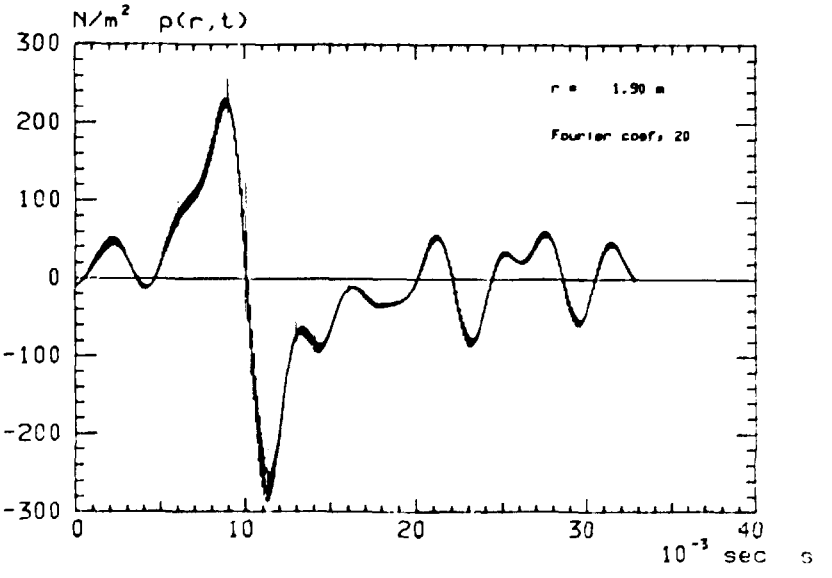

Fig. 168. Calculated pressure pulse.

From the above figures, the sensitivity of the pressure wave to changes in expansion rate is clearly demonstrated.

In Fig. 169 below the measured pressure is presented (note that the time scale differs from that in Figs. 167 and 168).

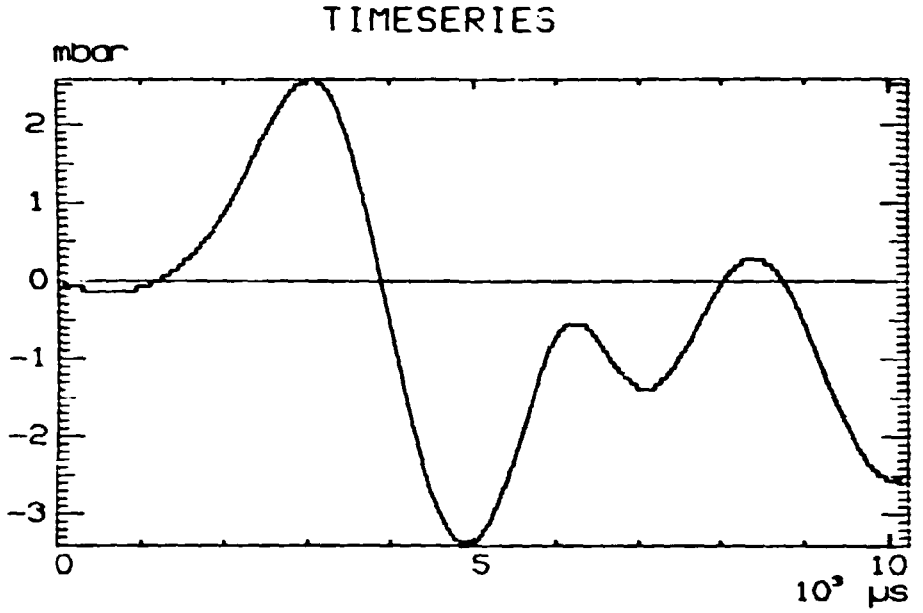

Fig. 169. Measured pressure pulse.

It is seen, that the agreement between Figs. 168 and 169 is reasonably good concerning the peak pressures and the variation in time, whereas Fig. 167 gives acceptable peak values but different time variation.

The high speed camera and the pressure recording system were not synchronized, and the absolute time values should therefore not be compared.

To sum up it has been demonstrated, that the generated pressure wave is very sensitive to changes in the expansion rate (and for small Mach numbers this effect can be expected to dominate nonlinear effects).

The unsatisfactory reproducibility of the pressure level observed in the experiments can be explained by small variations in the deflagration rate.

5. SUMMARY

The measurements have been performed with blast waves arising from homogeneous and well defined mixtures of methane, oxygen and nitrogen, contained within spherical balloons with controlled initial dimensions.

Blast waves without influence from reflected waves have been investigated, and a significant difference between near and far field has been observed, in the sense that the far fields possess rotational symmetry, whereas the near fields do not. Moreover, the attenuation is not as strong as that of the acoustic 1/R point source.

In the case of blast waves influenced by reflected waves from a hard surface it has been demonstrated that the flow field near the surface has a rather stochastic character due to scattering and diffraction effects. These effects are decreased with increasing distance from the reflecting surface.

When obstacles are placed on the surface an even more complicated flow field is obtained. Diffraction and scattering effects highly influence the pressure measurements on the obstacles, but generally the front pressure is larger than the side, top and back pressure, which is of the same order of magnitude. The maximum front pressure is obtained near the bottom in the middle of the surface. The maximal pressure build-up is in the range 1.5-2.0 times the pressure which would exist at the actual position in the absence of the obstacle.

No clear demarcation of end effects can be stated on the basis of the present experiments.

Wave-wave interaction phenomena have been observed when two obstacles are present in the flow field, if these are placed on a line from the center of the source and with moderate distance between them. If the boxes are placed besides each other the wave-wave interaction phenomenon is not initiated.

An acoustic approximation has been used to model the blast wave originating from an expanding sphere. It has been demonstated,

that the generated pressure pulse is very sensitive to the expansion rate. Calculated and measured data have been compared, and a reasonable agreement has been found.

REFERENCES

(1) Andrews, G.E. and Bradley, D. (1972). The burning velocity of methane-air mixtures. Combust. Flame 19, 275-288.

(2) Strehlow, R.A., Luckritz, R.T., Adamczyk A.A. and Shimpi, S.A. (1979). The Blast Wave Generated by Spherical Flames. Combust. Flame 35, 297-310.

(3) Landolt - Börnstein (1967). Zahlenwerte und Funktionen aus Physik - Chemie - Astronomie - Geophysik - Technik, Sechste Auflage, IV. Band, Technik, 4. Teil Wärmetechnik, Bandteil a (Springer, Berlin) 944 pp.

(4) Bo, P., Risø National Laboratory (Private Communication).

(5) Larsen, G., Roed, J. and Andersen, S.I. (1984). Gas explosion characterization, wave propagation (half-scale experiments), CEC Contract No. 025 SR DK, Final Report, Risø-R-499 163 pp.

(6) Lighthill, J. (1980). Waves in Fluids (Cambridge University Press, Cambridge) 504 pp.

(7) Achenbach, J.D. (1973). Wave Propagation in Elastic Solids (North Holland, Amsterdam) 425 pp.

(8) Taylor, G.I. (1946). The air wave surrounding an expanding sphere. Proc. R. Soc. London A 186, 273-292.

(9) Deshaies, B. and Leyer, J.C. (1981). Flow field induced by unconfined spherical accelerating flames. Combust. Flame, 40, 141-153.

(10) Gradshteyn, J.S. and Ryzhik, J.M. (1965). Table of Integrals, Series and Products (Academic Press, London) 1086 pp.

(11) Schmidt, H. and Krenk, S. (1982). Pressure wave generated by an expanding sphere. An acoustical approximation. TPM-82/1 (Risø National Laboratory) internal report. 14 pp.

LIST OF SYMBOLS

The most important designations and symbols, used in the present report, are listed and explained below.

A_i ; $i = 0,\cdots,4$	The coefficients in a polynomial expression for the heat capacity of steam.
B_i ; $i = 0,\cdots,4$	The coefficients in a polynomial expression for the heat capacity of carbon dioxide.
C_i ; $i = 0,\cdots,5$	The coefficients in a polynomial expression for the heat capacity of nitrogen.
D	The diameter of an expanding gas cloud.
L	The length of an obstacle.
P	The pressure.
P_M	The maximum peak pressure.
P_{p-p}	The peak-to-peak pressure.
Q(T)	The heat of the combustion at the temperature T.
$\tilde{Q}$	The effective heat addition.
R	The gas constant.
R(t)	The radius of an expanding sphere.
$R_1(X)$	The distance traveled by a "direct" signal.
$R_2(X)$	The distance traveled by a "reflected" signal.
T	The absolute temperature.
T	The time.
V	The volume.

X	The horizontal distance between the point of measurement and the source.
c_0	The speed of sound.
c_{pi} ; $i = 1,\cdots,3$	The heat capacity of component number i.
h	The measuring level.
h	The enthalpy.
m_i ; $i = 1,\cdots,3$	The mol fraction of component number i.
$\bar{q}$	The dimensionless heat added by the flame.
r	The measuring distance.
s	A transformed time variable.
t	The time.
Δt_c	The calculated time difference.
u	The velocity.
x	The position of a measuring point.
α	The expansion factor for the gasmixture.
α	The Mach number.
β_i ; $i = 3,4$	The parameters in a hyperbola fitted to the equilibrium Hugoniot for the gas mixture.
γ_1	The heat capacity ratio of the unburned mixture.
γ_2	The heat capacity ratio of the burned mixture.
λ	The Lamé constant.
ρ	The density.
$\sigma_{\%}$	The standard deviation in percentage of the mean value.

τ	The time.
ϕ	The velocity potential.

SUBSCRIPT

o	The ambient conditions.

SUPERSCRIPTS

(1)	The state before combustion.
(2)	The state after combustion.

SYMBOLS

*	The source.
·	A measuring point.
< >	A mean value.

APPENDIX 1

In this appendix the measured and theoretical expansion factors are compared for the actual stochiometric mixture.

Assuming that the burnt gas is in a homogeneous state, the measured expansion factor is given as the cubed ratio of the final to initial diameter of the gas cloud. The final diameter is in this context defined as the mean of the horizontally and vertically measured values.

Using the five final and initial diameters corresponding to the experiments performed with stochiometric mixtures, the values given in Table A1.1 are obtained

TEST NO.	69	70	71	73	74
α	8.24	8.00	8.00	8.00	6.03

$$\langle\alpha\rangle = 7.65$$

$$\sigma_{\%} = 11.9\%$$

Table A1.1 Measured expansion factors.

where α denotes an expansion factor

$\langle\alpha\rangle$ denotes the mean expansion factor

$\sigma_{\%}$ denotes the coefficient of variation corresponding to the above five values of α

The theoretical expansion factor has been calculated by means of the "Two-Gamma" heat-addition model given in (2)

$$\alpha = \frac{(\gamma_2 - 1)}{(\gamma_1 - 1)} \frac{\gamma_1}{\gamma_2} + \frac{\tilde{q}}{\gamma_2} \qquad \text{(A1.1)}$$

where

γ_1 denotes the heat-capacity ratio of the unburned mixture

γ_2 denotes the heat-capacity ratio of the burnt mixture

$\tilde{q}$ denotes the dimensionless heat added by the flame

The values for γ_1, γ_2 and $\tilde{q}$ are modified compared to the values given in (2), in accordance with the actual mixture and the actual temperature conditions. The modified values are given in Table A1.2.

γ_1	γ_2	$\tilde{q}$
1.4	1.088	8.253

Table A1.2. Values for γ_1 γ_2 and $\tilde{q}$.

The computation of these quantities is presented in Appendix 2

The expansion factor can then be calculated using formula (A1.1) and values given in Table A1.2. The following value is then obtained:

$$\alpha = 7.87$$

APPENDIX 2

The values of γ_1, γ_2 and q used in the calculation of the expansion factor α in APPENDIX 1 are evaluated in the following for the process

$$0.526\ N_2 + 0.158\ CH_4 + 0.316\ O_2 \rightarrow 0.158CO_2 + 0.526\ N_2 + 0.316\ H_2O$$

For one mole of the mixture, the Hugoniot and the equation of state for ideal gases are given in the form

$$h^{(2)} - h^{(1)} = -Q\left(T^{(1)}\right) + \sum_{i=1}^{3} m_i^{(2)} \int_{T^{(1)}}^{T^{(2)}} C_{pi}^{(2)}\, dT$$

$$= \tfrac{1}{2}\left(P^{(2)} - P^{(1)}\right)\left(V^{(2)} + V^{(1)}\right) \qquad \text{(A2.1)}$$

$$P^{(1)}V^{(1)} = R\,T^{(1)}\left(\sum_{i=1}^{3} m_i^{(1)}\right) = R \cdot T^{(1)} \qquad \text{(A2.2)}$$

$$P^{(2)}V^{(2)} = R\,T^{(2)}\left(\sum_{i=1}^{3} m_i^{(2)}\right) = R \cdot T^{(2)} \qquad \text{(A2.3)}$$

where

- h denotes the enthalpy,
- Q(T) denotes the heat of the combustion,
- m_i denotes the molar fraction of component number i,
- C_{Pi} denotes the heat capacity of component number i,
- T denotes the absolute temperature,
- P denotes the pressure,
- V denotes the volume,

R denotes the gas constant,

and superscripts (1) and (2) refer to the state before and after the combustion, respectively.

For fixed $P^{(2)}$, the value of $V^{(2)}$ can be computed from (A2.1) and (A2.3).

The special case, where $P^{(1)} = P^{(2)}$ shall be treated separately.

$P^{(1)} = P^{(2)}$:

$$\sum_{i=1}^{3} m_i^{(2)} \int_{T^{(1)}}^{T^{(2)}} C_{Pi}{}^{(2)} \, dT = Q\left(T^{(1)}\right) \tag{A2.4}$$

$$V^{(2)} = \frac{T^{(2)} \cdot R}{P^{(2)}} \tag{A2.5}$$

In all other cases we have

$P(1) \neq P^{(2)}$,

$$\sum_{i=1}^{3} m_i^{(2)} \int_{T^{(1)}}^{T^{(2)}} C_{Pi}{}^{(2)} \, dT - \frac{R}{2}\left(P^{(2)} - P^{(1)}\right)\frac{T^{(2)}}{P^{(2)}} =$$

$$Q\left(T^{(1)}\right) + \frac{R}{2}\left(P^{(2)} - P^{(1)}\right)\frac{T^{(1)}}{P^{(1)}} \tag{A2.6}$$

$$V^{(2)} = \frac{T^{(2)} \cdot R}{P^{(2)}} \tag{A2.7}$$

The values for C_{Pi} are given in (3) and (4). As the combustion products have been treated as ideal gases the C_P values corresponding to the ideal gas state have been used. The disso-

ciation of the steam has been taken into account. These C_p values have been plotted as a function of the absolute temperature in Figs. A2.1-3.

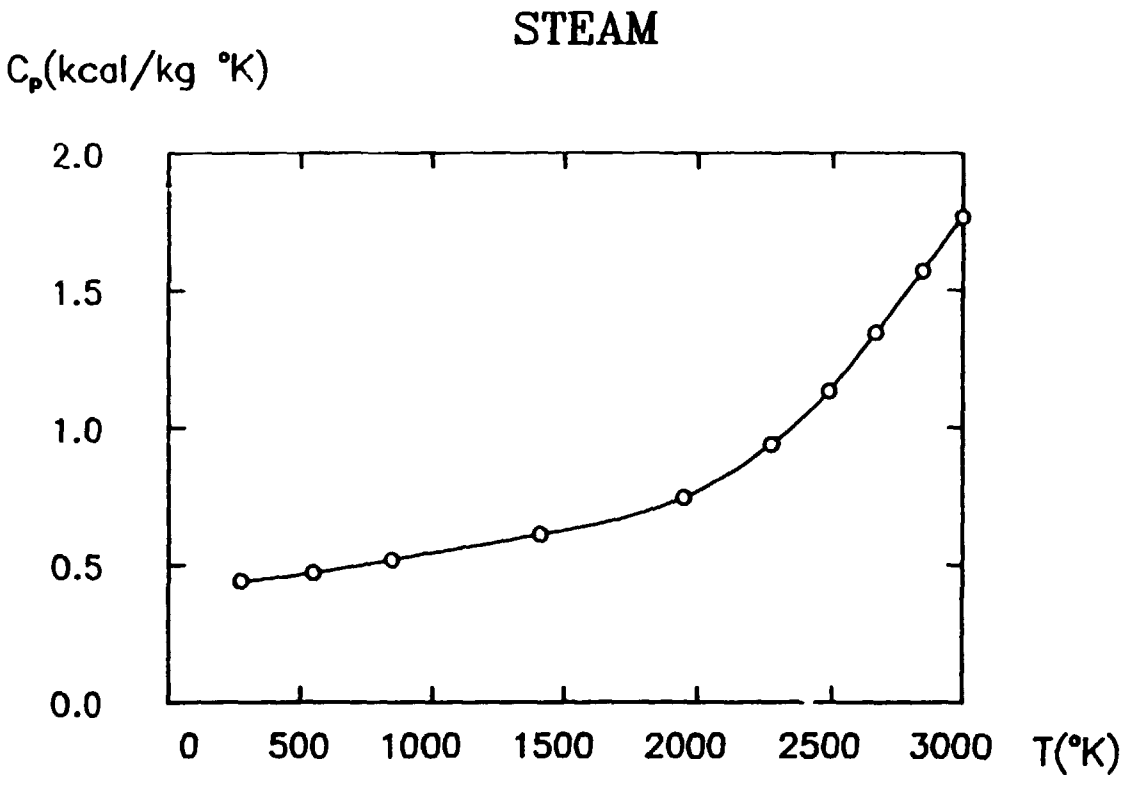

Fig. A2.1. C_p for steam as a function of the temperature.

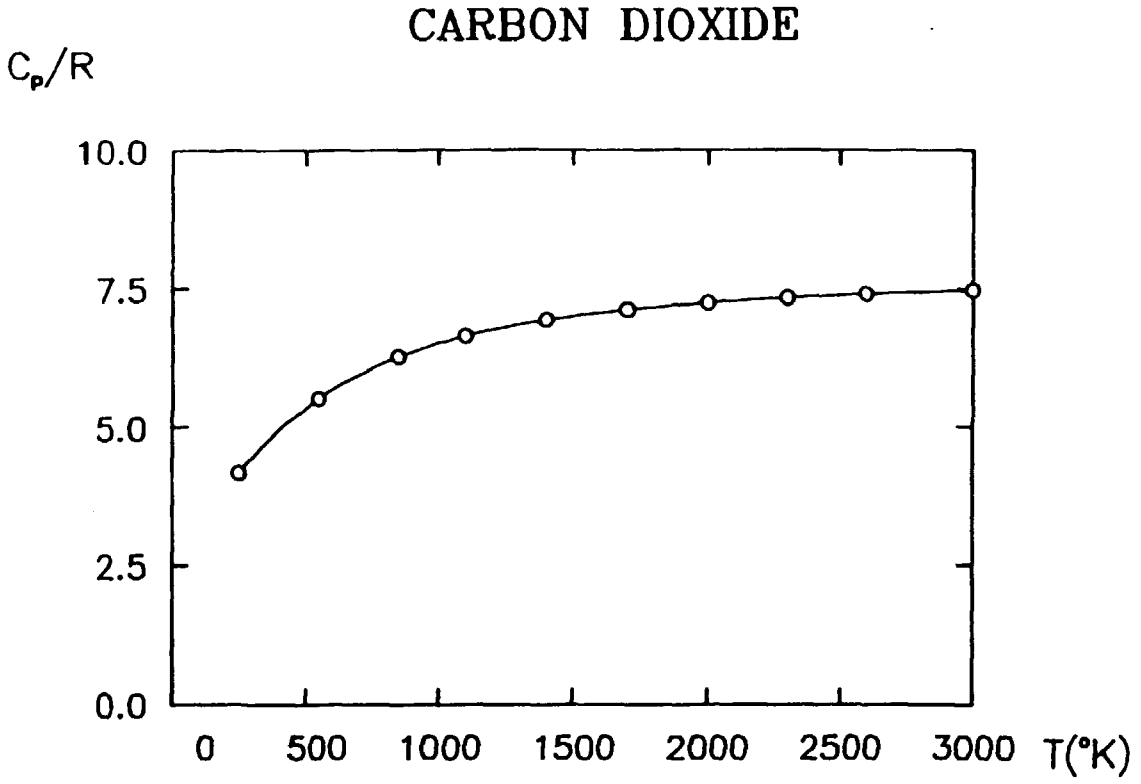

Fig. A2.2, C_p/R for carbon dioxide as a function of the temperature.

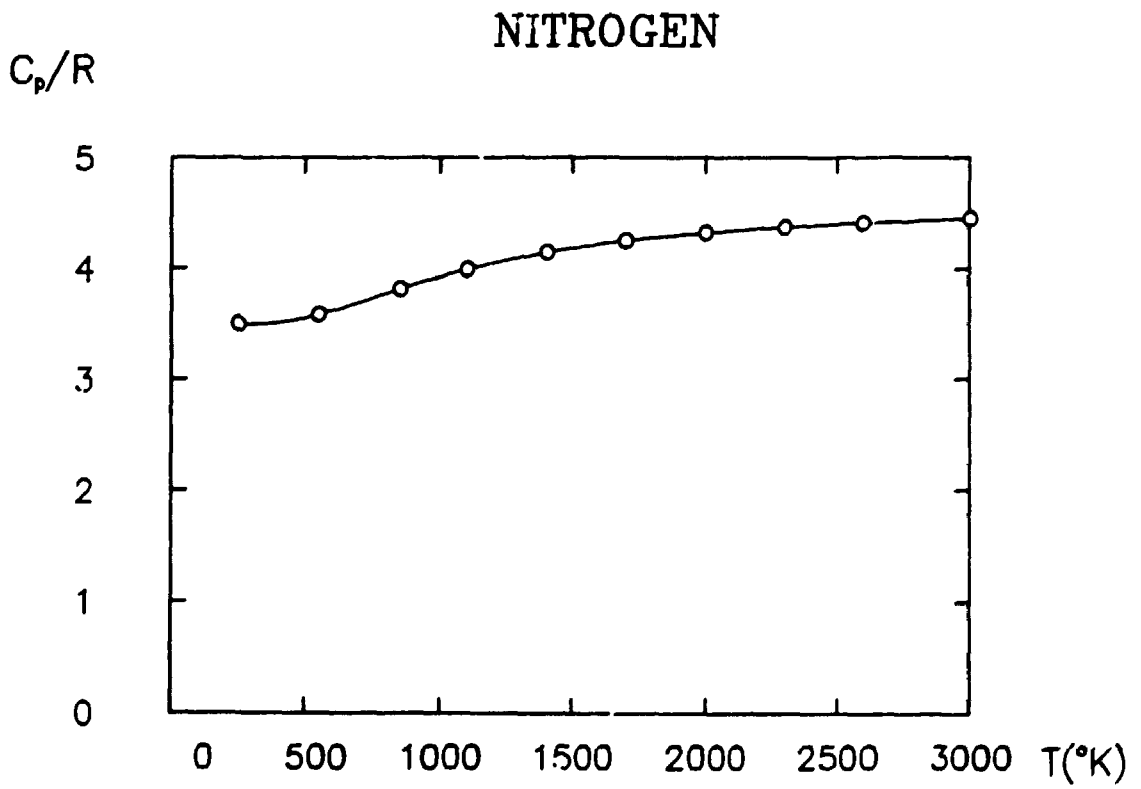

Fig. A2.3, C_p/R for nitrogen as a function of the temperature.

The C_P values are now expressed as polynomials of the temperature. On the basis of the figures A2.1-3 the following polynomials have been chosen

$$C_{P1}^{(2)} = C_{P,STEAM} = A_0 + A_1T + A_2T^2 + A_3T^3 + A_4T^4 \qquad (A2.8)$$

$$C_{P2}^{(2)} = \frac{C_{P,CO2}}{R} = B_0 + B_1T + B_2T^2 + B_3T^3 + B_4T^4 \qquad (A2.9)$$

$$C_{P3}^{(2)} = \frac{C_{P,N2}}{R} = C_0 + C_1T + C_2T^2 + C_3T^3 + C_4T^4 + C_5T^5 \qquad (A2.10)$$

The coefficients have been found by a least square fit in the temperature range 250°K - 3000°K. For each fit 10 points have been used, and the following values have been obtained.

$$\begin{aligned}
A_0 &= 0.35490638 \\
A_1 &= 0.37353714 \cdot 10^{-3} \\
A_2 &= -0.30155810 \cdot 10^{-6} \\
A_3 &= 0.10961716 \cdot 10^{-9} \\
A_4 &= 0.81363817 \cdot 10^{-15}
\end{aligned}$$

$$\begin{aligned}
B_0 &= 0.25835872 \cdot 10 \\
B_1 &= 0.76507162 \cdot 10^{-2} \\
B_2 &= -0.50716299 \cdot 10^{-5} \\
B_3 &= 0.15715755 \cdot 10^{-8} \\
B_4 &= 0.18329810 \cdot 10^{-12}
\end{aligned}$$

$$\begin{aligned}
C_0 &= 0.36636960 \cdot 10 \\
C_1 &= -0.13535724 \cdot 10^{-2} \\
C_2 &= 0.33151806 \cdot 10^{-5} \\
C_3 &= 0.23183266 \cdot 10^{-8} \\
C_4 &= 0.69361671 \cdot 10^{-12} \\
C_5 &= -0.76438232 \cdot 10^{-16}
\end{aligned}$$

For a mixture at 20°C and at 1 atm, the following values are valid

$$Q(T^{(1)}) = 1248 \text{ l·atm}$$

$$m_1^{(2)} = m_{H2O} = 0.316$$

$$m_2^{(2)} = m_{CO2} = 0.158$$

$$m_3^{(2)} = m_{N2} = 0.526$$

$$P^{(1)} = 1 \text{ atm}$$

$$T^{(1)} = 293^{\circ}K$$

$$V^{(1)} = 24.0551 \text{ l}$$

$$R = 8.206 \cdot 10^{-2} \text{ l·atm}/^{\circ}K$$

$$= 4.5123 \cdot 10^{-2} \frac{\text{kcal}}{\text{kg}\cdot^{\circ}K}$$

Corresponding values of $P^{(2)}$, $T^{(2)}$ and $V^{(2)}$ are now obtained from (A2.4), (A2.5) and from (A2.7), (A2.8). These are given in Table A2.1 below.

$p^{(2)}$(atm.)	t(2)(K)	$v^{(2)}$(1)
1	2321	190.5
2	2335	95.8
3	2349	64.3
4	2363	48.5
5	2377	39.0
6	2390	32.7
7	2404	28.2
8	2417	24.8
9	2430	22.2
10	2444	20.1
11	2457	18.3
12	2470	16.9
13	2483	15.7
14	2496	14.6
15	2508	13.7
16	2521	12.9
17	2533	12.2
18	2546	11.6
19	2558	11.0
20	2570	10.5

Table A2.1 Corresponding values of $p^{(2)}$, $v^{(2)}$ and $T^{(2)}$.

From (2) it is seen, that the values given in Table A2.1 can be fitted to a rectangular hyperbola of the form

$$\left(\frac{p^{(2)}}{p^{(1)}} + \beta_3\right)\left(\frac{v^{(2)}}{v^{(1)}} - \beta_3\right) = \beta_4$$

By a least square-fit to the 20 points given in Table A2.1, the following values for β_3 and β_4 are obtained

$$\beta_3 = 0.4212 \cdot 10^{-1}$$
$$\beta_4 = 7.9538410$$

This gives:

$$\gamma_2 = \frac{1 + \beta_3}{1 - \beta_3} = 1.088$$

With $\gamma_1 = 1.4$, $\tilde{Q}$ can be determined as

$$\tilde{Q} = \left[\beta_4 - \frac{2(\gamma_1 + \gamma_2)(\gamma_2 - 1)}{(\gamma_2 + 1)^2 (\gamma_1 - 1)}\right] \frac{\gamma_2 + 1}{\gamma_2 - 1} \frac{P^{(1)} V^{(1)}}{2}$$

$$= 2198 \text{ l} \cdot \text{atm}.$$

Hence

$$\tilde{q} = [(\gamma_2 - 1)\, \tilde{Q}/P_0 V_0] = 8.255$$

where $P_0 = 1$ atm and $V_0 = 23.43$ l refer to the ambient conditions. The ambient conditions have been chosen as a mean of the P_0 and the V_0 values corresponding to the experiments recorded by the high-speed camera.

Sales distributors:
G.E.C. Gad Strøget
Vimmelskaftet 32
DK-1161 Copenhagen K, Denmark

Available on exchange from:
Risø Library, Risø National Laboratory,
P.O.Box 49, DK-4000 Roskilde, Denmark

ISBN 87-550-1122-5
ISSN 0106-2840